THE UNIVERSITY OF QUEENSLAND

AUSTRALIA

Developing lipid-coated calcium carbonate/phosphate hybrid nanoparticles as a gene/drug co-delivery platform for combined cancer therapy

Yilun Wu

Bachelor of Engineering, Master of Engineering

A thesis submitted for the degree of Doctor of Philosophy at

The University of Queensland in 2019

Australian Institute for Bioengineering and Nanotechnology

Abstract

Cancer is one of the most life-threatening types of diseases. Various agents, such as chemical drugs, oligonucleotides, and bioactive proteins, are developed for cancer treatment. Due to the unsatisfied outcomes of treatment relying on single anticancer agent, more studies are focused on developing regimens for combination therapy. Nowadays, nanoparticle (NP) based drug carriers have shown great potential to increase the anticancer agent efficacy as they are able to provide protection during circulation and improve tumour site accumulation via targeting delivery. Moreover, a proper NP-based carrier can deliver multiple anticancer agents with the similar efficacy for combinational treatment of tumours. This Ph.D. project aims to engineer lipid-coated calcium carbonate/phosphate (LCCP) hybrid nanoparticles (NPs), with optimised cargo release property, to carry two anti-cancer agents and achieve effective cancer therapy.

Calcium carbonate (CaC) and calcium phosphate (CaP) are the most commonly used inorganic materials for gene delivery. The difference between the dissolution behaviours of CaC/CaP nanoparticles suggests that the pH for the release of loaded therapeutic agents is adjustable by controlling the composition of mixed CaC/CaP nanoparticle core. The coated bilayer phospholipids endow the particles with good colloidal stability, and are able to load hydrophobic drug. Moreover, the bilayer lipids can be conjugated with target moieties for target delivery to cancer cells. This Ph.D. thesis first optimised the LCCP core composition (i.e. carbonate to phosphate molar ratio) to achieve gene release at endosomal pH using dsDNA-cy5 as an example. The obtained LCCP NPs showed good colloidal stability with the average particle size of 40 nm, high gene loading capacity (~60%), desirable gene release profile, and enhanced cellular uptake efficacy. Compared to lipid-coated calcium phosphate (LCP) NPs, LCCP NPs achieved higher sensitivity and quicker release under mild acidic pH conditions (6.0-5.5). As-prepared LCCP hybrid NPs were then used to deliver small interference RNA (siRNA) for mouse programme death ligand 1 (PD-L1) and polo-like kinase 1 (PLK1) to B16F10 melanoma cancer cells, with the delivery efficacy higher than Oligofectamine®. This tendency endows faster siRNA release during the endocytosis and quicker gene down-regulation after NP endocytosis, but not affect their long term gene silencing efficacy.

Folic acid (FA) was then conjugated on the surface to enhance the delivery efficacy via interacting with the FA receptor overexpressed on cancer cells. Subsequently, the hydrophobic anticancer drug, α-tocopheryl succinate (α-TOS), was loaded in the lipid bilayer in combination with Allstar Cell Death siRNA (CD siRNA) in the core of target LCCP NPs for

combined target therapy of melanoma cells. The optimised FA density was 5% of lipids on the outer layer, as determined by cellular uptake of NPs by B16F0 cells. The combination of CD siRNA and α-TOS in LCCP NPs effectively inhibited the cell growth via an additive/synergic way.

To further preventing cancer metastasis, α-TOS loaded LCCP NPs (NP-TOS15) were employed to treat 4T1 tumour in combination with interferon-gamma (IFN-γ). The optimised NP-TOS15 showed an α-TOS loading efficiency of ~60%, and enhanced the uptake by 4T1 metastatic cancer cells. The IFN-γ/NP-TOS15 treatment significantly induced 90% cell death and inhibited migration of tumour cells. Moreover, NP-TOS15 upregulated the anticancer immunity via downregulating program death ligand 1 (PD-L1) expression induced by IFN-γ, and remarkably prevented the lung metastasis (metastasis index decreased from 10800 to 500), particularly in combination with IFN-γ. Further investigation revealed that this combination therapy also modulated the $CD4^+$ and $CD8^+$ cytotoxic lymphocyte infiltration into the tumour tissue for tumour elimination. Taken together, the NP delivery of α-TOS in combination with IFN-γ provides an applicable strategy for cancer therapy.

In summary, the LCCP NPs were well developed to be a promising platform for gene/drug co-delivery to combined cancer treatment.

Declaration by author

This thesis is composed of my original work, and contains no material previously published or written by another person except where due reference has been made in the text. I have clearly stated the contribution of others to jointly-authored works that I have included in my thesis.

I have clearly stated the contribution of others to my thesis as a whole, including statistical assistance, survey design, data analysis, significant technical procedures, professional editorial advice, financial support and any other original research work used or reported in my thesis. The content of my thesis is the result of work I have carried out since the commencement of my higher degree by research candidature and does not include a substantial part of work that has been submitted to qualify for the award of any other degree or diploma in any university or other tertiary institution. I have clearly stated which parts of my thesis, if any, have been submitted to qualify for another award.

I acknowledge that an electronic copy of my thesis must be lodged with the University Library and, subject to the policy and procedures of The University of Queensland, the thesis be made available for research and study in accordance with the Copyright Act 1968 unless a period of embargo has been approved by the Dean of the Graduate School.

I acknowledge that the copyright of all material contained in my thesis resides with the copyright holder(s) of that material. Where appropriate I have obtained copyright permission from the copyright holder to reproduce material in this thesis and have sought permission from co-authors for any jointly authored works included in the thesis.

Publications during candidature

Peer-reviewed papers:

1. **Wu Y**, Chen W, Gilliard M; Xu Z, Gu W. PD-L1-based cancer immunotherapy: blocking, knocking down, or inhibition. (Under reviewing in Front. Immunol.)

2. **Wu Y**, Gu W, Xu Z. Enhanced combination cancer therapy using lipid-calcium carbonate/phosphate nanoparticles as a targeted delivery platform. *Nanomedicine*, **2018**, 14(1): 77-92.

3. **Wu Y**, Gu W, Tang J, Xu Z. Devising new lipid-coated calcium phosphate/carbonate hybrid nanoparticles for controlled release in endosomes for efficient gene delivery. *J Mater. Chem. B*, **2017**, 5(34): 7194-7203.

4. Kong L, **Wu Y**, Alves C.S. Shi X. Efficient delivery of therapeutic siRNA into glioblastoma cells using multifunctional dendrimer-entrapped gold nanoparticles. *Nanomedicine*, **2016**, 11(23): 3103-3115.

5. Ding L, Hu Y, Luo Y, Zhu J, **Wu Y**, Yu Z, Cao X, Peng C, Shi X, Guo R. LAPONITE (R)-stabilized iron oxide nanoparticles for in vivo MR imaging of tumors. *Biomater. Sci*, **2016**, 4(3): 474-482

Conference abstracts:

1. Lipid-coated Calcium Phosphate/Carbonate Hybrid Nanoparticles for Precise Control Release. 8th International NanoMedicine Conference. Sydney's Coogee Beach at the Crowne Plaza Hotel from July 3 to 5, 2017 (Oral presentation).

2. Lipid-coated calcium carbonate/phosphate hybrid nanoparticles as a novel vector for gene delivery to cancer cells. 8th International Symposium on Nano & Supramolecular Chemistry. The University of Queensland, 13-16 July 2016 (Oral presentation).

3. Lipid coated calcium carbonate/phosphate nanoparticles as a novel gene/drug co-delivery platform for cancer treatment. 11th European Foundation for Clinical Nanomedicine. Basel, Switzerland, 2-5 Sept 2018 (Poster presentation)

4. Lipid-coating Calcium Carbonate/Phosphate (LCCP) Nanoparticles as a Novel Gene/Drug Delivery Platform for Cancer Therapy. International Conference on Nanomedicine and Nanobiotechnology. Rome, Italy, 26-29 Sept 2018 (Oral presentation)

Publications included in this thesis

1. **Wu Y**, Chen W, Gilliard M; Xu Z, Gu W. PD-L1-based cancer immunotherapy: blocking, knocking down, or inhibition. (*Under reviewing in Front. Immunol*.)

Contributor	Statement of contribution
Author Yilun Wu (Candidate)	Conception and design (40%) Analysis and interpretation (70%) Drafting and production (80%) Language check (25%)
Author Weiyu Chen	Drafting and production (10%)
Author Marianne Gilliard	Language check (25%)
Author Zhi Ping (Gordon) Xu	Conception and design (10%) Analysis and interpretation (10%) Drafting and production (5%) Language check (25%)
Author Wenyi Gu	Conception and design (50%) Analysis and interpretation (20%) Drafting and production (5%) Language check (25%)

2. **Wu Y**, Gu W, Xu Z. Enhanced combination cancer therapy using lipid-calcium carbonate/phosphate nanoparticles as a targeted delivery platform. *Nanomedicine*, **2018**, 14(1): 77-92.

Contributor	Statement of contribution
Author Yilun Wu (Candidate)	Conception and design (70%) Analysis and interpretation (80%) Drafting and production (70%)
Author Wenyi Gu	Conception and design (15%) Analysis and interpretation (10%) Drafting and production (10%)
Author Zhi Ping (Gordon) Xu	Conception and design (15%) Analysis and interpretation (10%) Drafting and production (20%)

3. **Wu Y**, Gu W, Tang J, Xu Z. Devising new lipid-coated calcium phosphate/carbonate hybrid nanoparticles for controlled release in endosomes for efficient gene delivery. *J Mater. Chem. B*, **2017**, 5(34): 7194-7203.

Contributor	Statement of contribution
Author Yilun Wu (Candidate)	Conception and design (70%) Analysis and interpretation (80%) Drafting and production (70%)
Author Jie Tang	Conception and design (10%)
Author Wenyi Gu	Conception and design (10%) Analysis and interpretation (10%) Drafting and production (10%)
Author Zhi Ping (Gordon) Xu	Conception and design (10%) Analysis and interpretation (10%) Drafting and production (20%)

Contribution by others to the thesis

TEM was performed by Dr Weiyu Chen and Ms Bei Li. XPS and XRD were performed by Dr Barry J Wood (Scientific manager in centre for microscopy and microanalysis, CMM). ICPAES was conducted by Dr David Appleton (Senior Scientific Officer, Agriculture and Food Sciences). H&E staining was prepared by Dr Darryl Whitehead (Research Manager, Histology Facility, School of Biomedical Sciences).

Statement of parts of the thesis submitted to qualify for the award of another degree

None.

Research involving human or animal subjects

All animal work was approved by the anatomical Biosciences Animal Ethics Committee (AEC). A copy of the ethics approval letter is included in the thesis appendix.

Acknowledgements

Firstly, I would like to thank my supervisor team. I'd like to express my sincere appreciation to my supervisor Prof. Zhi Ping (Gordon) Xu for all the intellectual support and guidance. Great thanks to Gordon for all the critical thinking, cautious attitude, and practical knowledge I've learned from him during the 4 year Ph.D. time, and the friendly guide to my career development. It's a great honour to have such a wise intellectual as my supervisor. Also, I would like to express fully gratitude to my co-supervisor Dr Wenyi Gu for his kind help in my PhD research work. Many thanks to Dr Gu for his help in scientific thinking and paper design. It's very lucky and grateful to have such a knowledgeable mind in my supervisor team. In specific, I would like to appreciate the kind advice from my confirmation examiners Dr Harendra Parekh and Dr Deanne Whitworth.

Meanwhile, I'm genuinely appreciated for the assistance and pleasure teamwork to all my group members: Dr Li Li, Dr Peng Li, Dr Run Zhang, Dr Hang Ta, Dr Zi Sophia Gu, Dr Huali Zuo, Dr Wenyu Chen, Dr Shiyu Yan, Dr Jie Tang, Mr Yanheng Wu, Miss Bei Li, Ms Fatemeh Movahedi, Miss Pei Cao, Miss Jianping Liu, Mr Bing Sun, Mr Khuram Shahzad, Miss Luyao Sun, Mr Guanyu Hao, Mr Jiaxi Yong, Dr Hua Chen, Dr Mengxue Li, and Miss Xing Zhang. Also, I would like to acknowledge the office managers for the safety guidance and other lab convenience due to their endeavours: Ms Cheryl Berquist and Ms Colette Godfrey. Sincere appreciation to the staff and colleagues in AIBN, CMM, ANFF, SBS, and UQBR for their technical support and contributions. Special thanks to the awesome AIBN IT helpdesk team. Many times they save my Ph.D. life by rescuing my poor laptop.

All the financial supports are sincerely appreciated. Many thanks to the Australian government for offering me the Research training program (RTP) scholarship and liver allowance to support my Ph.D. study. Many thanks to the domestic and international travelling grants from AIBN for sponsoring my conference attendance in Sydney, Zurich, and Roma.

Finally, I would like to express my deepest gratitude to my beloved parents, grandfather, and boyfriend Fanfan Fu. You are always on my side, giving me everlasting love, irreplaceable support, and infinite courage to face the unknown, chase the dream, and see the beautiful. I love you all forever.

Financial support

This research was financially supported by Australian Government Research Training Program (RTP) Scholarship, Australian Research Centre (ARC) Discover Project (DP) grant (DP170104643).

Keywords

Lipid-coated calcium carbonate/phosphate nanoparticle, gene delivery, drug delivery, combination cancer therapy, alpha-tocopheryl succinate, immunotherapy, interferon-gamma, programme death ligand 1, cancer metastasis

Australian and New Zealand Standard Research Classifications (ANZSRC)

ANZSRC code: 090302 (Biomedical Engineering, 40%)

ANZSRC code: 100708 (Nanomaterials, 30%)

ANZSRC code: 111204 (Cancer therapy, 30%)

Fields or Research (FoR) Classification

FoR code: 0903, Biomedical Engineering, 40%

FoR code: 1007, Natechnology, 30%

FoR code: 1112, Oncology and Carcinogenesis, 30%

Table of Contents

List of Figures

Chapter 2

is characterised by TEM. Reprinted with the permission from Xu et al. [64]. Copyright (2013) Elsevier B.V.

Figure 2.8 Different polymorphs of CaC NPs. Vaterite belongs to the hexagonal crystal system, whereas calcite occurs in the trigonal and aragonite in the orthorhombic systems. The morphological forms of CaC are related to the synthesis conditions, such as the concentration of reactants, temperature and nature of additives. Reprinted with the permission from Maleki D.S. et al. [67]. Copyright (2015) Taylor & Francis.

Figure 2.9 Example of carbon dioxide gas generation from CaC based NPs for tumour imaging application. (A) Schematic illustration of the pH triggered gas generation; **(B)** optical micrographs of CO2 generating from CaC based NPs incubated in PBS at pH (i) 6.8 and (ii) 7.4 for 90 min; **(C)** ultrasound imaging of the SCC-7 tumour bearing mouse by intratumoural injection of CaC based NPs; and **(D)** the histogram of an ultrasound intensity profile from tumour size as a function of time. Reprinted with the permission from Min KH et al.[118]. Copyright (2015) American Chemical Society.

Figure 2.10 LCC NPs for peptide delivery. (A) The TEM image of LCC NPs, **(B)** tumour growth inhibition of LCC NPs with EV peptide in an H460 tumour bearing nude mouse model. **(C)** The disruption of the CaC cores measured by dynamic light scattering, and **(D)** SDS-PAGE image of the EV peptide release from LCC NPs under different pHs. Reprinted with the permission from Kim et al. [65] Copyright (2013) Elsevier. B.V.

Figure 2.11 Scheme showing the synthesis and structure of Ce6(Mn)@CaCO3-PEG NPs. Reprinted with the permission from Dong et al.[128]. Copyright (2016) Elsevier. B.V.

Figure 2.12 Immunotherapy based on PD-1/PD-L1 interaction. (A) The interaction of PD-1/PD-L1 causes tumour immune tolerance. The PD-1/PD-L1 interaction stimulates the downstream signals to suppress T cell activation, resulting in tumour cell survival. **(B)** Breakdown of the PD-1/PD-L1 interaction reactivates T cells and related immune responses. Without the PD-1/PD-L1 interaction, the suppression signal is removed, thus leading to T cell activation, proliferation, and cytokine generation and tumour cell elimination.

Figure 2.13 Immunomodulation effects of IFN-γ. IFN-γ produced by immune cells affects the behaviour of distinct immune cells within the tumour microenvironment. Specifically, IFN-γ activates anticancer immunity by promoting the activity of CD4 Th1 cells, CD8 cytotoxic T lymphocytes (CTLs), natural killer (NK) cells, dendritic cells (DCs), and macrophages

Figure 4.8 Down-regulation of PD-L1 expression in B16F10 cells. (A) PD-L1 protein expression on the surface of cells at 48 h post transfection; (B) Fold change of PD-L1 mRNA expression. PD-L1 siRNA: 40 nM.

Figure 4.9 The viability of B16F10 cells upon PLK1 siRNA transfection using P3C1 and P4C0 NPs**. (A)** The inhibition of cancer cell growth; **(B)** The growth inhibition comparison of P4C0-PLK1 siRNA and P3C1-PLK1 siRNA transfection for 48 h.

Figure 4.10 (A) The schematic pH responsive release of CaC and/or CaP cores. The hybrid CaC/CaP cores show unique release profile within pH 6.0-5.5, and the release percentage of CaC/CaP is more than that of CaP**. (B)** The fate of P4C0 and P3C1 NPs after internalisation. The clathrin-mediated endocytosis undergoes the endosome/ lysosome digestion pathway. The pH value dropped from 7.4 in Step 1 to 5.0-4.0 in Step 5 (lysosome). Sorted by dissolution pH value, the release of P4C0 and P3C1 NPs might be mainly in Step 3-4 and Step 4-5, respectively. siRNA released in Step 5 might be partially degraded because of lysosomal enzymes.

Figure S 4.1 (A) The hydrodynamic diameter of LCCP NPs, represented by Number (%); and **(B)** XRD pattern of P4C0 and P3C1 cores.

Figure S4.2 TEM image of P3C1 NPs negative staining with 1% uranyl acetate.

Figure S4.3 XPS survey scan of **(A)** P4C0 and **(B)** P3C1 cores coated with DOPA. The details of P3C1 were shown in high resolution scan of **(C)** P2p and **(D)** C1s.

Figure S4.4 FTIR spectrum for the LCCP cores.

Figure S4.5 (A) P2C2 release profile; **(B)** DNA band intensity in Figure 4 normalized by the first lane dsDNA in corresponding line; **(C)** The release trend of P4C0 and P3C1 cores under different pH values.

Figure S4.6 The effect of P/C ratios on the taken up of particles with 25 nM dsDNA-cy5, represented by MFI.

Figure S4.7 The positive cell percentage of B10F10 treated with P4C0 or P3C1 with dsDNA-cy5 at 25 nM cy5 concentration. Cells were cultured in DMEM containing 10% FBS for 4 h with P4C0 or P3C1 NPs.

Figure S4.8 CLSM images of the same region of cells at different z stacks. The z = 6 and 7 planes were focused on the central of most cells in the selected area. The individual channels

and three-view diagrams based on the images at z = 6 position of each series (blue framed) was chosen as examples and shown in Figure 4.7.

Figure S4.9 The down regulation of PD-L1 expression for B16F10 cells treated with Oligo-PDL1 (40 nM)

Chapter 5

Scheme 5.1 Schematic illustration of the structure of LCCP NPs, loaded with CD siRNA/α-TOS and FA conjugated onto the surface.

Figure 5.1 (A) Models of LCCP NP with α-TOS replacing DOPC and cholesterol. **(B)** TEM image of CD/TOS/FA NPs. **(C)** The size distribution of NPs obtained from DLS. **(D)** FT-IR spectrum of α-TOS, LCCP and LCCP-TOS, with new peaks shown in red (1480-1400 cm^{-1}), green (1100-1050 cm^{-1}) and blue (879 cm^{-1}).

Figure 5.2 Cellular uptake of various LCCP NPs. **(A)** The effect of FA amount on cellular uptake of NPs with 25 nM dsDNA-cy5 for 4 h in DMEM medium with 10% FBS. **(B)** FA blocking assay. **(C)** and **(D)** The effect of dose and time on the cellular uptake of FA10-PEG10 NPs.

Figure 5.3 B16 cell viability after treatment for 48 h. Cells treated with **(A)** CD/FA, **(B)** scr/TOS/FA, **(C)** CD/TOS, or **(D)** CD/TOS/FA NPs.

Figure 5.4 The effect of NPs on ROS production by B16 cells after 6 h treatment. ROS production (green) was examined using CLSM **(A)** and quantified using flow cytometry **(B)**. The concentration used was: [CD siRNA] = 24 nM and [α-TOS] = 10 μM.

Figure 5.5 Flow cytometric analysis of cell distribution for early/late apoptosis and necrosis on B16F0 cells after typical treatment with **(A)** CD/FA, **(B)** scr/TOS/FA, **(C)** CD/TOS/FA, or **(D)** scr/FA NP treatment for 24 h. The average percentage of cells under apoptosis or necrosis status was calculated after three parallel tests and shown **(E)**.

Figure 5.6 The suppression of Bcl-2 protein expression by treatment with NPs for 48 h. **(A)** Western blot analysis; **(B)** Densitometry analysis of Bcl-2 expression against β-actin. The concentration used was: [CD siRNA] = 24 nM and [α-TOS] = 10 μM.

Figure 5.7 Cell cycle analysis by staining the DNA in B16F0 cells after 24 h treatment. **(A)** control; **(B)** CD/FA NPs; **(C)** scr/TOS/FA NPs; and **(D)** CD/TOS/FA NPs. The distribution of

different cell cycle phases in gated cells was counted **(E)**, and the fold change in G1 phase after NP treatment was calculated and normalized to that of the control **(F)**.

Figure 5.8 Proposed mechanism for CD siRNA and α-TOS B16 cancer cell growth inhibition. The anticancer action leads to (1) apoptosis and (2) cell cycle arrest. The treatment induces ROS production and Bcl-2 suppression, resulting in the damaged mitochondrion and cell apoptosis. Here, α-TOS further contributes to cell cycle arrest in G1 phase. Dash arrows: weak interactions; Black arrows: strong interactions.

Figure 5.9 The inhibitory effect of NPs on 4T1 cells and the xenograft tumour growth. (A) The inhibition of 4T1 cancer cell growth by NPs in vitro. **(B)** Tumour growth curve represented by tumour size, **(C)** the tumour weight at Day 14, and **(D)** the body weight curves of mice with various treatment. Coloured stars indicating the statistical analysis results between the corresponding group and saline control. Black stars indicating the analysis result between the two indicated groups. Purple arrows indicating the injections of NPs and saline.

Figure 5.10 The metastasis detection in lung and liver. **(A)** Digital images of metastatic clone stained with crystal violet, and **(B)** the statistical data of metastasis index.

Figure 5.11 Histological examination of lung tissue sections with hematoxylin and eosin staining after treatment. Samples were taken with a 10× objective lens. **Black arrows:** typical metastatic tumour nodules.

Figure 5.12 Histological examination of liver tissue sections with hematoxylin and eosin staining after treatment. **(A)** Section images captured with a 10× objective lens. **(B)** Enlargement of a typical CV in the dash line area in (A). **Black arrows:** typical metastatic tumour clusters.

Figure 5.13 Images of heart, spleen and kidney sections stained with hematoxylin and eosin under 4× objective lens.

Figure S5.1 (A) The models after α-TOS intercalation. Surface area of each model was calculated by the topological surface area values from PubChem database (see in Table S5.3), and compared with the initial LCCP NP. **(B)** The similarity of α-TOS to DOPC and cholesterol, with similar structure marked.

Figure S5.2 Negative staining TEM image for **(A)** LCCP NPs and **(B)** LCCP with 15% α-TOS.

Figure S5.3 The mean fluorescence intensity comparison of cells treated FA10-PEG10 NPs with and without 15% alpha-TOS in the outer layer lipid. Cells were co-cultured with NPs with 25 nM dsDNA-cy5 for 4 h in DMEM with 10% FBS.

Figure S5.4 Effect of scr/FA and CD/FA (100 mg/L) on B16F0 cell growth.

Figure S5.5 The comparison of cancer cell inhibition effect of free CD siRNA/α-TOS and particle-loaded. Two conditions were chosen: (1) 12 nM of CD siRNA with 5 μM of α-TOS; (2) 24 nM of CD siRNA with 10 μM of α-TOS.

Figure S5.6 RT PCR at 24 h post transfection. Cells were treated with NPs containing 24 nM CD siRNA and/or 10 uM TOS. The Bcl-2 expression was normalized by the corresponding β-actin expression.

Chapter 6

Figure 6.1 Characterisation of LCCP NPs with α-TOS loading (NP-TOS NPs). (A) Hydrodynamic size, and **(B)** morphology from TEM images of NP-TOS0, NP-TOS15 and redispersed NP-TOS15; **(C)** zeta potential of NP-TOS NPs in deionised water; **(D)** the loading efficiency of α-TOS for NP-TOS with different composition.

Figure 6.2 Cellular uptake and intracellular distribution of NP-TOS15-FI/PE. (A) The model of dual labelled NP-TOS15-FI/PE NP; Cellular uptake of 4T1 cells incubated with **(B)** free PE lipids or NP-TOS15-FI/PE, and **(C)** the influence of incubation time on positive cell percentage; **(D)** Intracellular distribution of NP-TOS15-FI/PE after incubating with 4T1 cells for 4 h.

Figure 6.3 The effect of NP-TOS15 and α-TOS combined with IFN-γ on cell growth and migration. (A) The inhibition of NP-TOS15 and free α-TOS to cells after 48 h treatment. **(B)** The effect of IFN-γ dose on the cells in 48 h combination. The influence on **(C)** apoptosis induction and **(D)** cell cycle arrest to 4T1 cells with 5 ng/mL IFN-γ, 20 μM α-TOS, and/or 10 μM NP-TOS15 for 24 h. Migration distance of 4T1 cells in vitro with **(E)** 0 ng/mL and **(F)** 5ng/mL IFN-γ.

Figure 6.4 The influence of α-TOS on IFN-γ induced PD-L1 expression and translocation of NF-κB. (A) The PD-L1 regulation effect of α-TOS and IFN-γ after 48 h. **(B)** The western

blotting bands for NF-κB p65 protein located in nuclei and cytoplasm after 1 h treatment. **(C)** Immunofluorescent images for visualising the intracellular distribution of p65 subunit in NF-κB complex. **(D)** The p65 index obtained from fluorescence located in nuclei area.

Figure 6.5 The anticancer effect of NP-TOS15 combined with IFN-γ in vivo. (A) Tumour growth curve, and **(B)** tumour weight in corresponding groups at day 10 post first injection were shown. (n = 5). Dosage for each injection: [IFN-γ] = 0.25 mg/kg, and/or [α-TOS] = 5 mg/kg in NP-TOS15.

Figure 6.6 Inhibition of lung metastasis. (A) Images of 4T1 clones in plates, and **(B)** the histogram of metastasis index after selective incubation for 40 days with 60 μM of 6-thioguanine.; **(C)** Typical images of lung tissue sections with H&E staining taken with 10× lens were shown. Black arrows indicate typical tumour nodules.

Figure 6.7 Modulation of the immune microenvironment. (A) Cell sorting information to obtain cancer cells for PD-L1 analysis. **(B)** PD-L1 expression in tumour population. Analysis of **(C)** $CD4^+$, **(D)** $CD8^+$, and **(E)** $PD\text{-}1^+$ TILs in tumour.

Figure 6.8 Schematically illustration of the effect of IFN-γ/NP-TOS15 treatment in different organs. (A) In the lung, IFN-γ boosts the immunity and prevents metastasis, while NP-TOS15 NPs may lack accumulation due to the integrity of vessels. **(B)** In the tumour site, IFN-γ treatment results in high PD-L1 expression and failure of tumour inhibition, while IFN-γ/NP-TOS15 combination treatment effectively controlled tumour progression, with a reverse of PD-L1 overexpression on tumour cells.

Figure S6.1 Characterization of LCCP NPs with α-TOS loading. **(A)** Hydrodynamic size and **(B)** corresponding morphology from TEM images. Black arrow in **(B)** indicating the abnormal structures (non-LCCP shaped structures). **Scale bar:** 50 nm.

Figure S6.2 The combined inhibition of IFN-γ with **(A)** α-TOS or **(B)** NP-TOS15 for 48 h. The combination index (CI*) values for **(C)** α-TOS and **(D)** NP-TOS15.

Figure S6.3 The influence on **(A)** apoptosis induction and **(B)** cell cycle arrest to 4T1 cells with 5 ng/mL IFN-γ, 20 μM α-TOS, and/or 10 μM NP-TOS15 for 24 h. Colors indicating different phases in cell cycle. Grey, sub-G1; red, G1; green, S; and blue, G2/M.

Figure S6.4 (A) and (B) Images of cells with different treatment, with dashed red line schematically shown the wound distance. **(C) and (D)** Statistical data.

Figure S6.5 (A) The cell viability of 4T1 and B16 to α-TOS at different concentrations for 48 h. **(B)** Surface expression of PD-L1 in 4T1 cells with 48 h treatment of α-TOS. **(C)** Surface expression of PD-L1 in B16 cells with 48 h treatment of α-TOS. The number (upper right corner) in (B) and (C) indicated the PD-L1 positive percentage.

Figure S6.6 Quantification of the PD-L1 mRNA expression after 24 h treatment

Figure S6.7 Intracellular PD-L1 expression with IFN-γ and/or α-TOS for 48 h. After co-culturing upon IFN-γ/α-TOS, the cells with different treatments were represented as following: **Ab+Sap**, PD-L1 antibody staining, followed by saponin treatment; **Ab+Sap+Ab,** PD-L1 antibody staining, saponin treatment, followed by a second time PD-L1 antibody staining; **Sap+Ab**, isotype antibody staining, saponin treatment, followed by PD-L1 antibody staining. Ddetailed data and calculation refers to **Table S6.3**.

Figure S6.8 The inhibition of IFN-γ induced PD-L1 expression by free α-TOS after 48 h treatment.

Figure S6.9 Densitometry of western blot bands for **(A)** Nuclei and **(B)** cytoplasm.

Figure S6.10 (A) Tumor images and **(B)** a representative organ image in each group.

Figure S6.11 Body weight of mice with different treatment.

Figure S6.12 Histological images of major organs with hematoxylin & eosin staining.

Figure S6.13 PD-L1 positive percentage in the CD45/MHC-II (+) population.

Figure S6.14 FACS images indicating the gating of cells to analyze **(A)** CD4+ and **(B)** CD8+ lymphocytes.

Figure S6.15 The gating information of PD-1 expression in tumor cite.

Figure S6.16 CD45 positive population percentage in different groups.

List of Tables

List of Abbreviations used in the thesis

AE: Adverse effects

siRNA: Small interference RNA

NP: Nanoparticle

EPR effect: Enhanced permeability and retention effect

CaP: Calcium phosphate

CaC: Calcium carbonate

LCP: Lipid coated calcium phosphate

LCC: Lipid coated calcium carbonate

LCCP: lipid coated calcium carbonate/phosphate

PEG: Polyethylene glycol

CD siRNA: Cell death siRNA

α-TOS: α-tocopheryl succinate

VE: Vitamin E

W/O: Water in oil

DOPA: 1,2-dioleoyl-sn-glycero-3 phosphate sodium salt

DOPC: 1,2-dioleoyl-sn-glycero-3-phosphocholine

DSPE-PEG$_{2000}$: 1,2-distearoyl-sn-glycero-3-phosphoethanolamine-N-(polyethylene glycol)-2000

DSPE-PEG$_{2000}$-FA: 1,2-distearoyl-sn-glycero-3-phosphoethanolamine-N-[folate(polyethylene glycol)-2000]

DOTAP: 1,2-dioleoyl-3-trimethylammonium propane

FA: Folic acid

MPS: Mononuclear phagocyte system

VEGF: Vascular endothelial growth factor

EGFR: Epidermal growth factor receptor

GTP: Gemcitabine triphosphate

CTL: Cytotoxic T-lymphocyte

ROS: Singlet oxygen species

HIF: Hypoxia inducible factor

PDT: Photodynamic therapy

PTT: Photothermal therapy

DOX: Doxorubicin

CKD: Chronic kidney disease

Ce6: Chorin e6

ICG: Indocyanine green

IL: Interleukin

IFN-γ: Interferon-gamma

TGF: Tumour growth factor

TNF: Tumour necrosis factor

CTLA-4: Cytotoxic T-lymphocyte-associated protein 4

PD-1: Programmed death 1

PD-L1: Programmed death ligand 1

ORR: Objective responsive rate

NSCLC: Non-small cell lung cancer

mPD-L1: Membrane PD-L1

cPD-L1: Cytoplasm PD-L1

nPD-L1: Nuclear PD-L1

sPD-L1: Serum PD-L1

WB: Westerner blot

IHC: Immunohistochemistry

ELISA: Enzyme-linked immunosorbent assay

TIL: Tumour infiltrated lymphocyte

ICD: Immunogenic cell death

JAK: Janus kinases

STAT: Signal Transducer and Activator of Transcription protein

MHC-I: Major histocompatibility complex class I

TAM: Tumour associated macrophages

Th1: T helper 1

Treg: Regulatory T

APC: Antigen presenting cell

RGD: arginine-glycine-aspartic acid

PDI: Polydispersity index

TEM: Transmission electron microscope

SEM: Scanning Electron Microscope

DLS: Dynamic light scattering

XRD: X-ray diffraction

UV-vis: Ultraviolet–visible spectroscopy

ATR: Attenuated total reflectance

FTIR: Fourier transform infrared

EA: Element analysis

ICP-AES: Inductively coupled plasma atomic emission spectroscopy

XPS: X-ray photoelectron spectroscopy

FBS: Fetal bovine serum

DMEM: Dulbecco's Modified Eagle Medium

P/S: Penicillin/ streptomycin

FACS: Flow cytometry analysis

CLSM: Confocal laser scanning microscopy

PBS: Phosphate buffer saline

PFA: Paraformaldehyde

MTT: 3-[4,5-dimethylthiazol-2-yl]-2,5-diphenyl tetrazolium bromide

PI: Propidium iodide

DCFH-DA: 2',7'-dichlorofluorescin diacetate

H&E staining: Haematoxylin and eosin staining

FSC: Forward scatter channel

SSC: Side scatter channel

RT-PCR: Reverse transcription quantification polymerase chain reaction

cDNA: Complementary DNA

Bcl-2: B-cell lymphoma 2

SDS-PAGE: Sodium dodecyl sulphate polyacrylamide gel electrophoresis

NF-κB: Nuclear factor-kappa B

RNAi: RNA interference

PLK: Polo-like kinase

PVDF: Polyvinylidene difluoride

MFI: Mean fluorescence intensity

CV: Central vain

Chapter 1

Introduction

This chapter presents an overview to introduce the brief background of this thesis. The objectives and significance of this research are outlined, with the proposed aims to achieve. The outline of this thesis is documented in the order of chapters.

1.1 Background

Cancer is one of the leading causes of disease-related death worldwide [1]. A variety of therapeutic molecules, such as chemical drugs, natural products, oligonucleotides, and proteins, are employed to treat cancers. Generally, these therapeutics require a proper delivery platform to achieve efficacious tumour accumulation and further internalisation by tumour cells [2]. In this aspect, development of nanoparticles (NPs) provides diverse delivery opportunities. The NPs would achieve tumour accumulation due to their suitable size range, and integrate multiple functions via delicate designs. As an ideal platform for cancer therapy, the NPs are required to be biocompatible and biodegradable. More importantly, the NP delivery system should be efficient in loading numerous drugs, and controllable in release.

In this thesis, we have specifically focused on developing novel lipid-coated calcium carbonate/phosphate (LCCP) NPs with the adjustable payload release profile to deliver therapeutics for combined cancer therapy. The LCCP NPs were firstly developed for gene delivery. Then the drug loading strategy was further improved to broaden the deliverable drug range. As an example, a hydrophobic nature product, alpha-tocopheryl succinate (α-TOS), was loaded and delivered for gene/drug combination cancer therapy. At last, suitable NP based

regimens were developed to optimise interferon-gamma (IFN-γ) related combination cancer therapy.

In general, lipid-coated calcium-based NPs, such as lipid-coated calcium phosphate (LCP) and lipid-coated calcium carbonate (LCC), can meet the criteria for cancer therapy. The drug release of these NPs is majorly controlled by the instinct pH sensitivity of core materials such as calcium phosphate or carbonate. In practice, the pH response range of LCP NPs indicates that the release may happen in the late endosome/lysosome, which may cause the enzymatic degradation of cargoes and lysosomal swelling [3]. On the other hand, the sensitivity of calcium carbonate to even neutral pHs (such as pH 6.8-7.0) indicates some therapeutics leakage in the tumour extracellular environment or even in blood [4]. Based on this knowledge information, this thesis has focused on ameliorating these NP delivery systems with an adjustable release profile, in order to optimise the release profile for enhanced cancer therapy.

As is well known, the lipid-coated calcium-based NPs can load therapeutics by co-precipitation within their calcium-based cores. This strategy is suitable for hydrophilic molecules, such as gene and protein, while it may be limited in the delivery of hydrophobic and amphiphilic molecules. In cancer therapy, some hydrophobic/amphiphilic nature products, such as α-TOS, are applied to amplify the anticancer efficiency in combination with other drugs [5, 6]. Therefore, a suitable loading strategy for delivering hydrophobic/amphiphilic nature products by our NPs was specifically designed, and the NPs were used to co-deliver gene and α-TOS for combined cancer therapy in this thesis.

Moreover, a suitable NP based regimen is developed to optimise cytokine-related cancer therapy. Cytokines play a vital role in the anti-tumour immune system, and can suppress tumour growth and metastasis [7, 8]. However, long term exposure to cytokines such as IFN-γ causes adaptive cancer immune resistance [9, 10]. To reverse the adaptive immune resistance caused by cytokines, the LCCP NPs were employed to efficiently deliver α-TOS to the tumour site in the presence of exogenous IFN-γ in this thesis, in order to positively modulate the tumour microenvironment and more efficiently inhibit the tumour growth and metastasis.

Of note, successfully completing this Ph.D. project may provide a novel LCCP platform for gene/drug delivery to treat cancer in some kinds of combination.

1.2 Research objectives and significance

The overall aim of this project is to develop LCCP NPs with precise endosomal release character for efficacious combination cancer therapy. To achieve this aim, the folic acid-modified LCCP NPs were synthesised with the variable carbonate/phosphate ratio to achieve controllable cargo release and target delivery. This thesis also provides some practical regimens for LCCP NPs as efficient delivery systems for combination cancer therapy.

Therefore, the objectives of this project are specified as follows:

(1) To develop novel LCCP hybrid NPs for effective siRNA loading and target endosomal pH release;

(2) To understand the therapeutic efficacy by co-delivering α-tocopheryl succinate (α-TOS) and cell death siRNA (CD siRNA) using LCCP NPs for target drug/gene combination cancer therapy;

(3) To determine a suitable regimen by combining interferon-γ (IFN-γ) and LCCP delivered α-TOS for enhanced cancer immunotherapy

Aiming to engineer such LCCP NPs as a gene/drug co-delivery platform for combination cancer therapy, this project may have the significance in (1) development of novel co-delivery platforms, i.e. LCCP NPs with adjustable pH-responsive release profile and capacity of loading various deliverable therapeutics, and (2) provision of a suitable regimen to enhance the cancer therapy efficacy using the combination strategy.

1.3 Thesis outline

This thesis is written under the guidelines of The University of Queensland. The outcomes of this Ph.D. thesis are presented in the form of journal publications. In detail, the chapters in this thesis are illustrated in the following sequence.

Chapter 1 *Introduction*

This chapter presents an overview to introduce the brief background of this thesis. The objectives and significance of this research are proposed and this thesis is outlined in each chapter.

Chapter 2 *Literature review*

This chapter reviews the recent progress in applying calcium-based nanoparticles (NPs) for cancer therapy. The merits of organic/inorganic NPs leads to the development of biocompatible calcium-based organic/inorganic composite NPs. A comprehensive review of calcium phosphate (CaP) and calcium carbonate (CaC) based NPs are presented, with their variety of applications in cancer therapy and immunotherapy. Sequentially, the LCCP-based strategy is proposed to solve the remained challenges.

Chapter 3 *Strategical Methodology*

This chapter summarises the methodology adopted in this PhD project. In specific, the synthetic methods for LCCP NPs, the characterisation techniques, biological techniques, and statistical considerations are documented.

Chapter 4 *Devising New Lipid-coated Calcium Phosphate/Carbonate Hybrid NPs to Control Release in Endosome for Efficient Gene Delivery*

This chapter reports the design and development of the new lipid-coated calcium carbonate/phosphate (LCCP) nanoparticles (NPs). Lipid-coated calcium phosphate (LCP) NPs are proven to be an effective vehicle for gene and some drug delivery, while it is not desirable for NPs to release gene/drug in late endosome/lysosome. To achieve the early endosome release and escape, we have designed and developed these new LCCP hybrid NPs. The new hybrid LCCP NPs had a spherical structure with an average diameter of 40 nm and a high gene loading capacity, and released most of the loaded dsDNA/siRNA was under mildly acidic conditions (pH 6.0-5.5). LCCP NPs were also effectively internalised by B16F10 cells in a dose and time dependent way. The delivery efficacy was further demonstrated using two functional siRNAs, i.e. programmed death ligand 1 (PD-L1) siRNA for PD-L1 silencing and polo-like kinase 1 (PLK1) siRNA for growth inhibition of B16F10. As expected, the LCCP loaded PD-L1 siRNA showed a quicker PD-L1-mRNA inhibition than LCP NPs, indicating that LCCP NPs improve the siRNA silencing capacity probably via release of most siRNA in endosome and endosomal escape.

Chapter 5 *Enhanced Combination Cancer Therapy using Lipid-Calcium Carbonate/ Phosphate NPs as a Targeted Delivery Platform*

This chapter reports the modification of LCCP NPs as targeting NPs, and co-delivery of cell death (CD) siRNA and α-tocopheryl succinate (α-TOS) drug for combination cancer therapy in vitro and in vivo. CD siRNA is a commercialised siRNA that can cause cell death, while α-

TOS is a derivative of vitamin E that holds great anticancer potentiality. In this chapter, LCCP NPs were modified with polyethylene glycol (PEG) and folic acid (FA). After modification, LCCP NPs exhibited an FA-enhanced cellular uptake by cancer cells with FA receptor overexpression. The modified LCCP NPs provided high payloads of CD siRNA and α-TOS drug. The in vitro study indicated the synthesised NPs (CD/TOS/FA) enhanced the inhibition to B16F0 melanoma growth with a moderate synergy. The mechanism of the high combined inhibition to B16F0 cell growth may be associated with the effective induction of cell apoptosis and arrest of the cell cycle at the G1 phase.

Moreover, the in vivo anticancer efficacy of CD/TOS/FA NPs was evaluated in a metastatic 4T1 mouse model. With FA mediated delivery of two combined therapeutics, CD/TOS/FA NPs significantly inhibited 4T1 tumour growth in situ, and prevented its metastasis to lung and liver remarkably. No significant toxicity to major organs was observed during the therapy. In conclusion, the well-designed CD/TOS/FA NPs held great potential as an efficiency anticancer agent delivery platform, and may be used to deliver therapeutics for combination therapy for other cancers.

Chapter 6 *Enhanced Prevention of Breast Tumour Metastasis by Nanoparticle-delivered Vitamin E in Combination with Interferon-gamma Treatment*

Preventing cancer metastasis is one of the remaining challenges in cancer therapy. To improve the efficacy and bioavailability of α-TOS, the lipid-coated calcium carbonate/phosphate (LCCP) nanoparticles (NPs) with folic acid and PEG modification were synthesised for efficient delivery of α-TOS to 4T1 cancer cells. The optimised LCCP-FA NPs (NP-TOS15) showed an α-TOS loading efficiency of ~60%, and enhanced the uptake by 4T1 metastatic cancer cells. Consequently, the NP-TOS15 NPs significantly enhanced the anticancer effect in combination with interferon-gamma (IFN-γ) treatment in terms of apoptosis facilitation and migration inhibition. Importantly, NP-TOS15 upregulated the anticancer immunity via downregulating program death ligand 1 (PD-L1) expression induced by IFN-γ, and remarkably prevented the lung metastasis, particularly in combination with IFN-γ. Further investigation revealed that this combination therapy also modulates the cytotoxic lymphocyte infiltration into the tumour tissue for tumour elimination. Taken together, the NP delivery of α-TOS in combination with IFN-γ provides an applicable strategy for cancer therapy.

Chapter 7 *Conclusion and Future Recommendation*

This chapter presents the general discussion and conclusion of this thesis, and the outlook for future research directions.

1.4 References

[1] R.L. Siegel, K.D. Miller, A. Jemal, Cancer statistics, 2019, CA Cancer J. Clin. 69(1) (2019) 7-34.
[2] X. Xu, W. Ho, X. Zhang, N. Bertrand, O. Farokhzad, Cancer nanomedicine: From targeted delivery to combination therapy, Trends. Mol. Med. 21(4) (2015) 223-232.
[3] J. Li, Y.-C. Chen, Y.-C. Tseng, S. Mozumdar, L. Huang, Biodegradable calcium phosphate nanoparticle with lipid coating for systemic siRNA delivery, J. Controlled Release 142(3) (2010) 416-421.
[4] K.H. Min, H.S. Min, H.J. Lee, D.J. Park, J.Y. Yhee, K. Kim, I.C. Kwon, S.Y. Jeong, O.F. Silvestre, X. Chen, pH-controlled gas-generating mineralized nanoparticles: a theranostic agent for ultrasound imaging and therapy of cancers, ACS Nano 9(1) (2015) 134-145.
[5] J. Neuzil, T. Weber, A. Schröder, M. Lu, G. Ostermann, N. Gellert, G.C. Mayne, B. Olejnicka, A. Nègre-Salvayr, M. Stícha, Induction of cancer cell apoptosis by α-tocopheryl succinate: Molecular pathways and structural requirements, FASEB J. 15(2) (2001) 403-415.
[6] X. Zhang, X. Peng, W. Yu, S. Hou, Y. Zhao, Z. Zhang, X. Huang, K. Wu, Alpha-tocopheryl succinate enhances doxorubicin-induced apoptosis in human gastric cancer cells via promotion of doxorubicin influx and suppression of doxorubicin efflux, Cancer Lett. 307(2) (2011) 174-181.
[7] A. Giannopoulos, C. Constantinides, E. Fokaeas, C. Stravodimos, M. Giannopoulou, A. Kyroudi, A. Gounaris, The immunomodulating effect of interferon-γ intravesical instillations in preventing bladder cancer recurrence, Clin. Cancer Res. 9(15) (2003) 5550-5558.
[8] G. Dranoff, Cytokines in cancer pathogenesis and cancer therapy, Nat. Rev. Cancer 4(1) (2004) 11.
[9] F. Castro, A.P. Cardoso, R.M. Gonçalves, K. Serre, M.J. Oliveira, Interferon-gamma at the crossroads of tumor immune surveillance or evasion, Front. Immunol. 9 (2018) 847.
[10] D.M. Pardoll, The blockade of immune checkpoints in cancer immunotherapy, Nat. Rev. Cancer 12(4) (2012) 252.

Chapter 2

Literature Review

This chapter reviews the current progress on the application of calcium carbonate/phosphate nanoparticles (NPs) in cancer therapy. It firstly overviews the application of general organic/inorganic NPs in cancer therapy (Section 2.1), then focuses on the development of calcium phosphate (Section 2.2) and calcium carbonate (Section 2.3) NPs and their applications, respectively. Next, the calcium-based hybrid NPs and their application in cancer therapy are summarised (Section 2.4). To extend, this chapter briefly reviews the principle and applications of immunotherapy, with current NP-based strategies to achieve better therapeutic effects (Section 2.5). Finally, current challenges are proposed, and the basic strategies for this research are outlined (Section 2.6). **The review in Section 2.5 is under review for publication in Front. Immunol. (2019, review paper).**

2.1 Nanotechnology for cancer therapy

2.1.1 Current cancer therapies

Cancer is one of the most life-threatening diseases in the world. As reported, 22% of death was related to cancer in the United States in 2016 [1]. Traditionally, the conventional methods (such as chemotherapy, radiotherapy, and surgery) and more recent methods (such as gene therapy, and protein/peptide-based therapy) are effective in eliminating tumour in situ. Nevertheless, these strategies may be limited by severe adverse effects (AEs), and the therapeutic efficacy.

Nowadays, immunotherapy opens a new chapter for cancer treatments. Compared to the traditional regimens, the involvement of the immune system will (1) relieve the AEs, (2) broaden the applicable patient cohort, and (3) most importantly, bring more efficacious treatment outcomes in both eliminating tumour in situ and preventing cancer metastasis.

For both the traditional and immune regimens, the anticancer therapeutics are required. Assorted by the molecules involved in, the therapeutics include (1) chemical anticancer drugs and inhibitors, (2) nature products, (3) interference oligonucleotides, (4) antibodies, (5) other bioactive agents like cytokines. However, most of these molecules show high cytotoxicity to cancer cells, and also other proliferative cells in normal tissues. This cytotoxicity leads to side effects and therefore limits the clinical application. Indeed, these anticancer agents are quickly metabolised in the blood, resulting in low accumulation at the lesion site. Specifically, the oligonucleotides for cancer therapy, the majority of which are interference RNAs (siRNA, shRNA, or miRNA), also face challenges such as low efficiency in cellular uptake, and quick degradation upon exposure in the enzymatic environment. Therefore, developing effective approaches for systematic delivery of therapeutics is of great importance.

2.1.2 The advantages of using nanotechnology in cancer therapy

The emerging nanotechnology brings new paradigms to cancer therapies. The application of nanotechnology relies on nanomaterials, which refer to the materials with at least one dimension of size constrained in 1-100 nanometers (nm). The nanomaterials, especially nanoparticles (NPs), provide several benefits for cancer therapies. In general, these NPs are used as carriers for therapeutic delivery to optimise the treatment efficacy. Particularly, the nanotechnology can also benefit other cancer-related aspects, such as imaging, diagnosis, vaccine development, and establishment of the personalised treatment regimen.

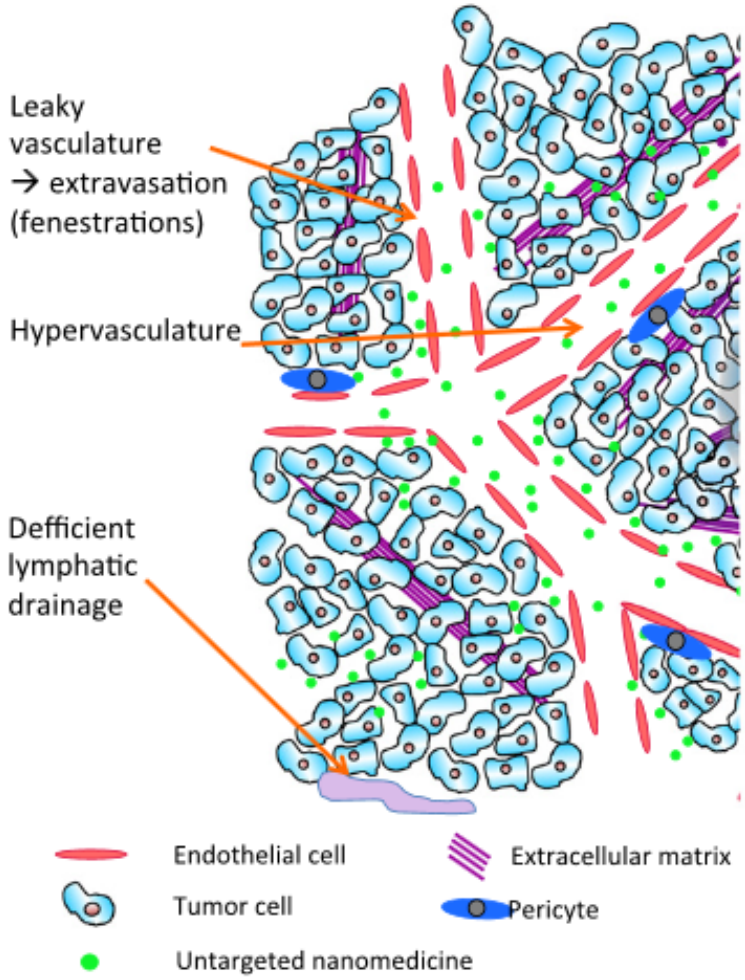

Figure 2.1. Schematic representation of the EPR effect of nanomedicine. Reprinted with the permission from F. Danhier et al. [2]. Copyright (2016) Elsevier.

Firstly, the NPs exhibit definitive accumulation at the tumour site. As shown in Figure 2.1, due to the instinct small size, the nanoparticles can be leaked from the hyperpermeable neovasculature to the interstitial microenvironment in the tumour tissue [2, 3]. Simultaneously, the lack of functional lymphatic vessels contributes to nanoparticle's entrapment and retention in the tumour tissue. Taken together, this process profiles the features of Enhanced Permeability and Retention (EPR) effect, the fundamental of NP application in cancer therapy. Moreover, NP delivery enhances the pharmaceutical properties of the loaded therapeutics. After payload, the therapeutics show improvement in their stability, solubility, and half-life in circulation [3]. These improvements also reduce side effects. Furthermore, nanotechnology facilitates the transcytosis of cancer therapeutics across some special epithelial barriers, such as the blood-brain barrier [4] and gastrointestinal tract [5]. For the delivery of some special

bio-macromolecular drugs like oligonucleotides and proteins, NPs provide protection during the delivery to maintain their bioactivities [6]. In specific, some NPs hold the inherent characteristics that can be used for controlled release, diagnosis, immune boost, and even cancer elimination.

2.1.3 Current application of NPs in cancer therapy

Currently, the application of nanotechnology to cancer therapy attracts growing attention. Several therapeutic NP products have been marketed for cancer treatments, such as Doxil® (liposomal doxorubicin [7]), Abraxane® (albumin-bound paclitaxel [8]), Onivyde® (liposomal irinotecan [9]), and Nanotherm® (iron oxide [10]). Here we review some organic and inorganic NPs in terms of their properties and discuss the advantages and disadvantages of each kind of NPs for the cancer therapy application.

2.1.3.1 Organic NPs

As shown in Figure 2.2A and B [11], there are several NPs approved by FDA for clinic use, and most of them are organic NPs. The most commonly used materials for organic NPs are liner/branched polymers, lipids, nanocrystals, metallic materials, and proteins. Some lipids can act as the precursor/monomer to self-assemble into NPs. According to the surface and internal compartment, these NPs can be sorted as micelle (closed monolayer lipid without compartment) and liposome (bilayer lipid with an aqueous internal compartment).

FDA approved nanomedicines are mainly organic NPs consisting of the above materials (Figure 2.2A and B). Figure 2.2C and D show the statistical data of clinical trials, suggesting the investigation preference in terms of the material categories. Significantly, organic materials such as micelles and proteins come through the development process [11]. Moreover, more protein-based nanomedicines were approved recently. The instinct biological functions of these proteins endow advantageous applications in cancer therapy.

Although there are some other applications such as imaging and diagnostics, anticancer drug delivery is the most important application of these organic NPs. The marketed liposomal nanomedicine Doxil® is an ideal paradigm. Since approval in 1995, Doxil® is widely used for cancer therapy. Compared to conventional doxorubicin drug formulations, the NP formulation achieves much better therapeutic outcomes, with favourable toxicity profiles and less adverse

effects [7]. Moreover, the structure of liposomal NPs broadens their application in drug delivery, endowing the loading of both hydrophilic and hydrophobic drugs in the aqueous compartment and the lipid bilayer, respectively. Meanwhile, other organic NPs may also achieve payload of other hydrophilic/hydrophobic drugs. For example, dendrimers and carbon nanotubes provide a hydrophobic internal chamber for hydrophobic drug delivery, such as curcumin [12], analogues of vitamin E [13], paclitaxel [14, 15], and cisplatin [16, 17].

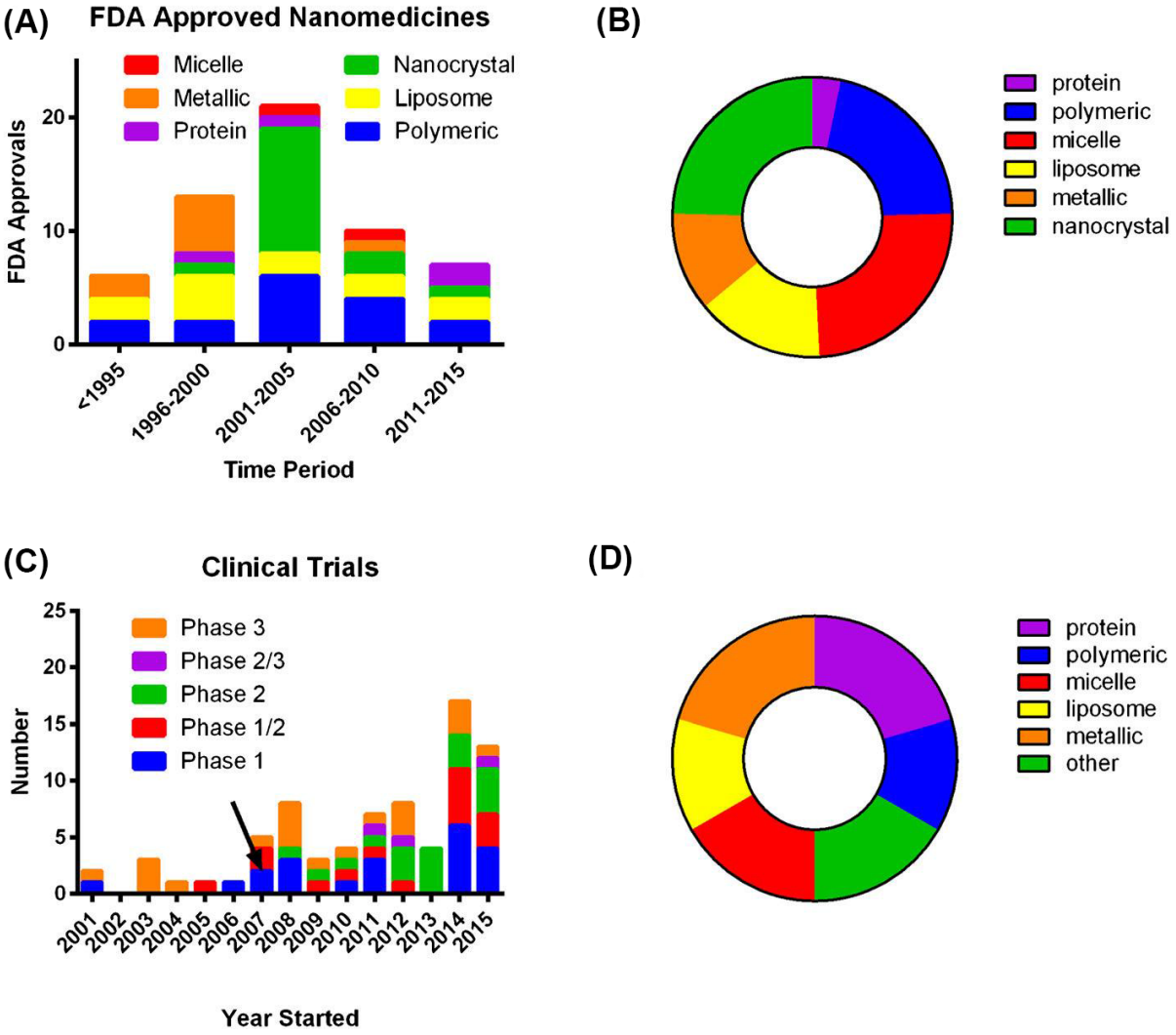

Figure 2.2 Trends of the NP based medicines. (A) FDA-approved nanomedicines stratified by time and NP category; **(B)** overall of FDA-approved nanomedicines catalogued by NPs; **(C)** ongoing clinical trials identified in clinical trials.gov from 2001 to 2015, with arrow indicating the start date of FDAAA 801 US law that requiring reporting to FDA database; **(D)** overall of nanomedicines under clinical trial assorted by NP category. Reprinted with the permission from Bobo D. et al.[11]. Copyright (2016) Springer Nature.

2.1.3.2 Inorganic NPs

According to the component elements, the inorganic NPs may include some of the following highlights: (1) magnetic behaviour, (2) potential for diagnosis and sensor development, (3) cell death induction ability via photo-thermal effect, photodynamic effect, or other mechanisms, and (4) affinity to bio-components, especially to bone and tooth tissues. Table 2.1 summarises the unique advantages of inorganic NPs catalogued by their composition.

Table 2.1. Characteristics of inorganic NPs assorted by composition.

Composition of NPs	**Features**	**Cancer therapy application**	**Ref**
Iron oxide	Magnetic properties	Magnetic mediated targeting drug delivery to the lesion area	[18-20]
	Imaging ability	Diagnosis	[21-23]
Gold	Photo-thermal transduction	Photo-thermal therapy	[24-26]
	Imaging ability	Diagnosis	[27-29]
Zinc phosphate	High affinity to protein and immune regulation	Loading and delivery of peptide-based anticancer agents and vaccine development	[30, 31]
Copper sulphide	Photo-thermal transduction	Photo-thermal therapy	[32, 33]
	Imaging ability	Diagnosis	[34, 35]
Manganese oxide	Imaging ability	Diagnosis	[36]
Gadolinium-chelate	Imaging ability	Diagnosis	[37, 38]
Calcium phosphate	Gene transfection	Gene delivery	[39, 40]
	Bone affinity	Bone metastasis and other osteoblast cancer therapy	[41, 42]

Notably, inorganic NPs including calcium are reported to have a high affinity to target bio-components or tissues. As the most commonly used bone substitutes, calcium phosphate materials are suitable for bone-targeted drug delivery, particularly to treat cancers with bone

metastasis potential [43]. Furthermore, calcium phosphate is known as a commonly used nonviral vector for gene transfection, though the process is not entirely understood. Recent studies exhibit good regimens to utilise calcium phosphate-based NPs for gene delivery in cancer therapy [44]. Although calcium iron acts as a second messenger in cell signalling, the calcium NPs are biosafe and do not bring significant influence to cells in most cases. The previous study has elucidated how the ion efflux processes to ensure the calcium homeostasis in cells [45]. However, due to the pH response under acidic conditions, a large portion of Ca NPs may be cytotoxic to cells. After endocytosis, NPs dissolve and release Ca ions to the endosome/lysosome, which may cause endosomal/lysosomal ruptures and cell necrosis [46, 47]. This Ca-induced cell death can be reversed by supplementing NaCl to raise the intracellular osmotic pressure [46].

The major drawback of inorganic NPs is the relatively high toxicity and poor biocompatibility. Indeed, most inorganic NPs show high cytotoxicity if they lack proper modifications. The metabolism of metal-doped NPs will increase burdens to organs, such as liver and kidney, causing organ exhaustion [48-50]. In certain cases, inorganic NPs may also have stability issues under physiological conditions and in circulation [51].

2.1.4 Inorganic-organic hybrid NPs

Generally, organic NPs perform better in extending the biocompatibility and colloidal stability, offering opportunities for easy modification [52], while they face problems such as rapid clearance and mechanically fragile structure [53]. On the other hand, inorganic NPs provide the mechanical and thermal stability, and possess specific features in magnetic, redox, photothermic, photodynamic, and/or chemical properties [21, 27, 35], while they show limitation like nonbiodegradability, lack of biocompatibility and colloidal stability, and high cytotoxicity [51]. To take advantages of both organic and inorganic NPs and overcome their drawbacks, the inorganic-organic hybrid NPs are designed and applied. The organic/inorganic hybrid NPs refer to those composites showing mixed organic/inorganic components at the molecular scale, with a characteristic length scale in the nanometer size [54]. Thus, the properties of hybrid NPs do not just result from the sum-up of individual components such as the simple physical mixtures. Indeed, some unique characters are present in the hybrid materials, especially the organic/inorganic interface related characters [54-56].

Since the last decades, hybrid nanomaterials have been developed on a large scale, with the number increased in both research publication and patent application [57]. Importantly, some hybrid NPs succeed in clinical translations. Up to 2016, about ten hybrid NP/formula products have been approved by the FDA, and three of them are for cancerous applications (Table 2.2) [11, 58]. Others are majorly focused on deficiency in chronic kidney disease (CKD) with iron-based NPs. Moreover, clinical trials on gold and silica NPs are recruiting, focusing majorly on cancer imaging, with some trials on tumour thermal ablation [58]. Generally, the clinical translation products for hybrid NPs on cancer therapy aspects are rare, suggesting a great potential of development.

Table 2.2 List of FDA-approved hybrid nanomedicines for cancerous application. Reprinted and modified with the permission from B. Daniel et al.[11] and A. Aaron et al.[58]. Copyright (2016) Springer Nature, and (2015) Springer Nature.

Trade name	**Material description**	**Indication(s)**	**Year(s) of approval**
Feridex I.V.®; Endorem®	Iron oxide NPs coated with dextran	MRI Imaging of liver lesions	1996
Resovist®; Cliavist	Iron oxide NPs coated with carboxydextran	MRI imaging of liver lesions	2001 (Approved by EMA)
Nanotherm®	Iron oxide NPs coated with aminosilane	Thermal therapy for glioblastoma	2010

Apart from iron-, gold-, and silica-based nanomaterials, the calcium-based hybrid nanomaterials also show great potential in cancer therapy as a promising anticancer delivery candidate for a variety of therapeutics such as oligonucleotides [39, 59], peptides [60, 61], and hydrophilic/hydrophobic anticancer drugs [62-64]. Among the variety formula of calcium products, calcium phosphate and calcium carbonate are highlighted as there are some successful FDA-approved applications in bone structure mimics, acid indigestion, and treatment of calcium deficiency [44, 63, 65]. Therefore, devising calcium-based organic-inorganic hybrid NPs is of great interests. Calcium based NPs, such as calcium phosphate (CaP)

and calcium carbonate (CaC), exhibit broad biomedical utilisation due to their biocompatibility and biodegradability. Traditionally, these materials are applied in nutrition supplementation, orthopaedic and dental substitutes [43, 65]. With the development of nano-sized CaP/CaC, their application as drug/gene delivery system in cancer therapy has been developed. As the focused nanomaterials in this study, CaP- and CaC-based NPs in cancer therapy are reviewed in detail in the next sections.

2.2 CaP-based NPs in cancer therapy

In this section, CaP-based NPs and their applications in cancer therapy are reviewed. First, the bare CaP NPs, including their properties and application, are discussed, and then the lipid-coating CaP (LCP) NPs are introduced specifically.

2.2.1 CaP NPs

2.2.1.1 The property of CaP NPs

The compound formula of CaP is diverse, as listed in Table 2.3 [66]. Generally, a higher Ca/P ratio leads to lower solubility [67]. For example, the solubility of CaPs decreases in the order of MCPM > DCPD = DCPA > OCP > β-TCP > HA at the physiological pH. The crystal form is controlled by precipitation conditions such as temperature, pH, Ca/P feeding ratio [65].

The CaP NPs are able to dissolve in the acidic organelles such as endosome and lysosome, increasing the osmotic pressure due to the dissolved ions. As a consequence, the endosome/lysosome swells and releases the payloads into the cytoplasm [61, 68]. Despite that the calcium ion concentration higher than 1 μM in the cytoplasm would lead to cell necrosis [69-72], most CaP nanomaterials show low to moderate cytotoxicity. Research on PEG-lipid coated CaP NP revealed that cells can overcome these exogenous calcium ion increase via pumping calcium ions out into the extracellular matrix or into mitochondria [73]. Therefore, CaP NPs are theoretically nontoxic materials to cells, and able to deliver and automatically release anticancer therapeutics after internalisation by cancer cells.

Table 2.3 Main calcium orthophosphate compounds. Taken and modified from the original version published by Bohner et al. [66].

Name	Formula	Ca/P	Mineral	Symbol[d]
Monocalcium phosphate monohydrate	$Ca(H_2PO_4)_2 .H_2O$	0.50	-	MCPM
Dicalcium phosphate	$CaHPO_4$	1.00	Monetite	DCPA
Dicalcium phosphate dihydrate	$CaHPO_4.2H_2O$	1.00	Brushite	DCPD
Octocalcium phosphate	$Ca_8H_2(PO_4)_6 .5H_2O$	1.33	-	OCP
Precipitated hydroxyapatite [a]	$Ca_{10-x}(HPO_4)_x(PO_4)_{6-x}(OH)_{2-x}$	1.33-1.67	-	PHA
Precipitated amorphous calcium phosphate	$M_u(Ca_3)(HPO_4)_{3v}(PO_4)_{3y}.zH2O)$[b,c]	0.67-1.50	-	ACP
Monocalcium phosphate	$Ca(H_2PO_4)_2$	0.50	-	MCP
α-Tricalcium phosphate	α-$Ca_3(PO_4)_2$	1.50	-	α-TCP
β-Tricalcium phosphate	β-$Ca_3(PO_4)_2$	1.50	-	β -TCP
Sintered hydroxyapatite	$Ca_{10}(PO_4)_6(OH)_2$	1.67	Hydroxyapatite	SHA
Oxyapatite	$Ca_{10}(PO_4)_6O$	1.67	-	OXA
Tetracalcium phosphate	$Ca_4(PO_4)_2O$	2.00	Hilgenstockite	TetCP

[a] x may vary between 0 and 2.

[b] *u* may vary between 0 and 3, *v* may vary between 0 and 1.5, *y* may vary between 0 and 0.667, and *z* is unclear at this point. M is typically a monovalent cation (Na^+, K^+, NH_4^+) which is only present if there is an overall negative charge on the calcium phosphate.

[c] ACP produced in basic conditions has generally $u = 0$, $v = 0$, $y = 0.667$, leading to the following composition: $Ca_3(PO_4)_2.zH_2O$ where $z = 3–4.5$. In acidic conditions, $u = 3$, $v = 1.5$, $y = 0$, leading to the following composition: $M_3(Ca_3(HPO_4)_{4.5}.zH_2O)$ where *z* is unknown.

[d] Symbol abbreviations: MCPM: monocalcium phosphate monohydrate; DCPA: dibasic calcium phosphate anhydrate; DCPD: dicalcium phosphate dehydrate; OCP: octacalcium phosphate; PHA: precipitated hydroxyapatite; ACP: amorphous calcium phosphate; MCP: monocalcium phosphate; TCP: tricalcium phosphate; SHA: sintered hydroxyapatite; OXA: oxyapatite; TetCP: tetracalcium phosphate.

2.2.1.2 CaP NPs in cancer therapy

CaP NPs are widely examined to deliver a variety of agents for cancer therapy, such as genes, proteins, and chemical drugs. In most of CaP NP applications, the anticancer agents are embedded into the CaP crystals by co-precipitation. As one of the most important non-virus gene delivery materials, CaP NPs manifest high payload and transfection efficacy. The payload efficacy is highly related to their stoichiometry (Ca/P ratio) due to that this ratio controls the precipitation and obtained compound formula. In general, an optimal Ca/P ratio ranging between 100 to 300 is adopted to get efficient condensation of genes [74]. Olton et al. investigated the naked CaP NPs and revealed how synthesis parameters affected the binding, condensation, and transfection of pDNA [74]. Moreover, Sokolova et al. tried to prepare a multi-shell structured CaP NP, as schematically shown in Figure 2.3. The hydrophilic DNAs here were not just simply loaded by CaP NPs, but also employed for colloidal stabilisation. [75].

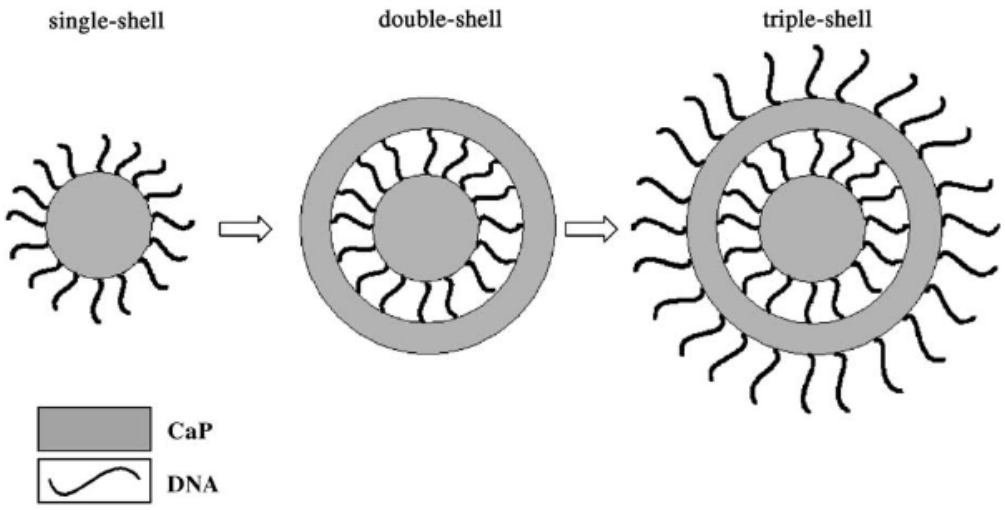

Figure 2.3 Schematic illustration of three types of calcium phosphate/DNA NPs. Single-shell NP: DNA coated CaP; double-shell NP: an external layer of CaP crystallised on the single-shell NP for DNA protection; and triple-shell NP: a second layer of DNA coating outside the double-shell NP for colloidal stabilisation. Reprinted with the permission from Sokolova et al. [75]. Copyright (2006) Elsevier B.V.

CaP NPs are also able to deliver chemical drugs for cancer therapy. An example is a ceramide that has poor water solubility [76]. Barth et al. suggested a micro-emulsion method to prepare ~20 nm CaP NPs for indocyanine green (ICG) delivery [77]. The ICG molecules can visualise

the in vivo distribution of CaP NPs via fluorescence imaging, enabling CaP NPs to perform as a theranostic modality. Despite the instinct pH responsive of CaP, the release of anticancer agents from CaP NPs may also be achieved by morphology transformation. Cai et al. reported an ultrasonic controlled morphology transformation of hollowed CaP NPs [78]. As shown in Figure 2.4, the hollow sphere-like CaP NPs were partially transferred to pin-like crystallites after 1 min ultrasonication, and this transformation quickly accomplished after 5 min ultrasonication. Therefore, the therapeutics that are loaded into the niches will be released accordingly.

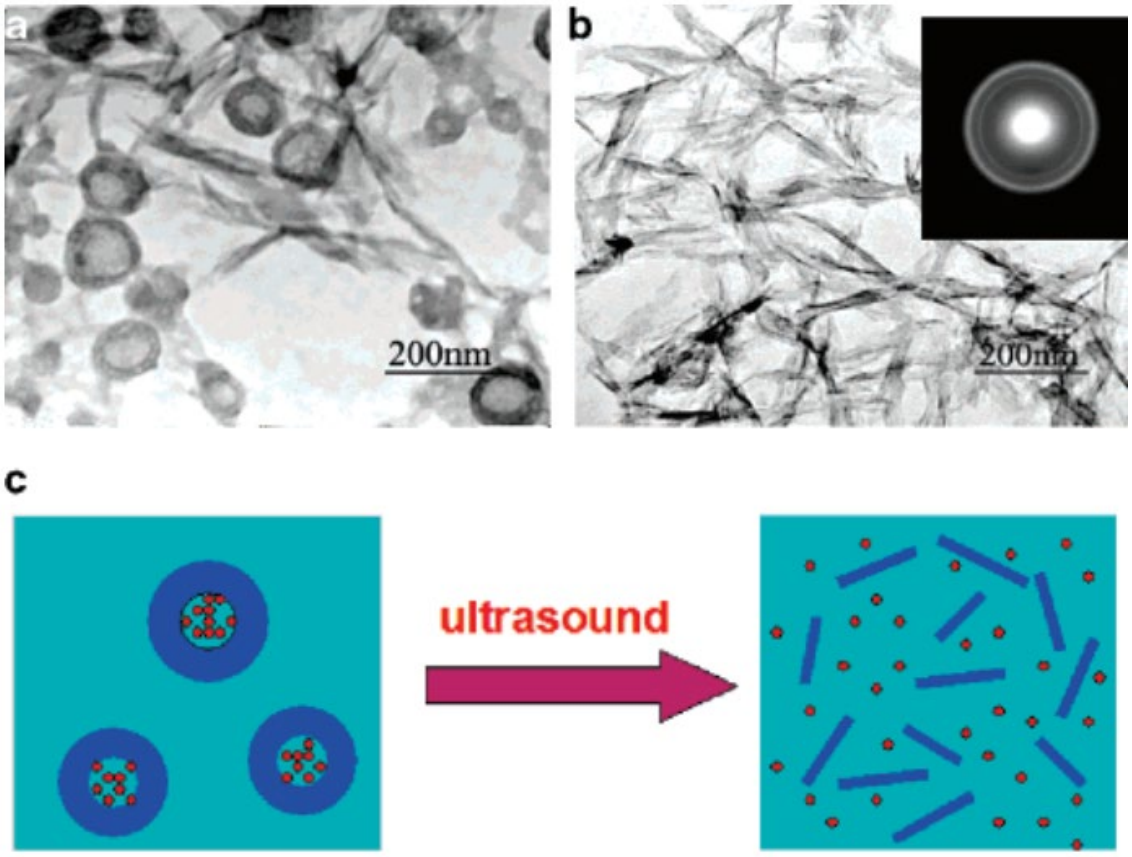

Figure 2.4 Illustration of an ultrasonic responsive morphology transformation of CaP NPs and the application for anticancer agent release. (A) TEM images of an interim stage, the co-existence of original sphere-like and transferred pin-like NPs after 1 min ultrasonic, **(B)** TEM and SAED of the final stage of this transformation after 5 min ultrasonic. **(C)** Scheme of the ultrasound controlled drug release. Reprinted with the permission from Cai et al. [78]. Copyright (2007) American Chemical Society.

2.2.2 Lipid-coated calcium phosphate (LCP) NPs

Although the application of bare CaP NPs has achieved some success, most of these investigations mentioned size control, stability, and agglomeration as the arch problems for CaP NP application. In most cases, CaP NPs need further modification or coating with organic substances before employment in cancer therapy in vivo. Among the tremendous approaches, the lipid coating provides a facile and practical way to gain CaP NPs with controlled size, shape and colloidal stability.

2.2.2.1 Synthesis and modification

The broad application in anticancer drug/gene delivery of CaP NPs requires surface modification to the precipitates to produce colloidally stable NPs. Moreover, these coated organic substances can affect the crystallisation of CaP, thus leading to the controllable size and shape of NPs. Liposomes are good examples to template CaP NP formation. Phospholipids such as1,2-dioleoyl-sn-glycero-3 phosphate sodium salt (DOPA) owning negatively charged head group help the deposition of calcium and phosphate ions around the liposomes, resulting in hollow and small-sized (around 40 nm) NPs [59, 68, 79].

Pioneeringly, Huang's lab reported the LCP preparation based on a water in oil (W/O) micro-emulsion [68, 80]. The typical LCP NP structure obtained is a bilayer phospholipid coated CaP core, as schematically shown in Figure 2.5. Briefly, an aqueous solution containing calcium ion is dispersed into the oil phase (cyclohexane) with surfactant (igepal as the most commonly used). A separate W/O dispersion containing phosphate and inner layer lipid (dioleoylphosphatydic acid, DOPA) is added dropwise into the calcium dispersion. The cores of LCP NPs are then formed due to precipitation of calcium and phosphate or phospholipid (DOPA). After washing with ethanol, the cores are collected and then re-dispersed in chloroform containing outer layer lipids. Then a thin-film is obtained by solvent evaporation. Accordingly, the final LCP NPs are prepared after hydrating the film. The resulting LCP NPs have a small and uniform size distribution and good colloidal stability, combining the advantages of both CaP and liposome.

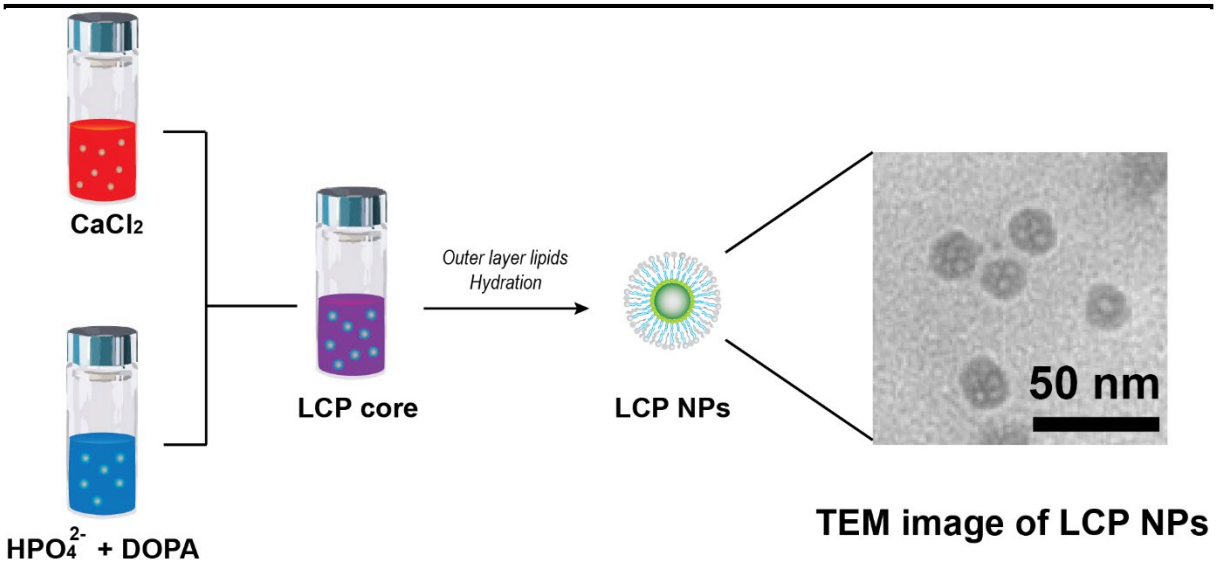

Figure 2.5 Schematic illustration of the preparation of LCP NPs via micro-emulsion method.

The LCP NPs have an average hydrodynamic size of 40 nm, with the CaP core size of around 15-20 nm [59, 68]. The well-designed W/O dispersant and the quick magnetic stirring attribute to the controlled size. Theoretically, the precipitation of CaP or Ca-phospholipid forms on the interfaces of dual phases [39, 81]. Therefore, the water/oil ratio could judge the size by affecting the interface. Similarly, the surfactant between water and oil phases is a second key factor for the LCP size [79]. The surfactant molecules stabilising water droplets provide a cage-like effect that can control the nucleation and growth of CaP precipitate [82]. Recent research has revealed that utilising Triton X-100 instead of Igepal CO-520 results in larger NP than 40 nm, due to the size increase of CaP cores [79]. Moreover, the Ca/P molar ratio is also reported to affect LCP size [59, 74, 82]. The possible mechanism may involve in the influence of CaP formula, polymorph, and precipitation amount [82].

The coated lipids can be used for NP modification. The special lipid molecules can be intercalated into the outer lipid layer. Basically, the outer layer lipids used for LCP contain 1,2-dioleoyl-sn-glycero-3-phosphocholine (DOPC) and cholesterol. The neutral charge of DOPC and cholesterol leads to a slightly negative zeta potential of LCP NPs (~15 mV) [40, 59]. With replacing DOPC by cationic lipids such as 1,2-dioleoyl-3-trimethylammonium propane (DOTAP), the surface charge of LCP NPs can be regulated in a broad range [83, 84]. Due to the similar structure compared to DOPC, a subset of phospholipids can be employed to modify LCP NPs to bring them multiple functions such as increased circulation longevity (distearoyl phosphatidylethanolamine, DSPE-PEG), targeting ability (folate conjugated DSPE-PEG),

grafting surface moiety (maleimide, carboxylic acid, or amine conjugated DSPE-PEG) and illumination (DSPE-PEG grafted with fluorescent groups) [85-87]. The modification of LCP NPs can also be achieved by lipid substitution in its outer layer. As known, PEGylation plays an important role in NP bio-application [88, 89]. The PEG chains minimise the mononuclear phagocyte system (MPS) recognition, thus increasing the circulation time of nanomaterials in blood [6, 90]. To achieve this MPS escape, the high surface density of PEG chains is required [91]. Despite that liposomes are unable to support more than 6% molar PEG-lipids modification during their formation [92], the LCP NPs exhibit the compatibility to as high as 20% molar ratio of PEG-lipid in the outer layer lipids, as a consequence of CaP core support [91]. This increase in PEG-lipid ratio definitely prolongs the LCP circulation in vivo, and influence the biodistribution of LCP NPs as well [93, 94].

2.2.2.2 Application of LCP NPs in cancer therapy

As the most popular non-viral gene vector, CaP materials perform good packaging ability to genetic materials such as DNA and RNA. The CaP crystal prevents DNase/RNase binding to its target oligonucleotides via steric hindrance and thus provide the protection of loaded genes. LCP NPs show effective gene loading, with an optimised 60% loading efficiency [59, 95]. The pristine LCP NPs can be internalised by a variety strain of cells, and their modification with targeting ligands facilitates the cellular uptake significantly. Especially, Tang et al. reported that dual targeting ligands on modified LCP NPs facilitated their quick and specific accumulation in vivo [93]. The delivered genes maintained their gene silencing ability. Yang et al. demonstrated the luciferase siRNA loaded with LCP NPs could silence 80% of its target gene at a dose as low as of 100 μg/kg (Figure 2.6A) [80]. They then evaluated the in vivo anticancer ability using an siRNA cocktail (siRNAs against MDM2, c-myc, and VEGF), suggesting that the LCP NP delivery would prolong tumour bearing mice survival, and eliminate the lung metastasis (Figure 2.6B). Similarly, plenty of work has been done on the gene delivery of LCP NP for cancer treatment [96-98].

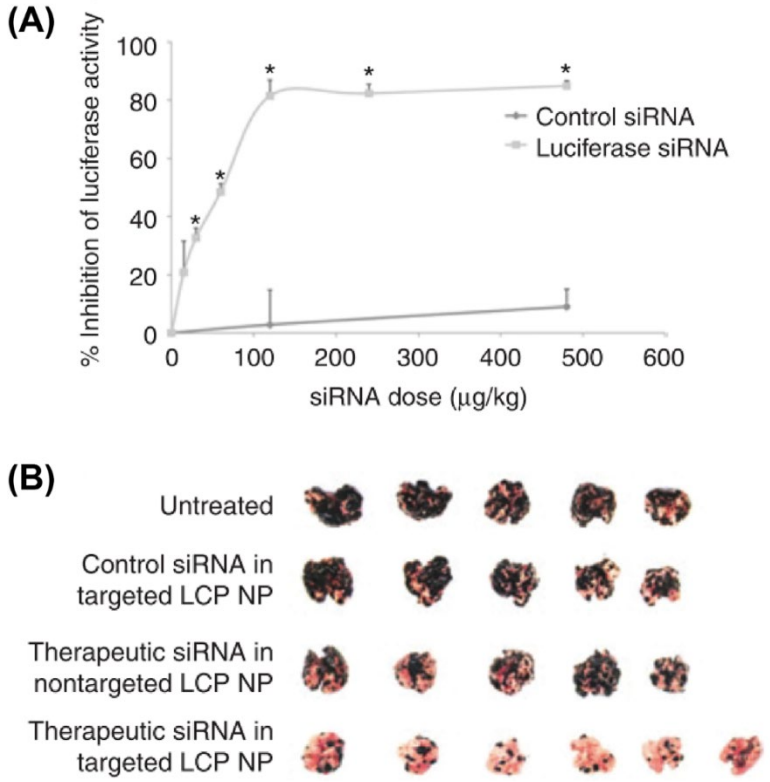

Figure 2.6 Evaluation of gene delivery effect of LCP NPs in vivo. (A) In vivo luciferase gene silencing effect of LCP delivered luciferase siRNA in a dose-responsive manner; and **(B)** photographs of lungs from tumour bearing mice showing the anti-metastasis efficacy of therapeutic siRNA cocktail in LCP NPs. Reprinted with the permission from Yang et al. [80]. Copyright (2012) Elsevier B.V.

Furthermore, LCP NPs have been employed as vehicles for a variety of anticancer drugs. Generally, co-precipitation of the drug molecules within the NP core is the most popular payload method. Due to the specific affinity with calcium ions, anticancer drug molecules with phosphate groups are easy to achieve a high payload. Gemcitabine triphosphate (GTP), a nucleoside analogue with anti-tumour therapeutic effect, was delivered by targeting LCP NPs (GTP-LCP-PEG-AA) to treat H460 and BxPC-3 solid tumour. After 4 injections at a GTP dose of 4 mg/kg, the tumour growth of both tumour models was inhibited compared to control groups [99]. Similarly, the delivery of gemcitabine monophosphate (GMP) [98], antiviral acyclovir monophosphate (ACVP) [100, 101] and zoledronate [102] were also achieved.

LCP NPs are also reported as the peptide delivery vehicle for cancer treatment [87, 103]. Xu et al. explored the modified tyrosinase-related protein 2 (p-Trp2) peptide payload by LCP NPs

as a vaccine for cancer therapy, with CpG oligonucleotide as an adjuvant (Figure 2.7) [60]. The mannose mediated dendritic cell (DC) cytosol delivery of exogenous antigen (p-Trp2 peptide) by LCP NPs led to the activation of endogenous antigen presenting pathway, resulting in the peptide presented by MHC-I complex on DCs to T cell receptor. The process activated $CD8^+$ lymphocytes proliferation and a strong cytotoxic T-lymphocyte (CTL) response in vivo.

In practical, LCP NPs can load more than one therapeutics to treat cancers in a combined method. In particular, LCP NPs are widely employed in gene therapy-related combination therapy. Chen et al. synthesised LCP NPs with dsRNA [poly (I:C)] and anticancer drug (zoledronic acid) to treat melanoma [104]. They further confirmed the superior antitumor activity in the tumour bearing mouse model. More significant results were obtained from the combination of gene therapy and photodynamic/photothermal therapy (PDT/PTT). In related studies, the volumes of tumour significantly shrank after treatment. In the presence of oxygen, photo-illumination can activate photosensitizing drugs, producing singlet oxygen species (ROS) and finally inducing tumour apoptosis [105]. Recent studies proved the HIF1α, which related to cell overcoming hypoxia mechanism, was upregulated during the PDT therapy, as resistance to PDT-induced hypoxia [106]. A co-delivery of a photosensitizing drug (PpIX) and HIF1α siRNA by LCP NPs, therefore, resulted in a ~40% decrease in tumour volume in the mouse model [107]. Moreover, the co-delivery of the PTT drug (indocyanine green, ICG) with cell death siRNA (CD siRNA) using the EGFR targeted LCP NPs can almost eliminate both small tumours (~100 mm^3) and large tumours (~500 mm^3) [108].

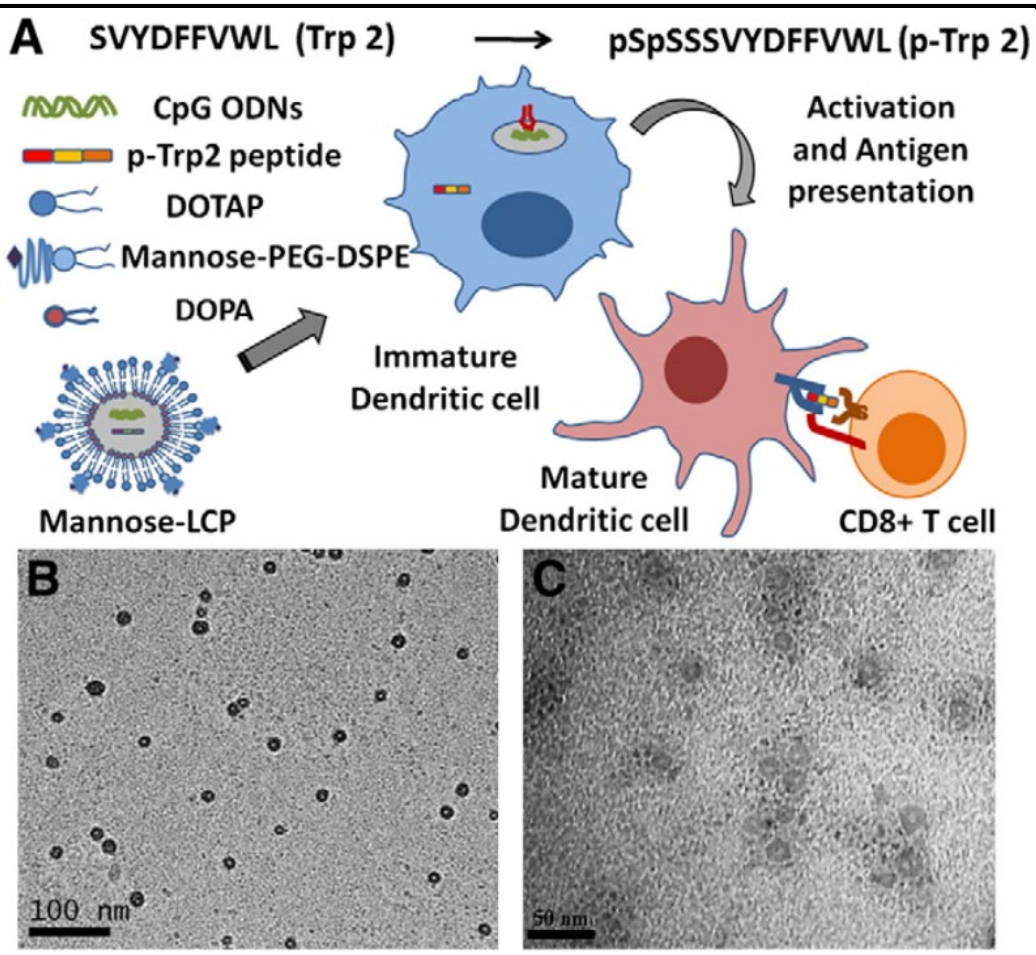

Figure 2.7 Design strategy and characterisation of mannose-LCP NP based vaccine. (A) Strategy illustration of LCP based vaccine to induce CD8+ lymphocyte dominated cytotoxic T-lymphocyte (CTL) response. The **(B)** CaP cores and **(C)** the final vaccine NP delivery system is characterised by TEM. Reprinted with the permission from Xu et al. [60]. Copyright (2013) Elsevier B.V.

2.3 CaC-based NPs in cancer therapy

Apart from CaP, calcium carbonate (CaC) is also an important calcium material. In general CaC NPs showed lots of similarity to CaP NPs, such as low cost, easy acquisition, and good biocompatibility/biodegradability. These features bring them the widespread interest in their medical applications. As inorganic materials, they also face problems in areas such as colloidal stability. In this section, we first review the bare CaC NPs, focusing on their unique characters compared to CaP NPs. Sequentially, the CaC NP's application in cancer therapy is summarised. Finally, the lipid-coated CaC (LCC) NPs with their application are reviewed.

2.3.1 CaC NPs

2.3.1.1 The property of CaC NPs

Compared to CaP, CaC exhibits differences in crystallisation and structure formation. The common formula of CaC is $CaCO_3$, with three crystal structures illustrated in Figure 2.8. The solubility of these polymorphs is slightly different (5.79×10^{-4} mol/L for calcite, 7.75×10^{-4} mol/L for aragonite, and 1.10×10^{-4} mol/L for vaterite). In addition, their mineral hardness varies, though rarely discussed in drug delivery applications. Among these polymorphs of CaC, the metastable vaterite is the most practicable due to its large porosity, surface area, rapid pH-response, and low thermodynamic stability.[81]

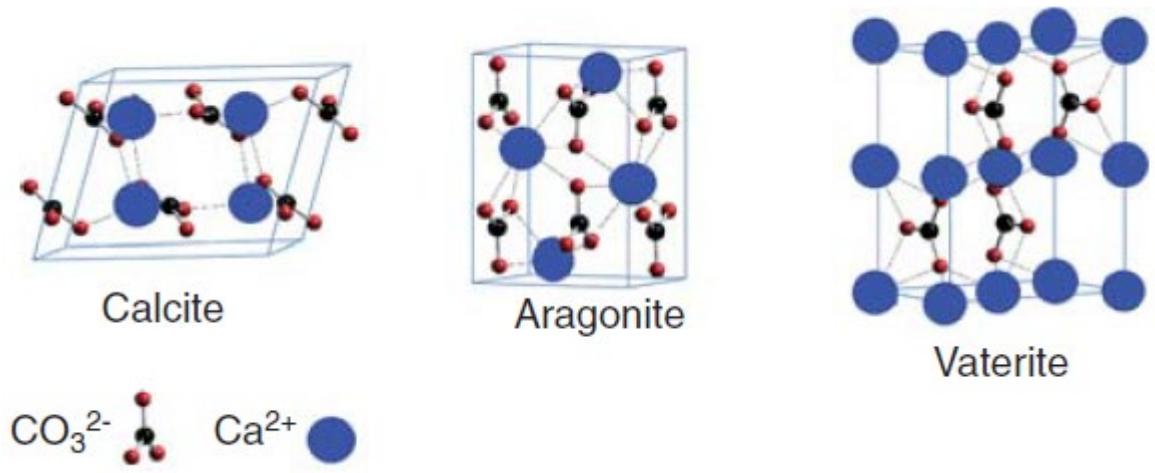

Figure 2.8 Different polymorphs of CaC NPs. Vaterite belongs to the hexagonal crystal system, whereas calcite occurs in the trigonal and aragonite in the orthorhombic systems. The morphological forms of CaC are related to the synthesis conditions, such as the concentration of reactants, temperature and nature of additives. Reprinted with the permission from Maleki D.S. et al. [63]. Copyright (2015) Taylor & Francis.

Although CaP and CaC are both responsible to pH changes, they show a slight difference in the sensitive range. Table 2.4 summarise some typical reports about the pH triggered release from CaP and/or CaC NPs. Generally, the reported responsive pH of CaC (6.0-6.8) is higher than that of CaP (4.5-6.0) in NP drug delivery applications. This is attributed to their Ksp of

CaP and CaC precipitates in various forms [81]. In particular, dissolution of CaC NPs generates carbon dioxide gas, which may lead to a higher solubility of CaC. This feature also endows CaC NPs a potential application in ultrasound-based cancer diagnosis.

Table 2.4 The pH-responsive release of CaP and/or CaC NPs.

NP	Cargo in delivery	Release pH	Ref
CaC based NPs			
Amorphous CaC coated with silica	DOX	6.5	[109]
CaC with gold nanostar	Indocyanine green	6.4	[110]
CaC (vaterite polymorph)	Cisplatin	6.0	[111]
Silica conjugating CaC	DOX	6.2-5.4	[112]
CaC linked hyaluronate	DOX	6.8-5.5	[113]
CaC	DOX	6.8	[114]
CaP based NPs			
Gold nanorod with polymer-CaP	DOX	5.0	[115]
Hyaluronan coated CaP	siRNA	5.0	[116]
Gold embedded polymer CaP	Gold and DOX	5.1	[117]
polymer coated CaP	Adenosine and DOX	6.0-4.5	[118]

2.3.1.2 CaC NPs in cancer therapy application

Due to the high affinity of calcium ions for the carboxyl groups, CaC NPs have been employed for therapeutic protein/peptide delivery [62]. In general, two different ways are adopted for protein payload. CaC NPs can (1) adsorb proteins onto their surface, or (2) co-precipitate with proteins when NPs are fabricated [119]. Similarly, some anticancer drugs can be loaded by CaC NPs. Wu et al. reported a facile approach to co-load and co-deliver hydrophobic and hydrophilic drugs at the same time [120]. In most examinations, the pH sensitivity of CaC is utilised for sustained release within an acidic pH value range corresponding to the tumour microenvironment.

Specifically, CaC NPs are potentially applied for cancer theranostics due to the carbon dioxide gas generated in the acidic environment. In particular, the gas generation can be trigged even under a very mild acidic pH. As shown in Figure 2.9, Min et al. developed CaC-based NPs for

ultrasound imaging and anticancer drug delivery.[114] The hypersensitive CaC NPs can dissolve and generate CO_2 gas at pH 6.8, thus leading to the extracellular gas generation in the acidic tumour microenvironment for tumour ultrasound imaging.

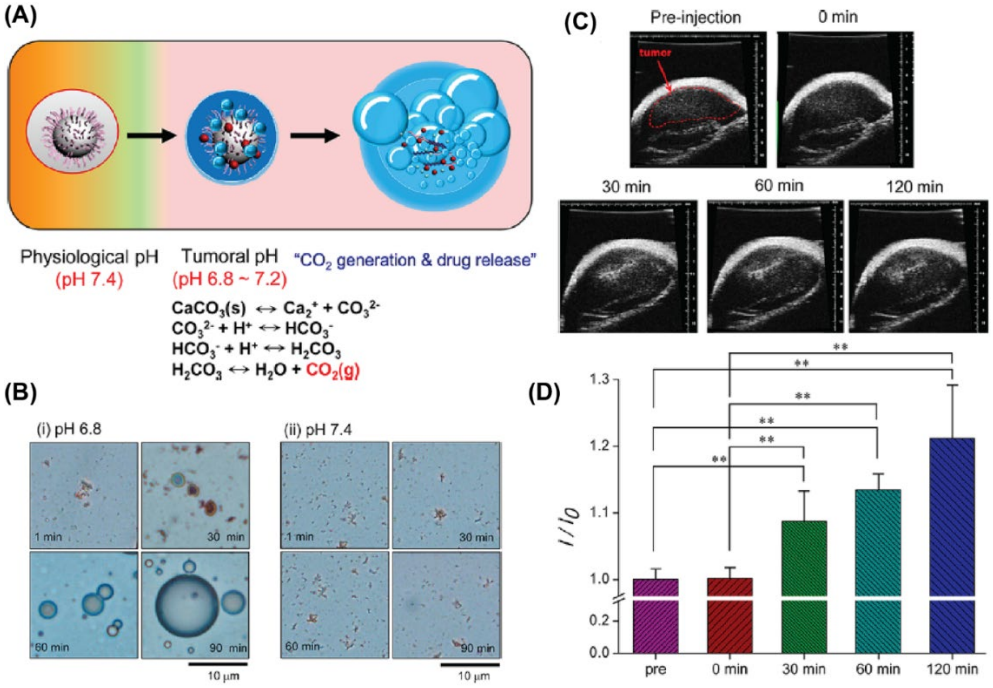

Figure 2.9 Example of carbon dioxide gas generation from CaC based NPs for tumour imaging application. (A) Schematic illustration of the pH triggered gas generation; **(B)** optical micrographs of CO2 generating from CaC based NPs incubated in PBS at pH (i) 6.8 and (ii) 7.4 for 90 min; **(C)** ultrasound imaging of the SCC-7 tumour bearing mouse by intratumoural injection of CaC based NPs; and **(D)** the histogram of an ultrasound intensity profile from tumour size as a function of time. Reprinted with the permission from Min KH et al.[114]. Copyright (2015) American Chemical Society.

2.3.2 Lipid-coated calcium carbonate (LCC) NPs applied in cancer therapy

Using a similar way for LCP synthesis and modification, LCC NPs with a bilayer coating can be prepared [61]. The obtained LCC NPs exhibit sphere yolk-shell structure, and the size of NPs is uniformly around 40 nm in diameter. Moreover, surface modification of CaC-based NPs uses additional organic substances containing carboxylic, hydroxyl, carboxylate, phosphonate, sulfonate and amino groups, inducing the formation of applicable vaterite CaC polymorph [64, 121-123].

Due to the high affinity of calcium ions for the carboxyl groups, LCC NPs are employed to load and deliver therapeutic protein/peptide delivery [62]. As shown in Figure 2.10, Kim et al. developed a therapeutic EV peptide (EEEEpYFELV) that mimics the Y845 site of EGFR and induces cell apoptosis via diminishing EGFR-initiated cell proliferation. They demonstrated that EV delivered by LCC NPs provoked a high tumour growth retardation effect. Notably, the LCC delivery system exhibited better efficacy than the hollow membrane/core lipid NP composed of the same lipids. The postulated reason for the enhanced therapeutic effect is the facile pH response of CaC cores in LCC improves the peptide release, decreasing retention of the dissociated peptide-encapsulating NPs in endosome.

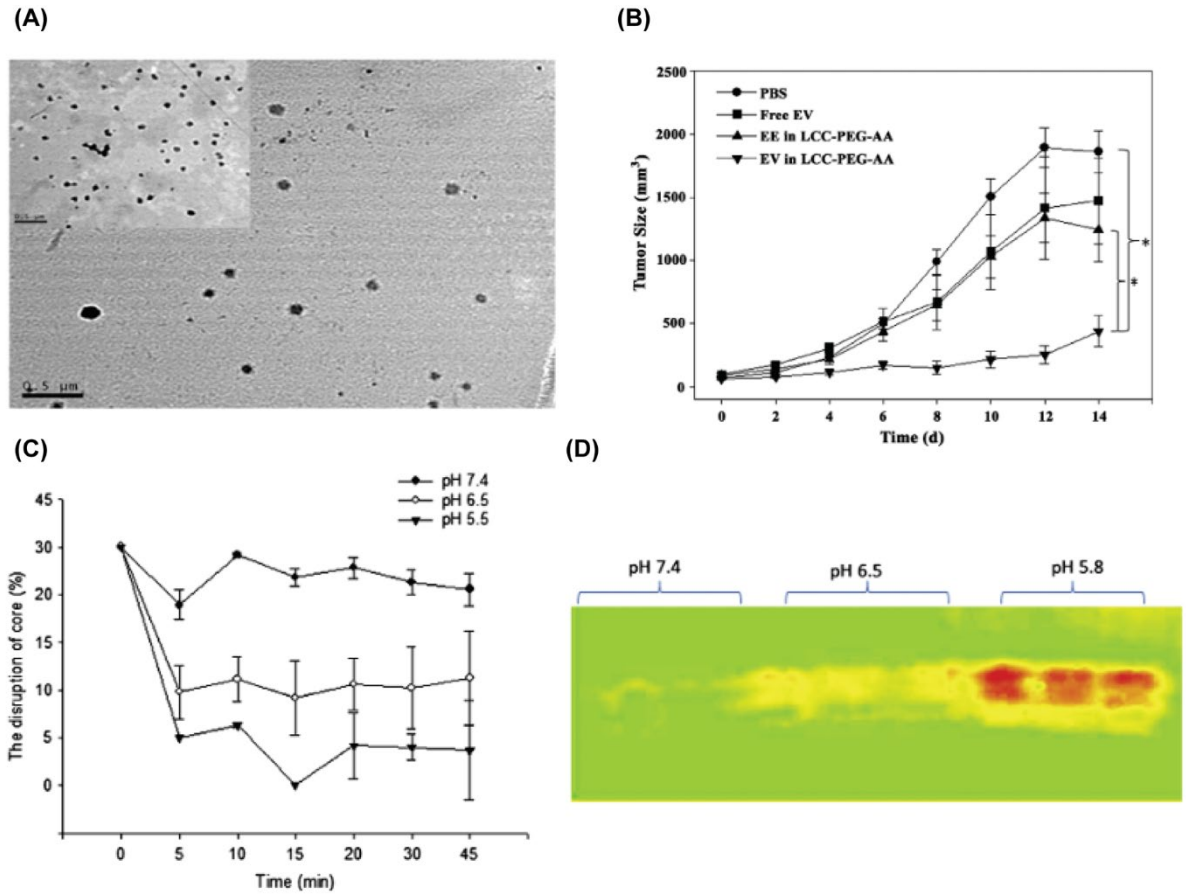

Figure 2.10 LCC NPs for peptide delivery. (A) The TEM image of LCC NPs, **(B)** tumour growth inhibition of LCC NPs with EV peptide in an H460 tumour bearing nude mouse model. **(C)** The disruption of the CaC cores measured by dynamic light scattering, and **(D)** SDS-PAGE image of the EV peptide release from LCC NPs under different pHs. Reprinted with the permission from Kim et al. [61] Copyright (2013) Elsevier. B.V.

Dong et al. developed an LCC-based NPs encapsulating Mn^{2+}-chelated chorin e6 (Ce6(Mn)) for cancer theranostics [124]. The Ce6(Mn) were mixed with calcium micro-emulsion, and co-precipitated when carbonate was added under vacuum. The drug-loaded core formation is postulated to be a consequence of manganese ion and carbonate combination. The bilayer lipids were next assembled to achieve biological and colloidal stability for further in vivo application. Detailed synthesis scheme is shown in Figure 2.11.

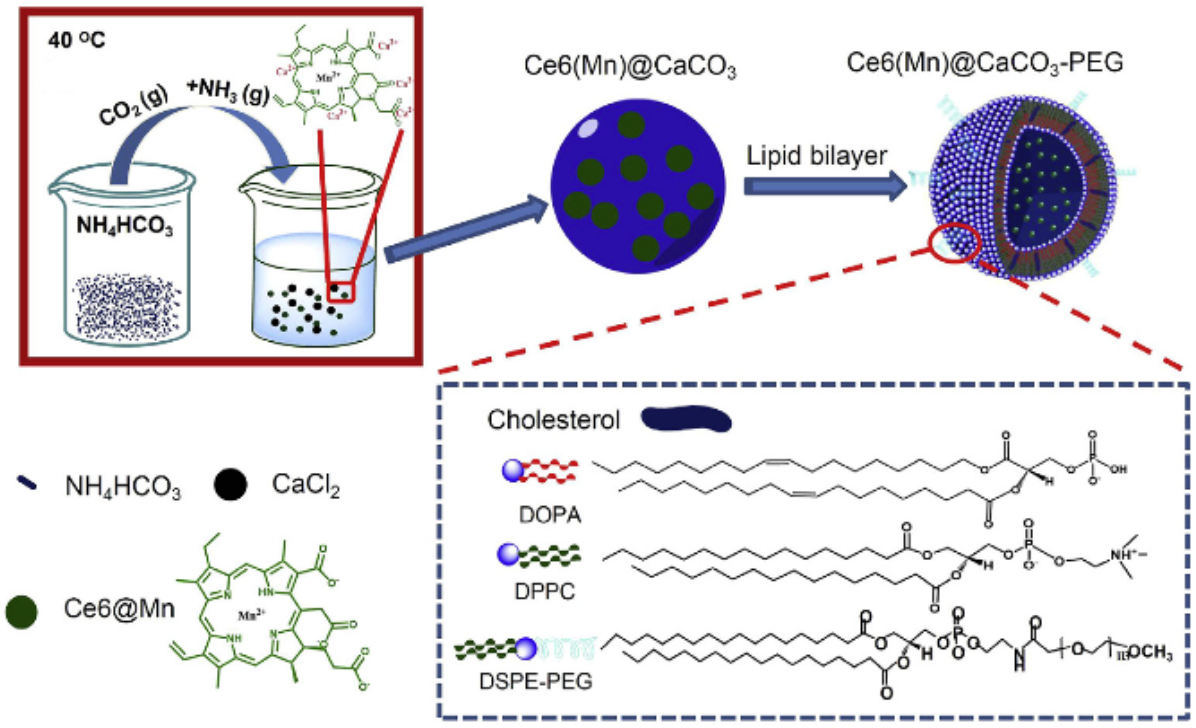

Figure 2.11 Scheme showing the synthesis and structure of Ce6(Mn)@CaCO3-PEG NPs. Reprinted with the permission from Dong et al.[124]. Copyright (2016) Elsevier. B.V.

Due to the high sensitivity of CaC to mild acidic pHs, the DNA/RNA delivery by LCC NPs are limited. Nevertheless, there are still certain successful outcomes in this aspect [121, 125, 126]. More investigations on LCC NPs are focused on protein and anticancer drug delivery. In general, the mild pH response indicates that NPs would be partially degraded in the tumour microenvironment (around 6.5-7.0), leading to a portion of undesirable gene leakage. According to the Ksp values, CaC crystals are more pH sensitive than CaPs, although the pH response of a particular NP differs slightly due to the formula changes. Therefore, we postulate the CaP based NPs are more suitable for gene delivery than CaC NPs.

2.4 Calcium-based hybrid NPs in cancer therapy

2.4.1 CaP/CaC hybrid NPs and their application

The unique advantages of CaP or CaC nanomaterials motivate us to strategically make a CaP/CaC hybrid nanomaterial that inherits the merits of both materials and overcome their drawbacks. Simply, incorporation of carbonate into CaP cores will endow its gas generation ability, which can be used for ultrasound imaging technique guided theranostics. The difference in pH responses between those of pure CaP and CaC suggests that the hybrid nanomaterials would own an adjustable in-between responsible pHs [40].

Despite the advantages of CaP-mediated gene delivery such as biosafety and non-toxicity, this method suffers from the lower consistent transfection efficiency and difficulty in controlling the condition for transfection [74, 127]. Incorporation of carbonate provides an attractive option for modification of this method [126, 128]. Notably, the mixture of CaP and CaC in the cores would lead to some improvement in size control when the co-precipitates form. The DNA encapsulation efficiency would not be affected, while the CaC crystal growth seems to be limited by the existence of CaP, with the smallest NP size obtained under the carbonate/phosphate initial molar ratio of 31/1 [126]. As a consequence, the gene transfection ability by the synthesised $CaCO_3$/CaP/DNA is enhanced tremendously with an appropriate phosphate doping ratio. This report provides an inspiring approach to control the particle size and crystallisation, improve the thermodynamic stability, and further enhance gene delivery efficiency with CaP/CaC hybrid NPs.

2.4.2 Polymer coated CaP/CaC hybrid NPs

To develop CaP/CaC hybrid NPs with ideal biocompatibility and biodegradability for in vivo applications, these materials are necessarily coated with biopolymers or lipids. Wu et al. reported a facile self-assembly approach to synthesise biotin-heparin/heparin/CaC/CaP hybrid NPs (HPB/HP/CaC/CaP NPs) to treat cancer [129]. The negatively charged heparin chains endow the NPs with good stability in the presence of serum, and provide anticancer activities in tumour progression and metastasis. The biotin on NP surfaces was to achieve cancer cell targeting. The obtained NPs were around 100 nm in deionized water, and slightly increased to

120-160 nm in medium containing 10% serum. Although NPs were protected by polymers, a significant increase in PDI was still noticed when the NPs were dispersed in medium with 10% serum. As revealed in TEM and SEM images, the NPs seemed to be somehow aggregated. These findings suggest that the polymer coating, although efficient, may need further optimisation for better colloidal stability. Notably, this is the only report on using the organic coating to improve the dispersity of CaP/CaC NPs. Therefore, more efforts are required in this aspect.

2.5 Nanotechnology in cancer immunotherapy

The past decade has witnessed the arising of cancer immunotherapy as an efficient cancer therapeutic strategy. Cancer immunotherapy is able to eliminate cancer cells by enhancing or modulating the host immune system. With the onset of cancer, multiple immune resistance mechanisms, such as local immune evasion, tolerance induction, and immune edition, are developed for tumour escape from immune surveillance [130, 131]. Immunotherapy is thus proposed to stimulate the effectors and/or counteract inhibitory mechanisms [132], including the regulation of immune cells (vaccine and T cell engineering), cytokines (ILs, IFNs, TGFs, TNFs, etc.) and immune checkpoints. Here we focus on both immune checkpoint blockade and cytokine regulation. The mechanism and influence on cancer immunity were reviewed, followed by the paradigms of how NPs improved their efficacy in cancer immunotherapy.

2.5.1 Immune checkpoints in immunotherapy with NP enhancement

Immune checkpoints refer to the regulator pairs in the immune system. Their interaction leads to either facilitating or preventing the immune process. Recent investigations revealed that cancer escape from immune surveillance is through the control of immunosuppressive checkpoints. In 2018, the Nobel Prize in physiology or medicine was awarded to those work on uncovering the immune activation to attack cancer based on immunosuppressive checkpoints, such as CTLA-4 (cytotoxic T-lymphocyte-associated protein 4) and PD-1 (Programmed Death 1) [133, 134]. These findings led to the successful marketing of several drugs (Table 2.5), which show significant therapeutic efficacy in selected patient cohorts with late-stage cancer, combining with remarkable pain relief and less adverse effects. Among the

immunosuppressive checkpoints, Programmed Death 1 (PD-1) and its major ligand (PD-L1) are focused.

Table 2.5 Marketed PD-L1 antibodies.

Name (Trade name)	Company	First FDA approval	Medical uses	ORR		tr-AE (Grade ≥3)
				PD-L1+	PD-L1-	
Atezolizumab (Tecentriq)	Roche Genetech	2016	Urothelial carcinoma, NSCLC	26%	9.5%	17%
Avelumab (Bavencio)	Merck Serono & Prizer	2017	Merkel-cell carcinoma	53.8%	4.2%	6.8%
Duralumab (Imfinzi)	AstraZeneca	2017	Urothelial carcinoma	31%	0%	4.9%

Abbreviations: ORR, objective response rate; AE, adverse event; tr-AE, treatment-related adverse event. NSCLC, non-small cell lung cancer.

Data source: Highlights of prescribing information for Tecentriq, Bavencio, and Imfinzi. ORR and AE data refer to references [135-138].

2.5.1.1 PD-1/PD-L1 checkpoint

PD-L1, also known as CD274 and B7-H1, is transmembrane protein commonly expressed on the surface of antigen presenting cells and tumour cells. PD-L1 specifically binds to its receptor, PD-1, which is expressed on the surface of immune-related lymphocytes, such as T cells, B cells, and myeloid cells [134, 139]. As shown in Figure 2.12, the binding of PD-L1 to PD-1 is able to activate the downstream signalling of PD-1 receptor in T cells, thus inhibiting the proliferation, cytokine generation and release, and cytotoxicity of T cell. This down-regulation guards against autoimmunity and chronic infection. However, many tumour cells also use this mechanism to protect themselves from immune attack, causing the tumour immune evasion [139]. Inhibition of either PD-1 or PD-L1 will enhance T cell responses to cancer. This approach is known as PD-1/PD-L1 based immunotherapy.

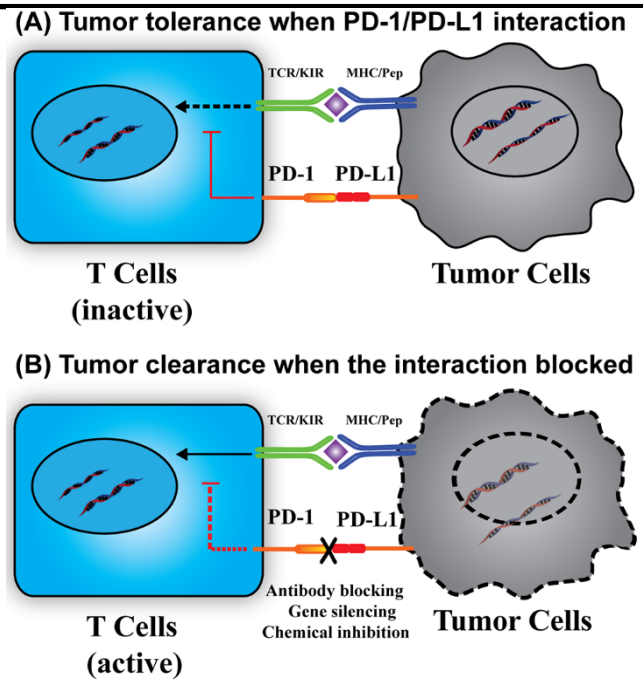

Figure 2.12 Immunotherapy based on PD-1/PD-L1 interaction. (A) The interaction of PD-1/PD-L1 causes tumour immune tolerance. The PD-1/PD-L1 interaction stimulates the downstream signals to suppress T cell activation, resulting in tumour cell survival. **(B)** Breakdown of the PD-1/PD-L1 interaction reactivates T cells and related immune responses. Without the PD-1/PD-L1 interaction, the suppression signal is removed, thus leading to T cell activation, proliferation, and cytokine generation and tumour cell elimination.

Based on this understanding, six antagonists have been developed and successfully approved by the FDA. These antagonists are monoclonal antibodies and can bind to the surface PD-1 or PD-L1. Notably, these antibodies have been demonstrated with remarkably durable and persistent antitumour responses, with some patients remaining free from cancer progression for many years [140, 141]. The success in PD-1/PD-L1 therapy regimens boosts the mechanism studies. Further studies of PD-L1 reveal its intracellular and extracellular existence, and lead to the issue of whether the antibody is the only optimal solution in all cancer cases. Moreover, the investigation of PD-L1 regulation provides targeted sites for PD-L1 therapy.

Despite that PD-L1 antibody treatment would be recommended to those patients with high PD-L1 expression, the objective response in this cohort is not always in concordance to their PD-L1 positive index in cancer (Table 2.5). Recent investigations suggest the broad distribution of PD-L1 in different cellular compartments. The known PD-L1 format includes membrane PD-L1 (mPD-L1) [142, 143], cytoplasm PD-L1 (cPD-L1) [143, 144], nuclear PD-L1 (nPD-L1) [144, 145], and serum PD-L1 (sPD-L1) [146, 147]. The reported PD-L1 formats and their functions are summarised in Table 2.6. With the understanding of PD-L1 distribution, we propose a new hypothesis that all PD-L1 formats, not only mPD-L1, are able to influence the response to the antibody. The intracellular PD-L1 formats may translocate to the membrane or secrete outside cells, and bind to antibodies, contributing to the ORR in PD-L1- cohort (Table 2.5). The mPD-L1, on the other hand, would translocate into cells as cPD-L1 under the stress of antibody, causing the low (<50%) ORR in PD-L1+ cohort (Table 2.5).

Table 2.6 The reported PD-L1 formats.

Format	**Location**	**Structure**	**Source**	**Possible functions**	**Treatment response**	**Detection ***	**Ref**
mPD-L1	Membrane	Integrity	Endogenous translation	Bind with PD-1 for immune regulation	Antibody, gene, and chemo-inhibitor	WB, IHC	[142, 143]
cPD-L1	Cytoplasm	-	Endogenous translation	Transfer to the membrane, shorten disease-free survival, and cell growth and migration	Gene and chemo-inhibitor	WB, IHC	[144]
nPD-L1	Nuclei	-	-	Enhance chemo-resistance	Gene and chemo-inhibitor	WB, IHC	[144, 145]

sPD-L1	Serum	Integrity	Secretion from cancer cells/matured APCs	Bind with PD-1, associated with immune state	Antibody, gene, and chemo-inhibitor	ELISA	[147]
	Serum	Without transmembrane motifs	Enzyme cleavage	Bind with PD-1, associated with immune state	Antibody, gene, and chemo-inhibitor	ELISA	[146]
-	-	Dimeric	Crystallisation	Functional units or evolution relic	-	-	[148]

* The typical detection method abbreviations: WB (Westerner blotting), IHC (Immunohistochemistry), and ELISA (Enzyme-linked immunosorbent assay).

2.5.1.2 NP-based application in PD-1/PD-L1 therapy

In general, NPs are involved in PD-1/PD-L1 based cancer immunotherapy in three major ways: (1) NP acting as a delivery platform of some PD-1/PD-L1 related agents, (2) PD-1/PD-L1 as the target molecule for NP's delivery, and (3) immunogenic booster for the anti-PD-1/PD-L1 therapies.

Elimination of PD-1/PD-L1 expression on the cancer cell surface can expose the cell to the immune system. Currently, the blockade of PD-1/PD-L1 can be achieved via three methods: (1) antibody blockade, (2) gene silencing, and (3) pathway inhibition. Most of the NP applications are focused on genes or inhibitors, with some efforts been paid to antibody delivery [149]. Pei et al demonstrated successful delivery of PD-L1 siRNA to EOC cells by polymer-based NPs could enhance T cell immunotherapy for EOC treatment via interrupting PD-1/PD-L1 interactions [150]. Wu et al. suggested simultaneous knockdown of PD-1 and PD-L1 led to more significantly increase in the killing efficiency of TILs obtained from patients [83]. In addition, the delivery of proper inhibitors by NPs can also achieve the PD-1/PD-L1 downregulation [151].

Preclinical studies have demonstrated PD-L1 is one of the overexpressed surface markers for late-stage cancer. Therefore, this molecule can be employed for targeting delivery of anticancer therapeutics to this cell cohort. Some works have been done to devise NPs conjugated with PD-L1 antibodies for targeting delivery, resulted in strongly enhanced cellular uptake within as early as 1 h [152, 153]. However, these in vitro works lacked attention on the influence of PD-L1 mediated endocytosis on immunotherapy. And they did not discuss the interaction between PD-L1 antibodies and intracellular PD-L1 molecules.

With efficacious delivery property, the NPs provide opportunities for boosting the anticancer immunity. Chen et al. employed PLGA NPs for cancer photothermal therapy to ablate primary tumour for tumour-associated antigen release [154]. The following immune checkpoint blockade therapy generated immunological responses and eliminating the remaining tumour prognosis. Similarly, Song et al. used chemical agent oxaliplatin (OxP) to induce immunogenic cell death (ICD), and the plasmid encoding PD-L1 trap protein was delivered to the tumour site by NPs [155]. Compared to the systematical injection of antibodies, this method triggered locally and transiently produce of PD-L1 agonist products in the targeted site, resulting in synergistic anticancer efficacy with low adverse effects.

2.5.2 Cytokines in immunotherapy application with NP enhancement

Cytokines in the tumour microenvironment play an important role in cancer pathogenesis [156]. Compellingly, the interferons (IFNs), some interleukins (ILs), and tumour necrosis factors (TNFs) endow cancer apoptosis via regulating the tumour immune environment to facilitate cancer inhibition by the immune system. Alternatively, there is a high risk that cancer cells exposing to cytokine environment may undergo malignant transformation [157], and gain adaptive immune resistance [158]. On this regard, one of the arch demand for cytokine based cancer immunotherapy is to diminish the acquirable resistance. In specific, we focus on IFN-γ, a typical cytokine with dual faces in cancer immunotherapy. The resistant mechanism and how NPs reverse this resistance are reviewed.

2.5.2.1 Cytokine IFN-γ and its dual faces in cancer immunotherapy

IFN-γ, a pluripotent cytokine that mainly produced by activated T cells and natural killer cells, plays a vital role in anti-tumour immunity, suppressing tumour growth and metastasis through various mechanisms. When binding to its receptors, IFN-γ can regulate JAK-STATs (Janus kinase- signal transducer and activator of transcription proteins) pathway to activate the STAT1 transcription factor, leading to a series of response [159, 160]. One of the most important responses is the upregulation of major histocompatibility complex class I (MHC-I), which induces cell-mediated immunity [161, 162]. Meanwhile, highly immunogenic cells such as $CD4^+$ and $CD8^+$ T cells, and the infiltration of M1 phase tumour associated macrophages (TAM) is recruited to the lesion site with high IFN-γ [163]. Type I CD4+ T helper (Th1) cells improve anticancer immunity, while regulatory T (Treg) cells facilitate tumour immune tolerance. IFN-γ, as the major product of Th1 cells, could stimulate these Th1 cells and inhibit the proliferation of Treg, simultaneously [164, 165]. In general, the major role of IFN-γ is anticancer. The major immunomodulation of IFN-γ to immune cells were shown in Figure 2.13[166].

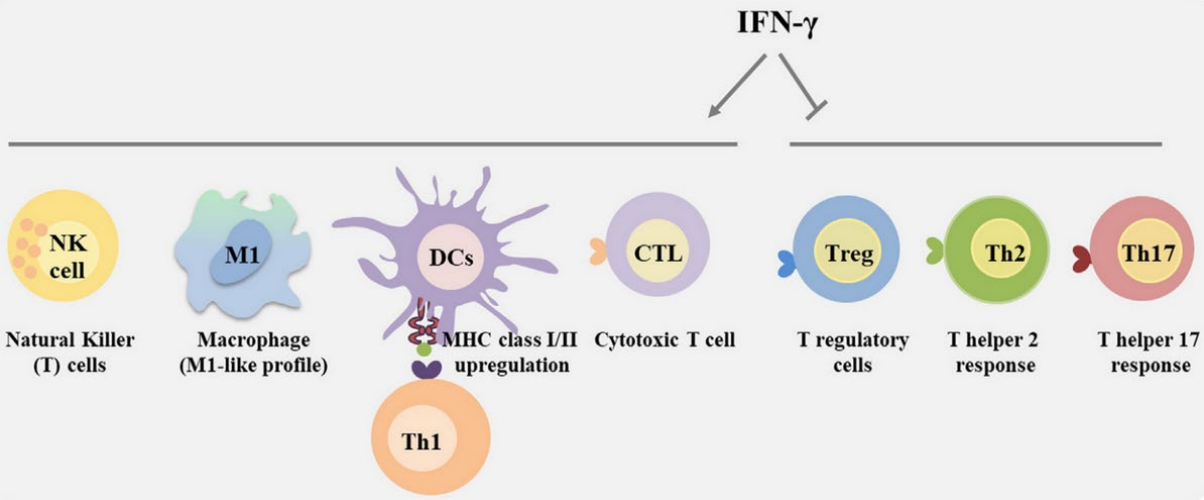

Figure 2.13 Immunomodulation effects of IFN-γ. IFN-γ produced by immune cells affects the behaviour of distinct immune cells within the tumour microenvironment. Specifically, IFN-γ activates anticancer immunity by promoting the activity of CD4 Th1 cells, CD8 cytotoxic T lymphocytes (CTLs), natural killer (NK) cells, dendritic cells (DCs), and macrophages promoting the antigen presentation. Additionally, IFN-γ activates macrophages towards a more pro-inflammatory and tumoricidal phenotype (M1 like). Alternatively, IFN-γ inhibits Treg cells, Th2, and Th17 differentiation and functions. Reprinted with the permission from Castro et al.[166]. Copyright (2019) Frontiers Media S.A.

Inconsistent with the conclusion in basic research, serval clinical outcomes indicant the controversial of IFN-γ in cancer therapy as well. IFN-γ treatment did not result in any meaningful outcomes in patients with metastatic renal cancer and colon cancer [167, 168]. These results indicate the dual faces of IFN-γ in cancer treatment. Recent studies on IFN-γ related PD-L1 induction and cancer adaptive immune resistance provide a theoretical postulation [158, 169].

As known, the expression of PD-L1 on cancer cells protects the cells from immune clearance, thus causes cancer immune resistance. Recent researches believe the PD-L1 expression can be divided into two kinds: the constitutive expression and the induced expression [169]. IFN-γ is reported as a cytokine that strongly induces PD-L1 expression, and this PD-L1 induction happens in a variety of cancer cell lines as well as in some host cells like APCs. Highly or lower constitutive expression of PD-L1 does not affect the cell responses to IFN-γ stimulation. The constitutive/inducible PD-L1 causes innate/adaptive immune resistance, correspondingly, as schematically illustrated in Figure 2.14 [158].

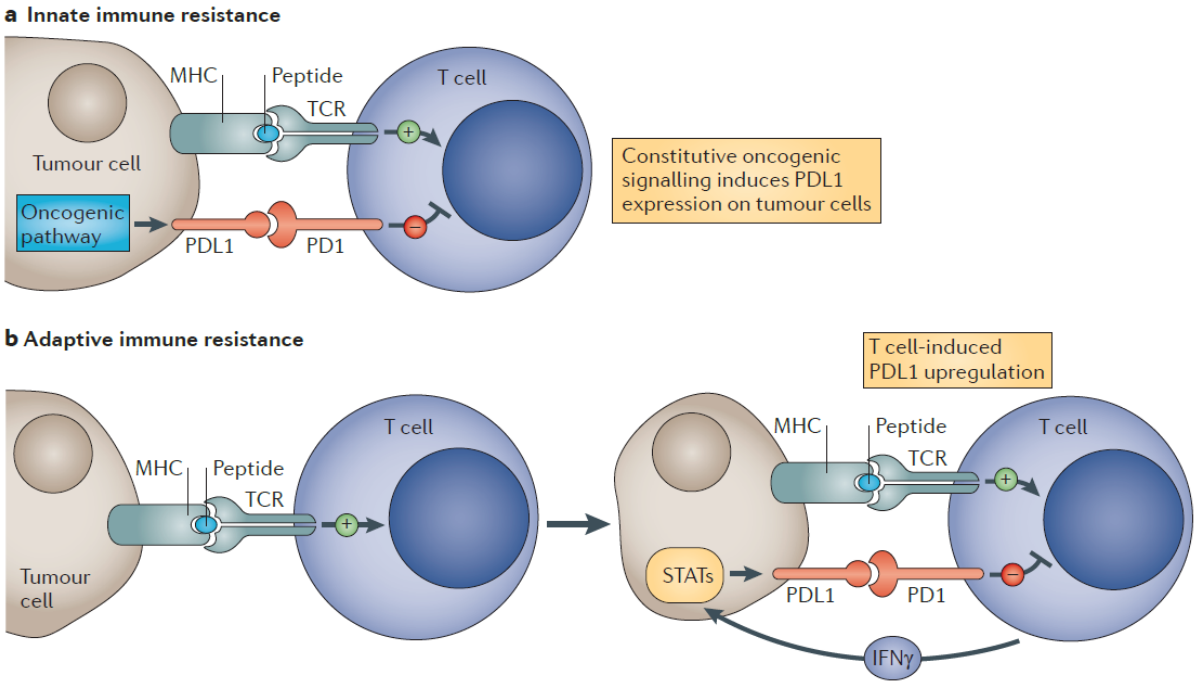

Figure 2.14 Two general mechanisms of expression of immune-checkpoint ligands on tumour and the concept of **(A)** innate and **(B)** adaptive cancer immune resistance. Reprinted with the permission from Drew M. Pardoll [158]. Copyright (2012) Springer Nature.

2.5.2.2 NP application in IFN-γ related cancer immunotherapy

In clinic, several products of recombined cytokine protein have been marketed. Actimmune (InterMune), a commercialized IFN-γ protein, showed enhanced anticancer effect in patients with bladder or colorectal carcinoma. Significant immune response and effective against cancer recurrence were observed [170-172]. In particular, IFN-γ combining with the standard treatment of platinum-based chemotherapy shows a synergistic anticancer effect. The results from a randomized phase III trial indicates subcutaneous administration of IFN-γ and cisplatin improves the complete response rates from 56% to 68%, with prolonged progression-free survival in patients [173, 174]. These advances enlighten the investigation of cytokine-related cancer immunotherapy.

With efficient delivery efficacy to cancer site, NPs hold a great potential to optimise cytokine related cancer immunotherapy. Here, the combination of cytokine and NPs provides two kinds of applications: (1) improving cytokine-mediated NP targeting ability, and (2) improving cytokine delivery to tumour by NPs. Gao et al developed polymeric NPs (IRNPs) modified with arginine-glycine-aspartic acid (RGD) and interleukin-13 (IL-13) peptide for targeted delivery to glioblastoma multiforme (GBM) cells and neovasculature cells [175]. With the peptide modification, RGD targeted to $\alpha_v\beta_3$ on neovasculature while IL-13 targeted to its receptor (IL13Rα2) on GMB cells. They demonstrated an enhanced targeting ability to these two cells in vivo, while did not mention any influence on immunity in this work. On the other hand, more efforts are endeavoured to enhancing cytokine delivery by NPs, and the application is not limited to cancer therapy, but also the treatment of virus infection [176, 177]. Mejias et al prepared magnetic NPs for IFN-γ delivery, and achieved enhanced antitumor effect on Pan02 xenograft tumour model [178]. A high degree of NP accumulation and cytokine delivery at tumour site was observed, with the increase of T cell and macrophage infiltrations. Co-delivering of anticancer drug DOX and cytokine (IFN-γ or interleukin 2) achieved better anticancer effect than that of every single free agent in vivo [179, 180].

As known, the anticancer ability of a cytokine is consisted of (1) their activation of immunity and (2) their pro-apoptosis to tumour cells. Although in vitro studies of cytokines focus more on how they interact and active immune cells, NP-based chemical drug-cytokine combination studies rely more on the direct anticancer functions of cytokines. The delivery of NP leads to strongly enhanced endocytosis, which is demonstrated with the in vitro data in all related studies. Considering the leakage of cytokine in the tumour microenvironment, these drug-

cytokine NPs could enhance local cytokine concentration to a certain degree, which can trigger infiltrated immune cells. However, this hypothesis lacks direct evidence in vitro and in vivo. Particularly for IFN-γ, the key for regimen optimisation may lie in PD-L1 downregulation, thus eliminating tumour adaptive immune resistance. To our knowledge, no attempts have been done in this aspect.

2.6 Challenges and strategy for this research

2.6.1 Challenges

To develop a proper NP for cancer therapy, we face the following challenges. Firstly, the responsive release pH of NPs needs to be improved **(the challenge for objective 1 in this research)**. As shown in Table 2.4, the instinct responsive range differs between CaC and CaP. The payload release pH from CaP based NPs indicates the majority of cargo release would happen in late endosome/lysosome stage, whereas the acidic and enzymatic condition in these organelles may be harmful to the anticancer agents, especially genes. On the other side, the CaC based NPs are too sensitive and may cause some release extracellularly and in blood circulation. In gene delivery application, both situations are not desirable. To lead to a sustained release within a precisely controlled pH range, CaP/CaC hybrid NPs may be considered. As reviewed in Section 2.4, current hybrid NPs based on calcium materials neglect effective surface coating to endow them good dispersity and stability. Inspired by some pioneer investigations on LCP and LCC NPs, it is reasonable to improve the lipid coating method for CaP/CaC hybrid NP preparation.

Furthermore, more attempts should be done to broaden the range of deliverable therapeutics **(the challenge for objective 2 in this research)**. We have noted that the current application of LCP and LCC NPs neglects the role of their lipid layer. Theoretically, anticancer drugs, depending on their hydrophilicity, can be encapsulated in both core and lipid bilayer of the NPs, as shown in Figure 2.15. Hydrophilic drug molecules, such as DNA/RNA chains, and most peptides/proteins are encapsulated in the core part. Hydrophobic drugs are loaded in the cavity of lipid layers. Amphiphilic molecules can be intercalated in the outer layer. Indeed, drugs loaded in the lipid layers are rarely reported. Most of the investigations utilised the cores to make co-precipitation of drugs with CaP or CaC, as introduced in Section 2.2 and 2.3. With more focused on the lipid layers of LCP/LCC NPs, the loading of hydrophobic/amphiphilic

anticancer drugs may be achieved. Inspired by some pioneer reports on liposome delivery, the outer lipid layer coated on LCP/LCC NPs provides a vehicle for the payload of a typical vitamin E (VE) based drug, α-tocopheryl succinate (α-TOS). The interaction of phenoxyl hydroxyl group by hydrogen bond to either carbonyl or phosphate oxygen of phospholipid can help to locate the chromanol head of VE analogue close to the aqueous interface, and the phytyl chain of this VE analogue is able to extend into the centre of bilayer due to its hydrophobicity [181, 182].

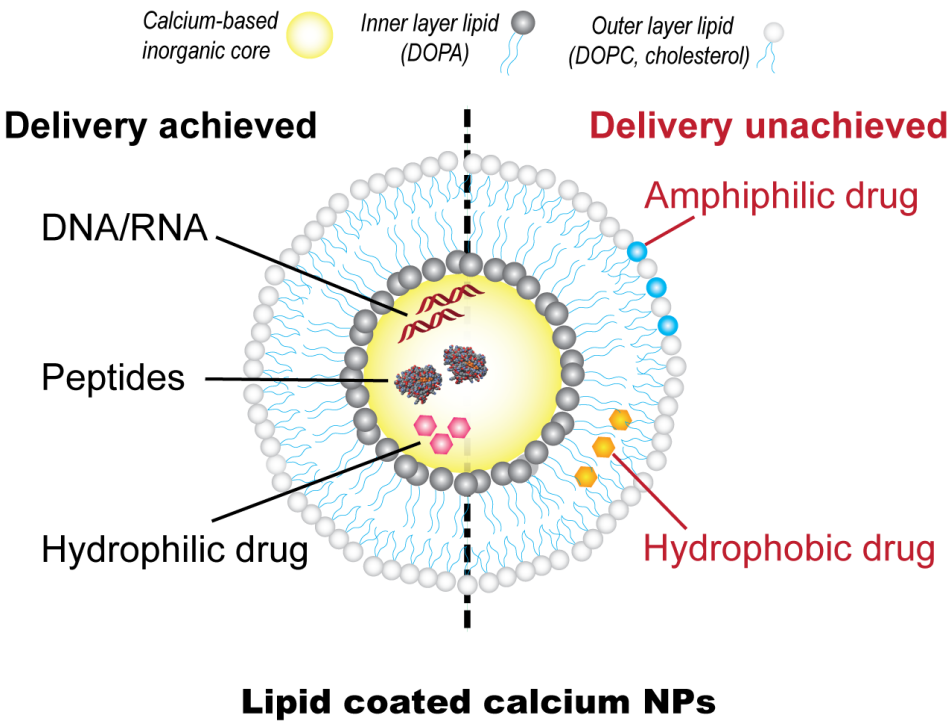

Figure 2.15 Schematic illustration of LCCP NPs and their drug delivery applications.

At last, proper approaches should be established to optimise cytokine-related cancer therapy in combination with LCP/LCC NPs **(the challenge for objective 3 in this research)**. As reviewed in Section 2.5, long term exposure to cytokines such as IFN-γ causes adaptive cancer immune resistance. When dealing with cytokine sensitive cancers, their adaptive immune resistance should be reversed to enhance anticancer immunity. Considering the strong correlations of immune system and cancer invasion, development of the cytokine-related cancer therapy would further benefit the prevention of cancer metastasis in combination with developed LCP/LCC NPs.

2.6.2 Strategy

Inspired by the exciting outcomes using CaP/CaC hybrid NPs and the merits of lipid coating to make organic-inorganic NPs, our strategy is to develop the lipid-coated calcium carbonate/phosphate (LCCP) NP platform to integrate the merits of CaP, CaC, and lipid coating for overcoming these challenges. For this new particle, its behaviour in gene loading efficiency, release profile, cellular uptake, and gene silencing ability are investigated. To enlarge the deliverable range of anticancer therapeutics, the outer lipid layer of LCCP NPs is manifested to deliver hydrophobic/amphiphilic anticancer drugs. A typical drug α-TOS is employed as an example. The LCCP NPs with FA and PEG modification is engineered for co-delivery of α-TOS and cell death siRNA for combined cancer therapy. In the end, the FA targeted LCCP NPs with α-TOS loading (NP-TOS) are combined with IFN-γ treatment for cancer chemotherapy/immunotherapy. The influence on cancer growth inhibition, metastasis prevention, and the reversal of PD-L1 mediated cancer adaptive immune resistance, are studied in this chemical drug/cytokine combination system. The challenges and strategy in this project are outlined in Figure 2.16.

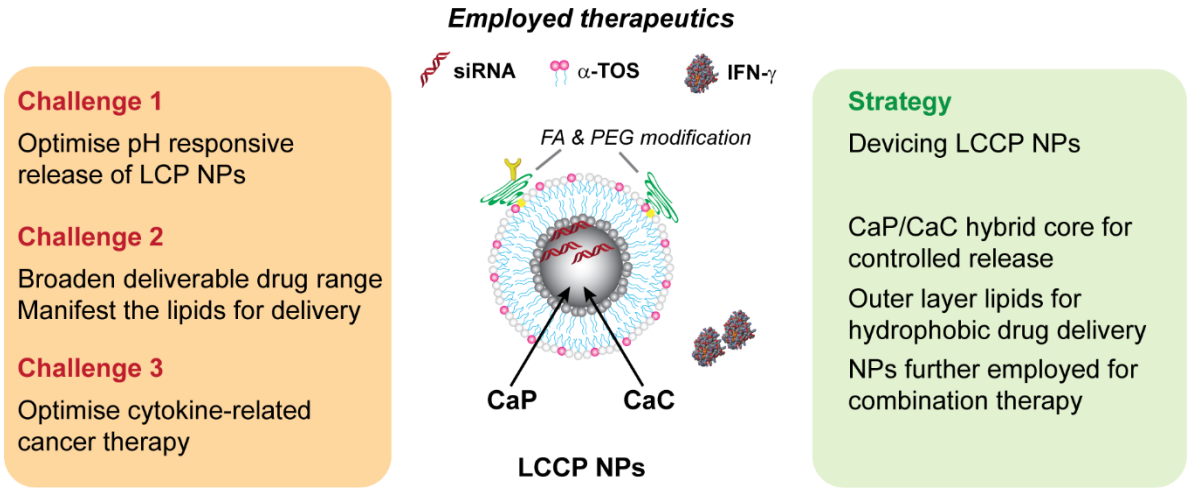

Figure 2.16 The challenges and strategy of this PhD project.

2.7 References

[1] R.L. Siegel, K.D. Miller, A. Jemal, Cancer statistics, 2019, CA Cancer J. Clin. 69(1) (2019) 7-34.
[2] F. Danhier, To exploit the tumor microenvironment: Since the EPR effect fails in the clinic, what is the future of nanomedicine?, J. Controlled Release 244 (2016) 108-121.

[3] J. Shi, P.W. Kantoff, R. Wooster, O.C. Farokhzad, Cancer nanomedicine: Progress, challenges and opportunities, Nat. Rev. Cancer 17(1) (2017) 20.
[4] Y. Zhou, Z. Peng, E.S. Seven, R.M. Leblanc, Crossing the blood-brain barrier with nanoparticles, J. Controlled Release 270 (2018) 290-303.
[5] M.-C. Chen, K. Sonaje, K.-J. Chen, H.-W. Sung, A review of the prospects for polymeric nanoparticle platforms in oral insulin delivery, Biomaterials 32(36) (2011) 9826-9838.
[6] S. Guo, L. Huang, Nanoparticles escaping RES and endosome: Challenges for siRNA delivery for cancer therapy, J. Nanomater. 2011 (2011) 11.
[7] Y.C. Barenholz, Doxil®—the first FDA-approved nano-drug: Lessons learned, J. Controlled Release 160(2) (2012) 117-134.
[8] M. Green, G. Manikhas, S. Orlov, B. Afanasyev, A. Makhson, P. Bhar, M. Hawkins, Abraxane®, a novel Cremophor®-free, albumin-bound particle form of paclitaxel for the treatment of advanced non-small-cell lung cancer, Ann. Oncol. 17(8) (2006) 1263-1268.
[9] F.C. Passero Jr, D. Grapsa, K.N. Syrigos, M.W. Saif, The safety and efficacy of Onivyde (irinotecan liposome injection) for the treatment of metastatic pancreatic cancer following gemcitabine-based therapy, Expert Rev Anticancer Ther. 16(7) (2016) 697-703.
[10] M.L. Etheridge, S.A. Campbell, A.G. Erdman, C.L. Haynes, S.M. Wolf, J. McCullough, The big picture on nanomedicine: the state of investigational and approved nanomedicine products, Nanomedicine 9(1) (2013) 1-14.
[11] D. Bobo, K.J. Robinson, J. Islam, K.J. Thurecht, S.R. Corrie, Nanoparticle-based medicines: A review of FDA-approved materials and clinical trials to date, Pharm. Res. 33(10) (2016) 2373-2387.
[12] T. Feng, Y. Wei, R.J. Lee, L. Zhao, Liposomal curcumin and its application in cancer, Int. J. Nanomed. 12 (2017) 6027.
[13] S. Koudelka, P.T. Knotigova, J. Masek, L. Prochazka, R. Lukac, A.D. Miller, J. Neuzil, J. Turanek, Liposomal delivery systems for anti-cancer analogues of vitamin E, J. Controlled Release 207 (2015) 59-69.
[14] N.K. Mehra, A.K. Jain, M. Nahar, Carbon nanomaterials in oncology: an expanding horizon, Drug Discov. Today 23(5) (2018) 1016-1025.
[15] E.N. de Carvalho Lima, J.R.C. Piqueira, D.A. Maria, Advances in Carbon Nanotubes for Malignant Melanoma: A Chance for Treatment, Mol. Diagnosis Ther. 22(6) (2018) 703-715.
[16] A. Guven, G.J. Villares, S.G. Hilsenbeck, A. Lewis, J.D. Landua, L.E. Dobrolecki, L.J. Wilson, M.T. Lewis, Carbon nanotube capsules enhance the in vivo efficacy of cisplatin, Acta Biomaterialia 58 (2017) 466-478.
[17] A. Mejri, D. Vardanega, B. Tangour, T. Gharbi, F. Picaud, Encapsulation into Carbon Nanotubes and Release of Anticancer Cisplatin Drug Molecule, J. Phys. Chem. B 119(2) (2015) 604-611.
[18] D. Bhattacharya, B. Behera, S.K. Sahu, R. Ananthakrishnan, T.K. Maiti, P. Pramanik, Design of dual stimuli responsive polymer modified magnetic nanoparticles for targeted anti-cancer drug delivery and enhanced MR imaging, New J. Chem. 40(1) (2016) 545-557.
[19] H. Xu, L. Cheng, C. Wang, X. Ma, Y. Li, Z. Liu, Polymer encapsulated upconversion nanoparticle/iron oxide nanocomposites for multimodal imaging and magnetic targeted drug delivery, Biomaterials 32(35) (2011) 9364-9373.
[20] K. El-Boubbou, Magnetic iron oxide nanoparticles as drug carriers: clinical relevance, Nanomedicine 13(8) (2018) 953-971.

[21] F. Li, Z. Liang, J. Liu, J. Sun, X. Hu, M. Zhao, J. Liu, R. Bai, D. Kim, X. Sun, Dynamically reversible iron oxide nanoparticle assemblies for targeted amplification of T1-weighted magnetic resonance imaging of tumors, Nano Lett. (2019).
[22] R. Khatik, Z. Wang, F. Li, D. Zhi, S. Kiran, P. Dwivedi, R.X. Xu, G. Liang, B. Qiu, Q. Yang, "Magnus nano-bullets" as T1/T2 based dual-modal for in vitro and in vivo MRI visualization, Nanomedicine 15(1) (2019) 264-273.
[23] J. Li, Y. Hu, Y. Hou, X. Shen, G. Xu, L. Dai, J. Zhou, Y. Liu, K. Cai, Phase-change material filled hollow magnetic nanoparticles for cancer therapy and dual modal bioimaging, Nanoscale 7(19) (2015) 9004-9012.
[24] A.K. Parchur, G. Sharma, J.M. Jagtap, V.R. Gogineni, P.S. LaViolette, M.J. Flister, S.B. White, A. Joshi, Vascular interventional radiology-guided photothermal therapy of colorectal cancer liver metastasis with theranostic gold nanorods, ACS Nano 12(7) (2018) 6597-6611.
[25] J. Nam, S. Son, L.J. Ochyl, R. Kuai, A. Schwendeman, J.J. Moon, Chemo-photothermal therapy combination elicits anti-tumor immunity against advanced metastatic cancer, Nat. Commun. 9(1) (2018) 1074.
[26] M. Shevtsov, Y. Zhou, W. Khachatryan, G. Multhoff, H. Gao, Recent Advances in Gold Nanoformulations for Cancer Therapy, Curr. Drug Metab. 19(9) (2018) 768-780.
[27] N. Elahi, M. Kamali, M.H. Baghersad, Recent biomedical applications of gold nanoparticles: A review, Talanta 184 (2018) 537-556.
[28] J. Lin, W. Hu, F. Gao, J. Qin, C. Peng, X. Lu, Folic acid-modified diatrizoic acid-linked dendrimer-entrapped gold nanoparticles enable targeted CT imaging of human cervical cancer, J. Cancer 9(3) (2018) 564.
[29] M.M. Mahan, A.L. Doiron, Gold nanoparticles as X-ray, CT, and multimodal imaging contrast agents: formulation, targeting, and methodology, J. Nanomater. 2018 (2018).
[30] X. Hu, T. Wu, X. Qin, Y. Qi, Q. Qiao, C. Yang, Z. Zhang, Tumor lysate-loaded lipid hybrid nanovaccine collaborated with an immune checkpoint antagonist for combination immunotherapy, Adv. Healthc. Mater. 8(1) (2019) 1800837.
[31] X. Zhuang, T. Wu, Y. Zhao, X. Hu, Y. Bao, Y. Guo, Q. Song, G. Li, S. Tan, Z. Zhang, Lipid-enveloped zinc phosphate hybrid nanoparticles for codelivery of H-2Kb and H-2Db-restricted antigenic peptides and monophosphoryl lipid A to induce antitumor immunity against melanoma, J. Controlled Release 228 (2016) 26-37.
[32] N. Li, Q. Sun, Z. Yu, X. Gao, W. Pan, X. Wan, B. Tang, Nuclear-targeted photothermal therapy prevents cancer recurrence with near-infrared triggered copper sulfide nanoparticles, ACS Nano 12(6) (2018) 5197-5206.
[33] B. Jang, M.S. Moorthy, L.X. Panchanathan Manivasagan, K. Song, K.D. Lee, M. Kwak, J. Oh, J.-O. Jin, Fucoidan-coated CuS nanoparticles for chemo-and photothermal therapy against cancer, Oncotarget 9(16) (2018) 12649.
[34] Y. Xiong, F. Sun, Y. Zhang, Z. Yang, P. Liu, Y. Zou, Y. Yu, F. Tong, C. Yi, S. Yang, Polydopamine-mediated bio-inspired synthesis of copper sulfide nanoparticles for T1-weighted magnetic resonance imaging guided photothermal cancer therapy, Colloids Surf. B 173 (2019) 607-615.
[35] B. Li, J. Tang, W. Chen, G. Hao, N. Kurniawan, Z. Gu, Z.P. Xu, Novel theranostic nanoplatform for complete mice tumor elimination via MR imaging-guided acid-enhanced photothermo-/chemo-therapy, Biomaterials 177 (2018) 40-51.
[36] Y. Chen, Q. Yin, X. Ji, S. Zhang, H. Chen, Y. Zheng, Y. Sun, H. Qu, Z. Wang, Y. Li, Manganese oxide-based multifunctionalized mesoporous silica nanoparticles for pH-responsive MRI, ultrasonography and circumvention of MDR in cancer cells, Biomaterials 33(29) (2012) 7126-7137.

[37] Z. Hai, Y. Ni, D. Saimi, H. Yang, H. Tong, K. Zhong, G. Liang, γ-glutamyltranspeptidase-triggered intracellular gadolinium nanoparticle formation enhances the T2-weighted MR contrast of tumor, Nano Lett. 19(4) (2019) 2428-2433.
[38] J. Lux, A.D. Sherry, Advances in gadolinium-based MRI contrast agent designs for monitoring biological processes in vivo, Curr. Opin. Chem. Biol. 45 (2018) 121-130.
[39] J. Li, Y. Yang, L. Huang, Calcium phosphate nanoparticles with an asymmetric lipid bilayer coating for siRNA delivery to the tumor, J. Controlled Release 158(1) (2012) 108-114.
[40] Y. Wu, W. Gu, J. Tang, Z.P. Xu, Devising new lipid-coated calcium phosphate/carbonate hybrid nanoparticles for controlled release in endosomes for efficient gene delivery, J. Mater. Chem. B 5(34) (2017) 7194-7203.
[41] M.A. Lopez-Heredia, G.B. Kamphuis, P.C. Thüne, F.C. Öner, J.A. Jansen, X.F. Walboomers, An injectable calcium phosphate cement for the local delivery of paclitaxel to bone, Biomaterials 32(23) (2011) 5411-5416.
[42] T. Anada, Y. Takeda, Y. Honda, K. Sakurai, O. Suzuki, Synthesis of calcium phosphate-binding liposome for drug delivery, Bioorg. Med. Chem. Lett. 19(15) (2009) 4148-4150.
[43] M.-P. Ginebra, T. Traykova, J.A. Planell, Calcium phosphate cements as bone drug delivery systems: A review, J. Controlled Release 113(2) (2006) 102-110.
[44] A. Maitra, Calcium phosphate nanoparticles: second-generation nonviral vectors in gene therapy, Expert Rev. Mol. Diagn. 5(6) (2005) 893-905.
[45] A.E. Ewence, M. Bootman, H.L. Roderick, J.N. Skepper, G. McCarthy, M. Epple, M. Neumann, C.M. Shanahan, D. Proudfoot, Calcium phosphate crystals induce cell death in human vascular smooth muscle cells: a potential mechanism in atherosclerotic plaque destabilization, Circ. Res. 103(5) (2008) e28-e34.
[46] Z. Liu, Y. Xiao, W. Chen, Y. Wang, B. Wang, G. Wang, X. Xu, R. Tang, Calcium phosphate nanoparticles primarily induce cell necrosis through lysosomal rupture: the origination of material cytotoxicity, J. Mater. Chem. B 2(22) (2014) 3480-3489.
[47] X. Zhao, S. Ng, B.C. Heng, J. Guo, L. Ma, T.T.Y. Tan, K.W. Ng, S.C.J. Loo, Cytotoxicity of hydroxyapatite nanoparticles is shape and cell dependent, Arch. Toxicol. 87(6) (2013) 1037-1052.
[48] I. Pujalté, I. Passagne, B. Brouillaud, R. Daculsi, M. Tréguer, C. Ohayon-Courtès, B. L'Azou, Study of different metallic nanoparticles on human kidney cells: Toxicity and oxidative stress, Toxicol. Lett. 205 (2011) S172.
[49] X. Feng, A. Chen, Y. Zhang, J. Wang, L. Shao, L. Wei, Central nervous system toxicity of metallic nanoparticles, Int. J. Nanomed. 10 (2015) 4321.
[50] H. Bahadar, F. Maqbool, K. Niaz, M. Abdollahi, Toxicity of nanoparticles and an overview of current experimental models, Iran. Biomed. J. 20(1) (2016) 1-11.
[51] A. Pugazhendhi, T.N.J.I. Edison, I. Karuppusamy, B. Kathirvel, Inorganic nanoparticles: a potential cancer therapy for human welfare, Int. J. Pharm. 539(1-2) (2018) 104-111.
[52] Vinhas R, Cordeiro M, Carlos FF, Mendo S, Fernandes AR, Figueiredo S, B. PV, Gold nanoparticle-based theranostics: disease diagnostics and treatment using a single nanomaterial, Nanobiosensors In Disease Diagnosis 4 (2015) 11-23.
[53] M.S. Draz, B.A. Fang, P. Zhang, Z. Hu, S. Gu, K.C. Weng, J.W. Gray, F.F. Chen, Nanoparticle-mediated systemic delivery of siRNA for treatment of cancers and viral infections, Theranostics 4(9) (2014) 872.
[54] L. Nicole, L. Rozes, C. Sanchez, Integrative approaches to hybrid multifunctional materials: from multidisciplinary research to applied technologies, Adv. Mater. 22(29) (2010) 3208-3214.

[55] C. Sanchez, G.d.A. Soler-Illia, F. Ribot, T. Lalot, C.R. Mayer, V. Cabuil, Designed hybrid organic− inorganic nanocomposites from functional nanobuilding blocks, Chem. Mater. 13(10) (2001) 3061-3083.
[56] C. Sanchez, C. Boissiere, S. Cassaignon, C. Chanéac, O. Durupthy, M. Faustini, D. Grosso, C. Laberty-Robert, L. Nicole, D. Portehault, Molecular engineering of functional inorganic and hybrid materials, Chem. Mater. 26(1) (2013) 221-238.
[57] S.H. Mir, L.A. Nagahara, T. Thundat, P. Mokarian-Tabari, H. Furukawa, A. Khosla, Organic-inorganic hybrid functional materials: An integrated platform for applied technologies, J. Electrochem. Soc. 165(8) (2018) B3137-B3156.
[58] A.C. Anselmo, S. Mitragotri, A review of clinical translation of inorganic nanoparticles, AAPS J. 17(5) (2015) 1041-1054.
[59] J. Tang, L. Li, C.B. Howard, S.M. Mahler, L. Huang, Z.P. Xu, Preparation of optimized lipid-coated calcium phosphate nanoparticles for enhanced in vitro gene delivery to breast cancer cells, J. Mater. Chem. B 3(33) (2015) 6805-6812.
[60] Z. Xu, S. Ramishetti, Y.-C. Tseng, S. Guo, Y. Wang, L. Huang, Multifunctional nanoparticles co-delivering Trp2 peptide and CpG adjuvant induce potent cytotoxic T-lymphocyte response against melanoma and its lung metastasis, J. Controlled Release 172(1) (2013) 259-265.
[61] S.K. Kim, M.B. Foote, L. Huang, Targeted delivery of EV peptide to tumor cell cytoplasm using lipid coated calcium carbonate nanoparticles, Cancer Lett. 334(2) (2013) 311-318.
[62] A.N. Koo, K.H. Min, H.J. Lee, J.H. Jegal, J.W. Lee, S.C. Lee, Calcium carbonate mineralized nanoparticles as an intracellular transporter of cytochrome c for cancer therapy, Chem. Asian J. 10(11) (2015) 2380-2387.
[63] S. Maleki Dizaj, M. Barzegar-Jalali, M.H. Zarrintan, K. Adibkia, F. Lotfipour, Calcium carbonate nanoparticles as cancer drug delivery system, Expert Opin. Drug Deliv. 12(10) (2015) 1649-1660.
[64] N. Qiu, H. Yin, B. Ji, N. Klauke, A. Glidle, Y. Zhang, H. Song, L. Cai, L. Ma, G. Wang, L. Chen, W. Wang, Calcium carbonate microspheres as carriers for the anticancer drug camptothecin, Mater. Sci. Eng. C 32(8) (2012) 2634-2640.
[65] W. Habraken, P. Habibovic, M. Epple, M. Bohner, Calcium phosphates in biomedical applications: Materials for the future?, Mater. Today 19(2) (2016) 69-87.
[66] M. Bohner, Design of ceramic-based cements and putties for bone graft substitution, Eur Cell Mater 20(1) (2010) 3-10.
[67] I.M. Mehdawi, A. Young, Antibacterial composite restorative materials for dental applications, Non-Metallic Biomaterials for Tooth Repair and Replacement, Elsevier2013, pp. 270-293.
[68] J. Li, Y.-C. Chen, Y.-C. Tseng, S. Mozumdar, L. Huang, Biodegradable calcium phosphate nanoparticle with lipid coating for systemic siRNA delivery, J. Controlled Release 142(3) (2010) 416-421.
[69] W.-X. Zong, C.B. Thompson, Necrotic death as a cell fate, Genes Dev. 20(1) (2006) 1-15.
[70] N. Vanlangenakker, T.V. Berghe, D.V. Krysko, N. Festjens, P. Vandenabeele, Molecular mechanisms and pathophysiology of necrotic cell death, Curr. Mol. Med. 8(3) (2008) 207-220.
[71] K. Wrogemann, S. Pena, Mitochondrial calcium overload: A general mechanism for cell-necrosis in muscle diseases, Lancet 307(7961) (1976) 672-674.
[72] E.J. Landon, R.J. Naukam, B.R. Sastry, Effects of calcium channel blocking agents on calcium and centrilobular necrosis in the liver of rats treated with hepatotoxic agents, Biochem. Pharmacol. 35(4) (1986) 697-705.

[73] Y.-C. Tseng, A. Yang, L. Huang, How does the cell overcome LCP nanoparticle-induced calcium toxicity?, Mol. Pharm. 10(11) (2013) 4391-4395.
[74] D. Olton, J. Li, M.E. Wilson, T. Rogers, J. Close, L. Huang, P.N. Kumta, C. Sfeir, Nanostructured calcium phosphates (NanoCaPs) for non-viral gene delivery: Influence of the synthesis parameters on transfection efficiency, Biomaterials 28(6) (2007) 1267-1279.
[75] V.V. Sokolova, I. Radtke, R. Heumann, M. Epple, Effective transfection of cells with multi-shell calcium phosphate-DNA nanoparticles, Biomaterials 27(16) (2006) 3147-3153.
[76] M. Kester, Y. Heakal, T. Fox, A. Sharma, G.P. Robertson, T.T. Morgan, E.I. Altinoglu, A. Tabakovic, M.R. Parette, S.M. Rouse, Calcium phosphate nanocomposite particles for in vitro imaging and encapsulated chemotherapeutic drug delivery to cancer cells, Nano Lett. 8(12) (2008) 4116-4121.
[77] B.M. Barth, R. Sharma, E.I. Altınogˇlu, T.T. Morgan, S.S. Shanmugavelandy, J.M. Kaiser, C. McGovern, G.L. Matters, J.P. Smith, M. Kester, Bioconjugation of calcium phosphosilicate composite nanoparticles for selective targeting of human breast and pancreatic cancers in vivo, ACS Nano 4(3) (2010) 1279-1287.
[78] Y. Cai, H. Pan, X. Xu, Q. Hu, L. Li, R. Tang, Ultrasonic controlled morphology transformation of hollow calcium phosphate nanospheres: a smart and biocompatible drug release system, Chem. Mater. 19(13) (2007) 3081-3083.
[79] Y.-C. Tseng, Z. Xu, K. Guley, H. Yuan, L. Huang, Lipid–calcium phosphate nanoparticles for delivery to the lymphatic system and SPECT/CT imaging of lymph node metastases, Biomaterials 35(16) (2014) 4688-4698.
[80] Y. Yang, J. Li, F. Liu, L. Huang, Systemic Delivery of siRNA via LCP Nanoparticle Efficiently Inhibits Lung Metastasis, Mol. Ther. 20(3) (2012) 609-615.
[81] A. Trofimov, A. Ivanova, M. Zyuzin, A. Timin, Porous inorganic carriers based on silica, calcium carbonate and calcium phosphate for controlled/modulated drug delivery: Fresh outlook and future perspectives, Pharmaceutics 10(4) (2018) 167.
[82] S. Singh, P. Bhardwaj, V. Singh, S. Aggarwal, U.K. Mandal, Synthesis of nanocrystalline calcium phosphate in microemulsion—effect of nature of surfactants, J. Colloid Interface Sci. 319(1) (2008) 322-329.
[83] Y. Wu, W. Gu, J. Li, C. Chen, Z.P. Xu, Silencing PD-1 and PD-L1 with nanoparticle-delivered small interfering RNA increases cytotoxicity of tumor-infiltrating lymphocytes, Nanomedicine 14(8) (2019).
[84] Y. Wu, W. Gu, L. Li, C. Chen, Z.P. Xu, Enhancing PD-1 gene silence in T lymphocytes by comparing the delivery performance of two inorganic nanoparticle platforms, Nanomaterials 9(2) (2019) 159.
[85] J.-Y. Wu, Z.-X. Wang, G. Zhang, X. Lu, G.-H. Qiang, W. Hu, A.-L. Ji, J.-H. Wu, C.-P. Jiang, Targeted co-delivery of Beclin 1 siRNA and FTY720 to hepatocellular carcinoma by calcium phosphate nanoparticles for enhanced anticancer efficacy, Int. J. Nanomed. 13 (2018) 1265.
[86] Y. Xiong, Y. Zhao, L. Miao, C.M. Lin, L. Huang, Co-delivery of polymeric metformin and cisplatin by self-assembled core-membrane nanoparticles to treat non-small cell lung cancer, J. Controlled Release 244 (2016) 63-73.
[87] Q. Liu, H. Zhu, Y. Liu, S. Musetti, L. Huang, BRAF peptide vaccine facilitates therapy of murine BRAF-mutant melanoma, Cancer Immunol. Immunother. 67(2) (2018) 299-310.
[88] D.E. Owens III, N.A. Peppas, Opsonization, biodistribution, and pharmacokinetics of polymeric nanoparticles, Int. J. Pharm. 307(1) (2006) 93-102.

[89] A.S. Karakoti, S. Das, S. Thevuthasan, S. Seal, PEGylated inorganic nanoparticles, Angew. Chem. Int. Ed. 50(9) (2011) 1980-1994.
[90] S.W. Jones, R.A. Roberts, G.R. Robbins, J.L. Perry, M.P. Kai, K. Chen, T. Bo, M.E. Napier, J.P. Ting, J.M. DeSimone, Nanoparticle clearance is governed by Th1/Th2 immunity and strain background, J. Clin. Investig. 123(7) (2013) 3061-3073.
[91] L. Huang, Y. Liu, In vivo delivery of RNAi with lipid-based nanoparticles, Annu. Rev. Biomed. Eng. 13 (2011) 507-530.
[92] P.S. Uster, T.M. Allen, B.E. Daniel, C.J. Mendez, M.S. Newman, G.Z. Zhu, Insertion of poly (ethylene glycol) derivatized phospholipid into pre-formed liposomes results in prolonged in vivo circulation time, FEBS letters 386(2-3) (1996) 243-246.
[93] J. Tang, C.B. Howard, S.M. Mahler, K.J. Thurecht, L. Huang, Z.P. Xu, Enhanced delivery of siRNA to triple negative breast cancer cells in vitro and in vivo through functionalizing lipid-coated calcium phosphate nanoparticles with dual target ligands, Nanoscale 10(9) (2018) 4258-4266.
[94] M. Silvander, M. Johnsson, K. Edwards, Effects of PEG-lipids on permeability of phosphatidylcholine/cholesterol liposomes in buffer and in human serum, Chemistry and physics of lipids 97(1) (1998) 15-26.
[95] Y. Wu, W. Gu, Z.P. Xu, Enhanced combination cancer therapy using lipid-calcium carbonate/phosphate nanoparticles as a targeted delivery platform, Nanomedicine 14(1) (2018) 77-92.
[96] C. Qiu, W. Wei, J. Sun, H.-T. Zhang, J.-S. Ding, J.-C. Wang, Q. Zhang, Systemic delivery of siRNA by hyaluronan-functionalized calcium phosphate nanoparticles for tumor-targeted therapy, Nanoscale 8(26) (2016).
[97] Z. Xu, Y. Wang, L. Zhang, L. Huang, Nanoparticle-delivered transforming growth factor-beta siRNA enhances vaccination against advanced melanoma by modifying tumor microenvironment, ACS Nano 8(4) (2014) 3636-3645.
[98] Y. Zhang, N.M.J. Schwerbrock, A.B. Rogers, W.Y. Kim, L. Huang, Codelivery of VEGF siRNA and gemcitabine monophosphate in a single nanoparticle rormulation for effective treatment of NSCLC, Mol. Ther. 21(8) (2013) 1559-1569.
[99] Y. Zhang, W.Y. Kim, L. Huang, Systemic delivery of gemcitabine triphosphate via LCP nanoparticles for NSCLC and pancreatic cancer therapy, Biomaterials 34(13) (2013) 3447-3458.
[100] K. Hu, L. Miao, T.J. Goodwin, J. Li, Q. Liu, L. Huang, Quercetin remodels the tumor microenvironment to improve the permeation, retention, and antitumor effects of nanoparticles, ACS Nano 11(5) (2017) 4916-4925.
[101] J. Yao, Y. Zhang, S. Ramishetti, Y. Wang, L. Huang, Turning an antiviral into an anticancer drug: nanoparticle delivery of acyclovir monophosphate, J. Controlled Release 170(3) (2013) 414-420.
[102] K.M. Au, A. Satterlee, Y. Min, X. Tian, Y.S. Kim, J.M. Caster, L. Zhang, T. Zhang, L. Huang, A.Z. Wang, Folate-targeted pH-responsive calcium zoledronate nanoscale metal-organic frameworks: Turning a bone antiresorptive agent into an anticancer therapeutic, Biomaterials 82 (2016) 178-193.
[103] T.J. Goodwin, L. Huang, Investigation of phosphorylated adjuvants co-encapsulated with a model cancer peptide antigen for the treatment of colorectal cancer and liver metastasis, Vaccine 35(19) (2017) 2550-2557.
[104] L. Chen, Y. Ding, Y. Wang, X. Liu, R. Babu, W. Ravis, W. Yan, Codelivery of zoledronic acid and doublestranded RNA from core-shell nanoparticles, Int. J. Nanomed. 8 (2013) 137.
[105] D.E. Dolmans, D. Fukumura, R.K. Jain, Photodynamic therapy for cancer, Nat. Rev. Cancer 3(5) (2003) 380.

[106] A. Ferrario, K.F. von Tiehl, N. Rucker, M.A. Schwarz, P.S. Gill, C.J. Gomer, Antiangiogenic treatment enhances photodynamic therapy responsiveness in a mouse mammary carcinoma, Cancer Res. 60(15) (2000) 4066-4069.
[107] W.-H. Chen, R.L.G. Lecaros, Y.-C. Tseng, L. Huang, Y.-C. Hsu, Nanoparticle delivery of HIF1α siRNA combined with photodynamic therapy as a potential treatment strategy for head-and-neck cancer, Cancer Lett. 359(1) (2015) 65-74.
[108] J. Tang, B. Li, C.B. Howard, S.M. Mahler, K.J. Thurecht, Y. Wu, L. Huang, Z.P. Xu, Multifunctional lipid-coated calcium phosphate nanoplatforms for complete inhibition of large triple negative breast cancer via targeted combined therapy, Biomaterials (2019) 119232.
[109] Y. Zhao, Z. Luo, M. Li, Q. Qu, X. Ma, S.H. Yu, Y. Zhao, A preloaded amorphous calcium carbonate/doxorubicin@ silica nanoreactor for pH-responsive delivery of an anticancer drug, Angew. Chem. Int. Ed. 54(3) (2015) 919-922.
[110] Y. Liu, X. Zhi, M. Yang, J. Zhang, L. Lin, X. Zhao, W. Hou, C. Zhang, Q. Zhang, F. Pan, Tumor-triggered drug release from calcium carbonate-encapsulated gold nanostars for near-infrared photodynamic/photothermal combination antitumor therapy, Theranostics 7(6) (2017) 1650.
[111] S. Dunuweera, R. Rajapakse, Encapsulation of anticancer drug cisplatin in vaterite polymorph of calcium carbonate nanoparticles for targeted delivery and slow release, Biomed. Phys. Eng. Express 4(1) (2017) 015017.
[112] P. Srivastava, S.K. Hira, D.N. Srivastava, V.K. Singh, U. Gupta, R. Singh, R.A. Singh, P.P. Manna, ATP-decorated mesoporous silica for biomineralization of calcium carbonate and P2 purinergic receptor-mediated antitumor activity against aggressive lymphoma, ACS Appl. Mater. Interfaces 10(8) (2018) 6917-6929.
[113] Y. Zhang, L. Cai, D. Li, Y.-H. Lao, D. Liu, M. Li, J. Ding, X. Chen, Tumor microenvironment-responsive hyaluronate-calcium carbonate hybrid nanoparticle enables effective chemotherapy for primary and advanced osteosarcomas, Nano Res. 11 (2018) 4806-4822.
[114] K.H. Min, H.S. Min, H.J. Lee, D.J. Park, J.Y. Yhee, K. Kim, I.C. Kwon, S.Y. Jeong, O.F. Silvestre, X. Chen, pH-controlled gas-generating mineralized nanoparticles: a theranostic agent for ultrasound imaging and therapy of cancers, ACS Nano 9(1) (2015) 134-145.
[115] G. Li, Y. Chen, L. Zhang, M. Zhang, S. Li, L. Li, T. Wang, C. Wang, Facile approach to synthesize gold nanorod@polyacrylic acid/calcium phosphate yolk–shell nanoparticles for dual-mode imaging and pH/NIR-responsive drug delivery, Nano-Micro Lett. 10(1) (2017) 7.
[116] C. Qiu, W. Wei, J. Sun, H.-T. Zhang, J.-S. Ding, J.-C. Wang, Q. Zhang, Systemic delivery of siRNA by hyaluronan-functionalized calcium phosphate nanoparticles for tumor-targeted therapy, Nanoscale 8(26) (2016) 13033-13044.
[117] L. Li, L. Zhang, T. Wang, X. Wu, H. Ren, C. Wang, Z. Su, Facile and scalable synthesis of novel spherical Au nanocluster assemblies@polyacrylic acid/calcium phosphate nanoparticles for dual-modal imaging-guided cancer chemotherapy, Small 11(26) (2015) 3162-3173.
[118] Z.-F. Zhou, T.-W. Sun, F. Chen, D.-Q. Zuo, H.-S. Wang, Y.-Q. Hua, Z.-D. Cai, J. Tan, Calcium phosphate-phosphorylated adenosine hybrid microspheres for anti-osteosarcoma drug delivery and osteogenic differentiation, Biomaterials 121 (2017) 1-14.
[119] A.I. Petrov, D.V. Volodkin, G.B. Sukhorukov, Protein—calcium carbonate coprecipitation: a tool for protein encapsulation, Biotechnol. Progress 21(3) (2005) 918-925.

[120] J.-L. Wu, C.-Q. Wang, R.-X. Zhuo, S.-X. Cheng, Multi-drug delivery system based on alginate/calcium carbonate hybrid nanoparticles for combination chemotherapy, Colloids Surf. B 123 (2014) 498-505.
[121] X. He, T. Liu, Y. Chen, D. Cheng, X. Li, Y. Xiao, Y. Feng, Calcium carbonate nanoparticle delivering vascular endothelial growth factor-C siRNA effectively inhibits lymphangiogenesis and growth of gastric cancer in vivo, Cancer Gene Ther. 15(3) (2008) 193.
[122] X. Wang, C. Wu, K. Tao, K. Zhao, J. Wang, H. Xu, D. Xia, H. Shan, J.R. Lu, Influence of ovalbumin on CaCO3 precipitation during in vitro biomineralization, J. Phys. Chem. B 114(16) (2010) 5301-5308.
[123] W. Wang, Y. Zhao, B.-B. Yan, L. Dong, Y. Lu, S.-H. Yu, Calcium carbonate-doxorubicin@silica-indocyanine green nanospheres with photo-triggered drug delivery enhance cell killing in drug-resistant breast cancer cells, Nano Res. 11(6) (2018) 3385-3395.
[124] Z. Dong, L. Feng, W. Zhu, X. Sun, M. Gao, H. Zhao, Y. Chao, Z. Liu, CaCO3 nanoparticles as an ultra-sensitive tumor-pH-responsive nanoplatform enabling real-time drug release monitoring and cancer combination therapy, Biomaterials 110 (2016) 60-70.
[125] S. Chen, D. Zhao, F. Li, R.-X. Zhuo, S.-X. Cheng, Co-delivery of genes and drugs with nanostructured calcium carbonate for cancer therapy, RSC Adv. 2(5) (2012) 1820-1826.
[126] D. Zhao, C.-Q. Wang, R.-X. Zhuo, S.-X. Cheng, Modification of nanostructured calcium carbonate for efficient gene delivery, Colloids Surf., B 118 (2014) 111-116.
[127] M. Jordan, A. Schallhorn, F.M. Wurm, Transfecting mammalian cells: optimization of critical parameters affecting calcium-phosphate precipitate formation, Nucleic Acids Res. 24(4) (1996) 596-601.
[128] S. Chen, F. Li, R.-X. Zhuo, S.-X. Cheng, Efficient non-viral gene delivery mediated by nanostructured calcium carbonate in solution-based transfection and solid-phase transfection, Mol. BioSyst. 7(10) (2011) 2841-2847.
[129] C. Wu, M.-Q. Gong, B.-Y. Liu, R.-X. Zhuo, S.-X. Cheng, Co-delivery of multiple drug resistance inhibitors by polymer/inorganic hybrid nanoparticles to effectively reverse cancer drug resistance, Colloids Surf. B 149 (2017) 250-259.
[130] P. Sharma, K. Wagner, J.D. Wolchok, J.P. Allison, Novel cancer immunotherapy agents with survival benefit: recent successes and next steps, Nat. Rev. Cancer 11(11) (2011) 805.
[131] K.M. Mahoney, P.D. Rennert, G.J. Freeman, Combination cancer immunotherapy and new immunomodulatory targets, Nat. Rev. Drug Discov. 14(8) (2015) 561.
[132] X. Cao, Immunology in China: The past, present and future, Nat. Immunol. 9(4) (2008) 339.
[133] D.R. Leach, M.F. Krummel, J.P. Allison, Enhancement of antitumor immunity by CTLA-4 blockade, Science 271(5256) (1996) 1734-1736.
[134] G.J. Freeman, A.J. Long, Y. Iwai, K. Bourque, T. Chernova, H. Nishimura, L.J. Fitz, N. Malenkovich, T. Okazaki, M.C. Byrne, Engagement of the PD-1 immunoinhibitory receptor by a novel B7 family member leads to negative regulation of lymphocyte activation, J. Exp. Med. 192(7) (2000) 1027-1034.
[135] C. Massard, M.S. Gordon, S. Sharma, S. Rafii, Z.A. Wainberg, J. Luke, T.J. Curiel, G. Colon-Otero, O. Hamid, R.E. Sanborn, Safety and efficacy of durvalumab (MEDI4736), an anti–programmed cell death ligand-1 immune checkpoint inhibitor, in patients with advanced urothelial bladder cancer, J Clin Oncol 34(26) (2016) 3119.

[136] A.B. Apolo, J.R. Infante, A. Balmanoukian, M.R. Patel, D. Wang, K. Kelly, A.E. Mega, C.D. Britten, A. Ravaud, A.C. Mita, Avelumab, an anti–programmed death-ligand 1 antibody, in patients with refractory metastatic urothelial carcinoma: results from a multicenter, phase ib study, J Clin Oncol 35(19) (2017) 2117.
[137] D.F. McDermott, J.A. Sosman, M. Sznol, C. Massard, M.S. Gordon, O. Hamid, J.D. Powderly, J.R. Infante, M. Fassò, Y.V. Wang, Atezolizumab, an anti–programmed death-ligand 1 antibody, in metastatic renal cell carcinoma: long-term safety, clinical activity, and immune correlates from a phase Ia study, J Clin Oncol 34(8) (2016) 833-842.
[138] Y.M. Ning, D. Suzman, V.E. Maher, L. Zhang, S. Tang, T. Ricks, T. Palmby, W. Fu, Q. Liu, K.B. Goldberg, FDA approval summary: Atezolizumab for the treatment of patients with progressive advanced urothelial carcinoma after platinum - containing chemotherapy, The Oncologist theoncologist 22(6) (2017) 743-749.
[139] H. Dong, S.E. Strome, D.R. Salomao, H. Tamura, F. Hirano, D.B. Flies, P.C. Roche, J. Lu, G. Zhu, K. Tamada, Tumor-associated B7-H1 promotes T-cell apoptosis: A potential mechanism of immune evasion, Nat. Med. 8(8) (2002) 793.
[140] D.S. Chen, I. Mellman, Oncology meets immunology: The cancer-immunity cycle, Immunity 39(1) (2013) 1-10.
[141] S.L. Topalian, M. Sznol, D.F. McDermott, H.M. Kluger, R.D. Carvajal, W.H. Sharfman, J.R. Brahmer, D.P. Lawrence, M.B. Atkins, J.D. Powderly, Survival, durable tumor remission, and long-term safety in patients with advanced melanoma receiving nivolumab, J Clin Oncol 32(10) (2014) 1020.
[142] O.C. Ukpo, W.L. Thorstad, J.S. Lewis, Jr., B7-H1 expression model for immune evasion in human papillomavirus-related oropharyngeal squamous cell carcinoma, Head and neck pathology 7(2) (2013) 113-121.
[143] D. Hua, J. Sun, Y. Mao, L.J. Chen, Y.Y. Wu, X.G. Zhang, B7-H1 expression is associated with expansion of regulatory T cells in colorectal carcinoma, World journal of gastroenterology 18(9) (2012) 971-978.
[144] S. Chowdhury, J. Veyhl, F. Jessa, O. Polyakova, A. Alenzi, C. MacMillan, R. Ralhan, P.G. Walfish, Programmed death-ligand 1 overexpression is a prognostic marker for aggressive papillary thyroid cancer and its variants, Oncotarget 7(22) (2016) 32318-32328.
[145] H. Ghebeh, C. Lehe, E. Barhoush, K. Al-Romaih, A. Tulbah, M. Al-Alwan, S.F. Hendrayani, P. Manogaran, A. Alaiya, T. Al-Tweigeri, A. Aboussekhra, S. Dermime, Doxorubicin downregulates cell surface B7-H1 expression and upregulates its nuclear expression in breast cancer cells: role of B7-H1 as an anti-apoptotic molecule, Breast cancer research : BCR 12(4) (2010) R48.
[146] X. Frigola, B.A. Inman, C.J. Krco, X. Liu, S.M. Harrington, P.A. Bulur, A.B. Dietz, H. Dong, E.D. Kwon, Soluble B7-H1: Differences in production between dendritic cells and T cells, Immunol. Lett. 142(1) (2012) 78-82.
[147] X. Zhu, J. Lang, Soluble PD-1 and PD-L1: predictive and prognostic significance in cancer, Oncotarget 8(57) (2017) 97671-97682.
[148] Y. Chen, P. Liu, F. Gao, H. Cheng, J. Qi, G.F. Gao, A dimeric structure of PD-L1: Functional units or evolutionary relics?, Protein Cell 1(2) (2010) 153-160.
[149] F. Ordikhani, M. Uehara, V. Kasinath, L. Dai, S.K. Eskandari, B. Bahmani, M. Yonar, J.R. Azzi, Y. Haik, P.T. Sage, Targeting antigen-presenting cells by anti–PD-1 nanoparticles augments antitumor immunity, JCI Insight 3(20) (2018).
[150] P.Y. Teo, C. Yang, L.M. Whilding, A.C. Parente - Pereira, J. Maher, A.J. George, J.L. Hedrick, Y.Y. Yang, S. Ghaem - Maghami, Ovarian cancer immunotherapy using

PD - L1 siRNA targeted delivery from folic acid - functionalized polyethylenimine: strategies to enhance T cell killing, Adv. Healthc. Mater. 4(8) (2015) 1180-1189.
[151] X. Jiang, J. Zhou, A. Giobbie-Hurder, J. Wargo, F.S. Hodi, The activation of MAPK in melanoma cells resistant to BRAF inhibition promotes PD-L1 expression that is reversible by MEK and PI3K inhibition, Clin. Cancer Res. 19(3) (2013) 598-609.
[152] S. Xu, F. Cui, D. Huang, D. Zhang, A. Zhu, X. Sun, Y. Cao, S. Ding, Y. Wang, E. Gao, PD-l1 monoclonal antibody-conjugated nanoparticles enhance drug delivery level and chemotherapy efficacy in gastric cancer cells, Int. J. Nanomed. 14 (2019) 17.
[153] F. Emami, A. Banstola, A. Vatanara, S. Lee, J.O. Kim, J.-H. Jeong, S. Yook, Doxorubicin and anti-PD-L1 antibody conjugated gold nanoparticles for colorectal cancer photo-chemotherapy, Mol. Pharm. (2019).
[154] Q. Chen, L. Xu, C. Liang, C. Wang, R. Peng, Z. Liu, Photothermal therapy with immune-adjuvant nanoparticles together with checkpoint blockade for effective cancer immunotherapy, Nat. Comm. 7 (2016) 13193.
[155] W. Song, L. Shen, Y. Wang, Q. Liu, T.J. Goodwin, J. Li, O. Dorosheva, T. Liu, R. Liu, L. Huang, Synergistic and low adverse effect cancer immunotherapy by immunogenic chemotherapy and locally expressed PD-L1 trap, Nat. Comm. 9(1) (2018) 2237.
[156] G. Dranoff, Cytokines in cancer pathogenesis and cancer therapy, Nat. Rev. Cancer 4(1) (2004) 11.
[157] B.N. Ames, L.S. Gold, W.C. Willett, The causes and prevention of cancer, Proc. Natl. Acad. Sci. U.S.A. 92(12) (1995) 5258-5265.
[158] D.M. Pardoll, The blockade of immune checkpoints in cancer immunotherapy, Nat. Rev. Cancer 12(4) (2012) 252.
[159] J.F. Bromberg, C.M. Horvath, Z. Wen, R.D. Schreiber, J.E. Darnell, Transcriptionally active Stat1 is required for the antiproliferative effects of both interferon alpha and interferon gamma, Proc. Natl. Acad. Sci. U.S.A. 93(15) (1996) 7673-7678.
[160] Y.E. Chin, M. Kitagawa, W.-C.S. Su, Z.-H. You, Y. Iwamoto, X.-Y. Fu, Cell growth arrest and induction of cyclin-dependent kinase inhibitor p21WAF1/CIP1 mediated by STAT1, Science 272(5262) (1996) 719-722.
[161] Y. Shirayoshi, P.A. Burke, E. Appella, K. Ozato, Interferon-induced transcription of a major histocompatibility class I gene accompanies binding of inducible nuclear factors to the interferon consensus sequence, Proc. Natl. Acad. Sci. U.S.A. 85(16) (1988) 5884-5888.
[162] J.M. Curtsinger, P. Agarwal, D.C. Lins, M.F. Mescher, Autocrine IFN-γ promotes naive CD8 T cell differentiation and synergizes with IFN-α to stimulate strong function, J. Immunol. 189(2) (2012) 659-668.
[163] X. Hu, L.B. Ivashkiv, Cross-regulation of signaling pathways by interferon-γ: Implications for immune responses and autoimmune diseases, Immunity 31(4) (2009) 539-550.
[164] R.A. Maldonado, D.J. Irvine, R. Schreiber, L.H. Glimcher, A role for the immunological synapse in lineage commitment of CD4 lymphocytes, Nature 431(7008) (2004) 527.
[165] Y. Zhang, R. Apilado, J. Coleman, S. Ben-Sasson, S. Tsang, J. Hu-Li, W.E. Paul, H. Huang, Interferon γ stabilizes the T helper cell type 1 phenotype, J. Exp. Med. 194(2) (2001) 165-172.
[166] F. Castro, A.P. Cardoso, R.M. Gonçalves, K. Serre, M.J. Oliveira, Interferon-gamma at the crossroads of tumor immune surveillance or evasion, Front. Immunol. 9 (2018) 847.

[167] M.E. Gleave, M. Elhilali, Y. Fradet, I. Davis, P. Venner, F. Saad, L.H. Klotz, M.J. Moore, V. Paton, A. Bajamonde, Interferon gamma-1b compared with placebo in metastatic renal-cell carcinoma, N. Engl. J. Med. 338(18) (1998) 1265-1271.
[168] M. Wiesenfeld, M.J. O'Connell, H.S. Wieand, N.J. Gonchoroff, J.H. Donohue, R.J. Fitzgibbons Jr, J.E. Krook, J.A. Mailliard, J.B. Gerstner, R. Pazdur, Controlled clinical trial of interferon-gamma as postoperative surgical adjuvant therapy for colon cancer, J. Clin. Oncol. 13(9) (1995) 2324-2329.
[169] K. Gowrishankar, D. Gunatilake, S.J. Gallagher, J. Tiffen, H. Rizos, P. Hersey, Inducible but not constitutive expression of PD-L1 in human melanoma cells is dependent on activation of NF-κB, PloS One 10(4) (2015) e0123410.
[170] A. Giannopoulos, C. Constantinides, E. Fokaeas, C. Stravodimos, M. Giannopoulou, A. Kyroudi, A. Gounaris, The immunomodulating effect of interferon-γ intravesical instillations in preventing bladder cancer recurrence, Clin. Cancer Res. 9(15) (2003) 5550-5558.
[171] K. Matsushita, T. Takenouchi, H. Shimada, T. Tomonaga, H. Hayashi, A. Shioya, A. Komatsu, H. Matsubara, T. Ochiai, Strong HLA-DR antigen expression on cancer cells relates to better prognosis of colorectal cancer patients: Possible involvement of c-myc suppression by interferon-γin situ, Cancer Sci. 97(1) (2006) 57-63.
[172] C.H. Miller, S.G. Maher, H.A. Young, Clinical use of interferon-γ, Ann. N. Y. Acad. Sci. 1182(1) (2009) 69-79.
[173] E. Pujade-Lauraine, J.-P. Guastalla, N. Colombo, E. Francois, P. Fumoleau, A. Monnier, M. Nooy, L. Mignot, R. Bugat, C. Oliveira, Intraperitoneal recombinant interferon gamma in ovarian cancer patients with residual disease at second look laparotomy, Ovarian Cancer 3, Springer1995, pp. 231-241.
[174] G. Windbichler, H. Hausmaninger, W. Stummvoll, A. Graf, C. Kainz, J. Lahodny, U. Denison, E. Müller-Holzner, C. Marth, Interferon-gamma in the first-line therapy of ovarian cancer: A randomized phase III trial, Br. J. Cancer 82(6) (2000) 1138.
[175] H. Gao, Y. Xiong, S. Zhang, Z. Yang, S. Cao, X. Jiang, RGD and interleukin-13 peptide functionalized nanoparticles for enhanced glioblastoma cells and neovasculature dual targeting delivery and elevated tumor penetration, Mol. Pharm. 11(3) (2014) 1042-1052.
[176] M.-Y. Lee, J.-A. Yang, H.S. Jung, S. Beack, J.E. Choi, W. Hur, H. Koo, K. Kim, S.K. Yoon, S.K. Hahn, Hyaluronic acid–gold nanoparticle/interferon α complex for targeted treatment of hepatitis C virus infection, ACS Nano 6(11) (2012) 9522-9531.
[177] M.W. Jøraholmen, P. Basnet, G. Acharya, N. Škalko-Basnet, PEGylated liposomes for topical vaginal therapy improve delivery of interferon alpha, Eur. J. Pharm. Biopharm. 113 (2017) 132-139.
[178] R. Mejías, S. Pérez-Yagüe, L. Gutiérrez, L.I. Cabrera, R. Spada, P. Acedo, C.J. Serna, F.J. Lázaro, Á. Villanueva, M. del Puerto Morales, Dimercaptosuccinic acid-coated magnetite nanoparticles for magnetically guided in vivo delivery of interferon gamma for cancer immunotherapy, Biomaterials 32(11) (2011) 2938-2952.
[179] Y. Yin, Q. Hu, C. Xu, Q. Qiao, X. Qin, Q. Song, Y. Peng, Y. Zhao, Z. Zhang, Co-delivery of doxorubicin and interferon-γ by thermosensitive nanoparticles for cancer immunochemotherapy, Mol. Pharm. 15(9) (2018) 4161-4172.
[180] J. Wu, C. Tang, C. Yin, Co-delivery of doxorubicin and interleukin-2 via chitosan based nanoparticles for enhanced antitumor efficacy, Acta Biomater. 47 (2017) 81-90.
[181] P.J. Quinn, Localization of vitamin E in membranes, Fat-Soluble Vitamins, Springer, Boston, MA1998, pp. 319-343.

[182] J.C. Gómez-Fernández, J. Villalaín, F.J. Aranda, Phase behavior of membranes containing bioactive lipids, Current topics in membranes, Academic Press1997, pp. 193-235.

Chapter 3

Strategical Methodology

This chapter mainly summarises the methodology applied in the whole PhD project, including synthetic methods and modifications, characterisation techniques, in vitro and in vivo tests, and finally biological techniques. A brief illustration of the methodology outline is shown in Figure 3.1.

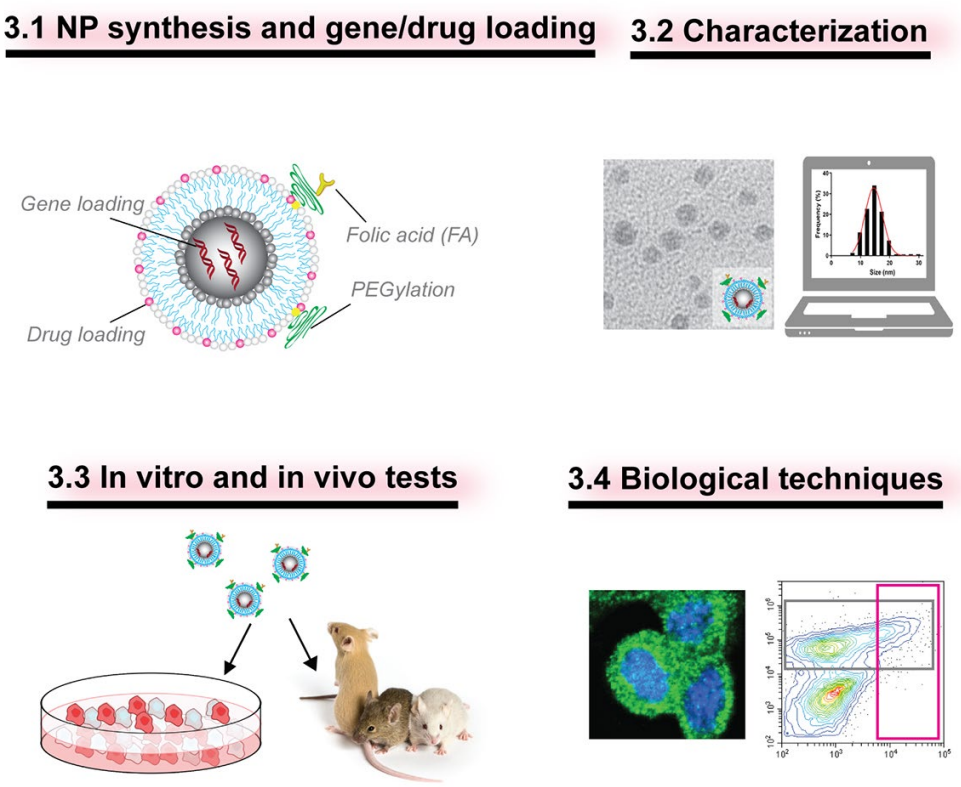

Figure 3.1 Outline of strategical methodology in this thesis.

3.1 Synthetic methodology of LCCP NPs with gene/drug loading

3.1.1 Synthesis of LCCP NPs

The synthetic method of LCCP hybrid NPs is based on the reported method for preparation of LCP NPs [1], with a modification to incorporate calcium carbonate (CaC) in the cores. Initially, the cores of NPs are prepared using a water in oil micro-emulsion for size control. The emulsion containing $NaHCO_3/Na_2HPO_4$ in a variable ratio is added in the second emulsion containing $CaCl_2$ to form the precipitate, i.e. calcium carbonate/phosphate core in the merged emulsion, with the first layer phospholipids surrounding the core. Sequentially, the collected lipid-cores are washed with ethanol and dispersed in chloroform. The outer layer lipids in chloroform are added to the lipid-core suspension and a thin film of NPs is obtained by solvent evaporation. The final nanoparticles, i.e. lipid-coated calcium carbonate/phosphates (LCCP), are obtained by thin-film hydration method. The synthesis routine is illustrated in Figure 3.2. Some treatments are conducted to maintain the LCCP NPs with a uniform size (~40 nm) and good dispersion, including ultrasonic probe, rotovap, and vortex. In particular, carbonate/phosphate ratio is carefully examined as this ratio strongly affects the gene loading and release profile.

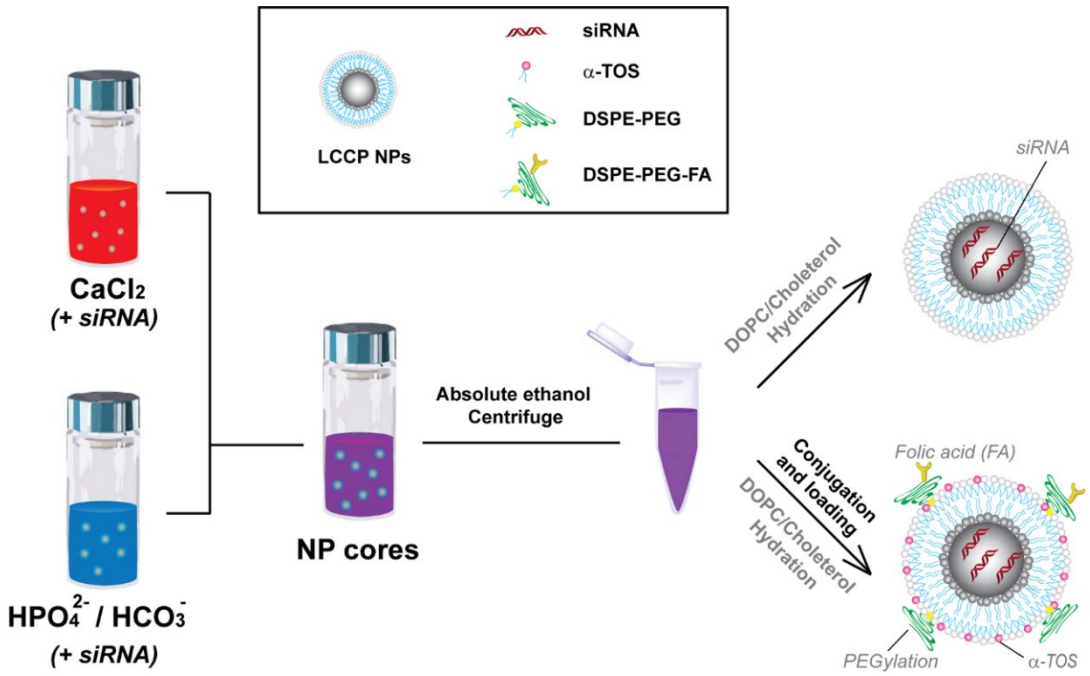

Figure 3.2 Schematic routine for LCCP NP synthesis, gene/drug loading, and modification.

3.1.2 Gene/drug loading strategy

The loading of gene/drug is schematically shown in Figure 3.2. The loading of genes is achieved by incorporating genes into the micro-emulsion containing $CaCl_2$ and/or $NaHCO_3$/ Na_2HPO_4 before mixing the two emulsions. In a typical synthesis, the aqueous solution containing $CaCl_2$ and/or $NaHCO_3$/Na_2HPO_4 are prepared and added dropwise into the organic solvent to make the water in oil micro-emulsions. The genes are loaded by co-precipitating within the core of NPs. In particular, the input amount and method are crucial to the loading efficiency of genes.

The loading of a hydrophobic anti-cancer drug, α-tocopheryl succinate (α-TOS), is achieved by replacing part of the outer layer lipids. During the synthesis, the core-lipids are dispersed in chloroform, and mixed with another chloroform solution containing the outer layer lipid, such as 1,2-dioleoyl-sn-glycero-3-phosphocholine (DOPC) and cholesterol. To load α-TOS, DOPC and/or cholesterol are replaced by the equal mole of α-TOS in chloroform before mixing. Of note, the total input mole and replaced lipids/cholesterol are crucial to loading efficiency, NP size distribution, and colloidal stability.

3.1.3 Modification of LCCP NPs

The surface modification to LCCP NPs is also demonstrated in Figure 3.2. In this study, LCCP surface modification was achieved in a method similar to α-TOS loading. The PEGylation and folic acid (FA) loading are achieved by using 1,2-distearoyl-sn-glycero-3-phosphoethanolamine-N-(polyethylene glycol)-2000 (DSPE-PEG_{2000}) and/or 1,2-distearoyl-sn-glycero-3-phosphoethanolamine-N-[folate(polyethylene glycol)-2000] (DSPE-PEG_{2000}-FA) to replace the equal mole of DOPC in the outer layer. Specifically, the molar ratio of DSPE-PEG_{2000} and DSPE-PEG_{2000}-FA is crucial to the targeting ability of LCCP NPs to cancer cell overexpressing the FA receptor.

3.2 Characterization

3.2.1 Dynamic light scattering (DLS)

The dynamic light scattering (DLS) is a convenient method that is used to measure the NP size and distribution in solution. The NP size affects the Brownian motion speed, leading to the different scattered light intensity, which can be converted to a hydrodynamic size distribution [2]. The particles can be dispersed in deionized water, PBS, or medium with serum for DLS analysis. The general conducted concentration is approximately 40-4000 μg/mL. Ultrasonication with a probe or in a water bath can be also applied if necessary before DLS analysis. The characterisation is generally performed at 25 °C with 0-120 s equivalent time on a Malvern Zetasizer Nano-ZS with triplicate measures. Meanwhile, the polydispersity index (PDI) is read at the same time to represent the variance of the NP size distribution.

3.2.2 Zeta potential

Zeta potential is the general parameter that represents the charge of NPs. Theoretically, the zeta potential refers to the potential difference between the medium and the stationary layer of NPs [3]. The zeta potential was quantified using a Malvern Zetasizer Nano-ZS in this thesis. In general, a solution of 40-4000 μg/mL NPs is infused into a folded capillary cuvette and the potential difference (i.e. zeta potential) is measured in triplicate.

3.2.3 Transmission electron microscopy (TEM)

The transmission electron microscopy (TEM) is often used to visualize the NPs for morphology and size, as well as the microstructure. The image of a specimen is formed by interacting sample electrons and the electron beam transmitted through. To make the specimen, a drop of NP suspension is dropped onto a copper grid coated with 300 mesh carbon, and dried with a filter paper under ambient condition, followed by images taken on a JEM-3010 or HT7700 operating under 100 kV. The grid can be negatively stained with 1% uranyl acetate for 1 min if necessary. The size of the LCCP NPs or the cores was estimated using Nanomeasure 1.2 software by measuring randomly selected 100-200 particles in this thesis.

3.2.4 X-ray diffraction (XRD)

The XRD is a useful method that is used to determine the crystal structure and regularity. According to the elastic scattering phenomenon, the X-ray is scattered by the electrons of specimen when passing through, and the formed scattering waves obey Bragg's law ($2d\sin\theta = n\lambda$, where d is the distance between two Miller planes in the crystal, θ is the scattering angle, n is a positive integer, and λ is the wavelength of the incident wave). In this project, wide-angel XRD patterns were obtained to determine the crystal structure of NPs using a Cu Kα radiation on a Philips PW 3040/60 X'Pert PRO diffractometer. In this thesis, the scanning was conducted from 10° to 70° at a rate of 2°/min and the pattern obtained compared to the standard XRD cards to judge the crystal form and estimate the NP size.

3.2.5 Ultraviolet–visible spectroscopy (UV-vis)

Molecules can absorb energy from ultraviolet to visible light in a characteristic wavelength range to excite its electrons to higher anti-bonding molecular orbitals, and the absorbance (A) obeys Lambert-Beer Law ($A = \varepsilon cL$, where ε is the molar attenuation coefficient, c is the concentration of sample, and L is the path length through the sample). Therefore, this technique can be used for quantification and qualification. In this thesis, UV-vis spectroscopy (UV-2450) was used to determine the absorbance from Arsenazo III-Ca at 655 nm, α-TOS at 285 nm, and some other molecules. A standard absorbance curve calculated from solutions with known concentration was first profiled, and the concentration from unknown samples was estimated by its absorbance using the fitting curve equation based on the standard curve.

3.2.6 Nanodrop

The Nanodrop (Thermo Scientific 1000) was used to quantify the concentration of biomolecules (such as nuclear acid and protein) via the UV-vis absorbance in a tiny volume (1-5 μL). For western blotting and RT PCR, the concentration of extracted protein/nuclear acid was determined by measuring the A260/A280 value to check the purification before subsequent experiments.

3.2.7 Agarose gel electrophoresis

The agarose gel electrophoresis is often used to separate and semi-quantify nuclear acids with different sizes. Under a constant electric field, the nuclear acid migrates in the agarose matrix.

The migration rate is determined by the molecular weight, charge, and shape. A biosafety GelRed dye is normally used to visualize the nuclear acid band and semi-quantification. In a typical test in the thesis, the specimen was loaded into the well of a 2% agarose gel and ran in TAE buffer at 100 V for 20 min. The NPs with dsDNA or siRNA were lysed in a lysis buffer or acidic condition to release the genes for measurement in this research.

3.2.8 Attenuated total reflectance-Fourier transform infrared spectroscopy (ATR-FTIR)

Attenuated total reflectance (ATR)-Fourier transform infrared (FTIR) spectroscopy can be used to analyse the composition of NPs through the specific infrared absorbance. The absorbance of infrared light when it passes through a certain specimen reflects the specimen characteristic chemical bonds. In this thesis, a powder sample was loaded onto the measurement crystal and the spectrum recorded using a NEXUS 670 FT-IR spectrometer (Thermo Nicolet) at a resolution of 2-4 cm^{-1} from 4000-400 cm^{-1} for 32 or 64 scans. A background of ATR is generally scanned for normalization and baseline correction before the sample measurement.

3.2.9 Element analysis (EA)

The element analysis (EA) was conducted in this research using a CHNS analyser (Thermo Scientific FLASH 2000 Organic EA) to determine the carbon content in samples. Cystine and pure sodium carbonate powders are used as the standards. All samples were carefully embedded into tin capsules and weighted. The carbon weight percentage was determined as the average of three individual repeats.

3.2.10 Inductively coupled plasma atomic emission spectroscopy (ICP-AES)

Inductively coupled plasma atomic emission spectroscopy (ICP-AES, Varian Vista) was used to quantify the chemical elements in NPs in this research. All samples were fully digested in 70% nitric acid, followed by dilution to a defined volume with a 50/50 (v/v) mixture of nitric acid (0.4% m/V) and H_2O_2 (30%) solution. The measurement of calcium concentration and phosphate was conducted in triplicate and the result was represented as the average.

3.2.11 X-ray photoelectron spectroscopy (XPS)

X-ray photoelectron spectroscopy (XPS) can quantitatively analyse elemental composition and the element valence states of a specimen. In this research, the carbon analysis of LCCP NP

cores coated with DOPA was carried out using XPS equipped with a state of the art Kratos Axis Ultra photoelectron spectrometer using mono Al Kα (1486.6 eV) X-rays. The energy for survey scan and high resolution scan was 200 and 20 eV, respectively. The XPS spectra were processed and analysed using CasaXPS software. The binding energy of C peak at 284.6 eV after fitting the curve of C 1s spectrum was used as the reference [4].

3.3 In vitro and in vivo tests

3.3.1 Cancer cell line culture

All cancer cells were handled in accordance with the PC2 laboratory guidelines in this research. B16F10, B16F0, and 4T1 cells were obtained from the American Type Culture Collection (ATCC, Manassas, VA), and routinely cultured under the guidance listed on the ATCC website. The B16F10 and B16F0 melanoma cells were cultured in Dulbecco's Modified Eagle Medium (DMEM) supplemented with 10% fetal bovine serum (FBS) and 1% penicillin/ streptomycin (P/S). The 4T1 breast cancer cells were grown in RPMI-1640 medium supplemented with 10% FBS and 1% P/S. All cells were cultured in an incubator at 37 °C and 5% CO_2 with 95% humidity. Cells were subcultured at 80% of confluence using a 0.25% trypsin-EDTA solution.

3.3.2 Cellular uptake

The cellular uptake of NPs is normally quantified by trancing the NP-related fluorescence signals using either flow cytometry analysis (FACS) or confocal laser scanning microscopy (CLSM). The continuously cultured cells are seeded in 12 well plates, and allowed one night to bring the cells to confluence. Then fresh medium containing 10 vol% of NPs' suspension (the concentration of LCCP was normally less than 200 μg/mL) is supplemented to the attached cells for a predetermined time period. All cell samples are collected using trypsin, and washed with PBS, followed by FACS analysis.

To visualize the intracellular fluorescence, the cells are seeded on a 14 mm coverslip (pre-treated with acid for polishing and 70% ethanol for sterile) in 24 well plates overnight to allow cell attachment. The next day, the cells are fed with medium containing 10 vol% of NPs' suspension and cultured for a certain period of time. Then the coverslips are rinsed with PBS and fixed in 4% PFA, and mounted on a slice with a drop of DAPI-fluoshield. A Zeiss 710 CLSM is generally used for observation.

3.3.3 Cell viability

Briefly, cells are seeded in 96 well plates with a density of 4,000 per well. Different treatment is conducted in the next day under various conditions, including the NP concentration, drug/gene concentration in the NP form, and incubation time. After culture, the viability of cells is quantified using the 3-[4,5-dimethylthiazol-2-yl]-2,5-diphenyl tetrazolium bromide (MTT) assay.

3.3.4 Apoptosis analysis

Apoptosis is a physiological process that can be induced by several stimuli, as schematically shown in Figure 3.3. During the process, the cell membrane structure changes, such as exposure of phosphatidylserine on the membrane surface at the early stage, and the loss of membrane integrity at the late stage [5]. Therefore, the apoptosis status can be detected using annexin V, a calcium dependent binding protein with high affinity for phosphatidylserine. The permeable membrane at the late apoptosis stage allows the propidium iodide (PI) to enter into the nuclear and stain the chromosome. Accordingly, this assay discriminates intact cells (FITC-/PI-), early apoptotic cells (FITC+/PI-) and late apoptosis cells (FITC+/PI+).

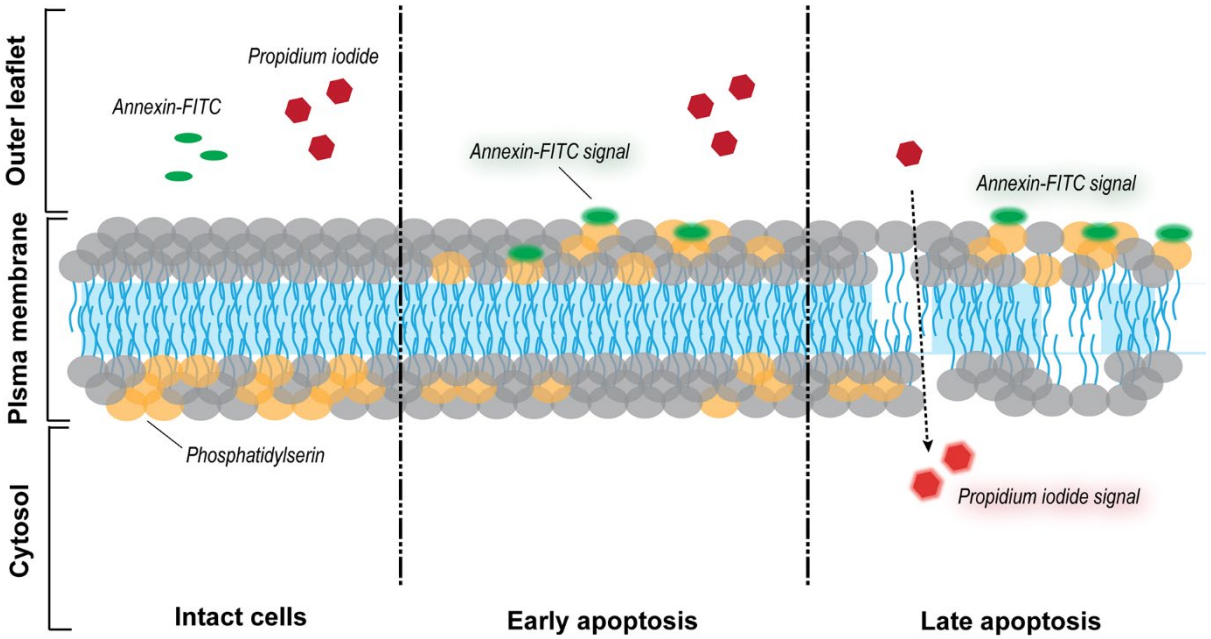

Figure 3.3 Scheme of the detection of apoptosis.

In this research, the apoptosis status was detected using the Annexin-FITC/PI kit. After cell treatment, the cells were collected and processed according to the manufactory's guide, and the annexin V-FITC and PI signals were collected and analysed using FACS.

3.3.5 Cell cycle assay

During the cells cycle, the chromatin quantity changes from G0/G1 (2N), S (2N~4N), to G2/M (4N). Accordingly, the cell cycle can be evaluated by the chromosome-dependent fluorescence intensity in singlet cells. In our experiments, the cells were treated and cultured in normoxia. After harvesting, all cells were fixed at 4 ℃ for 30 min using a pre-chilled 70% ethanol, followed by PI staining (50 μg/mL). The fluorescence intensity of each cell was recorded using FACS machine, and singlet cells were gated for analysing the PI intensity.

3.3.6 Reactive oxygen species (ROS) detection

ROS, including peroxide, superoxide, and singlet oxygen, are byproducts of cell metabolism, and affect cell signalling and homeostasis [6]. Excess ROS can cause cell damage and the injury of DNA and proteins, finally inducing cell apoptosis. In general, a cell-permeable probe 2',7'-dichlorofluorescin diacetate (DCFH-DA) is used to detect ROS, as ROS de-esterifies this dye into the fluorescence form. In this thesis, cells were co-cultured with 20 μM of DCFH-DA for 30 min, and rinsed before ROS detection using FACS or CLSM.

3.3.7 Mouse model

All animal work in this thesis was performed in accordance with the University of Queensland's Animal Ethics Committee (AE224_18), and conformed to the University of Queensland Institutional Animal Care and Use Committee guidelines. The animals were housed at the EnGeneIC Animal Facility under specific pathogen-free conditions (SPF). Female Balb/c mice (6-8 weeks old) were kept in filter-topped cages with standard rodent chow and water available ad libitum in a 12 h light/dark cycle.

The xenograft tumour model was established by subcutaneously injecting 2×10^6 4T1 cells (suspended in 100 μL RPMI-1640 medium) to the left flank of mice using a 27G needle syringe, and allowed to grow for 7 days before various treatments in this thesis. In general, the time-dependent profiles of the tumour size and the mouse body weight represent the inhibition of the tumour growth upon the treatment. These two parameters were measured every other day,

and the tumour size calculated using a formula ($0.5 \times length \times wide^2$). Mice were euthanized when the tumour size reached the ethics permission.

3.3.8 Organ dissociation and primary cell culture

In this thesis, freshly harvested mouse organs were minced by scissors, and then digested with Collagenase IV (1.5 mg/mL in PBS, Sigma-Aldrich) for 1 h in a 37 ℃ water bath with occasionally homogenising. The second step of digestion was performed in an Enzyme cocktail (2 mg/mL dispase and 0.1 mg/mL DNase in PBS, Sigma-Aldrich) for 10 min at 37 ℃. The excess medium was added to cease the digestion. The singlet cell suspension was obtained by passing the mixture through a 70 μm strainer. Cells were counted against trypan blue staining when necessary.

3.3.9 Primary cancer cell culture

Fresh organs were dissociated to obtain singlet cell suspension, as described in section 3.3.8. The primary cancer cells were seeded in 6-well plates with a series of dilutions. To select cancer cells (4T1) against normal tissue cells, 60 μM of 6-thioguanine was supplemented to the culture medium. The plates were cultured in normoxia with medium refreshment for a certain time when necessary.

3.3.10 Clone staining

The selected primary cancer cells in culture plates exhibit typical colony morphology, indicating the formation of cell clones. Crystal violet is therefore used to visualize the number and area of the clones. As a commonly used alkane dye, crystal violet can bind with proteins in permeabilised cells. In this thesis, the cell clones in plates were first fixed with 4% paraformaldehyde (PFA) for 30 min, followed by staining with 0.1% crystal violet for 30 min. The images were taken by a camera and analysed using ImageJ software for semi-quantification.

3.3.11 Surface marker detection

To detect surface marker expression, cancer cells after transfection treatment are normally stained with the corresponding antibody conjugated with a fluorescent dye. After 20-40 min

staining in FACS buffer (PBS containing 2% FBS blocking), the cells are then rinsed 3 times before analysis by FACS or CLSM.

For primary cells obtained from 4T1 xenograft tumour tissues in this thesis, the cell suspension with a density of 10^8/mL was obtained. The cells were stained with APC-anti CD45, APC-anti I-A/I-E, PE-anti PD-L1, FITC-anti CD4, PerCP-Cy5.5-anti CD8, and/or PE-anti PD-1 antibodies with recommended dilution. After staining for 30 min, the cells were then rinsed with FACS buffer and analysed in flow cytometry.

3.3.12 Histological staining

As one of the principal staining method in histological analysis, the haematoxylin and eosin staining (H&E staining) are often used to check the toxicity of NP to the organs. According to the pH affinity, the haematoxylin stains the nuclei blue, while eosin stains the extracellular matrix and cytoplasm pink. Other structures in specimen show a combination of these colours accordingly. Thus the H&E staining provides a general overview of the tissue structure.

In this thesis, the fixed organs embedded in paraffin were cut into 5 μm thick sections. H&E staining was next conducted. The sections were then imaged using an Olympus BX41 microscope with 4×, 10×, and 20× lens.

3.4 Biological techniques

3.4.1 Flow cytometry (FACS)

Flow cytometry (FACS) is a commonly-used technique for single cell sorting and analysis based on fluorescence signals. By suspending cells in the sheath fluid and passing through an electronic detection apparatus, the fluorescence signals are generated and recorded. In general, the scattered light signals collected from forward scatter channel (FSC) and side scatter channel (SSC) are used to distinguish the target population of cells in priority. FSC suggests the living cells and debris, while SSC provides information about the granularity or internal complexity [7]. In this thesis, FACS was used to detect fluorescence signals within cells or from cell surface markers using either an Accuri C6 flow cytometer (BD Biosciences) or a CytoFLEX flow cytometry (Beckman, IN), followed by corresponding analysis.

3.4.2 Confocal laser scanning microscopy (CLSM)

Confocal laser scanning microscopy (CLSM) enables the collection of high resolution images by “confocaling” light using a spatial pinhole to block off-focus light in image formation. Moreover, CLSM enables to obtain a series of two dimensional images along the optical axis (Z), resulting in a reconstructed three dimensional model of the specimen. In this thesis, a Carl Zeiss LCM 710 microscopy was used to examine cellular samples.

3.4.3 MTT assay

MTT assay is used to evaluate cell viability according to the activity of NADPH-dependent cellular oxidoreductase enzymes. These enzymes are able to reduce the MTT to an insoluble form, providing formazan precipitates in purple colour. The resulting intracellular formazan crystals can be dissolved in DMSO, and the UV absorbance can be used for live cell quantification. In this thesis, the cell viability of B16F10, B16F0, and 4T1 cells after treatment were assessed using MTT.

3.4.4 Reverse transcription quantification polymerase chain reaction (RT-PCR)

Reverse transcription quantification polymerase chain reaction (RT-PCR) is the technique for assessing the gene expression level. Generally, the mRNA is extracted, reversely transcripted into cDNA (complementary DNA), and amplified using a quantifiable PCR technique. The involved fluorescent DNA labelling techniques allows the copy number of a specific piece of DNA to be monitored during the molecular cloning, providing information for quantification. In this thesis, the RT-PCR technique was used for quantifying the expression of Bcl-2 and PD-L1 genes.

3.4.5 Western blot

Western blot is a widely used technique to analyse specific proteins [8]. In brief, the denatured protein samples are separated by gel electrophoresis [usually sodium dodecyl sulphate polyacrylamide gel electrophoresis (SDS-PAGE) electrophoresis] according to molecular weights, followed by transferring onto a PVDF membrane. After background blocking, the primary antibody for targeted protein is added and incubated. The labelled secondary antibody is then used to bind to the primary antibody for further visualization of the target proteins by

staining, immunofluorescence, and radioactivity. In this thesis, western blot was used to detect Bcl-2 expression and p65 subunit of NF-κB complex translocation.

3.4.6 BX-41 microscopy

The optical microscope can be used to directly magnify objects under visible light. In this experiment, the BX41 microscope was used to obtain H&E staining images with specified colours under visible light.

3.5 Statistics analysis

In all cases, experiments were performed at least two times. When applicable, statistical analysis was performed by student's t-test using GraphPad if no further instructions. Data with a p-value <0.05 difference were deemed significant at the minimum. *, $p < 0.05$; **, $p < 0.01$; ***, $p < 0.001$; and ****, $p < 0.0001$.

3.6 Reference

[1] J. Li, Y. Yang, L. Huang, Calcium phosphate nanoparticles with an asymmetric lipid bilayer coating for siRNA delivery to the tumor, J. Controlled Release 158(1) (2012) 108-114.
[2] B.J. Berne, R. Pecora, Dynamic light scattering: With applications to chemistry, biology, and physics, Courier Corporation2000.
[3] B.J. Kirby, Micro-and nanoscale fluid mechanics: Transport in microfluidic devices, Cambridge university press2010.
[4] W. Lee, J. Lee, P. Reucroft, XPS study of carbon fiber surfaces treated by thermal oxidation in a gas mixture of $O_2/(O_2+ N_2)$, Appl. Surf. Sci. 171(1-2) (2001) 136-142.
[5] I. Vermes, C. Haanen, H. Steffens-Nakken, C. Reutellingsperger, A novel assay for apoptosis flow cytometric detection of phosphatidylserine expression on early apoptotic cells using fluorescein labelled Annexin V, J Immunol. Methods 184(1) (1995) 39-51.
[6] P.D. Ray, B.-W. Huang, Y. Tsuji, Reactive oxygen species (ROS) homeostasis and redox regulation in cellular signaling, Cellular signalling 24(5) (2012) 981-990.
[7] O. Ornatsky, D. Bandura, V. Baranov, M. Nitz, M.A. Winnik, S. Tanner, Highly multiparametric analysis by mass cytometry, J Immunol Methods 361(1-2) (2010) 1-20.
[8] T. Mahmood, P.-C. Yang, Western blot: Technique, theory, and trouble shooting, N Am J Med Sci. 4(9) (2012) 429-434

Chapter 4

Devising New Lipid-coated Calcium Phosphate/Carbonate Hybrid NPs to Control Release in Endosome for Efficient Gene Delivery

This chapter reports the devising of the new lipid-coated calcium carbonate/phosphate (LCCP) nanoparticles (NPs). Lipid-coated calcium phosphate (LCP) NPs are proven to be an effective vehicle for gene and some drug delivery, while it is not desirable for NPs to release gene/drug in late endosome/lysosome. To achieve the early endosome release and escape, we have designed and developed new LCCP hybrid NPs. The new hybrid LCCP NPs had a spherical structure with an average diameter of 40 nm and a high gene loading capacity. We particularly demonstrated that the loaded dsDNA/siRNA was mostly released under mildly acidic conditions (pH 6.0-5.5). LCCP NPs were also effectively internalised by B16F10 cells in a dose and time-dependent way. The delivery efficacy was further demonstrated using two functional siRNAs, i.e. programmed death ligand 1 (PD-L1) siRNA for PD-L1 silencing and polo-like kinase 1 (PLK1) siRNA for growth inhibition of B16F10. As expected, the LCCP loaded PD-L1 siRNA shew a quicker PD-L1-mRNA inhibition than LCP NPs, indicating that LCCP NPs improved the siRNA release in endosome. **This part of work has been published in J. Mater. Chem. B (2017, full paper).**

4.1 Introduction

Gene therapy, especially RNA interference (RNAi) based therapy, has been intensively studied for the treatment of many types of diseases including cancers [1]. RNAi utilizes small interference RNA (siRNA) to regulate cellular machinery that allows efficient down-regulation of specific gene transcription, leading to death or growth inhibition of cancer cells [2]. The co-delivery of siRNA with anticancer drugs does not only help overcome multiple drug resistance (MDR) [3, 4], the high potency of RNAi also results in a much lower dose and weaker side effects in therapeutic applications compared to traditional chemotherapeutic drugs like doxorubicin, cisplatin, and camptothecin [5, 6]. However, the quick enzymatic degradation and limited cell membrane permeability limit the in vivo application of naked siRNA. Thus, proper nanoparticles (NPs) as gene delivery vehicles, including dendrimers [1], liposomes [7], layered double hydroxide (LDH) [8], calcium carbonate [9] and calcium phosphate [10] are recently proposed and developed for siRNA delivery.

An ideal gene delivery vehicle should process merits including (1) stability under physiological conditions, (2) high payload of gene materials, (3) low cytotoxicity and good biocompatibility [11], and (4) suitable release profile. In particular, the release kinetics is crucially important for the delivered oligonucleotides to function effectively. The quick dissolution and release within cells, or more specifically, within endosomes, will lead to the quick utilization of cargos and avoid lysosomal digestion [12-15]. According to the endocytic pathway, a clathrin-coated vesicle containing particles will sequentially mature into an endosome with pH of ~6.9-5.2, then into a lysosome with pH of ~5.2-4.5 [16-18]. Thus it is worth developing a gene delivery system that is able to release DNA/RNA just within the endosome and undergo the subsequent endosomal escape.

Lipid-coated calcium phosphate (LCP) NPs have been demonstrated as a promising gene delivery system [19-22]. DNA/RNA can be rapidly released from LCP NPs at pH 4-5, while maintained quite stable within the particle at pH > 6 [22, 23]. Therefore, it is plausible that the majority of DNA/RNA is released from LCP NPs in the late endosome/lysosome. In contrast, calcium carbonate (CaC) NPs release cargoes (genes and drugs) at a relatively high pH. For example, the release of anticancer drug from CaC NPs occurred at pH of ~6.8 [24, 25]. For *in vivo* applications, such a release might lose some cargoes in the blood during circulation,

particularly siRNA in the tumour extracellular environment (pH 6.5-6.9), thus reducing the siRNA delivery efficacy to tumour cells using CaC NPs.

Therefore, we designed and prepared lipid-coated calcium phosphate/carbonate (LCCP) hybrid NPs by partially substituting phosphate in LCP NPs with carbonate. We aim to achieve the gene release from LCCP NPs in endosome by elucidating the incorporated carbonate effects on (1) particle size and colloidal stability, (2) loading efficiency and release profile, (3) internalisation and intracellular distribution and (4) the efficacy of functional siRNA cellular delivery. Our results show that as-designed LCCP NPs released the loaded dsDNA/siRNA mainly in pH 6.0-5.5, which led to a quicker mRNA downregulation. To our knowledge, this is the first attempt to utilize calcium carbonate/phosphate hybrid nanoparticles to control gene release just in endosome.

4.2 Experimental methods

4.2.1 Materials

All the oligonucleotide duplexes and primers were purchased from IDTDNA or Sigma-Aldrich, with the detailed sequences shown in Table S4.1. All the oligonucleotides were dissolved in DNase/RNase free water and stored in a -20 °C freezer for further use according to the manufacturer's instructions. The phospholipids (DOPA and DOPC) were obtained from Avanti Polar Lipid. All other chemicals and reagents were purchased from Sigma-Aldrich. Lysosensor^{TM}-DND 189, Trizol^{TM} Reagent, High-Capacity cDNA Reverse Transcription Kit (RT kit), and 2X PCR Master Mix were purchased from Life Technologies Co. (Carlsbad, CA). The antibodies were obtained from Biolegend Inc. (San Diego, CA). All biochemicals and materials were used as received without any further purification unless specifically mentioned. Water used in this experiment was deionized Milli-Q water (Ω = 18.2 at ambient temperature).

4.2.2 Synthesis of LCCP NPs with different P/C ratios

The hybrid NPs were prepared based on a similar protocol reported previously with slight modification [22]. Briefly, 150 µL of 2.5 M $CaCl_2$ (pH = 7.0) aqueous solution was dispersed into 5 mL of cyclohexane/igepal-CO520 (7/3; v/v) dropwise under magnetic stirring to form water-in-oil emulsion. The similar emulsion was prepared by dispersing 150 µL of 25 mM Na_2HPO_4/$NaHCO_3$ (pH = 9.0) into 5 mL of cyclohexane/igepal-CO520 (7/3; v/v), followed by

adding 50 μL of 20 mM DOPA in chloroform dropwise. The Na_2HPO_4/$NaHCO_3$ molar ratio (P/C ratio) was set at 4/0, 3/1, 2/2 and 1/3. Then the latter emulsion was added dropwise into the former one, followed by magnetic stirring for 20 min. An equal volume of absolute ethanol was next added into the mixture, with continuous stirring for 5 min. The core hybrid NPs were collected *via* centrifugation at 12,500 g for 20 min, followed by 3 times of washing with absolute ethanol. The hybrid NP core pellet was then redispersed in 1 mL of chloroform, and mixed with 70 μL of DOPC/cholesterol (20 mM). After evaporation of the solvent under the reduced pressure, the lipid film was then hydrated in water or PBS buffer to form LCCP NP suspensions with gentle ultrasound treatment. The obtained LCCP NPs were denoted as P4C0, P3C1, P2C2 and P1C3, according to their corresponding phosphate/carbonate ratios (P/C ratios).

4.2.3 siRNA encapsulation

The loading of dsDNA/siRNA into LCCP NPs was performed using a similar procedure, where half the amount of dsDNA/siRNA was mixed with both aqueous solutions before emulsification. The dsDNA payload was optimised via changing the dsDNA amount from 1 to 4 nmol in each batch experiment. The P/C ratio for payload optimisation was fixed to 3/1. The payload of cy5-labelled dsDNA was estimated by measuring the fluorescence intensity of cyanine 5 (cy5) using a fluorescent plate reader (BioTek, Winooski, VT, USA). LCCP NPs samples were treated with lysis buffer (2 mM EDTA and 0.05% Triton X-100 in pH 7.8 Tris buffer) at 65 °C for 10 min for complete dissolution before measurement. All the experiments were done in triplicate.

4.2.4 Characterization

The hydrodynamic diameter and zeta potential of hybrid NPs with/without dsDNA were measured using a dynamic light scattering (DLS, zetasizer Nano, Malvern, UK) method. The morphology of these particles was profiled using transmission electron microscope (TEM, JEM-3010, ZEOL, Tokyo, Japan) by dropping aqueous solution containing 0.1 mg/mL of particles onto a 300 mesh carbon-coated cooper grid, and the diameter of the particle core was estimated using Nanomeasure 1.2 software by measuring 150 NPs (randomly selected). For negative staining, the grid was treated with 1 % uranyl acetate for 2 min, and dried on a filter paper. The chemical analysis of particle cores coated with DOPA was carried out using X-ray photoelectron spectrometer (XPS) equipped with a state of the art Kratos Axis Ultra

photoelectron spectrometer using mono Al Kα (1486.6 eV) X-rays. The energy for survey scan and high resolution scan was 200 and 20 eV, respectively. The XPS spectra were processed and analyzed using CasaXPS software. The binding energy of C peak at 284.6 eV after fitting the curve of C 1s spectrum was used as the reference [26].

The composition of particle cores without any lipids was examined using a Fourier transform infrared spectroscopy (FTIR, Nicolet 5700), UV/Vis, and CHN analyzer. The main elements (Ca, P, and C) were examined to predict the possible formula of the particle core. Arsenazo III-Ca method was used for Ca quantification [25, 27]. Samples were digested with 0.1 mL of HCl (1 M) for 10 min, then mixed with 2 mL of Arsenazo III solution (0.2 mM Arsenazo III, 150 mM NaCl, and HEPES buffer, pH = 7.4) for 30 min. The absorbance of Arsenazo III-Ca^{2+} at 655 nm was used to determine the Ca concentration using a UV-vis spectrometer (UV-2450, Shimadzu). Molybdate blue method was used for phosphate quantification [28, 29]. Samples were dissolved in 1 mL of HCl (1 M) for 10 min, then mixed equal volume of 5% ammonium molybdate solution, followed by adding 2 mL of 20% fresh Na_2SO_3 solution under stirring for 1 h. The absorbance of molybdenum blue at 710 nm was used to measure the P concentration using the UV-vis spectrometer. CHN analyzer was used to determine the carbon amount in samples. All the experiments were conducted in triplicate.

4.2.5 Colloidal stability

The colloidal stability of as-prepared LCCP NPs in suspensions was evaluated using DLS. Briefly, 50 µL of as-prepared LCCP NP suspension was diluted with DMEM medium containing 10% serum to 1 mL, then incubated at 37 °C for a predetermined time period from 0 to 48 h. The particle size was monitored by DLS at each time point.

4.2.6 *In vitro* release of dsDNA from LCCP NPs

The dsDNA release profile from hybrid LCCP NPs in solutions with pH = 7.4 to 5.0 was examined using agarose gel electrophoresis. The pHs were chosen to mimic physiological condition (7.4), early/late endosomal condition (6.0 and 5.5), and lysosomal condition (5.0) in B16F10 cells, based on a few reports [16, 17, 30, 31]. Briefly, 50 µL of LCCP-dsDNA NP suspension containing 25 µg of LCCP and 975 ng of dsDNA was mixed well with 450 µL of disodium hydrogen phosphate – citric acid buffer solution (0.2 M) with pH adjusted to 7.4, 6.0, 5.5, or 5.0, and incubated in a 37 ºC shaking water bath for 10 min to 4 h. At each predetermined time point, the sample was centrifuged at 20,000 g for 10 min at 4 ºC to remove non-dissolved

particles, and 10 μL of the supernatant (corresponding to 16 ng of dsDNA if 100% released) was loaded to a 2% agarose gel in 1 ×TAE buffer containing 5 μL of gel staining safe dye (GelRed, Nucleic Acid Gel Stain, 10,000 × in water, Biotium Inc., Hayward, CA). Ten microliters of dsDNA sample containing 16 ng dsDNA was added in the first lane as the reference. Electrophoresis was carried out under 100 V voltage for 30 min. The image of agarose gel was recorded using Geldoc (Bio-Rad Laboratories, Inc., Hercules, CA). The dsDNA concentration of each band was quantified using Geldoc and normalized by the first lane dsDNA in corresponding line.

4.2.7 Cellular uptake of hybrid LCCP NPs

The cellular uptake of LCCP-dsDNA-cy5 NPs was investigated using flow cytometry (FCM, BD Accuri™ C6, BD Biosciences, San Jose, CA). In brief, B16F10 cells were seeded in 12-well plates with a density of 1×10^5 per well, and cultured overnight to 70-80% confluence at 37 °C in 5% CO_2 humid environment. Then the DMEM medium was replaced with 0.5 mL of DMEM containing 1% penicillin/ streptomycin and LCCP-dsDNA-cy5 NPs where the cy5 concentration was 25 nM. After culture for 4 h, the medium was withdrawn and cells were rinsed by PBS for three times. The cells were trypsinized, centrifuge-collected, and resuspended in 4% PFA solution for FACS analysis.

Similarly, the cellular uptake of B16F10 cells was also examined in the medium containing LCCP hybrid NPs with the dsDNA-cy5 concentration varied from 0 to 50 nM for 4 h, or with a 25 nM dsDNA-cy5 for 0.5 to 6 h. Then the fluorescent intensity was evaluated as described above. All the experiments were done in triplicate.

4.2.8 Imaging cellular uptake of LCCP NPs using confocal laser scanning microscope

Fourteen mm round coverslips were pretreated with 5% hydrochloric acid, 30% nitric acid, and 75% ethanol sequentially before use. Cells were harvested and seeded on the pretreated coverslips at a density of 5×10^5 per well, and cultured for one day. Then the medium was replaced by 0.5 mL of DMEM containing LCCP-dsDNA-cy5 NPs (cy5 dsDNA: 25 nM). After 4 h incubation, the cells were rinsed by PBS for 3 times and stained with 2 μM lysosensor-DND 189 for 30 min to visually display the distribution of lysosome/endosome in cytoplasm. Then the cells were rinsed with PBS, followed by fixing with 4% PFA for 20 min. Finally the coverslips were mounted cell-side down on slides using mounting medium fluoshield with 4'6-diamidino-2-phenylindole (DAPI, Invitrogen). Cells were visualized using a Carl Zeiss LCM

510 confocal laser scanning microscope (CLSM, Carl Zeiss MicroImaging GmbH, Germany) with 40× objective lens. For 3-dimension imaging, 8 slices were taken for a 10 μm Z-stack with 40× objective lens and 2.0× zoom.

4.2.9 Knockdown of PD-L1 expression

To quantify surface PD-L1 protein expression using FACS, B16F10 cells were seeded in 12-well plates at a density of 5×10^4 per well, and cultured overnight to allow the cells to 70-80% confluence. The medium was then replaced with 500 μL of DMEM containing LCCP-PD-L1 siRNA (siRNA concentration: 40 nM). After transfection for 4 h without serum, the medium was discarded and 500 μL of fresh DMEM containing 10% FBS were added to continue the culture for 48 h. The surface PD-L1 protein expression was stained by PE conjugated anti-mouse PD-L1 antibodies. Untreated cells without any antibody staining were used to gate positive cells, and untreated cells stained with PD-L1 antibody as the positive control. Cells treated with LCCP-negative control siRNA at the same concentration were stained with an equal amount of anti-mouse IgG antibody as the negative control.

The PD-L1 mRNA expression level was also examined using real time reverse transcription qPCR (real time RT PCR). Briefly, B16F10 cells were seeded in 6-well plates with a density of 2×10^6 per well overnight. The transfection was performed using the same protocol described above. After 4 h transfection, the medium was replaced by fresh DMEM with 10% FBS. At each predetermined post transfection time point from 0 to 20 h, cells were harvested in 1 mL Trizol reagent. The RNA extraction was performed according to the standard protocol, followed by reverse transcription using RT Kit. Then RT qPCR was used to enlarge and quantify PD-L1 specific fragment. Mouse beta-actin gene was used as the internal control to normalize gene expression.

Similarly, B16F10 cells were cultured with medium containing P3C1-PLK1 siRNA NPs for functional siRNA transfection. Cells were seeded in a 96-well plate at a density of 4×10^3 per well. After overnight culture, the medium was replaced by 100 μL of DMEM containing P3C1-PLK1 siRNA NPs with the siRNA concentration from 10 to 80 nM and the cell cultured for 4 h. Then the medium was replaced with 100 μL of fresh DMEM containing 10% FBS. After treatment for 48 h, 20 μL of MTT (5 mg/mL in sterilized PBS solution) was added to react for 4 h, followed by adding 100 μL of DMSO to dissolve formazan. The cell viability was calculated by measuring the formazan absorbance at 490 nm using a plate reader (BioTek, Winooski, VT, USA). Cells treated with PBS were used as the control. Cells treated with naked

PLK1 siRNA (80 nM), Oligofectamine-PLK1 siRNA (80 nM), P3C1-scrambled siRNA (80 nM), and blank P3C1 NPs (40 mg/L) were used for comparison. All the experiments in this section were repeated 3 times.

4.2.10 Statistical analysis

Data presented as Mean ± SD were analyzed *via* t-test using GraphPad Prism 7.00 software; a p value < 0.05 was considered statistically significant. *, $p < 0.05$; **, $p < 0.01$; ***, $p < 0.001$.

4.3 Results

4.3.1 Physicochemical features of LCCP nanoparticles

As shown in Figure S4.1A and summarized in Table 4.1, the number mean hydrodynamic particle size of hybrid LCCP NPs was from 38.1±3.4 to 41.4±2.4 nm, similar to that reported for LCP NPs [22] (i.e. P4C0 NPs in this study). Given that the particle size is mainly controlled in the W/O micelles, it is plausible that the average particle size maintains unchanged after carbonate incorporation.

The polydispersity index (PDI, Table 4.1) of as-prepared LCCP hybrid NPs was slightly increased from 0.27 to 0.42-0.38 when more carbonate was incorporated. Overall, the particle size distribution was moderately narrow and slightly broad at P/C = 2/2 and 1/3, which might be due to the influence of mismatch of calcium carbonate phase with calcium phosphate phase in the hybrid system. At pH 8.0, the precipitates should be mostly composed of two different crystallites ($CaHPO_4$, PDF number 01-0653 and $CaCO_3$, PDF number 04-0636). However, the XRD pattern of P4C0 and P3C1 cores were similar without any characteristic peaks (Figure S4.1B), indicating calcium phosphate and carbonate were amorphous.

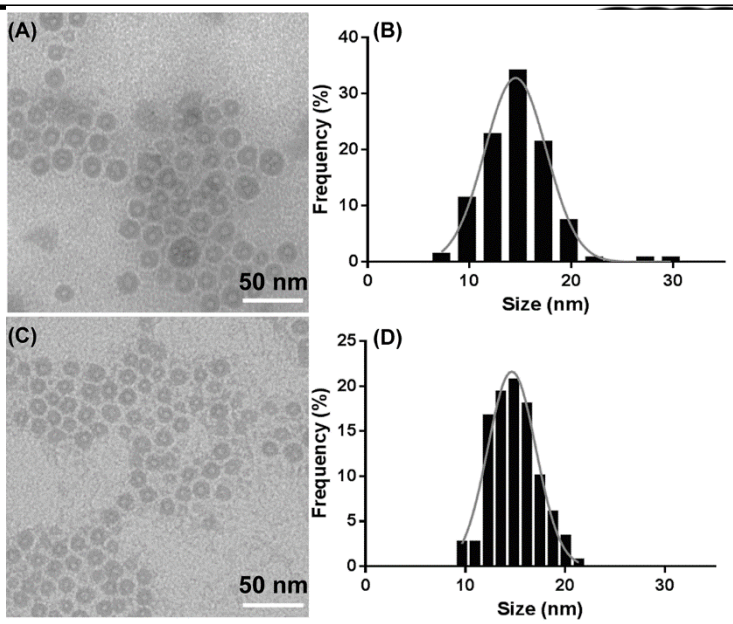

Figure 4.1 (A) and (C): TEM image of P4C0 NP cores and P3C1 NP cores; **(B) and (D):** The core diameter distribution collected using NanoMeasurer (count = 150).

The zeta potential of particles slightly increased from -18.8±0.9 to -15.6±1.2 mV when the P/C ratio changed from 4/0 to 1/3 (Table 4.1). Slight increasing of the zeta potential could be attributed to carbonate incorporation where the dangling phosphate groups (P-OH) may be relatively less. Note that when dsDNA was loaded, the zeta potential became a little more negative (-22.5±1.1 to -23.5±0.5 mV, Table 4.1) as there were more dangling P-OH groups in the system. As all genes used in this study (dsDNA or siRNA, see in Table S4.1) were 21 base pair in length, the influence of their sequence differences on the particle size, zeta potential, loading amount, and loading efficiency were very much limited. Therefore the data listed in Table 4.1 for P4C0 and P3C1 with/without gene should represent the size, PDI, and zeta potential of other LCCP NPs with/without gene loaded.

In particular, the TEM images show that both P4C0 and P3C1 NP cores were sphere-like with uniform hollows (Figure 4.1). The core diameters were 14.5±3.0 (P4C0) and 14.6±2.4 nm (P3C1) (Figure 4.1B and D). The boundary of lipids can hardly be recognized by TEM (Figure 4.1, A and C), but it can be clearly seen in the negatively stained images (Figure S4.2). After staining, a 15-20 nm increase in the nanoparticle diameter was observed corresponding to the lipid coating, in accordance with our previous report [22]. This increase would lead to a

hydrodynamic size of around 40 nm if the first lipid layer expectedly increases the diameter by another 5 nm.

Table 4.1 The number-mean particle size, PDI, zeta potential of LCCP NPs with different P/C ratios loaded with/without dsDNA

Sample code	Number-mean Particle Size (nm)	PDI	Zeta potential (mV)
P4C0	38.1±3.4	0.27±0.01	-18.8±0.9
P4C0 (with genes)	*40.3*±1.6	*0.36*±0.01	*-23.5*±0.5
P3C1	41.4±2.4	0.31±0.02	-18.6±0.8
P3C1 (with genes)	*41.1*±2.5	*0.33*±0.01	*-22.5*±1.1
P2C2	40.7±6.4	0.42±0.02	-16.7±1.3

P4C0 and P3C1 NP cores predominantly contained Ca, O, P, and C (Figure S4.3A and B), in accordance with the existence of amorphous $Ca(HPO_4)$ and $CaCO_3$ (Figure S4.1B), as well as DOPA. In the high resolution scan for P 2p in sample P3C1, the binding energy peak of P 2p3/2 was around 133.0 eV (Figure S4.3C), suggesting the main form of phosphorous in the core is phosphate [32]. The high resolution scan reveals that C 1s had a weak peak at 289.4 eV (Figure S4.3D), suggesting the existence of carbonate in sample P3C1 [33].

The FTIR spectrum (Figure S4.4) of P4C0 cores without any lipids was characteristic of orthophosphate-derived peaks at 1010-1020 (ν_3) and 566 (ν_4) cm^{-1} [34, 35]. New peaks appeared at 1420-1480 (ν_3 of carbonate) and 878 cm^{-1} (ν_2 of carbonate) after carbonate incorporation. With the increase of the carbonate portion (from P4C0 to P1C3), the intensity of carbonate-derived peaks was enhanced. The stretching band at 878 cm^{-1} implies that $CaCO_3$ might be mineralized in a vaterite form under this condition [24, 36], while the crystallites may be too tiny to detect in XRD (Figure S4.1B). Taken together, XPS and FTIR spectra verified the existence of PO_4^{3-} and CO_3^{2-}.

Furthermore, the components of particle cores without any lipids were quantified, as listed in Table S4.2. Overall, the incorporation of carbonate decreased the content of phosphate, but did not affect the amount of calcium. The C/P ratio determined was slightly higher than the theoretical value, probably due to (1) CO_2 absorption by alkaline solution as CO_3^{2-} which might incorporate simultaneously, and (2) the residual organic materials in the system. The chemical formula was estimated in the form of $Ca[(HPO_4)_x(CO_3)_y(OH)_{2-2x-2y}]$ (Table S4.2).

Figure 4.2 shows the change of the average particle hydrodynamic size of LCCP NPs in DMEM containing 10% FBS with the incubation time. The average size of P4C0 NPs remained unchanged in two days, consistent with our previous report [22]. The size of P3C1 and P2C2 NPs was also kept unchanged, while the size of P1C3 NPs seemed to increase from 39 to 50 nm at day 1 and 58 nm at day 2. The increasing size of P1C3 NPs may be attributed to the adsorption of macromolecules onto the surface and the slight dissolution of carbonate cores in medium, as discussed shortly.

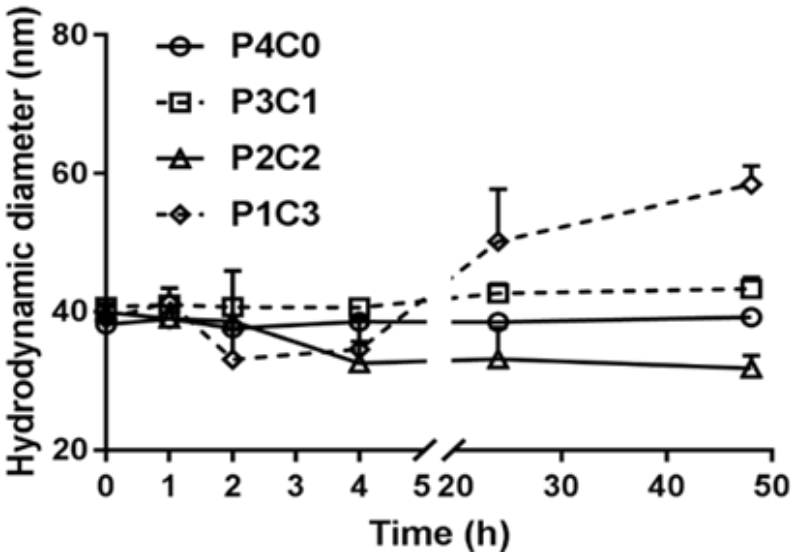

Figure 4.2 Colloidal stability of LCCP NPs in DMEM containing 10% FBS at 37 °C

4.3.2 Loading and release of dsDNA

As presented in Figure 4.3A, about 50 % of dsDNA was loaded into P4C0, P3C1 and P2C2 NPs. However, the loading efficiency was sharply decreased to 22.2% in sample P1C3, which may be attributed to the higher affinity of carbonate for calcium ion than phosphate group in dsDNA. In addition, the particle size was maintained around 40 nm after dsDNA encapsulation (Table 4.1). The zeta potential of these dsDNA-LCCP NPs slightly decreased to about -23 mV, due to the excess dangling phosphate groups (P-OH) of loaded dsDNA.

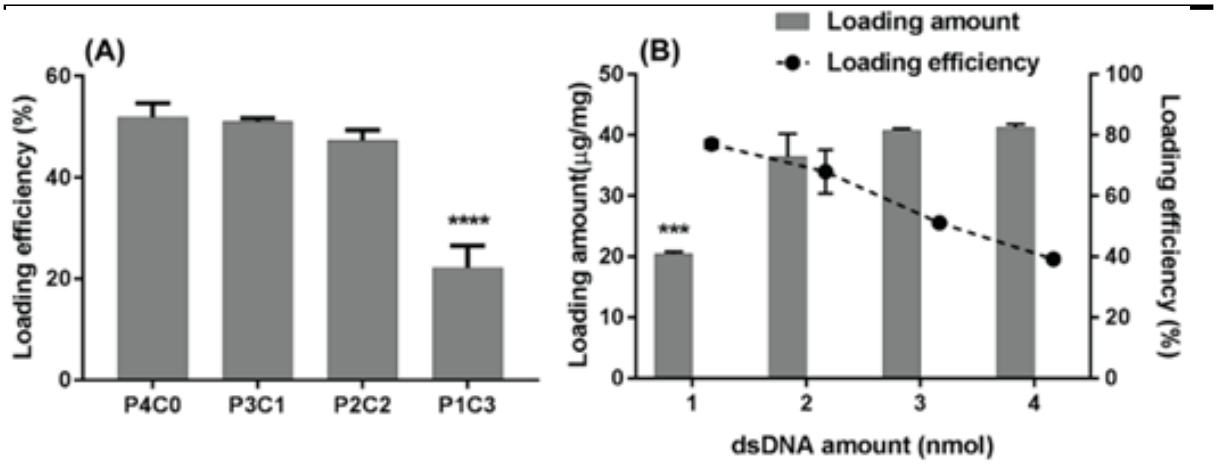

Figure 4.3 dsDNA loading efficiency and loading capacity. **(A)** The effect of P/C ratios on the dsDNA loading efficiency with 3 nmol dsDNA per batch; and **(B)** the effect of the initial dsDNA amount on the loading efficiency and loading capacity of P3C1 NPs.

As shown in Figure 4.3B, the loading amount of dsDNA in P3C1 sample increased with the initially added dsDNA amount from 1 to 4 nmol. This loading amount reached at 40 μg/mg and was remained unchanged when the initial dsDNA amount increased from 3 to 4 nmol. Reversely, the loading efficiency was kept declining from 75% to 38% when the initial dsDNA amount increased from 1 to 4 nmol. Taken together, P3C1 reached its capacity of dsDNA loading (40 μg/mg) at a reasonable loading efficiency (51%) when the initial dsDNA amount was 3 nmol, and thus was used in the subsequent experiments. The loading efficiency and payload capacity are all comparable to our previous report [22]. The majority of dsDNA loss may come from (1) the saturation of loading amount during the increasing of DNA input, and (2) the unavoidable sample loss during the collection, i.e. some sample adhered on the wall of glassware.

The dsDNA release kinetics was further profiled under different pH conditions (Figure 4.4 and S4.5A). For P4C0 NPs, almost no dsDNA was released at pH 7.4 in 2 h (<10%, Figure S4.5B), and only a small amount of released dsDNA was traced at pH 6.0 for 2 h (~20%, Figure S4.5B), indicating the stability of P4C0 NPs under physiological conditions. More dsDNA was released at pH 5.5 with the incubation time (~50%, Figure S4.5B) and almost all dsDNA released at pH 5.0 in 10 min (Figure 4.4). This observation is similar to previous reports [22, 23], with the release of dsDNA through the dissolution of calcium phosphate NPs in the acidic environment.

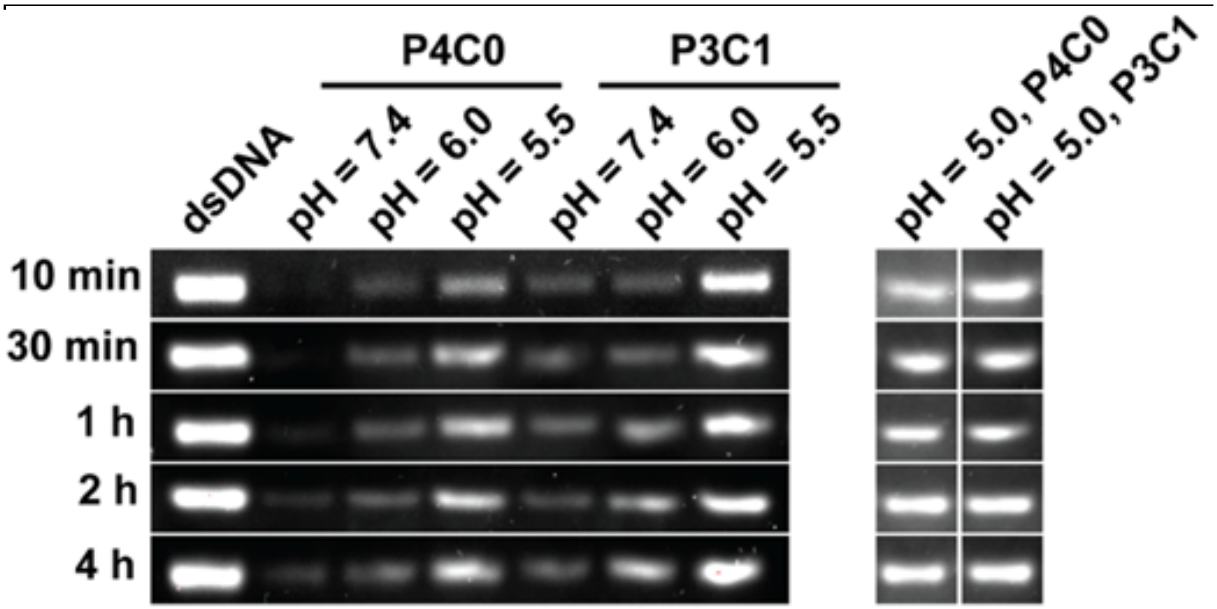

Figure 4.4 Sustained dsDNA release from P4C0 and P3C1 NPs within 4 h at different pHs.

In comparison, the release kinetics of dsDNA from P3C1 NPs seemed a bit faster at each pH compared with P4C0. At pH 5.5, most dsDNA was released from P3C1 NPs in 10 min (~60%, Figure S4.5B). At pH 6.0, the dsDNA band became stronger with the incubation time and much brighter than the corresponding one for P4C0 sample, with 35-40% dsDNA released in 1-2 h (Figure S4.5B). Even at pH 7.4, dsDNA was observed to be released from P3C1 in 1-2 h (10-20%, Figure S4.5B). Clearly, the main form of aqueous phosphate and carbonate is $H_2PO_4^-$ and HCO_3^-/H_2CO_3 at pH 6.0-5.5. Given that the solubility of $Ca(HCO_3)_2$ (16.6 g/100 g, Ksp = 4.1 [37]) is much higher than that of $Ca(H_2PO_4)_2$ (1.8 g/100 g, Ksp = 0.0018 [38]), we can reasonably postulate that P3C1 NPs dissolve more quickly than P4C0, releasing dsDNA in a much quicker way than P4C0 at pH 6.0 and 5.5. In addition, P2C2 NPs released dsDNA in a way similar to P3C1 under the same conditions (Figure S4.5A). Relatively, the release of dsDNA from LCCP cores without any lipids (Figure S4.5C) seemed a little quicker at pH 7.4 and 6.0, but dsDNA release at pH 5.5 similar in all cases. The slightly slower release of dsDNA from LCCPs at pH 6.0-7.4 may be attributed to the lipid bilayer protection on the core surface.

4.3.3 Efficient cellular uptake of LCCP NPs

The cellular uptake of LCCP NPs with different P/C ratios by B16F10 cells was further examined using FACS (Figure 4.5). The positive cell percentage of P3C1 group was the highest, but not statistically significant than that of P4C0 and P2C2, indicating the carbonate-incorporated NPs do not compromise their cellular uptake. The positive cell percentage of P1C3 treated group was just half of these groups and significantly lower, probably caused by the aggregation of P1C3 particles. FACS data of mean fluorescence intensity (MFI) (Figure S 4.6) show the trend similar to that of the positive cell percentage. Note that the cellular uptake of LCCP NPs here is much higher than the previous report [22], and the main reason is that this experiment was taken place in FBS free medium. The cellular uptake of P4C0 and P3C1 in DMEM containing 10% FBS was also performed (Figure S4.7), and this result (15-20% positive cell) is in accordance with the previous report [22].

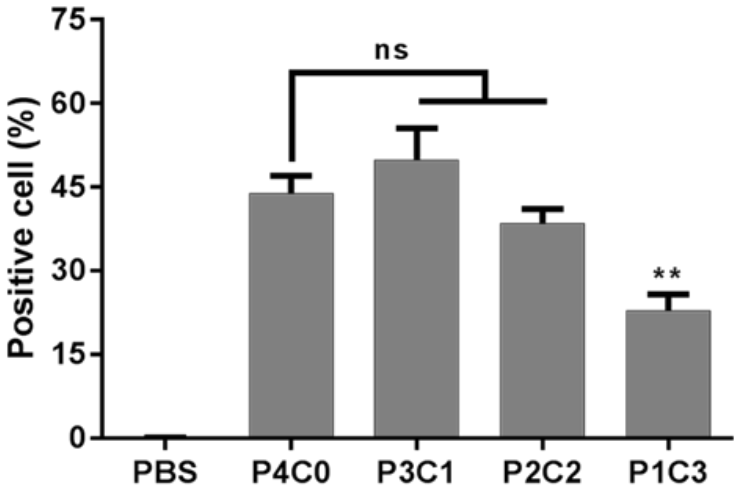

Figure 4.5 The effect of P/C ratio to cellular uptake of NPs with 25 nM dsDNA-cy5 for 4 h.

We next explored the effect of the dose and incubation time on the cellular uptake of LCCP NPs. As shown in Figure 4.6A, the cellular uptake of particles with dsDNA-cy5, represented by positive cell percentage, was increased with the dsDNA-cy5 concentration, indicating that the cellular uptake is dose-dependent. Note that the positive cell percentage using P4C0 and P3C1 was very similar under the same dsDNA-cy5 concentrations, in accordance with the result shown in Figure 4.5. As expected, the positive cell percentage was increased gradually with the incubation time in the first 4 h, and almost the same at 4 and 6 h (Figure 4.6B). This

trend suggests that the cellular uptake of LCCP NPs is time-dependent, and reaches the uptake saturation after 4 h incubation.

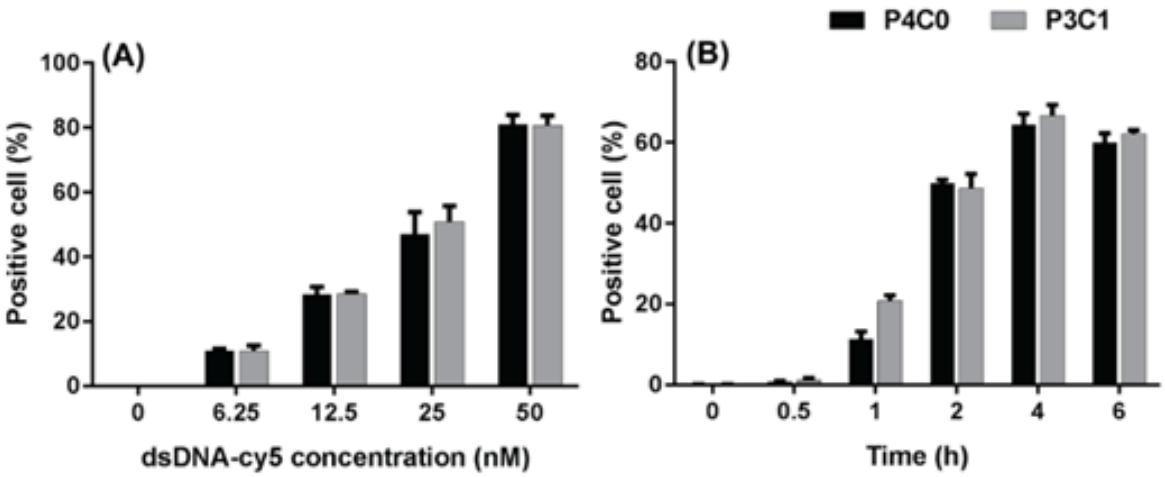

Figure 4.6 The effect of **(A)** dose and **(B)** incubation time on the internalisation of P4C0-dsDNA-cy5 and P3C1-dsDNA-cy5 NPs. **(A)** incubation time: 4 h; **(B)** dsDNA-cy5: 25 nM.

Furthermore, confocal laser scanning microscope (CLSM) images (Figure 4.7 and Figure S4.8) were recorded to reveal the localization of LCCP NPs within the cell as well as internalisation pathway. In Figure 4.7, it was obvious that both P4C0 and P3C1 NPs showed red dots located within the cell boundaries in the bright fields. The 3-D view diagrams show that four particular particles (arrow pointed) were located in the same confocal z-stacks around cell nuclei and in cytoplasm (Figure S4.7). Taken together, these dsDNA-cy5 related red dots were located in cytoplasm, suggesting the successful internalisation of LCCP NPs by B16F10 cells. It seems that the red fluorescence intensity is very similar in the case of P4C0 and P3C1 (Figure 4.7B and C).

Furthermore, the pH-dependent lysosensor green fluorescence signals in PBS treated group were very strong, indicating that there are many acidic organelles in PBS-treated cells. This is because that the lysosensor dye is an acidotropic probe and accumulates in acidic organelles in cytoplasm as a result of protonation, exhibiting a pH-dependent increase in green fluorescence intensity. However, this green fluorescence intensity was very much weakened in P4C0 and P3C1 treated cells, indicating the acidic organelles (such as endosome and lysosome) were well neutralized by the internalised P4C0 or P3C1 NPs to a higher pH value [39] due to dissolution of P4C0/P3C1 cores. Interestingly, few P4C0 NPs were co-localized with acidic organelles and appeared to be very weak yellow (Figure 4.7B, yellow arrow pointed Particle 1 and 2), while

the co-localization of P3C1 NPs and acidic organelles could hardly be found (Figure 4.7C, white arrow pointed Particle 3 and 4).

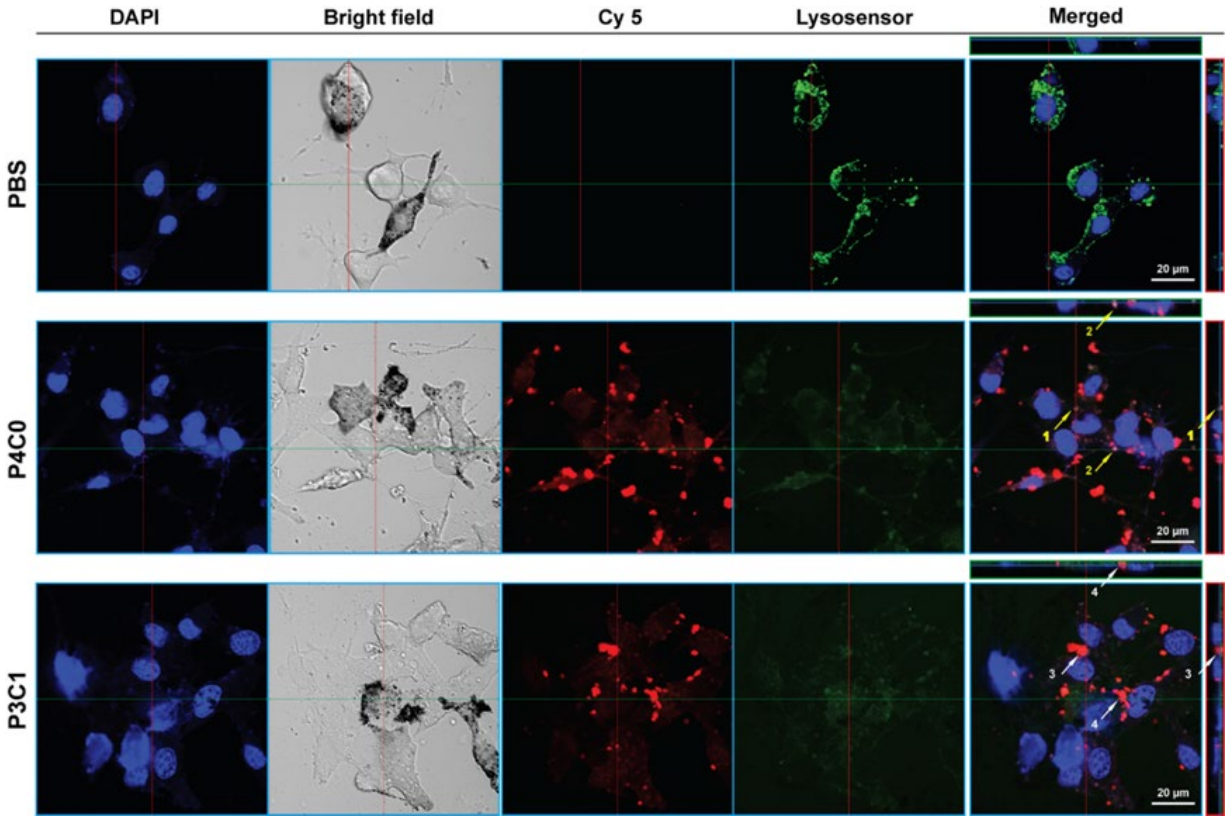

Figure 4.7 CLSM images for B16F10 cells treated with PBS, P4C0, and P3C1. Orthogonal images were shown. White arrows: dependent localization of dsDNA-cy5 red dots. Yellow arrows: co-localization of lysosensor green and dsDNA-cy5 red. Same dots shown in different diagrams were labelled with same numbers.

4.3.4 Effective inhibition and PD-L1 knockdown of skin cancer cells

For therapeutic applications, it is of importance to evaluate the efficacy of LCCP NPs delivering functional siRNA to silence the target gene or kill the cancer cells. Thus, P4C0 and P3C1 NPs with programmed death ligand 1 (PD-L1) siRNA were first used to deliver PD-L1 siRNA to B16F10 cells to down-regulate the PD-L1 expression (Figure 4.8). PD-L1 protein expressed on the surface of B16F10 cells was quantified by FACS with the fluorescence antibody (Figure 4.8A). The surface PD-L1 protein expression was initially 24% (positive control), and then declined to 14% and 12% after 48 h post transfection using P4C0 and P3C1 NPs, suggesting that about 50% of PD-L1 expression was down-regulated. Consistently, the

MFI was also significantly reduced after siRNA transfection using P4C0 and P3C1 NP. For comparison, the commercialized delivery vector Oligofectamine encapsulated with PD-L1 siRNA (Oligo-PD-L1) was also used to treat cells under the same conditions (Figure S4.9). The data suggested around 15% of PD-L1 expression was down-regulated (positive cell percentage declined from 33% to 28%). Taken together, the P4C0 and P3C1 NPs are more effective in inhibition of PD-L1 expression.

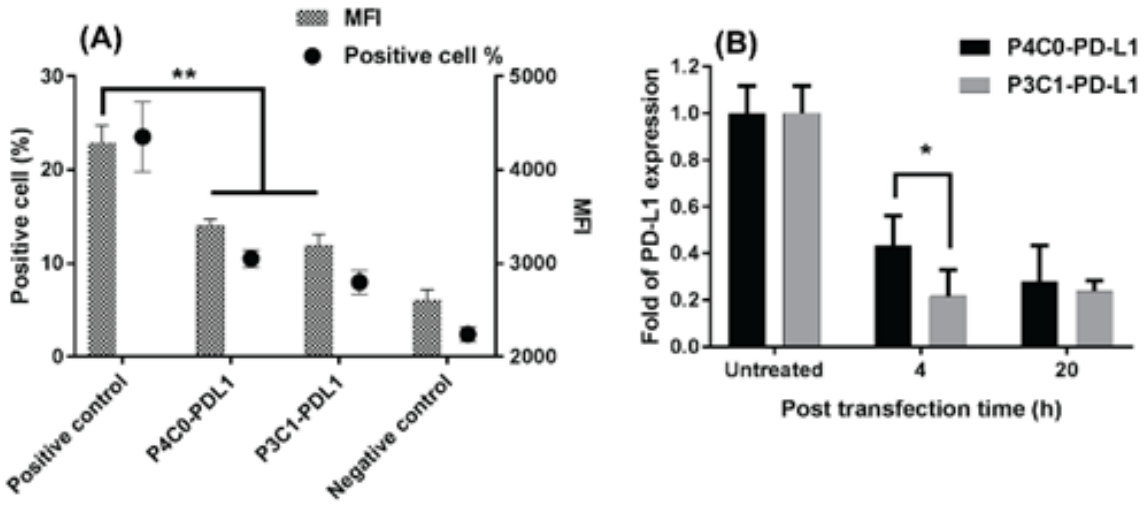

Figure 4.8 Down-regulation of PD-L1 expression in B16F10 cells. (A) PD-L1 protein expression on the surface of cells at 48 h post transfection; (B) Fold change of PD-L1 mRNA expression. PD-L1 siRNA: 40 nM.

To further show the efficacy, we next determined the mRNA expression using real time RT-PCR (Figure 4.8B). After 4 h transfection, PD-L1 mRNA expression by cells treated with P4C0-PD-L1 and P3C1-PD-L1 siRNA was 0.4 and 0.2 fold of the untreated group, respectively, and the low expression was maintained up to 20 h post transfection. The reduced mRNA expression level suggests continuous PD-L1 suppression, in accordance with the protein expression down-regulation (Figure 4.8A). In particular, P3C1-PD-L1 siRNA NPs down-regulated PD-L1 expression much more than P4C0 NPs (0.4 vs 0.2 fold), indicating an enhanced silencing ability within a short time period for P3C1 NPs (4 h, Figure 4.8B). Considering the similarity in the cellular uptake of LCCP NPs, more efficient silencing of the target gene using P3C1 NPs may be attributed to the quicker release of siRNA from P3C1 NPs in endosome (pH 5.5-6.0) and in cytoplasm (pH 7.4) (Figure 4.4). Nevertheless, this quicker

release does not affect long term suppression efficacy, as the release kinetics difference between P4C0 and P3C1 would diminish with the incubation time prolonging.

To further validate the gene delivery efficiency using LCCP NPs, we chose another functional siRNA, polo-like kinase 1 (PLK1) siRNA, to lethally knockdown PLK1 and kill B16F10 cells. Blank LCCP NPs, naked PLK1 siRNA, the commercialized delivery vector Oligofectamine^{TM} encapsulated PLK1 siRNA (Oligo-PLK1), P4C0 and P3C1 NPs with scrambled siRNA (Scr siRNA) were examined. As shown in Figure 4.9A, the proliferation inhibition of B16F10 cells treated with P3C1-PLK1 siRNA was dose-dependent. The viability of cells treated with P3C1-PLK1 siNRA at 80 nM was only 23%, significantly lower than that treated with 80 nM naked PLK1 siRNA (85%), Oligo-PLK1 (44%), and previous reported data (40%) [40], suggesting that the siRNA transfection efficacy has been significantly enhanced by P3C1 NPs. Also note that the cell viability of 20 nM P3C1-siRNA (47%) was the same as that of 80 nM Oligo-PLK1 (44%) (Figure 4.9A), meaning that the delivery efficacy is enhanced by nearly 4 times. Given that cells treated with P3C1 and P3C1-Scr siRNA did not show significant inhibition compared with untreated group, the proliferation inhibition is mainly attributed to the activity of PLK1 siRNA transfected into the cells.

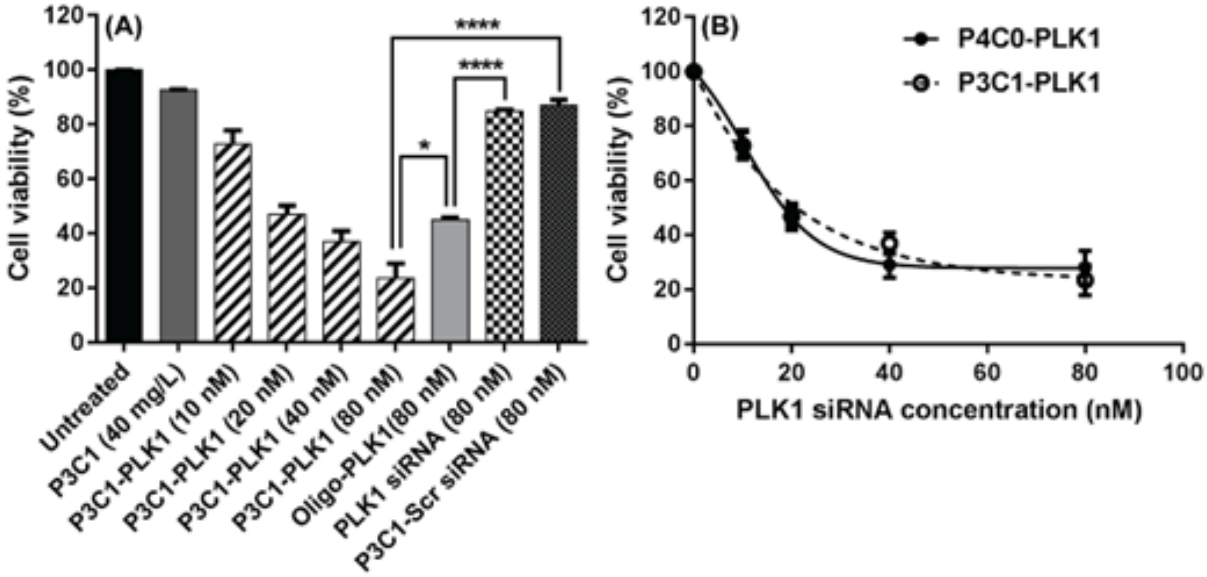

Figure 4.9 The viability of B16F10 cells upon PLK1 siRNA transfection using P3C1 and P4C0 NPs**. (A)** The inhibition of cancer cell growth; **(B)** The growth inhibition comparison of P4C0-PLK1 siRNA and P3C1-PLK1 siRNA transfection for 48 h.

In comparison, the inhibition efficacy of P4C0-PLK1 and P3C1-PLK1 siRNA NPs to B16F10 cells was quite similar (Figure 4.9B). The cell viability using P4C0-PLK1 siRNA NPs was also similar to that in our previous report [22]. The IC_{50} values of P4C0-PLK1 and P3C1-PLK1 were 19.8 and 22.0 nM. The similar inhibition efficacy may be attributed to the similar cellular uptake kinetics (Figure 4.5 and 4.6). Although the release profiles of P4C0 and P3C1 slightly differ at pH 6.0 and 5.5, the inhibition ability is not affected as the delivery test lasted for 48 h. Taken together, these two NPs are able to efficiently deliver siRNA to cancer cells and maintain similar gene silencing efficacy for 48 h.

4.4 Discussion

Here we have shown the physicochemical properties of lipid-coated calcium carbonate/phosphate (LCCP) hybrid NPs, and the influence of carbonate incorporation on physiological characters, dsDNA loading/release profile, cellular uptake, and gene silencing. The particle size and zeta potential of P3C1 and P2C2 NPs maintained unchanged (Table 4.1), with very similar gene loading efficacy and loading amount. These similarities might be the reason why P3C1 and P2C2 showed a similar internalisation manner to P4C0 (Figure 4.5 and 4.6). The colloidal stability does not change obviously when the P/C ratio was 4/0, 3/1 and 2/2 (Figure 4.2). However, a large portion of carbonate incorporation (P1C3) resulted in unstable LCCP NP suspension, and the poor colloidal stability could further influence loading and uptake efficiency (Figure 4.3 and 4.5).

It is significant that the dsDNA release profile from LCCP NPs is controlled by the P/C ratio. As reported previously [22, 25], the drug/gene release from calcium carbonate (CaC) and LCP (i.e. P4C0) NPs is mainly controlled by the dissolution of cores, and seldom influenced by the lipid coating outside [23]. The dissolution of cores are through the following dissolution reactions:

$$CaCO_3 + H^+ \rightarrow Ca^{2+} + HCO_3^- \quad (1)$$

$$CaHPO_4 + H^+ \rightarrow Ca^{2+} + H_2PO_4^- \quad (2)$$

These reactions result in the exposure of loaded dsDNA/siRNA and the subsequent release, and simultaneously increase the ion concentrations (i.e. Ca^{2+}, HCO_3^- and H_2PO^{4-}/HPO_4^{2-}) in endosome/lysosome. The increased ion concentration leads to the influx of water into the endosome/lysosome due to the reverse osmotic pressure, which thus swell and rupture

endosome/lysosome, and release NPs and dissociated dsDNA/siRNA into cytoplasm, as schematically presented in Figure 4.10B.

These reactions are also pH dependent. Reaction (1) for CaC NPs starts at pH 7.0 and probably completes at pH 6.0 [25], while Reaction (2) for P4C0 NPs starts at 6.0 and finishes at 5.0 (Figure 4.4 and S4.5), as simulated in Figure 4.10A. Therefore, CaC NPs may release the gene during the circulation and before cellular uptake (i.e. not so stable at pH 7.0), reducing the delivery efficacy. In contrast, P4C0 NPs may undergo the late endosome/lysosome escape, biodegrading some released gene molecules and reducing the delivery efficacy.

Very fortunately, P3C1 and P2C2 NPs start the gene release at >6.0 and release most genes at pH 5.5 within 10 min, which exactly leads to the endosomal escape for efficient cellular delivery (Figure 4.10A), avoiding the gene release during the circulation and the gene biodegradation during the late endosome/lysosome escape. The faster release from P3C1 NPs is confirmed by the real time PCR (Figure 4.8), i.e. more mRNA inhibition was achieved using P3C1 NPs. Nonetheless, the inhibition efficacy of both PD-L1 and PLK1 expression using P4C0 and P3C1 NPs to deliver siRNAs do not show significant difference after 48 h, which may be relevant to other factors, such as the dose and the incubation time.

Moreover, we postulate that LCCP NPs may undergo quicker endosomal/lysosomal escape than other materials that engaged in gene delivery, such as cationic polymers and Au NPs. As known, this escape process is explained by the proton sponge theory [41]. This theory implies the positively charged materials, such as poly ethylene imine (PEI) and gold NPs, would consume protons that are pumped into the endo-/lysosomes while they do not affect the compensated anion (like Cl^-) influx [41-43]. This escape is achieved by evolving osmotic imbalance, causing water entrance then endo-/lysosomal swelling. Note these materials maintain their integrity during the whole process, even without gene release in some cases [43]. In contrast, the proton consumption of LCCP NPs results in the dissolve of their cores and the generation of extra irons (Ca^{2+}, HCO_3^-, and $H_2PO_4^-$). Considering the anion influx would not be affected, more irons are trapped in endo-lysosomes, leading to higher osmotic pressure and quicker endo-/lysosomal swelling. Additionally, the loaded genes are partly released for gene silencing when the endo-lysosome is ruptured. To conclude, the LCCP NPs are suitable for gene delivery, and worthy to be applied for further studies.

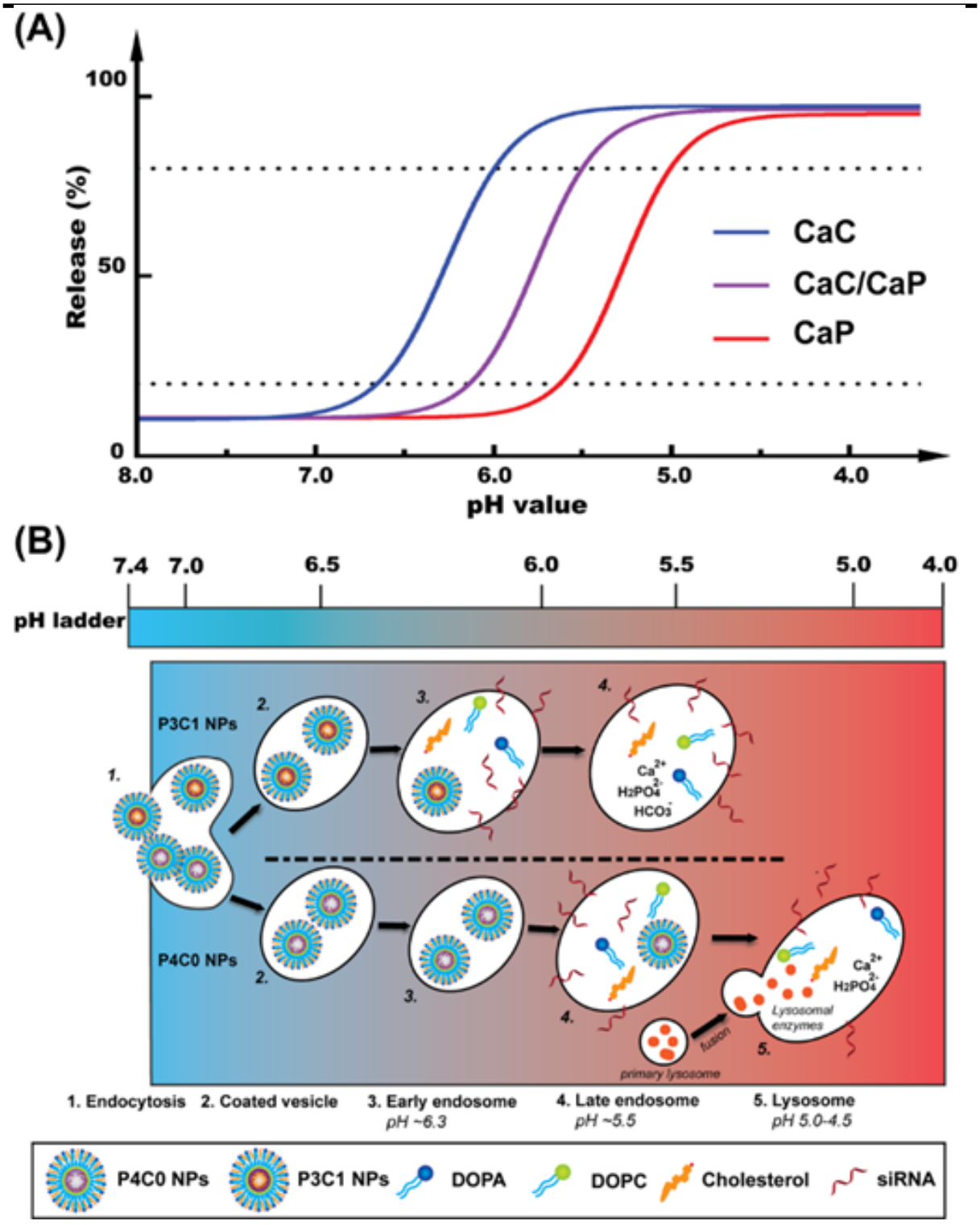

Figure 4.10 (A) The schematic pH responsive release of CaC and/or CaP cores. The hybrid CaC/CaP cores show unique release profile within pH 6.0-5.5, and the release percentage of CaC/CaP is more than that of CaP**. (B)** The fate of P4C0 and P3C1 NPs after internalisation. The clathrin-mediated endocytosis undergoes the endosome/ lysosome digestion pathway. The pH value dropped from 7.4 in Step 1 to 5.0-4.0 in Step 5 (lysosome). Sorted by dissolution pH value, the release of P4C0 and P3C1 NPs might be mainly in Step 3-4 and Step 4-5, respectively.

siRNA released in Step 5 might be partially degraded because of lysosomal enzymes. Intracellular pH ranges were referred to Ref[31] [30]and[16].

4.5 Conclusion

In conclusion, we developed LCCP NPs for precisely controlled release at the endosomal pH. LCCP NPs were prepared by partially substituting phosphate with carbonate. The obtained LCCP NPs were comparable with LCP NPs in colloidal stability, gene loading capacity, and cellular uptake efficacy. Moreover, LCCP NPs have higher sensitivity and quicker release under mild acidic pH conditions (6.0-5.5) than LCP NPs. This tendency endows faster siRNA release during the endocytosis and quicker gene down-regulation after NP endocytosis. However, the release profile divergence between LCCP and LCP did not affect their long term gene silencing efficacy. Considering the good colloidal stability, high gene loading capacity, and quick uptake ability, LCCP NPs hold the potential as a promising gene delivery vehicle candidate with the precise release property at the endosome pH.

4.6 References

[1] L.D. Kong, Y.L. Wu, C.S. Alves, X.Y. Shi, Efficient delivery of therapeutic siRNA into glioblastoma cells using multifunctional dendrimer-entrapped gold nanoparticles, Nanomedicine 11(23) (2016) 3103-3115.
[2] R.W. Carthew, E.J. Sontheimer, Origins and mechanisms of miRNAs and siRNAs, Cell 136(4) (2009) 642-655.
[3] M. Saad, O.B. Garbuzenko, T. Minko, Co-delivery of siRNA and an anticancer drug for treatment of multidrug-resistant cancer, Nanomedicine 3(6) (2008) 761-776.
[4] X.-B. Xiong, A. Lavasanifar, Traceable multifunctional micellar nanocarriers for cancer-targeted co-delivery of MDR-1 siRNA and doxorubicin, ACS Nano 5(6) (2011) 5202-5213.
[5] L. Aagaard, J.J. Rossi, RNAi therapeutics: Principles, prospects and challenges, Adv. Drug Delivery Rev. 59(2-3) (2007) 75-86.
[6] M.E. Davis, J.E. Zuckerman, C.H.J. Choi, D. Seligson, A. Tolcher, C.A. Alabi, Y. Yen, J.D. Heidel, A. Ribas, Evidence of RNAi in humans from systemically administered siRNA via targeted nanoparticles, Nature 464(7291) (2010) 1067-1140.
[7] Y. Li, R. Liu, J. Yang, G. Ma, Z. Zhang, X. Zhang, Dual sensitive and temporally controlled camptothecin prodrug liposomes codelivery of siRNA for high efficiency tumor therapy, Biomaterials 35(36) (2014) 9731-9745.
[8] L. Li, W. Gu, J. Chen, W. Chen, Z.P. Xu, Co-delivery of siRNAs and anti-cancer drugs using layered double hydroxide nanoparticles, Biomaterials 35(10) (2014) 3331-3339.

[9] D. Zhao, R.-X. Zhuo, S.-X. Cheng, Modification of calcium carbonate based gene and drug delivery systems by a cell-penetrating peptide, Mol. BioSyst. 8(12) (2012) 3288-3294.
[10] Z. Xu, Y. Wang, L. Zhang, L. Huang, Nanoparticle-delivered transforming growth factor-beta siRNA enhances vaccination against advanced melanoma by modifying tumor microenvironment, ACS Nano 8(4) (2014) 3636-3645.
[11] Z. Gu, H. Zuo, L. Li, A. Wu, Z.P. Xu, Pre-coating layered double hydroxide nanoparticles with albumin to improve colloidal stability and cellular uptake, J. Mater. Chem. B 3(16) (2015) 3331-3339.
[12] D. Kim, E.S. Lee, K.T. Oh, Z.G. Gao, Y.H. Bae, Doxorubicin-loaded polymeric micelle overcomes multidrug resistance of cancer by double-targeting folate receptor and early endosomal pH, Small 4(11) (2008) 2043-2050.
[13] E.S. Lee, K. Na, Y.H. Bae, Polymeric micelle for tumor pH and folate-mediated targeting, J. Controlled Release 91(1–2) (2003) 103-113.
[14] R. Duncan, Polymer conjugates for tumour targeting and intracytoplasmic delivery. The EPR effect as a common gateway?, Pharm. Sci Technol Today 2(11) (1999) 441-449.
[15] M. Dominska, D.M. Dykxhoorn, Breaking down the barriers: siRNA delivery and endosome escape, J Cell Sci 123(8) (2010) 1183-1189.
[16] E.J. Blott, G.M. Griffiths, Secretory lysosomes, Nat. Rev. Mol. Cell Biol. 3(2) (2002) 122-131.
[17] Z.-Y. Qiao, C.-Y. Hou, W.-J. Zhao, D. Zhang, P.-P. Yang, L. Wang, H. Wang, Synthesis of self-reporting polymeric nanoparticles for in situ monitoring of endocytic microenvironmental pH, Chem. Commun. 51(63) (2015) 12609-12612.
[18] K.C. Kondapalli, J.P. Llongueras, V. Capilla-González, H. Prasad, A. Hack, C. Smith, H. Guerrero-Cázares, A. Quiñones-Hinojosa, R. Rao, A leak pathway for luminal protons in endosomes drives oncogenic signalling in glioblastoma, Nat. Commun. 6 (2015).
[19] V. Sokolova, T. Knuschke, A. Kovtun, J. Buer, M. Epple, A.M. Westendorf, The use of calcium phosphate nanoparticles encapsulating Toll-like receptor ligands and the antigen hemagglutinin to induce dendritic cell maturation and T cell activation, Biomaterials 31(21) (2010) 5627-5633.
[20] F. Pittella, M. Zhang, Y. Lee, H.J. Kim, T. Tockary, K. Osada, T. Ishii, K. Miyata, N. Nishiyama, K. Kataoka, Enhanced endosomal escape of siRNA-incorporating hybrid nanoparticles from calcium phosphate and PEG-block charge-conversional polymer for efficient gene knockdown with negligible cytotoxicity, Biomaterials 32(11) (2011) 3106-3114.
[21] Y. Zhang, N.M.J. Schwerbrock, A.B. Rogers, W.Y. Kim, L. Huang, Codelivery of VEGF siRNA and gemcitabine monophosphate in a single nanoparticle formulation for effective treatment of NSCLC, Mol. Ther. 21(8) (2013) 1559-1569.
[22] J. Tang, L. Li, C.B. Howard, S.M. Mahler, L. Huang, Z.P. Xu, Preparation of optimized lipid-coated calcium phosphate nanoparticles for enhanced in vitro gene delivery to breast cancer cells, J. Mater. Chem. B 3(33) (2015) 6805-6812.
[23] J. Li, Y.-C. Chen, Y.-C. Tseng, S. Mozumdar, L. Huang, Biodegradable calcium phosphate nanoparticle with lipid coating for systemic siRNA delivery, J. Controlled Release 142(3) (2010) 416-421.
[24] J. Lee, H.-S. Min, D.G. You, K. Kim, I.C. Kwon, T. Rhim, K.Y. Lee, Theranostic gas-generating nanoparticles for targeted ultrasound imaging and treatment of neuroblastoma, J Controlled Release 223 (2016) 197-206.

[25] K.H. Min, H.S. Min, H.J. Lee, D.J. Park, J.Y. Yhee, K. Kim, I.C. Kwon, S.Y. Jeong, O.F. Silvestre, X. Chen, pH-controlled gas-generating mineralized nanoparticles: a theranostic agent for ultrasound imaging and therapy of cancers, ACS nano 9(1) (2015) 134-145.
[26] W.H. Lee, J.G. Lee, P.J. Reucroft, XPS study of carbon fiber surfaces treated by thermal oxidation in a gas mixture of O2/(O2+N2), Appl. Surf. Sci. 171(1–2) (2001) 136-142.
[27] G. Weissmann, T. Collins, A. Evers, P. Dunham, Membrane perturbation: studies employing a calcium-sensitive dye, arsenazo III, in liposomes, Proc. Natl. Acad. Sci. U.S.A. 73(2) (1976) 510-514.
[28] Z. He, C.W. Honeycutt, A modified molybdenum blue method for orthophosphate determination suitable for investigating enzymatic hydrolysis of organic phosphates, Commun. Soil Sci. Plant Anal. 36(9-10) (2005) 1373-1383.
[29] S. Zaruba, A.B. Vishnikin, V. Andruch, Application of solidification of floating organic drop microextraction for inorganic anions: Determination of phosphate in water samples, Microchem. J. 122 (2015) 10-15.
[30] T. Suma, K. Miyata, T. Ishii, S. Uchida, H. Uchida, K. Itaka, N. Nishiyama, K. Kataoka, Enhanced stability and gene silencing ability of siRNA-loaded polyion complexes formulated from polyaspartamide derivatives with a repetitive array of amino groups in the side chain, Biomaterials 33(9) (2012) 2770-2779.
[31] D.G. Russell, Mycobacterium tuberculosis: here today, and here tomorrow, Nat. Rev. Mol. Cell Biol. 2(8) (2001) 569-586.
[32] L. Xu, F. Pan, G. Yu, L. Yang, E. Zhang, K. Yang, In vitro and in vivo evaluation of the surface bioactivity of a calcium phosphate coated magnesium alloy, Biomaterials 30(8) (2009) 1512-1523.
[33] M. Ni, B.D. Ratner, Differentiating calcium carbonate polymorphs by surface analysis techniques—an XPS and TOF‐SIMS study, Surf. Interface Anal. 40(10) (2008) 1356-1361.
[34] J. Liu, X. Ye, H. Wang, M. Zhu, B. Wang, H. Yan, The influence of pH and temperature on the morphology of hydroxyapatite synthesized by hydrothermal method, Ceram. Int. 29(6) (2003) 629-633.
[35] S. Kannan, A. Lemos, J. Ferreira, Synthesis and mechanical performance of biological-like hydroxyapatites, Chem. Mater. 18(8) (2006) 2181-2186.
[36] H. Shi, L. Li, Z.-M. Su, Designed preparation of polyacrylic acid/calcium carbonate nanoparticles with high doxorubicin payload for liver cancer chemo-therapy, Cryst. Eng. Comm. 17(26) (2015) 4768-4773.
[37] S.L. Goss, K.A. Lemons, J.E. Kerstetter, R.H. Bogner, Determination of calcium salt solubility with changes in pH and PCO2, simulating varying gastrointestinal environments, J. Pharm. Pharmacol. 59(11) (2007) 1485-1492.
[38] K. Nasri, H. El Feki, P. Sharrock, M. Fiallo, A. Nzihou, Spray-dried monocalcium phosphate monohydrate for soluble phosphate fertilizer, Ind. Eng. Chem. Res. 54(33) (2015) 8043-8047.
[39] W.Y. Chen, B. Zhang, T. Mahony, W.Y. Gu, B. Rolfe, Z.P. Xu, Efficient and durable vaccine against intimin beta of diarrheagenic E-Coli induced by clay nanoparticles, Small 12(12) (2016) 1627-1639.
[40] Y. Wang, J. Li, Y. Chen, D. Oupický, Balancing polymer hydrophobicity for ligand presentation and siRNA delivery in dual function CXCR4 inhibiting polyplexes, Biomater Sci 3(7) (2015) 1114-1123.
[41] O. Boussif, F. Lezoualc'h, M.A. Zanta, M.D. Mergny, D. Scherman, B. Demeneix, J.P. Behr, A versatile vector for gene and oligonucleotide transfer into cells in

culture and in vivo: Polyethylenimine, Proc. Natl. Acad. Sci. U.S.A. 92(16) (1995) 7297-7301.

[42] Lee D U, Park J Y, Kwon S, et al. Apoptotic lysosomal proton sponge effect in tumor tissue by cationic gold nanorods. Nanoscale, 11(42) (2019) 19980-19993.

[43] Bus T, Traeger A, Schubert U S. The great escape: how cationic polyplexes overcome the endosomal barrier. Journal of Materials Chemistry B, 6(43) (2018) 6904-6918.

4.7 Supplementary Information

Table S4.1 Information of oligonucleotides

Name	Supplier	Sequence
dsDNA-cy5 (sense)	IDTDNA	TTCTCCGAACGTGTCACGTTT-cyanine 5
dsDNA-cy5 (antisense)	IDTDNA	AAACGTGACACGTTCGGAGAA
PD-L1 (sense)	Sigma	AGACGUAAGCAGUGUUGAA
PD-L1 (antisense)	Sigma	UUCAACACUGCUUACGUCU
Negative control (sense)	Sigma	CUUACGCUGAGUACUUCGA
Negative control (antisense)	Sigma	UCGAAGUACUCAGCGUAAG
PD-L1 primer (Forward)	Sigma	CCCTCTGATCGTCGATTGGC
PD-L1 primer (Forward)	Sigma	GCTTAGCAGTGTCTCCCTGG
Plk1 (sense)	IDTDNA	CCAUUAACGAGCUGCUUAA
Plk1 (antisense)	IDTDNA	CCAUUAACGAGCUGCUUAA
Scramble-Plk1 (sense)	IDTDNA	UUCUCCGAACGUGUCACGU
Scramble-Plk1 (antisense)	IDTDNA	ACGUGACACGUUCGGAGAA

Table S4.2 The component element analysis of LCCP cores with different P/C ratios.

Molar ratio (P:C)	Ca (mmol/g)	P (mmol/g)	C (mmol/g)	C/P molar ratios (calculated/theoretical)	Possible formula*
4:0	9.38	6.84	0.69	0.26/0.00	$Ca[(HPO_4)_{0.8}(CO_3)_{0.1}(OH)_{0.2}]$
3:1	9.55	5.80	1.73	0.46/0.33	$Ca[(HPO_4)_{0.7}(CO_3)_{0.2}(OH)_{0.2}]$
2:2	9.46	3.72	4.16	1.26/1.00	$Ca[(HPO_4)_{0.4}(CO_3)_{0.5}(OH)_{0.2}]$
1:3	9.44	2.09	7.15	3.44/3.00	$Ca[(HPO_4)_{0.2}(CO_3)_{0.7}(OH)_{0.2}]$

* Assuming the existence patterns of phosphorous and carbo are HPO_4^{2-} and CO_3^{2-}, respectively.

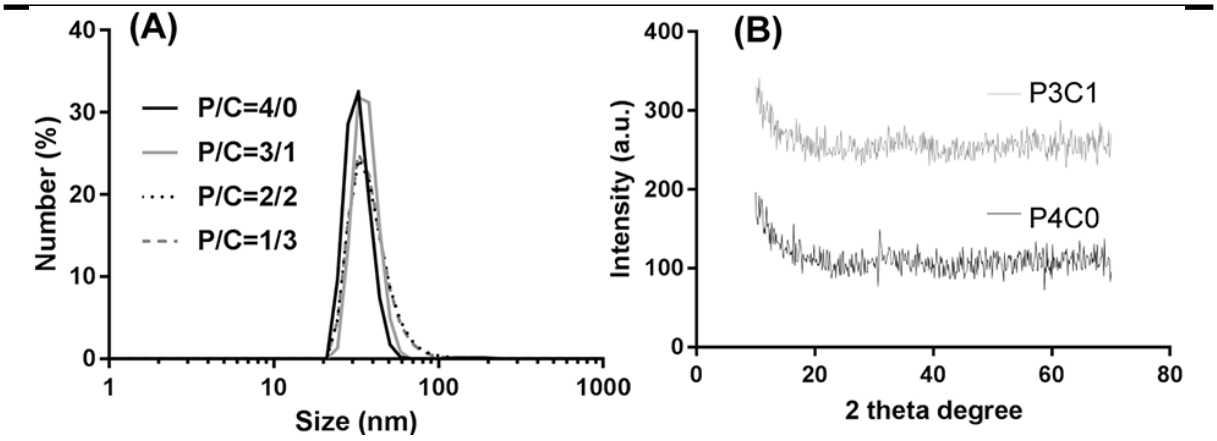

Figure S 4.1 (A) The hydrodynamic diameter of LCCP NPs, represented by Number (%); and **(B)** XRD pattern of P4C0 and P3C1 cores.

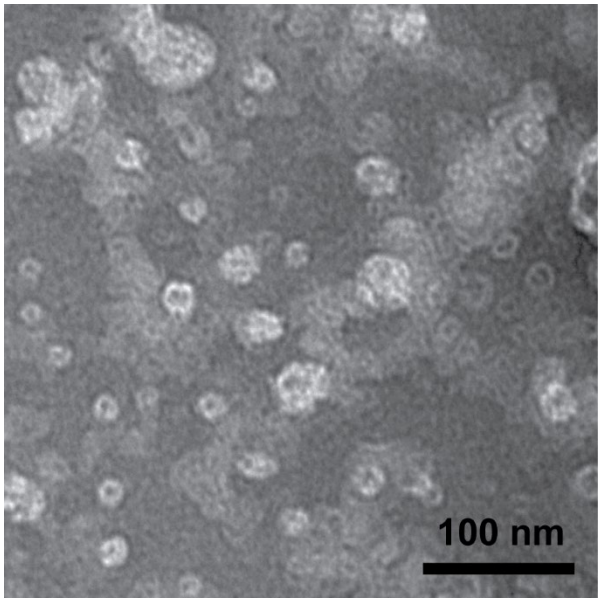

Figure S4.2 TEM image of P3C1 NPs negative staining with 1% uranyl acetate.

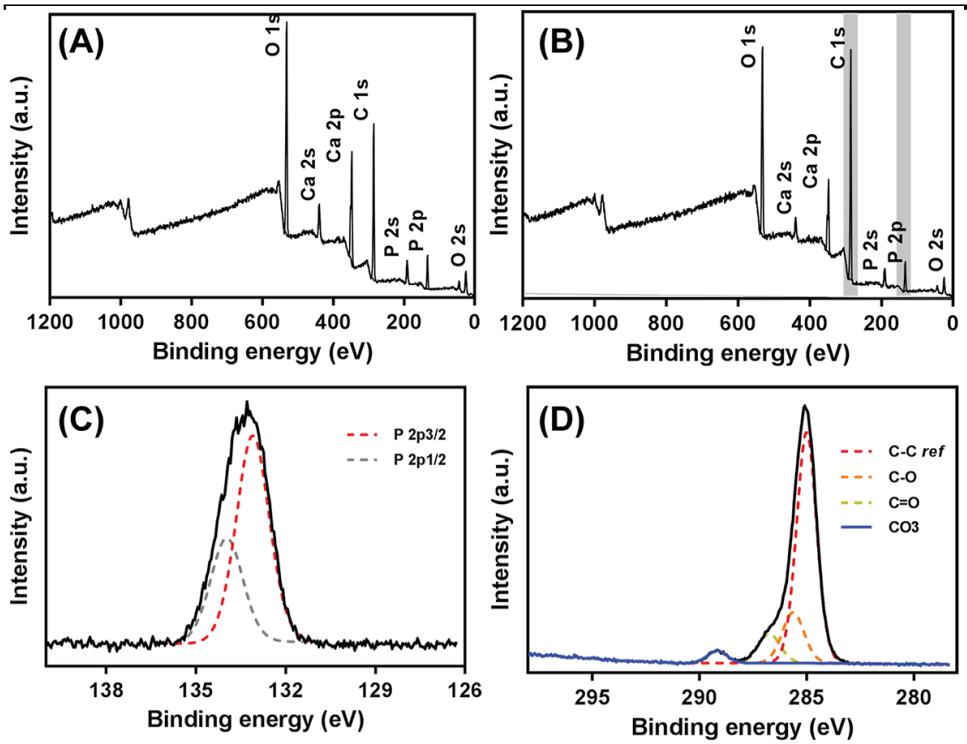

Figure S4.3 XPS survey scan of **(A)** P4C0 and **(B)** P3C1 cores coated with DOPA. The details of P3C1 were shown in high resolution scan of **(C)** P2p and **(D)** C1s.

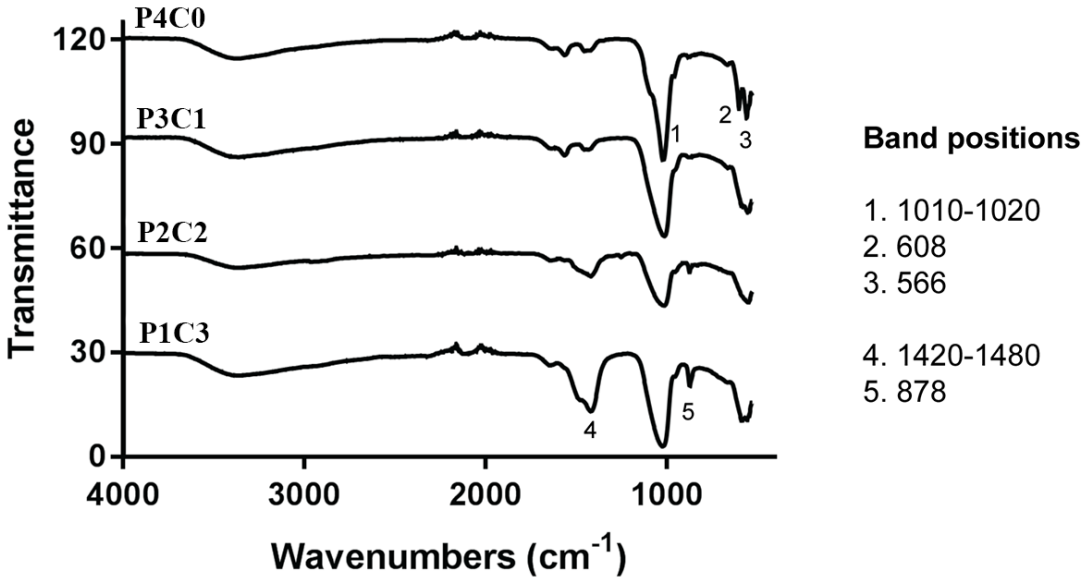

Figure S4.4 FTIR spectrum for the LCCP cores.

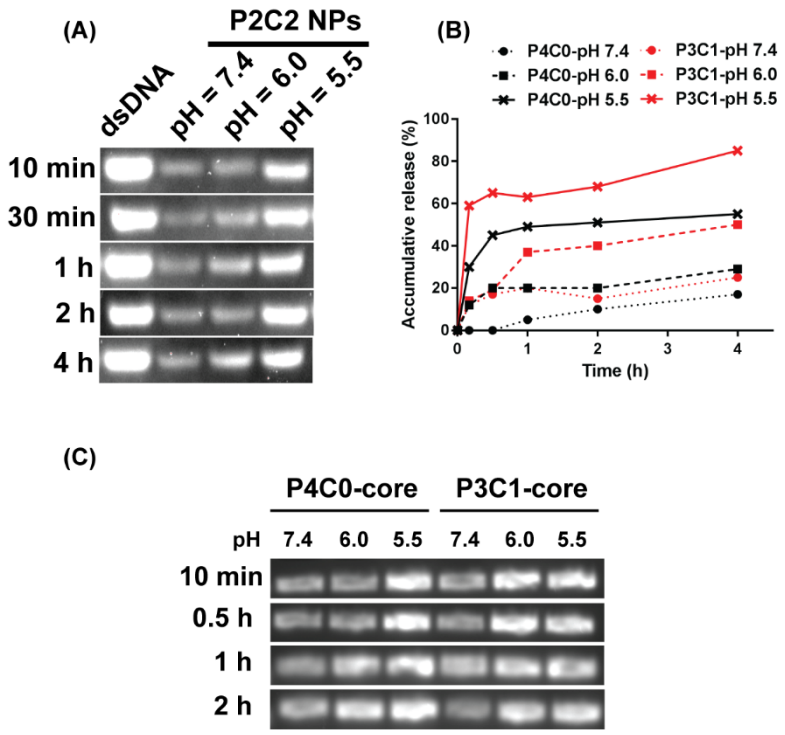

Figure S4.5 (A) P2C2 release profile; **(B)** DNA band intensity in Figure 4 normalized by the first lane dsDNA in corresponding line; **(C)** The release trend of P4C0 and P3C1 cores under different pH values.

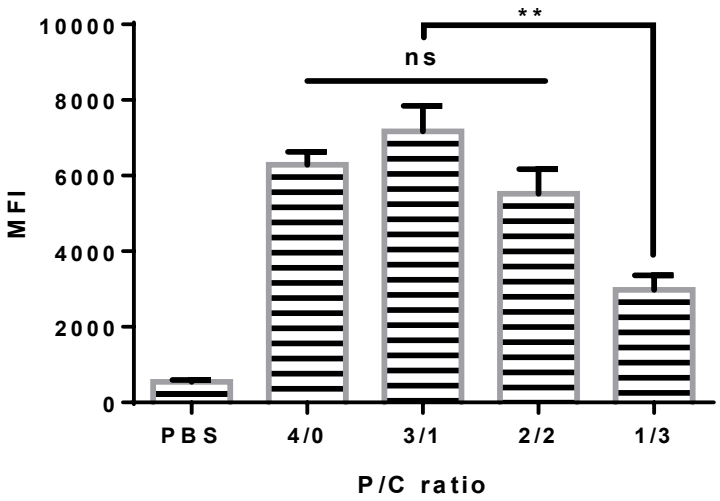

Figure S4.6 The effect of P/C ratios on the taken up of particles with 25 nM dsDNA-cy5, represented by MFI.

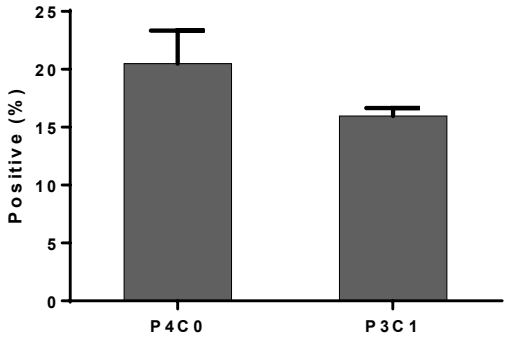

Figure S4.7 The positive cell percentage of B10F10 treated with P4C0 or P3C1 with dsDNA-cy5 at 25 nM cy5 concentration. Cells were cultured in DMEM containing 10% FBS for 4 h with P4C0 or P3C1 NPs.

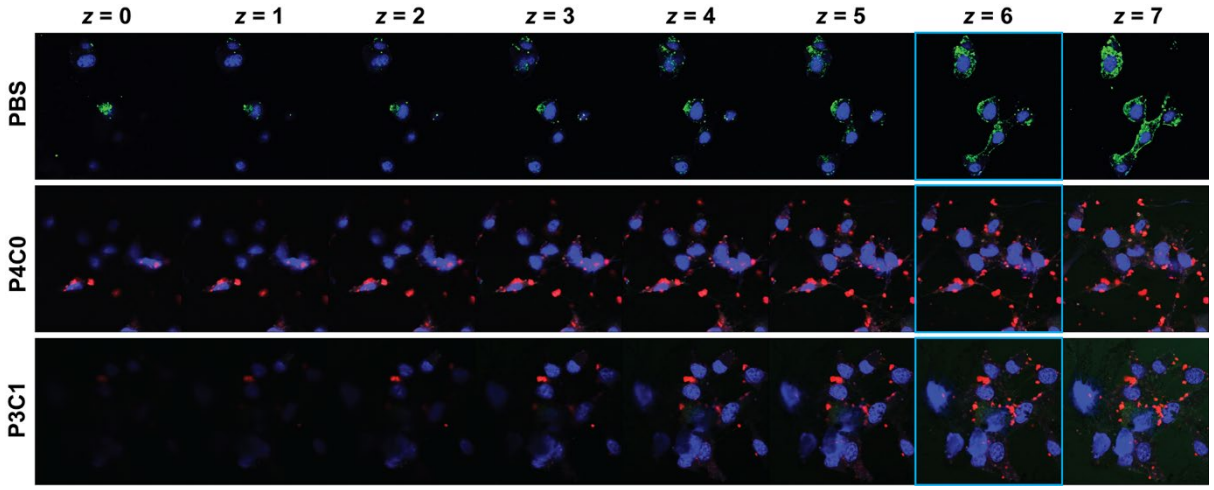

Figure S4.8 CLSM images of the same region of cells at different z stacks. The z = 6 and 7 planes were focused on the central of most cells in the selected area. The individual channels and three-view diagrams based on the images at z = 6 position of each series (blue framed) was chosen as examples and shown in Figure 4.7.

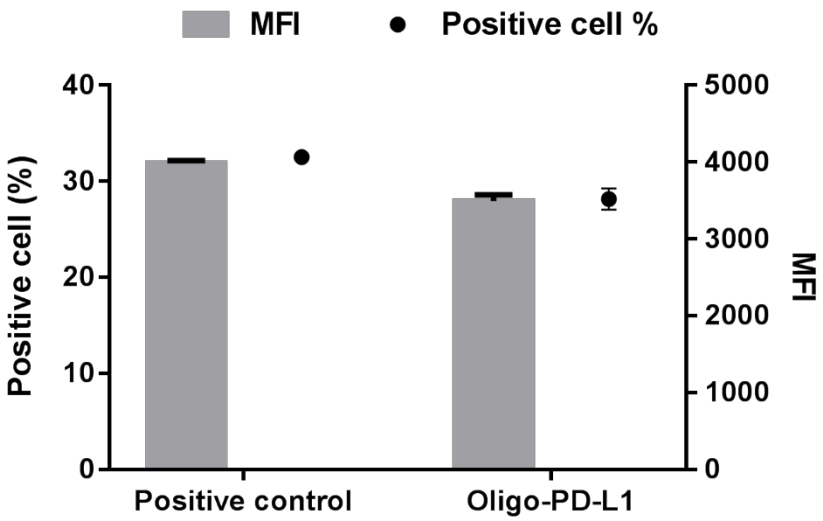

Figure S4.9 The down regulation of PD-L1 expression for B16F10 cells treated with Oligo-PDL1 (40 nM)

Chapter 5

Enhanced Combination Cancer Therapy using Lipid-Calcium Carbonate/Phosphate NPs as a Targeted Delivery Platform

This chapter reports the modification of LCCP NPs as targeting NPs, and co-delivery cell death (CD) siRNA and α-tocopheryl succinate (α-TOS) drug for combination cancer therapy in vitro and in vivo. In this chapter, we designed and synthesised LCCP NPs modified with polyethylene glycol (PEG) and folic acid (FA). After modification, the LCCP NPs exhibited an FA-enhanced cellular uptake in cancer cells with FA receptor overexpression. The modified LCCP NPs provided high payload to CD siRNA and α-TOS drug. The in vitro study in B16F0 melanoma cells indicated the synthesised NPs (CD/TOS/FA) enhanced the inhibition to cancer growth with a moderate synergy. The mechanism of the high combined inhibition to B16F0 cell growth may be associated with the effective induction of cell apoptosis and arrest of cell cycle at the G1 phase. **This part of in vitro work was in section 5.1, and has been published in Nanomedicine (2018, full paper).**

Moreover, the in vivo anticancer efficacy of CD/TOS/FA NPs was evaluated in a metastatic 4T1 mouse model. With FA mediated efficiency delivery of the combined two therapeutics, CD/TOS/FA NPs significantly inhibited 4T1 tumour growth in situ, and prevented its metastasis to lung and liver remarkably. No significant toxicity to major organs was observed during the therapy. In conclusion, the well-designed CD/TOS/FA NPs held great potential as an efficiency anticancer agent delivery platform, and may be further used to deliver therapeutics for combination cancer therapy.

5.1 In vitro work

In this section, a new FA receptor-targeted LCCP NP was devised and loaded with the CD siRNA and α-TOS in the core and outer lipid layer, respectively. Herein, the new NPs had a high gene/drug payload and an FA-enhanced cellular uptake, exhibiting a high inhibition to cancer cell growth due to combination therapy of CD siRNA and α-TOS with a moderate synergy. This high combination inhibition to cancer cell growth may be associated with the effective apoptosis induction and cell cycle arrest at the sub G1 phase. The *in vitro* work section thus indicates this LCCP-based NP platform is potential as a new vehicle for combined cancer therapy.

5.1.1 Introduction

Melanoma is the most life-threatening type of skin cancer and accounts for the majority of deaths [1]. Clinical therapy for melanoma relies heavily on single chemical drug treatment, such as doxorubicin [2], cisplatin [3], and 5-fluorouracil [4] often with unsatisfactory outcomes. The main issue with chemotherapy is the side effects caused by high toxicity of the chemical drugs. To date, the most commonly used strategy is combination therapy, aiming to improve therapeutic efficacy with minimized doses of drugs and reduced side effects. This includes the combination of two drugs or one drug with an oligonucleotide or a signalling pathway inhibitor or an antibody. The combination therapy may benefit from the additive or even synergistic effect if two therapeutics have interactive effects and cooperatively suppress cancer cell growth [5].

α-tocopheryl succinate (α-TOS) is the most effective derivative of vitamin E and exerts a therapeutic effect on a broad spectrum of cancers including melanoma [6]. The main obstacles preventing α-TOS from wider medical applications are poor hydrophilicity and the high dosages required. However, the combination of α-TOS with other drugs is able to achieve effective therapeutic outcomes [7-9]. Most of these studies focused on the co-delivery of two chemical drugs, while the combination of α-TOS with small interfering RNAs (siRNAs) has not been reported. We have expected that combination therapy with siRNAs might achieve a similar anti-cancer efficacy with less side effects as siRNA is more effective and much more biocompatible than chemical drugs. However an efficient delivery system for α-TOS/siRNA co-delivery is required for potential combination therapy of melanoma.

Calcium phosphate and calcium carbonate-based nanoparticles (NPs) have been proven to be promising gene delivery systems [10-12]. Maitra et al demonstrated that calcium phosphate nanoparticles were able to load pDNA and increase the transfection efficacy in HeLa cells [13]. Huang et al optimised calcium phosphate nanoparticles with bilayer lipid coating for better colloidal stability, biocompatibility, and further modification [11]. Inspired by these outcomes, lipid-coated calcium carbonate/phosphate (LCCP) NPs were designed, with precise endosomal release characteristics, and efficient siRNA loading and release [14]. In this study, we demonstrated that LCCP NPs can be internalized by B16F10 cells with a moderate uptake efficiency due to the negative surface charge [14]. To increase the delivery efficacy and melanoma targeting capability for in vivo use, a targeting molecule is essential. Many targeting ligands have been studied, including folic acid, mannose, and hyaluronic acid [15-17], whose receptors are normally overexpressed on the surface of some cancer cells. Folic acid (FA) is the most widely used one as the FA receptor is overexpressed in melanoma cells [16, 18, 19]. Apart from the siRNA loading and FA modification to enhance the delivery efficacy, we have uniquely co-loaded the hydrophobic α-TOS in the hydrophobic region of lipid bilayer for combination therapy to further improve the therapy, which is schematically illustrated in Scheme 5.1.

Thus using LCCP nanoparticles to co-deliver hydrophobic α-TOS and hydrophilic CD siRNA with FA molecule on the surface as the targeting ligand is a new concept. In this work, FA receptor-targeted LCCP NPs were first prepared and loaded with certain amounts of α-TOS and Allstars Cell Death siRNA (CD siRNA). Then the new CD/TOS/FA NPs were utilized to treat B16 melanoma cells and we found an enhanced anticancer effect with the new delivery system. CD siRNA and α-TOS inhibited melanoma cell growth by increasing ROS level, cell apoptosis, and disturbing the cell cycle. To our knowledge, this is the first attempt to co-deliver a hydrophobic (α-TOS) and a hydrophilic (siRNA) therapeutic using one NP (LCCP) for combination cancer treatment.

5.1.2 Experimental methods

5.1.2.1 Materials

All the chemicals and oligonucleotide duplexes were purchased from Sigma-Aldrich if not specifically mentioned. CD siRNA (AllStars Cell Death siRNA) was purchased from QIAGEN

Pty. Ltd. (Vic, Australia). All lipids were obtained from Avanti Polar Lipid. The kits and reagents for RT-PCR were purchased from Life Technologies Co. (Carlsbad, CA). Bcl-2 and beta-actin antibodies were purchased from BioLegend Inc. (San Diego, CA). The predesigned forward/reverse mouse-Bcl-2 primers were bought from Sigma-Aldrich. All chemicals and biomaterials were received and used according to the manufacturer's guidelines, without further modification. Water used for all experiments was deionized Milli-Q water (Ω = 18.2 at ambient temperature). All siRNAs sequences are shown in Table S5.1.

5.1.2.2 Synthesis and optimisation of targeted nanoparticles with dual drug loading

The synthesis of LCCP NPs was based on the reported protocol with some modifications [10, 14]. Briefly, 150 μL of 25 mM Na_2HPO_4/$NaHCO_3$ (3/1 molar ratio, pH = 9.0, aq.) was dispersed in 5 mL oil phase (cyclohexane/igepal CO 520 = 7/3, v/v) and then added dropwise into 150 μL of 2.5 M $CaCl_2$ (pH = 7.0, aq.) dispersed in 5 mL oil phase (cyclohexane/igepal CO 520 = 7/3, v/v), followed by adding 1 μmol DOPA under magnetic stirring (Scheme 5.1). After 20 min, the LCCP cores were collected *via* centrifugation after washing with a total of 30 mL of absolute ethanol (3 times). The obtained LCCP core pellet was redispersed in chloroform with 70 μL of DOPC/cholesterol (20 mM, 1/1, v/v) for coating the second layer lipids. After solvent evaporation, the final LCCP NPs were obtained by hydrating the formed film in 1.6 mL of water or PBS.

For dsDNA/siRNA loading, 15 μL of 20 μM dsDNA/siRNA in DNase/RNase free water was mixed with aqueous calcium and phosphate/carbonate solutions, respectively, prior to dispersion in the oil phase. The dsDNA/siRNA were loaded into LCCP cores during the formation of calcium phosphate.

For α-TOS and/or folic acid (FA) loading, the modification was made by incorporating DSPE-PEG-FA and/or α-TOS into the outer layer of lipids. The portion of α-TOS was 15%, replacing an equal portion of DOPC and/or cholesterol to form α-TOS loaded LCCP NPs (Table S5.2). A total of 14 μL of DOPC (equalled to 20% of DOPC) was replaced by DSPE-PEG/DSPE-PEG-FA to achieve PEGylation and FA mediated targeting. The NPs were named CD/FA, scr/TOS/FA, and CD/TOS/FA for LCCP (with 10 % DSPE-PEG-FA and 10 % DSPE-*m*PEG) loading with CD siRNA, scrambled siRNA/α-TOS, and CD siRNA/α-TOS, respectively. LCCP loaded with CD siRNA and α-TOS with 20 % DSPE-*m*PEG was named CD/TOS. The details of the outer layer composition and DNA/RNA input were shown in Table S5.2.

5.1.2.3 Characterization

The hydrodynamic nanoparticle size distribution and surface charge were measured by a Malvern NanoSizer (Malvern, UK) series using a dynamic light scattering (DLS) method. NPs were diluted in either water or PBS to a concentration of about 40 μg/mL. The morphology of NPs was visualized using a transmission electron microscope (TEM, JEM-3010, ZEOL, Tokyo, Japan). Ten microliters of NP suspension was dropped onto a 300 mesh carbon-coated copper grid and dried on a filter paper at room temperature. Then the grid was negatively stained with 1% uranyl acetate for 1 min, and observed in the TEM. The core diameter of NPs was estimated using Nano Measure software, and the mean size was calculated by counting 200 randomly selected NPs. The composition of LCCP with/without α-TOS was examined using Fourier transform infrared spectroscopy (FTIR).

5.1.2.4 Loading efficiency

To determine the loading efficiency of siRNA, a mimic oligo dsDNA labelled with cyanine 5 (cy5) was used as a model and encapsulated into the nanoparticles in the same way. The loading efficiency of dsDNA-cy5 was determined by measuring the cy5 fluorescence intensity (Ex = 488 nm, and Em = 665 nm) of the nanoparticle lysate after nanoparticles were completely dissolved in Tris buffer containing 2 mM EDTA and 0.05% Triton X-100 at pH 7.8 using a plate reader (BioTek, Winooski, VT, USA). Similarly, the yield of FA was also determined by measuring the dissolved NPs using the plate reader (Ex = 270 nm, and Em = 450 nm).

The NPs with α-TOS were centrifuged at 12000 g for 10 min to collect NP pellets and discard supernatant that may contain free α-TOS. The NPs were dissolved in citric acid-sodium citric acid buffer at pH = 5, and the α-TOS loading amount in NPs was calculated from the absorbance at λ_{max} = 278 nm using UV-vis spectroscopy. Baseline measurements were done on NPs without α-TOS.

5.1.2.5 Cellular uptake of NPs

B16F0 cells were cultured routinely in DMEM medium containing 10% fetal bovine serum (FBS), 1% penicillin/streptomycin and seeded in a 12 well plate with a density of 1×10^5 cells per well and cultured overnight in an incubator at 37 °C with 5% CO_2. The culture medium was then replaced by 0.5 mL fresh medium containing FA modified NPs encapsulating dsDNA-cy5 (25 nM). After 4 h incubation, the cells were washed 3 times with PBS, followed

by treatment with 0.25% trypsin and centrifugation. The cell pellets were redispersed in 0.2 mL of paraformaldehyde (PFA, 4 %) for fixation and the cy5 fluorescence intensity of the fixed cells was determined using BD Accuri C6 FACS flow cytometer (BD Biosciences, San Jose, CA).

To illustrate the specificity of FA receptor targeting delivery, cellular uptake was examined under an FA blocking condition. LCCP-dsDNA-cy5 NPs with 10% DSPE-PEG-FA and 10% DSPE-*m*PEG were used. Cells were blocked in PBS containing FA (0.1 mM or 1 mM) for 1 h, followed by NP treatment in FA free PBS for another 1 h. The cy5 concentration in this experiment was 25 nM. The control group was cells cultured in FA-free PBS for the initial 1 h, followed by the NP treatment. Cells treated in PBS containing 1 mM FA alone for 2 h were also analyzed to verify the influence of FA blockade on cy5 fluorescence intensity.

Furthermore, B16F0 cells were treated with LCCP NPs modified with 10% DSPE-PEG-FA and 10% DSPE-*m*PEG for cellular uptake assay. The cells were incubated in the medium containing these targeted NPs with 25 nM dsDNA-cy5 for 0.5 to 6 h, or with 3 to 100 nM dsDNA-cy5 for 4 h. Cells treated with LCCP NPs modified with 20% DSPE-*m*PEG containing 25 nM dsDNA-cy5 for 4 h were also tested for comparison. The cellular uptake of these LCCP NPs was determined and experiments were repeated 3 times.

5.1.2.6 MTT assay

B16F0 cells (4×10^3 /well) were seeded in a 96-well plate and incubated overnight. Cells were treated with CD/FA, scr/TOS/FA, CD/TOS, or CD/TOS/FA at a CD siRNA concentration of 3 to 48 nM and an α-TOS concentration of 1.3 to 20 μM. Cells treated with LCCP-FA NPs loaded with scrambled siRNA (scr/TOS/FA) were used as controls. After 48 h culture in medium with nanoparticles, the cell viability was determined using standard MTT assay protocol. As controls, free α-TOS or CD siRNA were supplemented in medium containing CD/FA, scr/TOS/FA or LCCP-FA for cell treatment. The cell viability was determined similarly after 48 h treatment.

5.1.2.7 Reactive oxygen species (ROS) detection

B16F0 cells were seeded in a 12 well plate at a density of 1×10^5 cells per well, and cultured overnight to bring to confluence, followed by treatment with FA-loaded LCCP NPs containing 24 nM CD siRNA and/or 10 μM α-TOS at 37 °C for 6 h. Then the cells were co-cultured with

20 μM 2`,7`-dichlorodihydrofluorescein diacetate (DCFH-DA, Sigma Aldrich, MO, USA) for another 30 min. After washing 3 times with PBS, the amount of ROS was immediately analyzed using either flow cytometry (Accuri C6 flow cytometer, BD Biosciences) or confocal laser scan microscopy (CLSM).

5.1.2.8 Reverse transcription PCR (RT-PCR)

B16F0 cells were seeded in a 6-well plate (4×10^5 cells/well) and incubated overnight. Cells were then treated with FA-loaded NPs containing 24 nM CD siRNA and/or 10 μM α-TOS for 24 h, and then harvested in 1 mL Trizol. Total RNA was extracted and reverse transcription was conducted according to the manufacturer's protocol. Real time RT-PCR was carried out as described previously [20]. Mouse beta-actin gene was assayed in the same way as a housekeeping gene to normalize the expression of Bcl-2.

5.1.2.9 Western Blot analysis

B16F0 cells were seeded in a 6-well plate at 4×10^5 cells/well and treated with FA-loaded NPs for 48 h (CD siRNA = 24 nM and/or α-TOS = 10 μM). The cells were then lysed in 120 μL chilled RIPA buffer, followed by 10 s sonication for complete lysis. After centrifugation at 12,000 g for 5 min, the supernatant was collected, and the protein concentration was measured using a Nanodrop 1000 (ThermoFisher). Samples were heated for 5 min at 95 ºC with loading buffer and proteins were separated by a 4-15% gradient SDS-polyacrylamide gel electrophoresis (SDS-PAGE) with 100 μg of total protein loaded, followed by transfer onto a polyvinylidene difluoride (PVDF) membrane (wet transfer method). The membrane was then blocked using freshly prepared Tris buffer saline (TBS) containing 5% skim milk overnight at 4 °C. After rinsing 3 times with TBST (TBS with 0.1% Tween 20), the membrane was incubated in the primary antibody solution (1:1000, diluted in TBS containing 3% BSA and stored at 4 °C before use) overnight at 4 °C, followed by TBST rinse and incubation with the HRP conjugated secondary antibody solution (1:5000, diluted in TBS containing 3% BSA and stored at 4 °C before use) for 1 h at 24 °C. All incubations were performed with constant shaking. Then the membrane was rinsed 3 times with TBST, and immersed in 2 mL Clarity ECL blotting substrate (Bio-Rad Laboratories, Inc., Hercules, CA) for 1 min. The blot image was acquired using Geldoc (Bio-Rad Laboratories, Inc., Hercules, CA). Mouse beta-tubulin protein was assayed as the loading control. All the experiments were repeated 3 times, and the band intensity was calculated using Geldoc software.

5.1.2.10 Apoptosis analysis

B16F0 cells were seeded in a 12-well plate at 2×10^5 cells/well and treated with FA-loaded NPs for 24 h (CD siRNA = 48 nM and/or α-TOS = 20 μM). After incubation, the cells were washed twice with cold PBS, followed by collecting cells using 0.25% trypsin and centrifuging at 2,000 rpm for 5 min. Any detached cells in the supernatant were also collected in the same tube by centrifugation. The cell pellets were resuspended in 0.1 mL Annexin V Binding Buffer (from the FITC Annexin V Apoptosis Detection Kit with PI, BioLegend), followed by adding 5 μL of FITC Annexin V and 10 μL of propidium iodide (PI) solution and incubating in the dark for 15 min. Then 400 μL of Annexin V Binding Buffer was added to each tube to stop the staining. The samples were analyzed using a CytoFLEX flow cytometer (Beckman, IN). Untreated cells were stained with FITC Annexin V and/or PI as the control. Cells with single staining were used to adjust the compensation between these two fluorescent channels.

5.1.2.11 Cell cycle analysis

B16F0 cells were seeded in a 12-well plate at 1×10^5 cells/well and cultured for 48 h, followed by cell collection and counting to roughly estimate the period of one life-cycle for B16F0 cells growing at confluence. For analysis, cells were seeded in a 12-well plate with a density of 2×10^5 cells per well and cultured overnight to bring them to confluence. Then cells were treated with FA-loaded NPs for another 24 h (CD siRNA = 48 nM and/or α-TOS = 20 μM). The cells were washed 3 times with PBS and harvested using trypsinization and centrifugation at 2,000 rpm for 5 min. The cells were then fixed by adding dropwise 200 μL of cold 70% ethanol to the pellets while vortexing to minimize clumping. After incubating at 4 °C for 30 min, the cells were spun down at 2,000 rpm for 5 min with caution, and washed twice with PBS. Two hundred microliter of PI (50 mg/L) was added to each sample for staining, followed by analysis using a CytoFLEX flow cytometer. The cell-cycle phase of the gated singlet cells was identified according to their PI fluorescence intensity: sub G1 (100 k-180 k), G1 (180 k – 220 k), S (220 k – 360 k), and G2/M (360 k – 440 k).

5.1.2.12 Statistical analysis

Data is presented as Mean ± SD and analyzed via t-test using GraphPad Prism 7.00 software; a p value < 0.05 was considered statistically significant. *, $p < 0.05$; **, $p < 0.01$; ***, $p < 0.001$. The t-test in the software was used to compare the statistical difference between two groups as it is more accurate. One-way ANOVA analysis method with post hoc Turkey test

was also performed to assess multiple group experimental data, and a p value < 0.05 was considered statistically significant. #, $p < 0.05$; ##, $p < 0.01$; ###, $p < 0.001$.

5.1.3 Results

5.1.3.1 Physicochemical features of LCCP NPs loaded with CD siRNA and α-TOS

α-TOS was loaded onto LCCP NPs (without DSPE-PEG and DSPE-PEG-FA modification) by replacing approximately 15% of outer layer lipids (Table 5.1 and Figure 5.1A). The NPs were named as α/DOPC, α/ChoL, and α/DOPC/ChoL according to the outer layer lipid composition (detailed information listed in Table 5.1 and Table S5.2, ESI). Compared to LCCP NPs without α-TOS (α/BLK), the α-TOS loaded NPs had a similar hydrodynamic diameter (~40 nm). Meanwhile, PDI increased from 0.22 to 0.33-0.35 after α-TOS loading, meaning that loading α-TOS resulted in a broader size distribution.

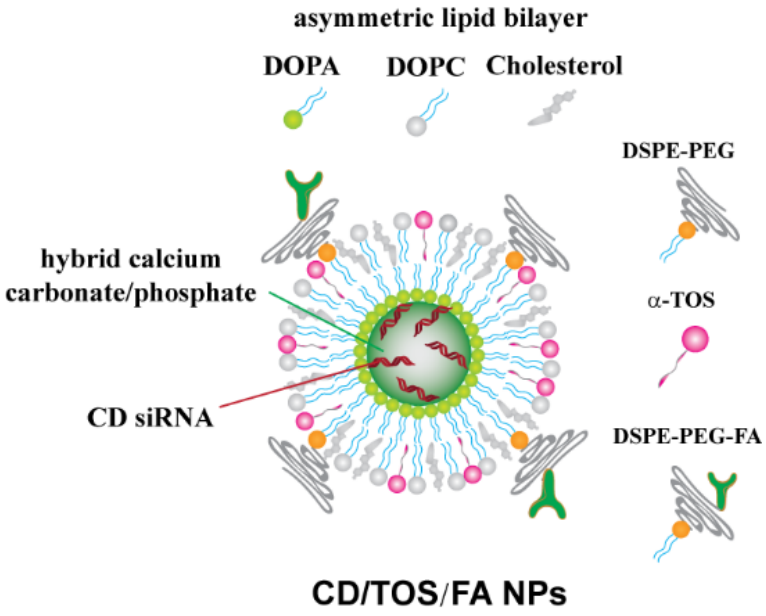

Scheme 5.1 Schematic illustration of the structure of LCCP NPs, loaded with CD siRNA/α-TOS and FA conjugated onto the surface.

The zeta potential of the α/BLK sample was -15.1 mV (Table 5.1). Loading α-TOS decreased the zeta potential to -16.8 for α/ChoL and -18.8 mV for α/DOPC/ChoL, but increased to -12.8 mV for α/DOPC. Previously, we showed that the surface charge of LCP NPs was mainly attributed to negative charged DOPA, but not the neutral DOPC/cholesterol in the outer layer

[10]. Similarly, the change in NP surface charge in this study should be mainly attributed to the loading of negatively charged α-TOS, not the change in DOPC/cholesterol composition. Notably, a slight increase of zeta potential in sample α/DOPC may be related to the lowest α-TOS loading yield.

Table 5.1 The hydrodynamic particle size, zeta potential, PDI, and α-TOS loading yield of LCCP NPs.

Sample code	Outer layer composition (DOPC/ChoL/α-TOS %)	Size (nm)	PDI	Zeta (mV)	TOS yield (%)
α/DOPC/ChoL	42.5/42.5/15	40.8±1.4	0.33±0.02	-18.8±1.3	59.3±5.2
α/DOPC	35/50/15	37.7±1.2	0.35±0.02	-12.8±0.6	23.2±4.3
α/ChoL	50/35/15	40.6±0.6	0.35±0.02	-16.8±0.8	58.7±7.1
α/BLK	50/50/0	39.8±0.2	0.22±0.01	-15.1±0.6	-

The yields of α-TOS loading in α/DOPC, α/ChoL, and α/DOPC/ChoL were 23.2±4.3%, 58.7±7.1%, and 59.3±5.2%, respectively, meaning that there were 8.9%, 3.5% and 8.9% of outer layer lipids being replaced by α-TOS in three samples, respectively. The unusually low yield of α-TOS in α/DOPC sample may be due to (1) the size mismatch of α-TOS with the lipid in the outer layer according to their structure, and (2) the poor outer layer coating caused by the defects in the outer layer under the DOPC insufficient conditions (detailed explanation given in Figure S5.1 and Table S5.3) [21].

As shown in Table S5.4, the loading of CD siRNA in α/DOPC/ChoL NPs resulted in particles with the size of 39.2 nm and the zeta potential of -22.6 mV. The loading of siRNA did not greatly affect the NP size, but resulted in slightly more negative charges with an increased loading efficiency of siRNA/dsDNA (63% vs. 51%), due to the smaller amount of siRNA/dsDNA used in the current synthesis (0.6 *vs.* 3 nmol used in the previous report) [14].

As shown in Figure 5.1B, the LCCP-TOS NPs were sphere-like, with a typical core-shell structure. The core size of NPs with a hollow hole was around 20 nm, with a semi-transparent lipid shell coating. Negative staining showed the lipid thickness was around 10 nm for α-TOS

loaded LCCP NPs (Figure S5.2), which was similar to that of the blank LCCP NPs in our previous report [14]. These experimental data suggest the salient structure of LCCP NPs is maintained after α-TOS loading. The hydrodynamic diameter of LCCP cores in chloroform was around 15 nm (Figure 5.1C). The overall NP size measured in TEM images was about 35 nm, slightly smaller than that measured using DLS (40 nm, Figure 5.1C and Table 5.1). These α-TOS-loaded LCCP NPs exhibited a similar structure and size to the previous reported LCCP NPs [14]. Further loading of dsDNA/siRNA resulted in an unchanged size distribution [10]. LCCP NPs with α-TOS in PBS solution remained stable as the NP size just slightly increased from 40 to 50 nm after 72 h (Figure 5.1C, LCCP-TOS *vs.* LCCP-TOS in PBS).

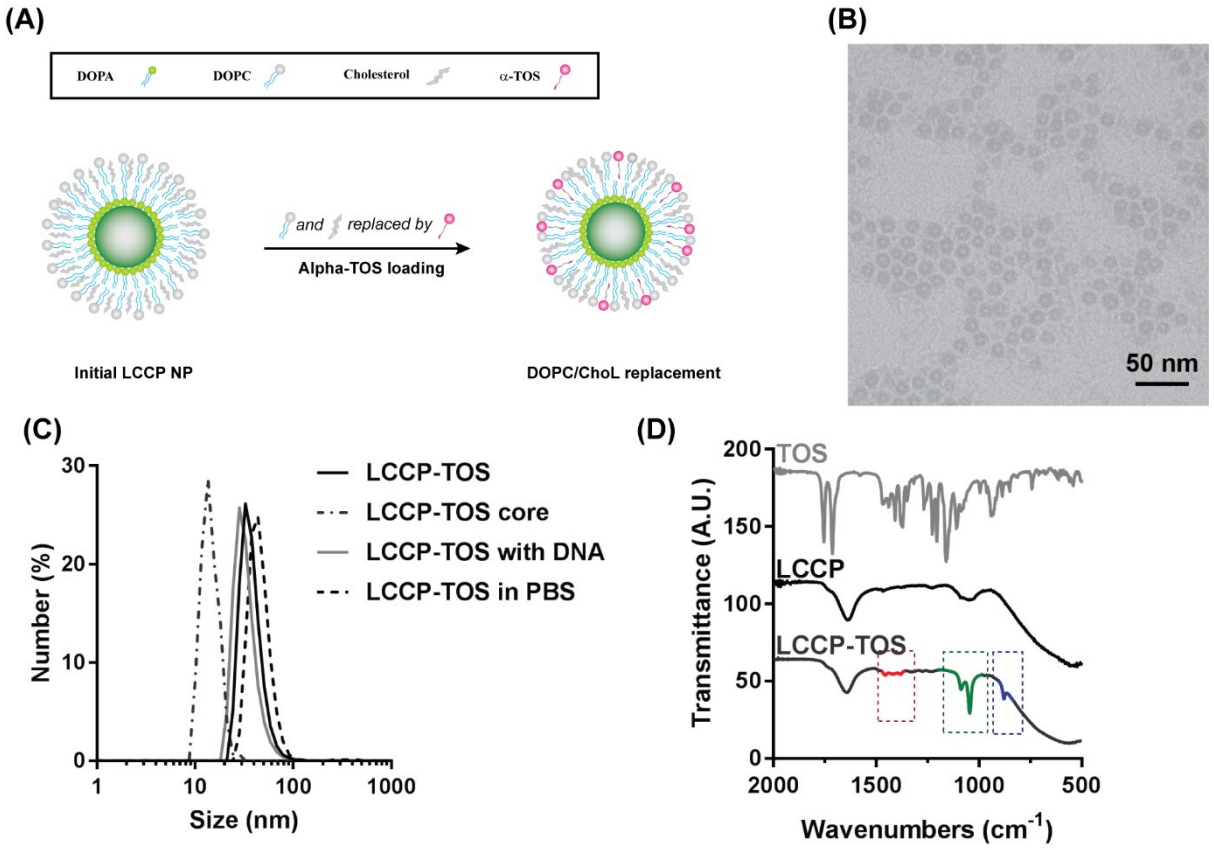

Figure 5.1 (A) Models of LCCP NP with α-TOS replacing DOPC and cholesterol. **(B)** TEM image of CD/TOS/FA NPs. **(C)** The size distribution of NPs obtained from DLS. **(D)** FT-IR spectrum of α-TOS, LCCP and LCCP-TOS, with new peaks shown in red (1480-1400 cm^{-1}), green (1100-1050 cm^{-1}) and blue (879 cm^{-1}).

The presence of α-TOS was further confirmed using FT-IR. As shown in Figure 5.1D, the spectrum of LCCP NPs shows peaks at 3300 (broad), 2915-2857, 1640, and 1050 cm^{-1},

corresponding to O-H bond (stretching), C-H (stretching), C=O (stretching), and P-O (stretching), respectively. The spectrum of LCCP-TOS NPs shows some extra peaks located at around 1480-1400, 1100-1050, and 879 cm^{-1}, associated with C-H bond of $–CH_2$/$-CH_3$ (bending), ether C-O-C bond (stretching), and substitution on benzene, respectively [22, 23]. The C=O from α-TOS was merged with a broad peak at around 1640 cm^{-1} from LCCP NPs.

5.1.3.2 FA mediated targeting delivery of nanoparticles

To optimise the FA density per NP, DSPE-PEG and DSPE-PEG-FA were used to replace 20% DOPC in the outer layer, for which the NPs (without α-TOS loading) were denoted as FA(n)-PEG(20-n), such as FA5-PEG15 and FA10-PEG10. The loading yield of DSPE-PEG-FA was around 60%, estimated from the FA fluorescence in all cases (data not shown).

As shown in Figure 5.2A, the cellular uptake of LCCP-dsDNA-cy5 increased with the FA percentage from 0% to 10% in the outer layer lipid, with the positive cell percentage being around 55%. When the FA density continuously increased from 10% to 20%, both the positive cell percentage and the mean fluorescence intensity (MFI) were very similar, suggesting that the interactions between FA in LCCP NPs and FA receptors on the cell membrane are saturated when there is 10% FA in the outer layer of lipids. Therefore, FA10-PEG10 LCCP NPs were used in subsequent experiments. According to the method reported [24], the number of FA molecules per PEG10-FA10 NP was estimated to be ~220. The optimum FA number per NP for targeting B16F0 cells in our study is different from that for MDA-MB-468 cells (220 *v.s.* 100) [24]. This difference may be caused by the FA receptor density variation between these two cancer cell lines.

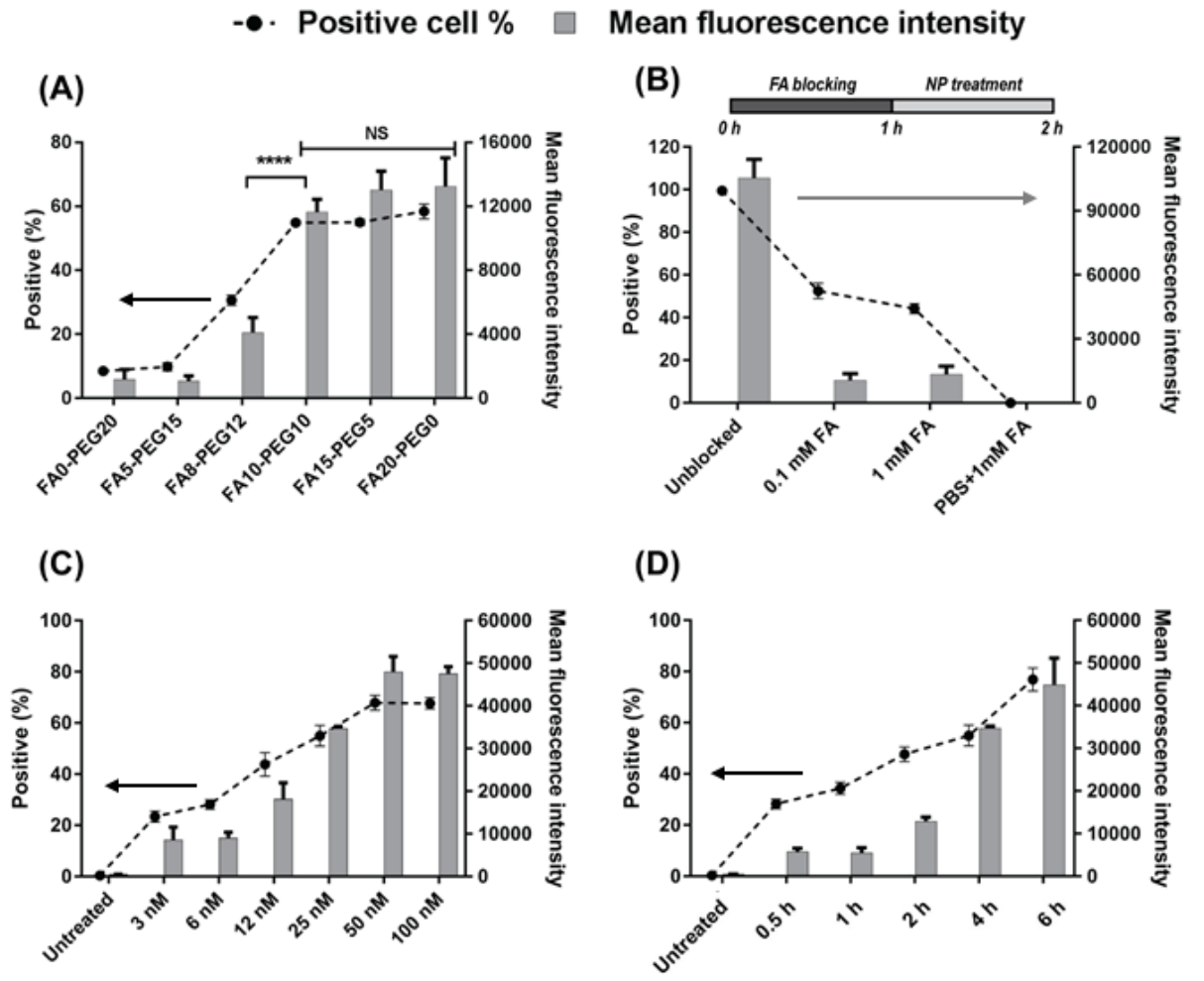

Figure 5.2 Cellular uptake of various LCCP NPs. **(A)** The effect of FA amount on cellular uptake of NPs with 25 nM dsDNA-cy5 for 4 h in DMEM medium with 10% FBS. **(B)** FA blocking assay. **(C)** and **(D)** The effect of dose and time on the cellular uptake of FA10-PEG10 NPs.

To verify that the increased cellular uptake of LCCP NPs is due to FA meditation, the FA receptors on the cell membrane were blocked with free FA and then the cells were treated with FA10-PEG10 NPs at 25 nM of dsDNA-cy5. As shown in Figure 5.2B, the positive cell percentage dropped from ~95% to ~50% after FA blocking. In terms of the MFI, the cellular uptake amount of LCCP NPs was reduced by 80-85% (Figure 5.2B). Interestingly, the positive percentage and MFI for cells blocked with 0.1 and 1.0 mM FA were almost the same, which can be attributed to non-FA mediated endocytosis. In addition, the effect of α-TOS loading on cellular uptake was also evaluated. As shown in Figure S5.3, cells treated with α-TOS-loaded

NPs showed a similar MFI to those treated with α-TOS free NPs, suggesting that loading α-TOS has no obvious influence on the cellular uptake of NPs.

As shown in Figure 5.2C, the uptake of NPs increased with the concentration of dsDNA-cy5 from 3 to 50 nM for 4 h, but then maintained a similar level when the dsDNA-cy5 concentration was 50-100 nM. Similarly, the uptake of NPs increased with longer incubation time (Figure 5.2D). Therefore, FA-modified NPs are taken up by B16 cells both in a dose and time dependent manner, with the optimal dsDNA-cy5 concentration being 50 nM.

5.1.3.3 Efficient inhibition of cancer cell growth

To evaluate the cancer cell growth inhibition ability of CD siRNA/α-TOS-loaded NPs, a series of LCCP NPs were prepared based on FA10-PEG10 NPs with FA modification and α-TOS/siRNA loading, with the NPs named scr/FA, CD/FA, scr/TOS/FA, CD/TOS, and CD/TOS/FA (basic physicochemical features are listed in Table 5.2). The growth inhibition of melanoma cancer cells by CD siRNA/α-TOS-loaded NPs was then determined. As shown in Figure 5.3, cell viability decreased upon treatment with CD/FA, scr/TOS/FA, CD/TOS, and CD/TOS/FA for 48 h (Figure 5.3A-D) in a dose-dependent manner. The cells treated by CD/FA had a viability of 70-80% at CD siRNA concentrations from 12-48 nM (Figure 5.3A), and the scr/TOS/FA treatment reduced the cell viability to 50% when the α-TOS concentration was 10-20 μM (Figure 5.3B). Obviously, the blank scr/FA NPs did not show any inhibition of cell growth at NP concentrations up to 100 mg/L (containing 54 nM scrambled siRNA, data shown in Figure S5.4), suggesting that nonspecific interference was limited.

Table 5.2 The zeta potential and gene/drug loading of nanoparticles.

Sample code	Zeta potential (mV)	FA number per NP	Gene loading efficiency (%)	α-TOS yield (%)
scr/FA*	-19.2±2.3	220	63.4%	-
CD/FA	-19.0±2.5	220	62.8%	-
scr/TOS/FA	-18.7±1.6	220	61.1%	57.7±1.4
CD/TOS	-17.2±1.1	0	62.5%	59.0±1.8
CD/TOS/FA	-19.3±2.6	220	58.7%	57.6±2.8

* *scrambled siRNA loaded FA10-PEG10 LCCP NPs*

Interestingly, when the cells were treated with siRNA/α-TOS-combined FA-target NPs (CD/TOS/FA), much stronger inhibition than either CD/FA or scr/TOS/FA in all cases was observed (Figure 5.3D). The combination effect was assessed using the method reported in the literature [25-27], as detailed in Table S5.5. The combination of CD siRNA and α-TOS in LCCP NPs showed an additive to moderately synergistic effect. Inhibition of cancer cell growth by non-FA-target CD/TOS NPs was also examined (Figure 5.3C). Inhibition by NPs without FA modification was significantly less than CD/TOS/FA NPs at doses from 12 to 48 nM for CD siRNA and 5 to 20 μM for α-TOS. This significant enhancement in cell growth inhibition by CD/TOS/FA NPs indicates that cells take up more FA-modified siRNA/α-TOS-loaded NPs via FA-mediated pathway.

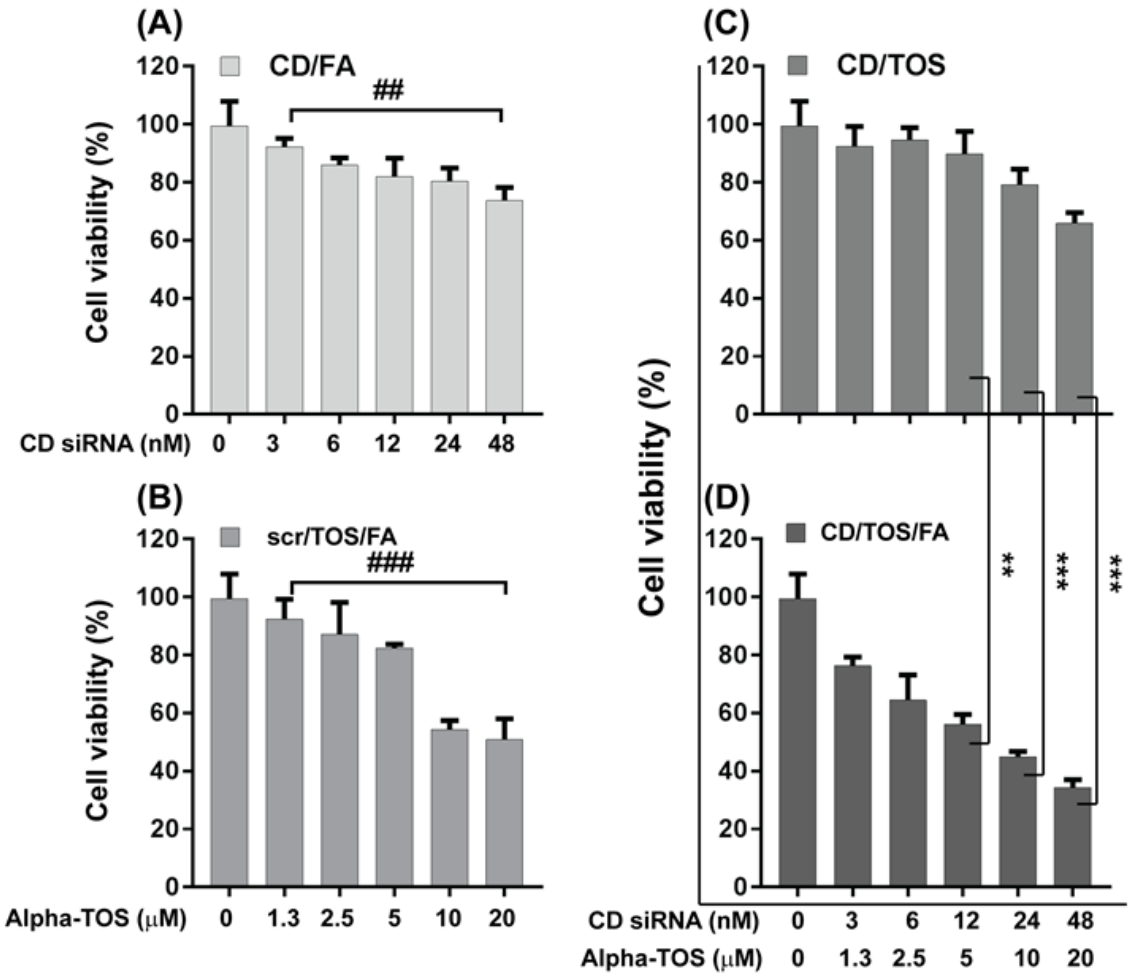

Figure 5.3 B16 cell viability after treatment for 48 h. Cells treated with **(A)** CD/FA, **(B)** scr/TOS/FA, **(C)** CD/TOS, or **(D)** CD/TOS/FA NPs.

For a better understanding of the inhibitory capacity of CD siRNA/α-TOS dual delivery by NPs, a supplementary experiment was performed by adding free CD siRNA and/or α-TOS in culture medium at the same concentrations. As shown in Figure S5.5 and Table S5.6, the corresponding inhibition effect in all cases was weaker than that in CD/TOS/FA NP-treated group, indicating the free CD siRNA and α-TOS cannot achieve the same anti-cancer effect. As is well known, free siRNA is vulnerable under culturing conditions due to the existence of RNase and is hardly taken up by cells. α-TOS has a lower water solubility and is also negatively charged at pH 7.4, which may hinder its cellular uptake. Therefore, neither free CD siRNA nor α-TOS is not efficiently taken up by cells. In a word, the targeted co-delivery of CD/TOS/FA NPs more effectively facilitates cellular uptake and inhibits B16 cell proliferation.

5.1.3.4 Induction of ROS and apoptosis upon NP treatment

ROS production by B16 cells treated with NPs for 6 h was examined by staining with 2', 7'-dichlorodihydrofluorescein diacetate (DCFH-DA) [28, 29]. CD siRNA or α-TOS delivered to B16 cells with NPs (CD/FA or scr/TOS/FA) led to an increase in intracellular ROS levels (Figure 5.4A). Moreover, the combination treatment with CD/TOS/FA NPs resulted in the significantly higher ROS production. Our results are consistent with previous studies that α-TOS induces ROS production in cells, causing damage to mitochondrion and DNA due to the relatively high oxidative stress [8].

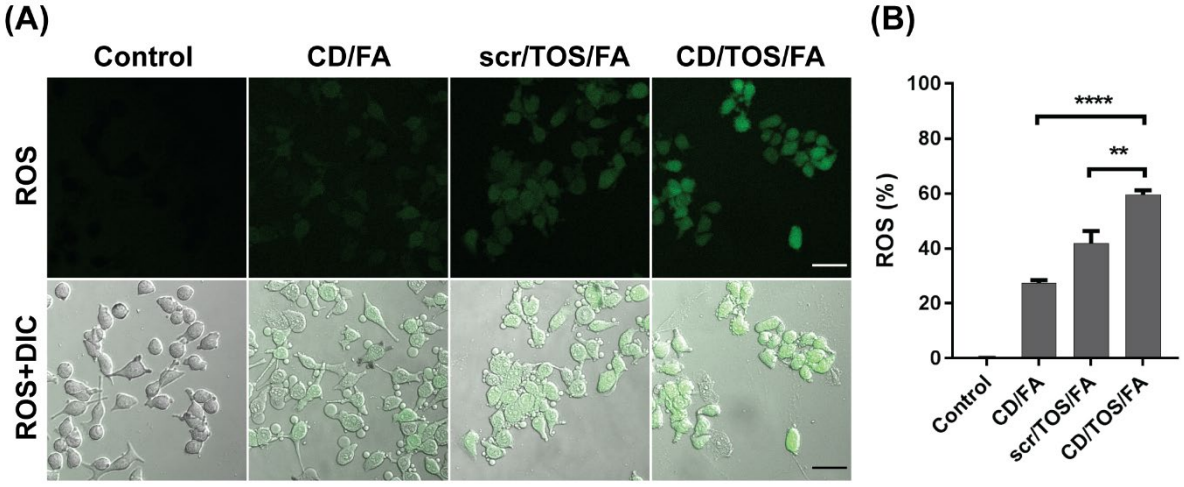

Figure 5.4 The effect of NPs on ROS production by B16 cells after 6 h treatment. ROS production (green) was examined using CLSM **(A)** and quantified using flow cytometry **(B)**. The concentration used was: [CD siRNA] = 24 nM and [α-TOS] = 10 μM.

Cell apoptosis was further analyzed using Annexin-PI staining method, as shown in Figure 5.5. Compared to the control group (Figure 5.5D), all other treatments significantly increased the cell percentage in both late apoptosis and necrosis, with a small portion of early apoptotic cells. The CD/FA NP treatment resulted in 10.1±2.4% apoptotic cells and 6.1±0.8% necrotic cells (Figure 5.5E). The scr/TOS/FA NP treatment led to more apoptosis and necrosis of cells (15.7±1.4% and 17.5±0.6%, Figure 5.5E). For cells treated with CD/TOS/FA NPs (Figure 5.5C), 35.4±1.9% cells were in late apoptotic status and 17.3±3.0% of cells were necrotic. These results suggest that both CD siRNA and α-TOS induced cell apoptosis, and the dual treatment (CD/TOS/FA) resulted in increased cell apoptosis (Figure 5.5E). In contrast, α-TOS also caused strong necrosis while CD siRNA seemed to only cause very weak necrosis (Figure 5.5E). In conclusion, all NPs showed cytotoxicity to B16F0 cells through induction of late apoptosis, with α-TOS inducing more necrosis. The additive effect may result from the high ROS levels generated when cells were treated with CD/TOS/FA (Figure 5.4), and may further indicate that CD siRNA and α-TOS involve different pathways to induce cell death, as discussed shortly.

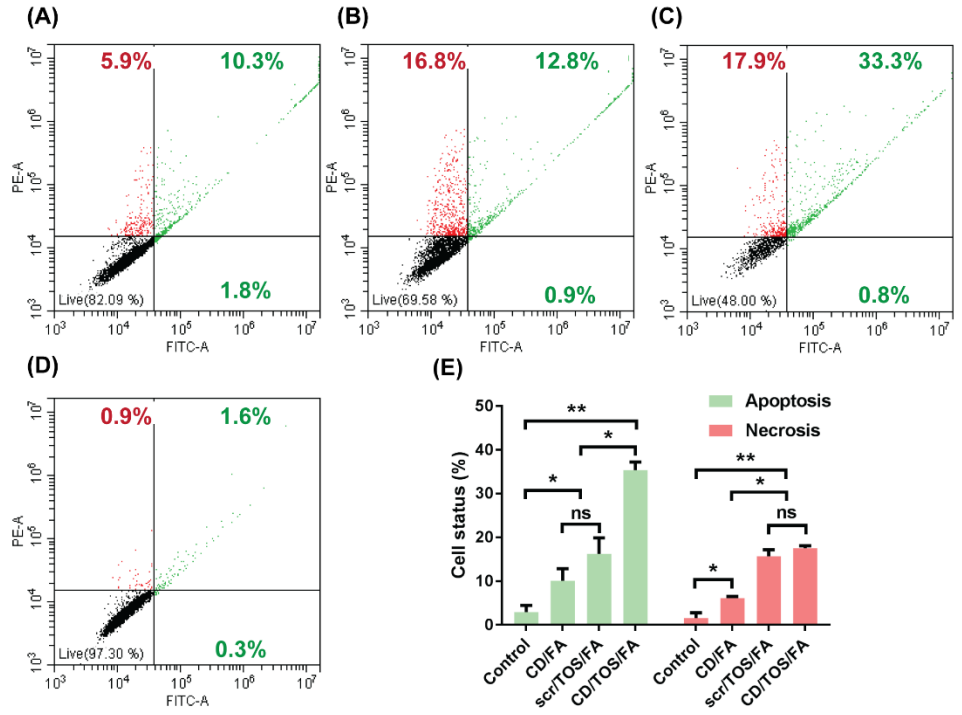

Figure 5.5 Flow cytometric analysis of cell distribution for early/late apoptosis and necrosis on B16F0 cells after typical treatment with **(A)** CD/FA, **(B)** scr/TOS/FA, **(C)** CD/TOS/FA, or **(D)** scr/FA NP treatment for 24 h. The average percentage of cells under apoptosis or necrosis status was calculated after three parallel tests and shown **(E)**.

5.1.3.5 Suppression of Bcl-2 expression and cell cycle G1 arrest upon NP treatment

The expression of Bcl-2 protein was examined in cells treated with LCCP NPs. As shown in Figure 5.6, compared to the control, the Bcl-2 protein level significantly decreased to ~60% and ~50% after CD/FA and CD/TOS/FA NP treatment, respectively, whereas the level just decreased to 80 % upon scr/TOS/FA NP treatment. Similarly, Bcl-2 mRNA expression level at 24 h post transfection decreased to around 0.6 fold compared to that of blank cells (Figure S5.6). Both assays suggest that the suppression of Bcl-2 expression is mainly attributed to the effect of CD siRNA delivered by LCCP NPs, in agreement with the previous report that CD siRNA is able to suppress anti-apoptotic Bcl-2 gene expression and thereby induce cancer cell death [30]. In contrast, the effect of α-TOS on the Bcl-2 gene expression was much weaker, and not significant (Figure 5.6).

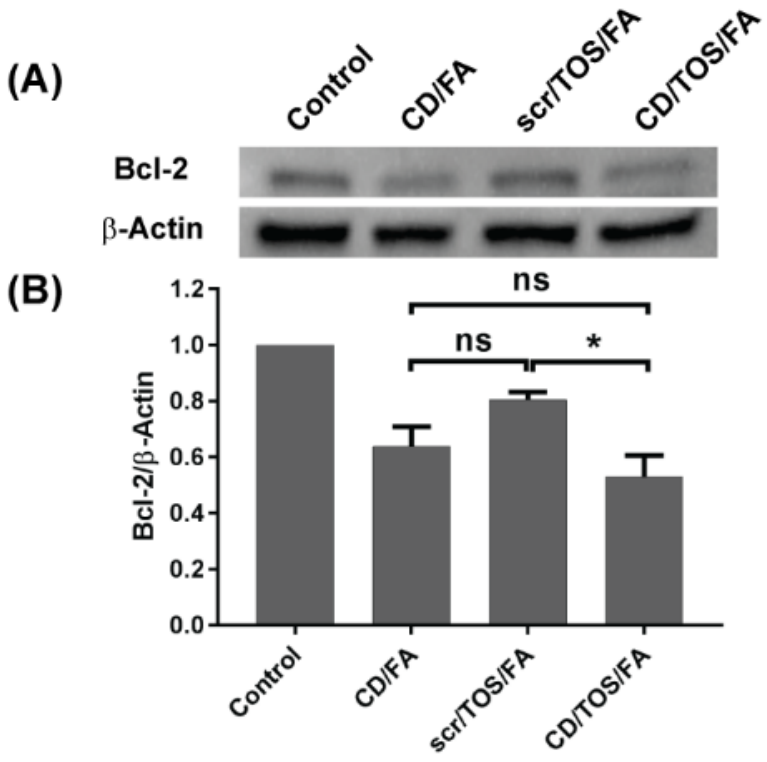

Figure 5.6 The suppression of Bcl-2 protein expression by treatment with NPs for 48 h. **(A)** Western blot analysis; **(B)** Densitometry analysis of Bcl-2 expression against β-actin. The concentration used was: [CD siRNA] = 24 nM and [α-TOS] = 10 μM.

Cell cycle changes in treated cells were further examined. As shown in Figure 5.7, the B16F0 cell cycle phases with CD/FA treatment were similar to the blank cells (Figure 5.7A, B and E),

indicating CD siRNA does not affect the B16F0 cell cycle. In comparison, cells treated with scr/TOS/FA and CD/TOS/FA showed obvious differences in cell cycles (Figure 5.7A, C, D and E). The G1 phase increased from 54% in blank cells to 66% and 72% for cells treated with scr/TOS/FA and CD/TOS/FA, respectively, while the S and G2/M phases decreased correspondingly. The results indicate that α-TOS is mainly responsible for G1 phase arrest in the cell cycle, consistent with the previous report [31]. Interestingly, CD siRNA assisted α-TOS (i.e. CD/TOS/FA NP treatment) to induce more G1 arrest (compared to scr/TOS/FA NP treatment, 1.45 v.s. 1.25 fold compared to BLK, Figure 5.7F), suggesting an additive treatment effect of both therapeutics. Because CD siRNA is a commercial product and the gene target is unclear, we postulate that this stronger G1 phase arrest may be due to: 1) overproduction of ROS that reduces ATP production of mitochondrion and ATP hydrolytic activity, and inactivates the mitochondrial electron transport chain components [32, 33]. With the high level of ROS produced in our studies, the CD/TOS/FA NP-treated cells (Figure 5.4) would be in a severe energy-insufficient condition; 2) the decrease in Bcl-2 that causes delay of S phase entry to some degree [34]. Thus, the significant Bcl-2 decrease in CD/TOS/FA NP-treated cells (Figure 5.6) may be involved in the arrest of G1 phase.

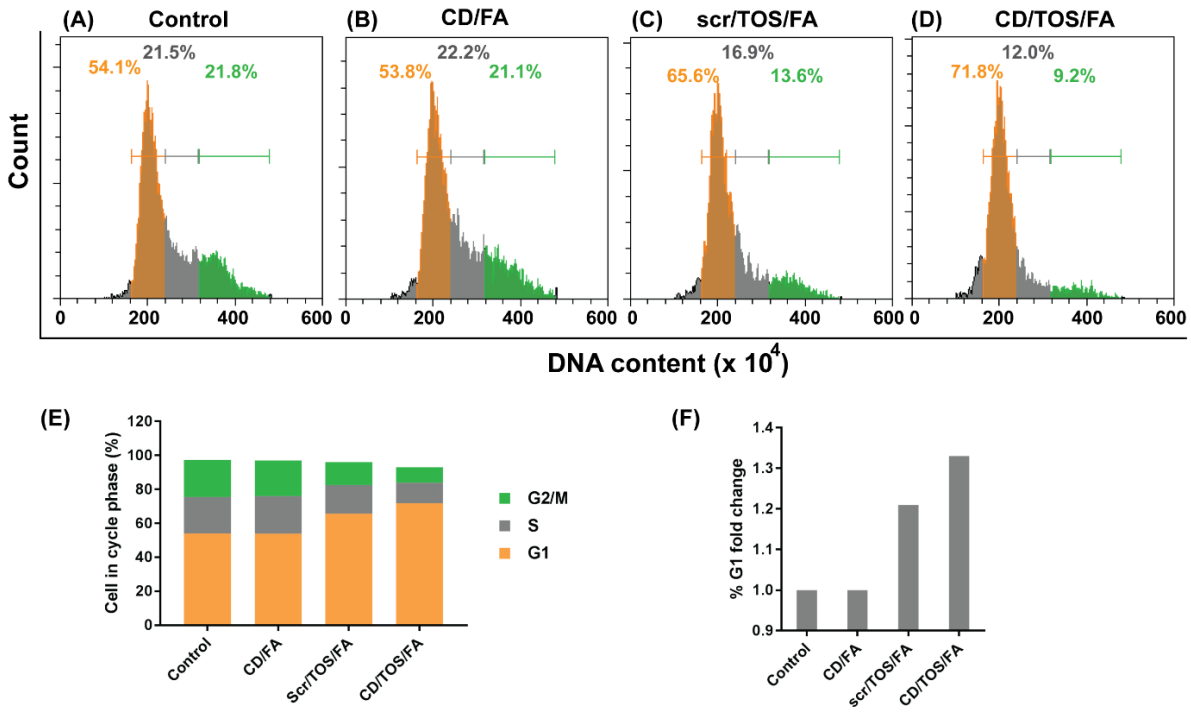

Figure 5.7 Cell cycle analysis by staining the DNA in B16F0 cells after 24 h treatment. **(A)** control; **(B)** CD/FA NPs; **(C)** scr/TOS/FA NPs; and **(D)** CD/TOS/FA NPs. The distribution of different cell cycle phases in gated cells was counted **(E)**, and the fold change in G1 phase after NP treatment was calculated and normalized to that of the control **(F)**.

5.1.4 Discussion

In this study, we demonstrated that LCCP NPs are an efficient targeted co-delivery system of hydrophobic anticancer drug α-TOS and hydrophilic functional CD siRNA for combination therapy of melanoma. The particle size and zeta potential of these α-TOS loaded LCCP NPs were similar to those of pristine LCCPs, when it just replaced 15% of DOPC/cholesterol in the outer lipid layer (Figure 5.1 and Table 5.1). To minimize the potential nonspecific interference in healthy cells, FA was conjugated on LCCP NPs to increase the targeted delivery to FA-receptor overexpressing tumour cells, including B16F0. As a result, the FA conjugation led to more efficient NP internalisation by B16 melanoma cells, with the cost-effective efficacy achieved using 10% DSPE-PEG-FA and 10% DSPE-PEG in the outer lipid layer (Figure 5.2). We then evaluated the combination therapy of CD siRNA and α-TOS co-delivered with LCCP NPs. The CD/TOS/FA NPs exhibited a dose-dependent anticancer effect (Figure 5.3), which is additive to moderately synergistic (Table S5.5) and much stronger than the free drugs (Figure S5.5). Our study suggests that the targeted delivery of CD siRNA and α-TOS with LCCP NPs is a promising approach for the more effective treatment of melanoma.

To understand the possible mechanism of the combination therapy, we examined the apoptotic status of cells treated with these NPs. CD siRNA and α-TOS together caused more cell apoptosis than single treatment (Figure 5.5). In this regard, the ROS production level and Bcl-2 protein expression were further quantified. As shown in Figure 5.4 and 5.6 and previous studies [7, 30, 35, 36], α-TOS induces ROS production while CD siRNA tends to suppress Bcl-2 expression. Interestingly, the combination of CD siRNA and α-TOS in LCCP NPs led to the highest ROS level and the strongest Bcl-2 suppression, which resulted in the highest inhibition of cell growth (Figure 5.3). In our opinion, these results may be a consequence of active interaction of the two pathways: (1) Bcl-2 down-regulation by increased ROS production; and (2) ROS level further enhanced by Bcl-2 suppression (Figure 5.8). It is well-known that ROS regulates Bcl-2 family proteins by both controlling expression levels and activity modulation via phosphorylation/ubiquitination [37, 38]. High intracellular ROS leads to the polyubiquitination of Bcl-2 protein, followed by degradation by ribosomal enzymes. On the other hand, Bcl-2 is able to prevent mitochondrion from producing excessive ROS due to its interaction and localization with GSH in mitochondrion [39, 40]. In our case, the scr/TOS/FA-treated cells showed a strong ROS up-regulation (Figure 5.4), leading to mitochondrial damage

and cell apoptosis. The CD siRNA induced down-regulation of Bcl-2 protein and cell apoptosis (Figure 5.6). Consequently, the co-delivery nanoparticle CD/TOS/FA resulted in the highest cell apoptosis rate, showing the strongest inhibitory effect.

Furthermore, the anticancer action also involved cell cycle arrest (Figure 5.7). α-TOS, as reported [31, 41], can cause G1 phase arrest, while the influence of CD siRNA on the cell cycle is not obvious. Therefore, the G1 phase arrest by CD/TOS/FA is mainly induced by α-TOS and can be facilitated by CD siRNA treatment because less Bcl-2 and more ROS cause mitochondrial damage [42-44], and leading to the cell cycle arrest at G1 [45].

Taken together, the CD/TOS/FA NPs cause cancer cell death more effectively due to the additive to moderately synergistic actions of α-TOS and CD siRNA in the induction of mitochondrial damage and cell apoptosis, and cell life cycle arrest in G1 phase (Figure 5.8).

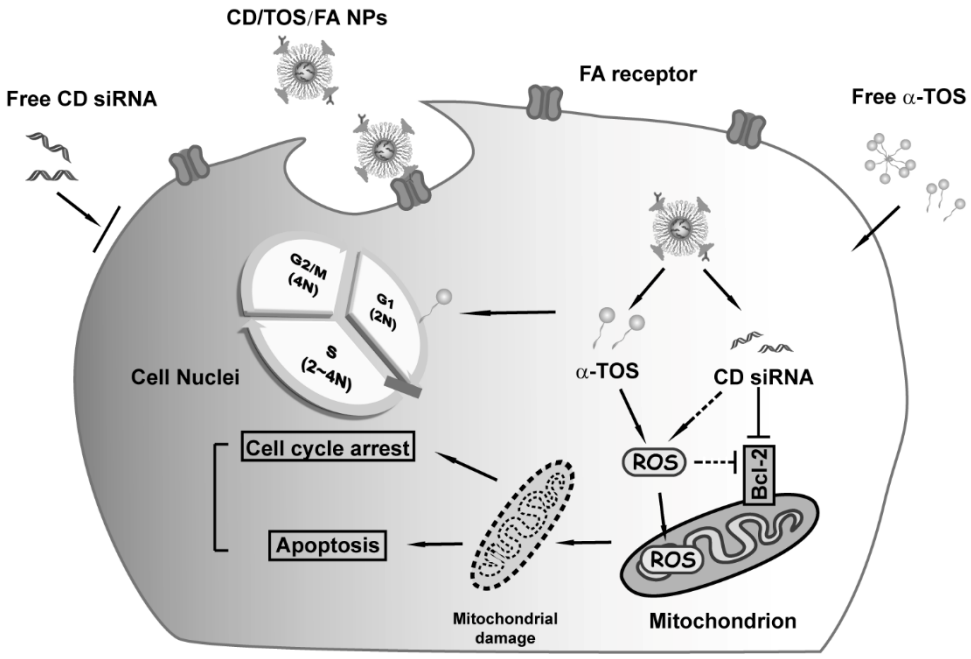

Figure 5.8 Proposed mechanism for CD siRNA and α-TOS B16 cancer cell growth inhibition. The anticancer action leads to (1) apoptosis and (2) cell cycle arrest. The treatment induces ROS production and Bcl-2 suppression, resulting in the damaged mitochondrion and cell apoptosis. Here, α-TOS further contributes to cell cycle arrest in G1 phase. Dash arrows: weak interactions; Black arrows: strong interactions.

5.1.5 Conclusions

We have developed LCCP based NPs for co-delivery of CD siRNA and α-TOS with FA to specifically target skin cancer cells. FA-lipid and α-TOS were loaded in NPs by replacing DOPC/cholesterol in the outer layer lipid. The designed CD/TOS/FA NPs, with similar physical structure and physicochemical properties, were taken up effectively by B16F0 cells *via* the FA-mediated pathway in a dose-dependent manner. In particular, the combination of CD siRNA and α-TOS in LCCP NPs more effectively inhibited cell growth in an additive/synergic manner. The mechanism may involve in (1) an enhanced apoptotic effect through interactions between ROS generation and Bcl-2 down-regulation, and (2) the cell cycle arrest in G1 phase. Thus the CD/TOS/FA NPs hold great potential as a promising anticancer formulation for melanoma therapy.

5.1.6 Future Perspective

The hybrid LCCP NPs developed in this study can be used as platforms for cancer theranostics in the future. The incorporation of calcium carbonate in the particle cores could generate carbon-dioxide under acidic conditions, which may be used for ultrasonic diagnosis of cancer. In addition, other hydrophobic drugs with similar structure to α-TOS (such as γ-tocotrienols) can be also loaded onto the LCCP NPs for cancer therapy. Moreover, other forms of therapeutic oligos, such as pDNA, dsDNA, and shRNA can be delivered by LCCP NPs for other combination therapy regimens. Nevertheless, more work is needed to develop lipid-coated calcium phosphate/carbonate materials for cancer diagnosis and/or therapy.

5.1.7 References

Papers of special note have been highlighted as: • of interest; •• of considerable interest

[1] S.S. Sulaimon, B.E. Kitchell, The basic biology of malignant melanoma: Molecular mechanisms of disease progression and comparative aspects, J. Vet. Int. Med. 17(6) (2003) 760-772.

[2] L. Seymour, K. Ulbrich, P. Steyger, M. Brereton, V. Subr, J. Strohalm, R. Duncan, Tumour tropism and anti-cancer efficacy of polymer-based doxorubicin prodrugs in the treatment of subcutaneous murine B16F10 melanoma, Br. J. Cancer 70(4) (1994) 636-641.

[3] T. Murata, H. Hibasami, S. Maekawa, T. Tagawa, K. Nakashima, Preferential binding of cisplatin to mitochondrial DNA and suppression of ATP generation in human malignant melanoma cells, Biochem. Int. 20(5) (1990) 949-955.
[4] C.J. Hitzman, W.F. Elmquist, L.W. Wattenberg, T.S. Wiedmann, Development of a respirable, sustained release microcarrier for 5-fluorouracil I: in vitro assessment of liposomes, microspheres, and lipid coated nanoparticles, J. Pharm. Sci. 95(5) (2006) 1114-1126.
[5] N. Yin, W. Ma, J. Pei, Q. Ouyang, C. Tang, L. Lai, Synergistic and antagonistic drug combinations depend on network topology, PloS One 9(4) (2014) e93960.
[6] K.N. Prasad, J. Edwards-Prasad, Effects of tocopherol (vitamin E) acid succinate on morphological alterations and growth inhibition in melanoma cells in culture, Cancer Res. 42(2) (1982) 550-555.
[7] Q. Li, Y. Wen, X. You, F. Zhang, V. Shah, X. Chen, D. Tong, X. Wei, L. Yin, J. Wu, Development of a reactive oxygen species (ROS)-responsive nanoplatform for targeted oral cancer therapy, J Mater. Chem. B 4(27) (2016) 4675-4682.
[8] A. Mallick, P. More, M.M.K. Syed, S. Basu, Nanoparticle-mediated mitochondrial damage induces apoptosis in cancer, ACS Appl. Mater. Interfaces 8(21) (2016) 13218-13231.
[9] A. Mallick, P. More, S. Ghosh, R. Chippalkatti, B.A. Chopade, M. Lahiri, S. Basu, Dual drug conjugated nanoparticle for simultaneous targeting of mitochondria and nucleus in cancer cells, ACS Appl. Mater. Interfaces 7(14) (2015) 7584-7598.
[10] J. Tang, L. Li, C.B. Howard, S.M. Mahler, L. Huang, Z.P. Xu, Preparation of optimized lipid-coated calcium phosphate nanoparticles for enhanced in vitro gene delivery to breast cancer cells, J. Mater. Chem. B 3(33) (2015) 6805-6812.
• Application of lipid-coated calcium phosphate nanoparticles for gene delivery
[11] Z. Xu, Y. Wang, L. Zhang, L. Huang, Nanoparticle-delivered transforming growth factor-beta siRNA enhances vaccination against advanced melanoma by modifying tumor microenvironment, ACS Nano 8(4) (2014) 3636-3645.
[12] Y. Zhang, A. Satterlee, L. Huang, In vivo gene delivery by nonviral vectors: overcoming hurdles?, Mol. Ther. 20(7) (2012) 1298-1304.
[13] I. Roy, S. Mitra, A. Maitra, S. Mozumdar, Calcium phosphate nanoparticles as novel non-viral vectors for targeted gene delivery, Int. J. Pharm. 250(1) (2003) 25-33.
• Pioneering work on calcium phosphate nanoparticles for gene delivery
[14] Y. Wu, W. Gu, J. Tang, Z.P. Xu, Devising new lipid-coated calcium phosphate/carbonate hybrid nanoparticles for controlled release in endosomes for efficient gene delivery, J Mater. Chem. B 5(34) (2017) 7194-7203.
•• Application of lipid-coated calcium carbonate/phosphate nanoparticles for gene delivery
[15] Z. Xu, S. Ramishetti, Y.-C. Tseng, S. Guo, Y. Wang, L. Huang, Multifunctional nanoparticles co-delivering Trp2 peptide and CpG adjuvant induce potent cytotoxic T-lymphocyte response against melanoma and its lung metastasis, J. Control. Release 172(1) (2013) 259-265.
[16] J. He, S. Duan, X. Yu, Z. Qian, S. Zhou, Z. Zhang, X. Huang, Y. Huang, J. Su, C. Lai, Folate-modified chitosan nanoparticles containing the IP-10 gene enhance melanoma-specific cytotoxic CD8+ CD28+ T lymphocyte responses, Theranostics 6(5) (2016) 752.
[17] X. Liang, L. Fang, X. Li, X. Zhang, F. Wang, Activatable near infrared dye conjugated hyaluronic acid based nanoparticles as a targeted theranostic agent for

enhanced fluorescence/CT/photoacoustic imaging guided photothermal therapy, Biomaterials 132 (2017) 72-84.

[18] Q. Liu, N. Xu, L. Liu, J. Li, Y. Zhang, C. Shen, K. Shezad, L. Zhang, J. Zhu, J. Tao, Dacarbazine-loaded hollow mesoporous silica nanoparticles grafted with folic acid for enhancing anti-metastatic melanoma response, ACS Appl. Mater. Interfaces (2017).

[19] M. A Elkhodiry, G. A Husseini, D. Velluto, Targeting the folate receptor: Effects of conjugating folic acid to DOX loaded polymeric micelles, Anti-Cancer Agents Med. Chem. 16(10) (2016) 1275-1280.

[20] Y. Qi, N. Wang, Y. He, J. Zhang, H. Zou, W. Zhang, W. Gu, Y. Huang, X. Lian, J. Hu, Transforming growth factor-β1 signaling promotes epithelial-mesenchymal transition-like phenomena, cell motility, and cell invasion in synovial sarcoma cells, PloS One 12(8) (2017) e0182680.

[21] M. Sardan, M. Kilinc, R. Genc, A.B. Tekinay, M.O. Guler, Cell penetrating peptide amphiphile integrated liposomal systems for enhanced delivery of anticancer drugs to tumor cells, Faraday Discuss. 166 (2013) 269-283.

[22] G. Hu, Y. Cai, Z. Tu, J. Luo, X. Qiao, Q. Chen, W. Zhang, Reducing the cytotoxicity while improving the anti-cancer activity of silver nanoparticles through α-tocopherol succinate modification, RSC Adv. 5(100) (2015) 82050-82055.

[23] A. Angulo-Molina, M.Á. Méndez-Rojas, T. Palacios-Hernández, O.E. Contreras-López, G.A. Hirata-Flores, J.C. Flores-Alonso, S. Merino-Contreras, O. Valenzuela, J. Hernández, J. Reyes-Leyva, Magnetite nanoparticles functionalized with α-tocopheryl succinate (α-TOS) promote selective cervical cancer cell death, J. Nanopart. Res. 16(8) (2014) 2528.

[24] J. Tang, C.B. Howard, S.M. Mahler, K.J. Thurecht, L. Huang, Z.P. Xu, Enhanced delivery of siRNA to triple negative breast cancer cells in vitro and in vivo through functionalizing lipid-coated calcium phosphate nanoparticles with dual target ligands, Nanoscale 10(9) (2018) 4258-4266.

• Calculation of outer layer lipid density

[25] Y. Zhao, J.-L. Gao, J.-W. Ji, M. Gao, Q.-S. Yin, Q.-L. Qiu, C. Wang, S.-Z. Chen, J. Xu, R.-S. Liang, Cytotoxicity enhancement in MDA-MB-231 cells by the combination treatment of tetrahydropalmatine and berberine derived from Corydalis yanhusuo WT Wang, J. Intercult. Ethnopharmacol. 3(2) (2014) 68.

[26] A. Ito, M. Fujioka, T. Yoshida, K. Wakamatsu, S. Ito, T. Yamashita, K. Jimbow, H. Honda, 4 - S - Cysteaminylphenol - loaded magnetite cationic liposomes for combination therapy of hyperthermia with chemotherapy against malignant melanoma, Cancer Sci. 98(3) (2007) 424-430.

[27] F. Gao, Z. Yan, J. Zhou, Y. Cai, J. Tang, Methotrexate-conjugated magnetic nanoparticles for thermochemotherapy and magnetic resonance imaging of tumor, J. Nanopart. Res. 14(10) (2012) 1160.

[28] B. Yerushalmi, R. Dahl, M.W. Devereaux, E. Gumpricht, R.J. Sokol, Bile acid-induced rat hepatocyte apoptosis is inhibited by antioxidants and blockers of the mitochondrial permeability transition, Hepatology 33(3) (2001) 616-626.

[29] J. Neuzil, M. Tomasetti, Y. Zhao, L.-F. Dong, M. Birringer, X.-F. Wang, P. Low, K. Wu, B.A. Salvatore, S.J. Ralph, Vitamin E Analogs, a Novel Group of "Mitocans," as Anticancer Agents: The Importance of Being Redox-Silent, Mol. Pharmacol. 71(5) (2007) 1185-1199.

[30] L. Li, W. Gu, J. Chen, W. Chen, Z.P. Xu, Co-delivery of siRNAs and anti-cancer drugs using layered double hydroxide nanoparticles, Biomaterials 35(10) (2014) 3331-3339.
[31] R. Alleva, M.S. Benassi, L. Pazzaglia, M. Tomasetti, N. Gellert, B. Borghi, J. Neuzil, P. Picci, α-Tocopheryl succinate alters cell cycle distribution sensitising human osteosarcoma cells to methotrexate-induced apoptosis, Cancer Lett. 232(2) (2006) 226-235.
• The influence of α-TOS on cell cycle
[32] G. Lippe, M. Comelli, D. Mazzilis, F.D. Sala, I. Mavelli, The inactivation of mitochondrial F1 ATPase by H2O2 is mediated by iron ions not tightly bound in the protein, Biochem. Biophys. Res. Commun. 181(2) (1991) 764-770.
[33] Y. Zhang, O. Marcillat, C. Giulivi, L. Ernster, K. Davies, The oxidative inactivation of mitochondrial electron transport chain components and ATPase, J. Biol. Chem. 265(27) (1990) 16330-16336.
[34] X. Du, X. Fu, K. Yao, Z. Lan, H. Xu, Q. Cui, E. Yang, Bcl-2 delays cell cycle through mitochondrial ATP and ROS, Cell Cycle 16(7) (2017) 707-713.
[35] J.-J. Hu, Q. Lei, M.-Y. Peng, D.-W. Zheng, Y.-X. Chen, X.-Z. Zhang, A positive feedback strategy for enhanced chemotherapy based on ROS-triggered self-accelerating drug release nanosystem, Biomaterials 128(Supplement C) (2017) 136-146.
[36] R. Wen, S. Dhar, Turn up the cellular power generator with vitamin E analogue formulation, Chem. Sci. 7(8) (2016) 5559-5567.
[37] D.A. Hildeman, T. Mitchell, B. Aronow, S. Wojciechowski, J. Kappler, P. Marrack, Control of Bcl-2 expression by reactive oxygen species, Proc. Natl. Acad. Sci. U. S. A. 100(25) (2003) 15035-15040.
•• The influence of ROS on Bcl-2 expression
[38] D. Li, E. Ueta, T. Kimura, T. Yamamoto, T. Osaki, Reactive oxygen species (ROS) control the expression of Bcl-2 family proteins by regulating their phosphorylation and ubiquitination, Cancer Sci. 95(8) (2004) 644-650.
[39] A.K. Zimmermann, F.A. Loucks, E.K. Schroeder, R.J. Bouchard, K.L. Tyler, D.A. Linseman, Glutathione Binding to the Bcl-2 Homology-3 Domain Groove A MOLECULAR BASIS FOR BCL-2 ANTIOXIDANT FUNCTION AT MITOCHONDRIA, J. Biol. Chem. 282(40) (2007) 29296-29304.
[40] S.J.F. Chong, I.C.C. Low, S. Pervaiz, Mitochondrial ROS and involvement of Bcl-2 as a mitochondrial ROS regulator, Mitochondrion 19 (2014) 39-48.
•• The influence of Bcl-2 expression on ROS
[41] S. Wada, Y. Satomi, M. Murakoshi, N. Noguchi, T. Yoshikawa, H. Nishino, Tumor suppressive effects of tocotrienol in vivo and in vitro, Cancer Lett. 229(2) (2005) 181-191.
[42] J.C. Reed, Bcl-2–family proteins and hematologic malignancies: history and future prospects, Blood 111(7) (2008) 3322-3330.
[43] L.A. Loeb, D.C. Wallace, G.M. Martin, The mitochondrial theory of aging and its relationship to reactive oxygen species damage and somatic mtDNA mutations, Proc. Natl. Acad. Sci. U. S. A. 102(52) (2005) 18769-18770.
[44] G. Kroemer, L. Galluzzi, C. Brenner, Mitochondrial membrane permeabilization in cell death, Physiol. Rev. 87(1) (2007) 99-163.
[45] T. Shimura, M. Sasatani, K. Kamiya, H. Kawai, Y. Inaba, N. Kunugita, Mitochondrial reactive oxygen species perturb AKT/cyclin D1 cell cycle signaling via oxidative inactivation of PP2A in lowdose irradiated human fibroblasts, Oncotarget 7(3) (2016) 3559.

5.1.8 Supplementary Information

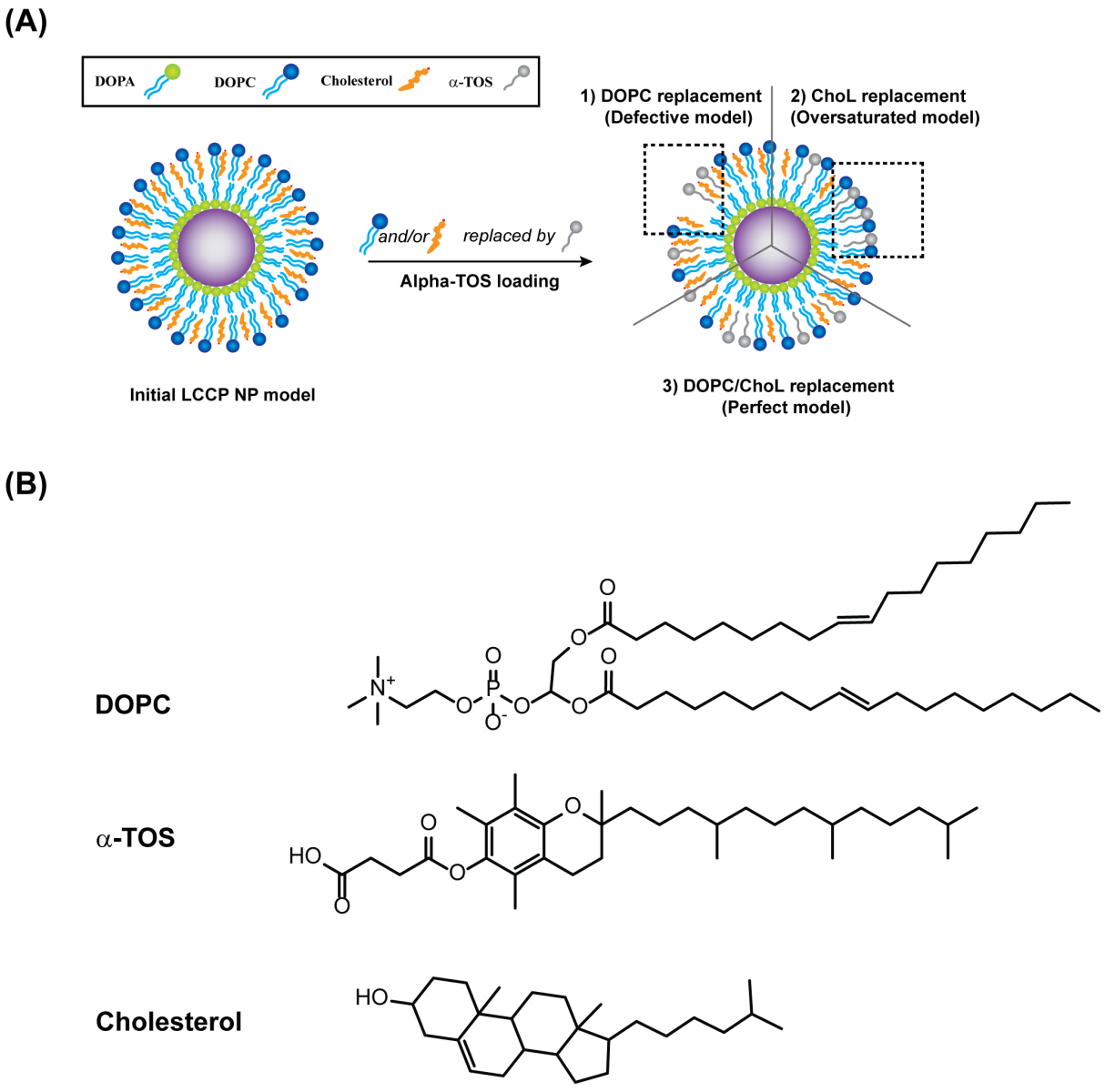

Figure S5.1 (A) The models after α-TOS intercalation. Surface area of each model was calculated by the topological surface area values from PubChem database (see in Table S5.3), and compared with the initial LCCP NP. **(B)** The similarity of α-TOS to DOPC and cholesterol, with similar structure marked.

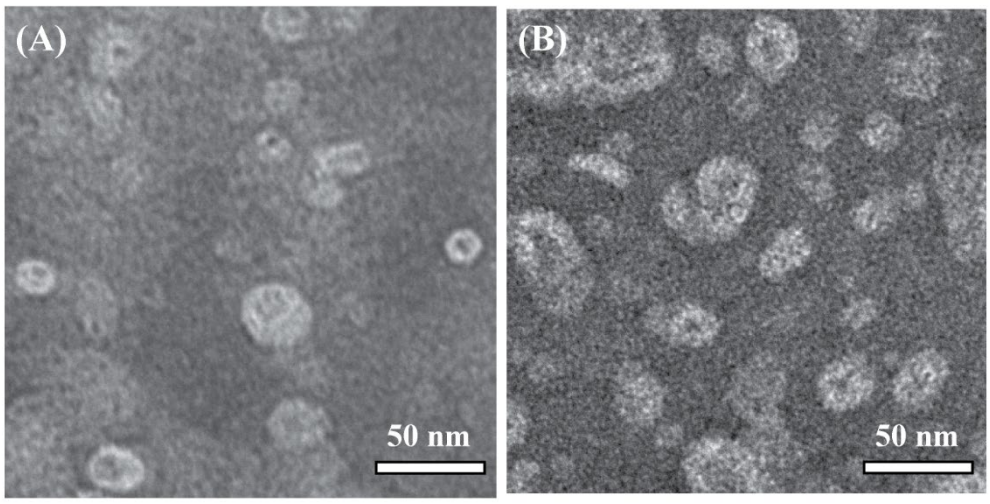

Figure S5.2 Negative staining TEM image for **(A)** LCCP NPs and **(B)** LCCP with 15% α-TOS.

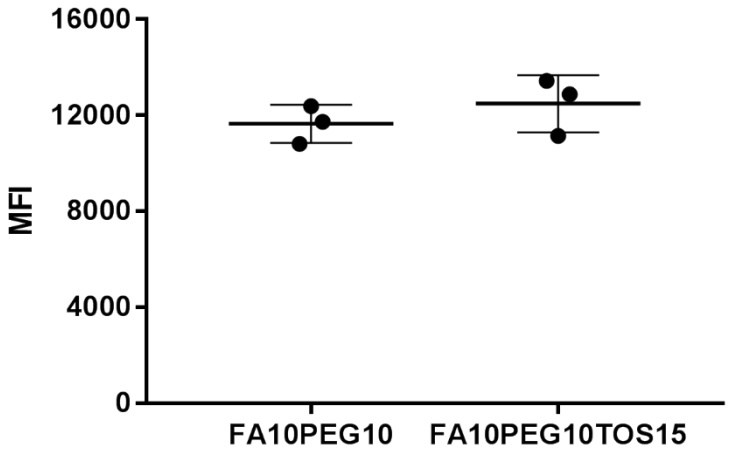

Figure S5.3 The mean fluorescence intensity comparison of cells treated FA10-PEG10 NPs with and without 15% alpha-TOS in the outer layer lipid. Cells were co-cultured with NPs with 25 nM dsDNA-cy5 for 4 h in DMEM with 10% FBS.

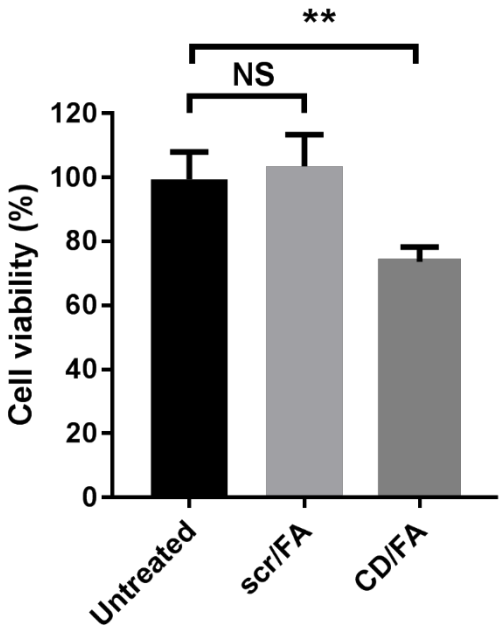

Figure S5.4 Effect of scr/FA and CD/FA (100 mg/L) on B16F0 cell growth.

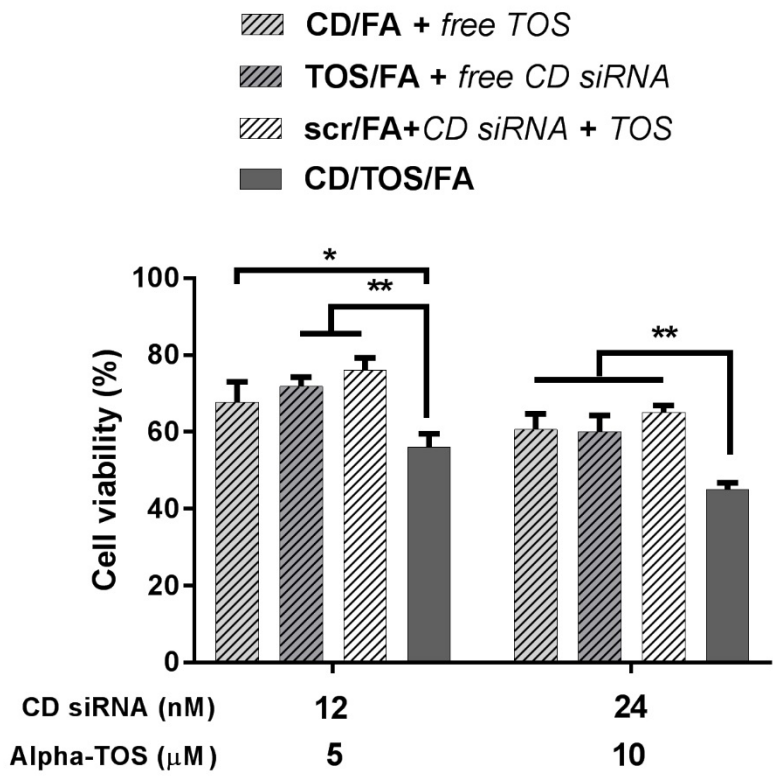

Figure S5.5 The comparison of cancer cell inhibition effect of free CD siRNA/α-TOS and particle-loaded. Two conditions were chosen: (1) 12 nM of CD siRNA with 5 μM of α-TOS; (2) 24 nM of CD siRNA with 10 μM of α-TOS.

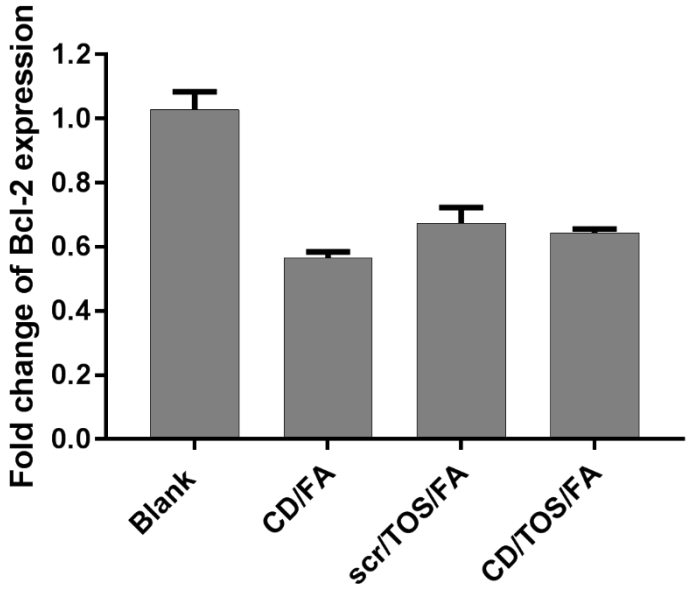

Figure S5.6 RT PCR at 24 h post transfection. Cells were treated with NPs containing 24 nM CD siRNA and/or 10 uM TOS. The Bcl-2 expression was normalized by the corresponding β-actin expression.

Table S5.1 The detailed sequences used in this work.

Name	Supplier	Sequence
dsDNA-cy5 (sense)	IDTDNA	TTCTCCGAACGTGTCACGTTT-cyanine 5
dsDNA-cy5 (antisense)	IDTDNA	AAACGTGACACGTTCGGAGAA
scramble control (sense)	Sigma	CUUACGCUGAGUACUUCGA
scramble control (antisense)	Sigma	UCGAAGUACUCAGCGUAAG

The sequence of CD siRNA is unrevealed by the company.

Table S5.2 Detailed outer layer lipid composition (%) and DNA/RNA loading (ng) of all nanoparticles mentioned.

Code	Outer layer lipid composition (%)					DNA/RNA input (nmol)		
	DOPC	Cholesterol	α-TOS	DSPE-PEG-FA	DSPE-PEG	dsDNA-cy5	Scramble siRNA	CD siRNA
α/DOPC	35	50	15	-	-	-	-	-
α/ChoL	50	35	15	-	-	-	-	-
α/DOPC/ChoL	42.5	42.5	15	-	-	-	-	-
α/BLK	50	50	0	-	-	-	-	-
FA0-PEG20	40	50	-	0	10	0.3	-	-
FA5-PEG15	40	50	-	2.5	7.5	0.3	-	-
FA8-PEG12	40	50	-	4	6	0.3	-	-
FA10-PEG10	40	50	-	5	5	0.3	-	-
FA20-PEG0	40	50	-	10	0	0.3	-	-
CD/FA	40	50	0	5	5	-	0	0.3
scr/TOS/FA	32.5	42.5	15	5	5	-	0.3	0
CD/TOS	32.5	42.5	15	0	10	-	0	0.3
CD/TOS/FA	32.5	42.5	15	5	5	-	0	0.3

Table S5.3 The estimation of NP's surface area changes according to their outer layer lipid composition. The topological polar surface area values were obtained from PubChem database as: DOPC = 111 Å^2, cholesterol = 20.2 Å^2, and alpha-TOS = 72.8 Å^2.

Sample code	Lipid molecule number			Area	A/A_{BLK}
	DOPC	*Cholesterol*	*Alpha-TOS*	(nm^2)	
α/BLK	3835	3835	0	5031.5	1.00
α/DOPC	2684	3835	1151	4591.8	0.91
α/DOPC/ChoL	3260	2684	1151	5115.0	1.02
α/ChoL	3835	2684	1151	5636.9	1.12

According to the literature, the lipid molecule number on each nanoparticle is estimated using the equation below:

$$N_{FA} = P \times 4\pi (d/2)^2/a$$

Where P is the percentage of the specific lipid in the outer layer, d is the diameter of nanoparticle obtained from light scattering measurement and taken as 40 nm, and a is the average area per lipid molecule, and calculated as $a = a_1N_1 + a_2N_2 + \ldots a_nN_n$, where N is the molar fraction of each component. The approximate area was shown in Table S5.1.

As the topological polar surface area (***a***) of DOPC is far larger than that of cholesterol (1.11 nm^2 *v.s. 0.*202 nm^2, data obtained from PubChem database), the decrease of DOPC in the outer layer from 50% to 35% may result in less close-contact outer layer (Figure S1A, defective model). On the contrary, the decrease of ChoL in the outer layer would lead to a crowded lipid outer layer (Figure S1A, oversaturated model). According to a calculation, 15% α-TOS replacement would cause about 10% surface area change (decrease in α/DOPC NPs and increase in α/ChoL NPs) compared to the pristine one (α/BLK NPs), whereas the α/DOPC/ChoL NPs remains similarly.

Table S5.4 The effect of gene loading on the physiological features of LCCP NPs with 15% alpha-TOS loading.

Particles	**Number-mean Particle Size (nm)**	**PDI**	**Zeta potential (mV)**	**Loading efficiency (%)**
Without genes	40.8±1.4	0.33	-18.8±1.3	-
With genes	39.2±1.2	0.38	-22.6±1.2	62.6%

Table S5.5 Analysis of the coefficient of drug interaction (CDI) of CD siRNA and alpha-TOS using the mean values of cell viability (%).

Concentrations		**Cell viability**			**CDI***	**Effect**
CD siRNA (nM)	**TOS (μM)**	**CD/FA**	**scr/TOS/FA**	**CD/TOS/FA**		
3	1.3	0.92	0.90	0.79	0.95	Moderate synergistic
6	2.5	0.86	0.87	0.64	0.86	Moderate synergistic
12	5	0.82	0.82	0.56	0.83	Moderate synergistic

24	10	0.80	0.54	0.44	1.01	Additive
48	20	0.74	0.51	0.34	0.90	Moderate synergistic

* CDI = [CD/TOS-FA] / ([CD/FA]*[TOS-FA])

Where CDI < 0.7 indicates a strong synergistic effect, CDI < 1 indicates a synergistic effect, CDI = 1 indicates an additive effect, and CDI > 1 indicates an antagonistic effect.

Table S5.6 The comparison of cell viability of CD/TOS-FA and other kind of NPs with free CD siRNA and/or alpha-TOS supplement.

CD siRNA (nM)	**TOS (μM)**	**CD/TOS/FA**	**CD/FA *+TOS***	**scr/TOS/FA *+CD***	**scr/FA *+CD/TOS***
3	1.3	79.27	95.36	97.83	93.05
6	2.5	64.43	75.00	96.13	89.78
12	5	56.04	66.40	71.80	76.02
24	10	44.97	60.59	60.06	65.91
48	20	34.32	54.82	56.60	65.06

5.2 In vivo work

In this section, we utilized the CD/TOS/FA NPs to treat a metastatic 4T1 tumour model in Balb/c mice. All NPs were synthesized using the optimised condition reported in the previous Section 5.1. The inhibition of tumour growth and metastasis was evaluated. We found that the CD/TOS/FA NPs significantly enhanced the efficacy of inhibiting cancer growth, compared with the control group. Moreover, fewer metastatic clones were found in both lung and liver. No significant cytotoxicity (pathology) were seen in major organs by the treatment. In conclusion, the designed CD/TOS/FA NPs have provided an enhanced anticancer ability by gene/drug combination therapy.

5.2.1 Experimental section

5.2.1.1 Materials

All chemicals used in this work were from Sigma-Aldrich (St Louis, MO) if no specific mentioned. NPs were prepared as previously described. The deionised Milli-Q water (Ω = 18.2 at 25 ℃) was used for all experiments. All materials were stored and used according to the manufactory's guide without further modification.

5.2.1.2 Cell culture

The mouse 4T1 cells were obtained from American Type Culture Collection (ATCC), and cultured in RPMI-1640 medium supplemented with 10% fetal bovine serum (FBS), and 1% penicillin/ streptomycin if no specific mention. The cells were routinely incubated in at incubator pre-set at 37 ℃ with 5% CO_2 under certain humidity. The 0.25% trypsin with EDTA was used to subculture cells.

5.2.1.3 Mouse model

All animal experiments were processed according to the protocols approved by the University of Queensland's Animal Ethics Committee (AE224_18). The 6-8 week old female Balb/c mice were randomly divided into the following 4 groups (n = 5): saline group, CD/FA group, scr/TOS/FA group, and CD/TOS/FA group. All mice were subcutaneously (s.c.) inoculated with 2×10^6 of 4T1 cells suspended in serum and antibiotics free medium to the left flank on day -14, followed by a second s.c. inoculation with 1×10^6 of 4T1 cells to the right flank on day -7. When the tumour volume reached 50-70 mm^3 at day 0, the mice were intraperitoneally injected with saline, or NP suspension containing 0.2 mg/kg CD siRNA and/or 5 mg/kg α-TOS.

The treatments were repeated at day 2, 4, and 6 with the same dosage. The tumour size and body weight were recorded every other day. Mice were sacrificed when the average tumour size of this group reached the ethics permission (1000 mm^3). The tumour volume (V) was calculated using a simple algorithm equation: $V = 0.5 \times length \times wide^2$.

5.2.1.4 Organ dissociation

The freshly harvested liver and lung were dissociated for metastasis clone culturing according to the reported protocol [1]. In brief, the whole organs were cut into dices and merged into collagenase IV (1.5 mg/mL in PBS, Sigma). After 1 h digestion at 37 ℃, the tissue was spun down and treated with a dispase (2 mg/mL in PBS with calcium/magnesium, Sigma) and DNase (0.1 mg/mL, Sigma) cocktail for 10 min at 37 °C. The digestion was ceased by exceeded medium to form 10 mL cell suspension (as 1:10 dilution), followed by passing through a 70 μm strainer to obtain the singlet cells. The cells were then cultured in 6-well plates in a series of dilution (1:10-1:250). All culturing was performed in medium containing 60 μM of 6-thioguanine to select 4T1 cancer cells. After 20 days selection, the 4T1 tumour clones were fixed with 4% paraformaldehyde (PFA) for 30 min, followed by visually staining by 0.1% crystal violet for another 30 min. The images were taken and analysed using ImageJ software to quantify the clone area. The metastasis index was calculated (clone area% × dilution) to represent the cancer metastasis.

5.2.1.5 Histopathological analysis and imaging

The freshly harvested organs were merged in 4% PFA, followed paraffin inclusion to prepare 5 μm thick sections. Haematoxylin-eosin (H&E) staining was performed for histological analysis. Tissue slides were imaged using an Olympus BX61 light microscope.

5.2.1.6 Statistical analysis

In all experiments, date shown were representatives that performed at least two time. When applicable, statistical analysis was performed by student's t-test using GraphPad if no further instructions. The difference with a p-value <0.05 was deemed significant at a minimum. *, $p < 0.05$; **, $p < 0.01$; ***, $p < 0.001$; and ****, $p < 0.0001$.

5.2.2 Results

The inhibitory effect on 4T1 cell growth by NPs was evaluated by MTT assay in vitro (Figure 5.9A). All NP treatments inhibited cell growth in a dose-dependent manner. In general, the

CD/TOS/FA NPs exerted a comparable efficacy to scr/TOS/FA NPs, but were more efficient than CD/FA NPs. These data suggest CD/FA NPs had a weaker influence on 4T1 cell growth. In comparison, these NPs performed similar inhibitory effect on 4T1 and B16F0 cells (Figure 5.9 vs. Figure 5.3), suggesting the CD/TOS/FA NPs could be applied as nanomedicines for the combination therapy of multiple types of cancer. The effects of NP treatment on 4T1 tumour growth in Balb/c mice were shown in Figure 5.9. The tumour size of mice with placebo (saline group) quickly reached 1000 mm^3 at day 10, whereas the mice treated with different NPs showed 57.8% (CD/FA group), 51.6% (scr/TOS/FA group), and 28.4% (CD/TOS/FA group) tumour sizes, compared to saline control group on that day (Figure 5.9B). At day 14, mice exerted 1036, 932, and 428 mm^3 of tumour in CD/FA, scr/TOS/FA, and CD/TOS/FA groups, respectively (Figure 5.9B). A similar trend was observed in tumour weight on the same day (Figure 5.9C). The average weight of tumour in these three groups were 1.20 g, 1.10 g, and 0.52 g. These data indicate all NPs can inhibit 4T1 tumour growth compared to the control group. Moreover, the CD/TOS/FA NP presented the strongest anticancer ability compared to CD/FA and scr/TOS/FA NPs in all cases, suggesting gene/drug combination therapy performs enhanced inhibition to in situ primary cancer growth. These results are in accordance with our in vitro data obtained with B16F0 [2] and 4T1 cells, suggesting CD/TOS/FA NPs exerts enhanced anticancer efficacy in multiple cancer cell lines. Generally, significant body weight loss indicated server adverse effect or other health concerns [3]. As shown in Figure 5.9D, a slight weight increase (< 2 g) was observed in all groups during the treatment period. The result suggested no noticeable systematic toxicity was observed.

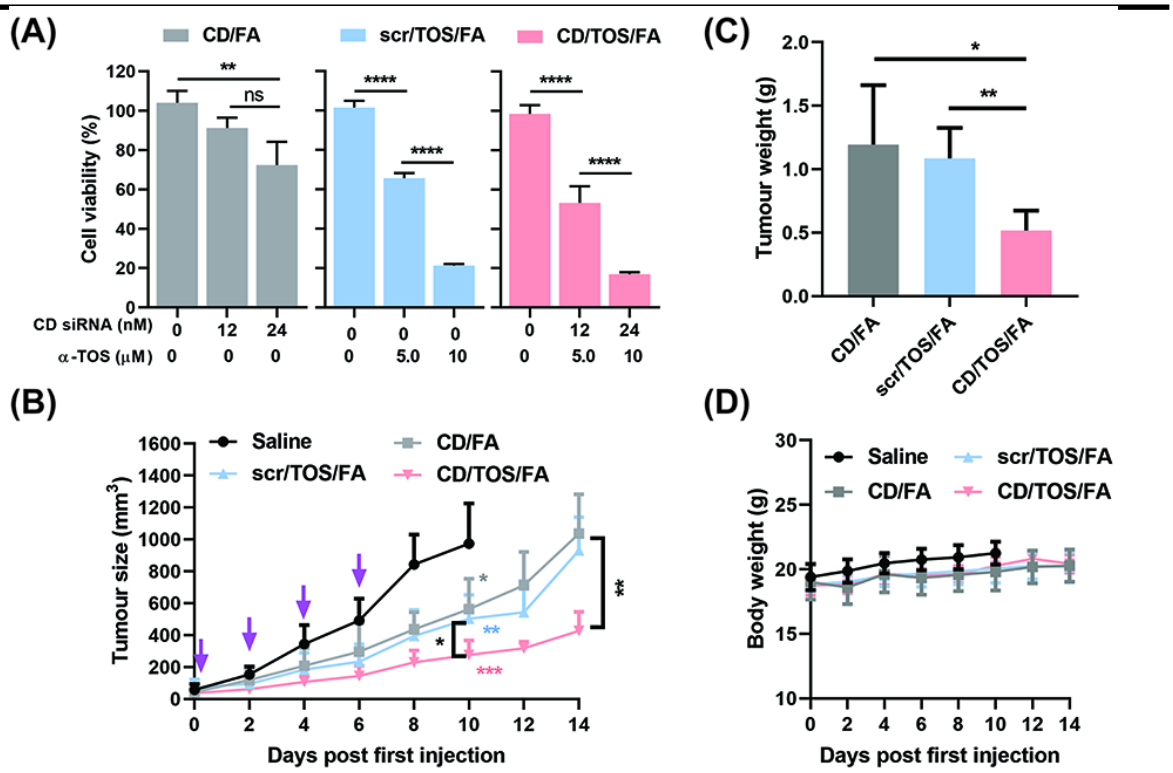

Figure 5.9 The inhibitory effect of NPs on 4T1 cells and the xenograft tumour growth. (A) The inhibition of 4T1 cancer cell growth by NPs in vitro. **(B)** Tumour growth curve represented by tumour size, **(C)** the tumour weight at Day 14, and **(D)** the body weight curves of mice with various treatment. Coloured stars indicating the statistical analysis results between the corresponding group and saline control. Black stars indicating the analysis result between the two indicated groups. Purple arrows indicating the injections of NPs and saline.

We next examined the effect of different treatments on 4T1 metastasis to lung and liver. As shown in Figure 5.10A, 4T1 clones (purple dots) were detectable in both lung and liver, with lung tissues presented more clones than liver in all cases. The metastasis index was calculated by purple area index × dilution, and used to quantify the severity of metastasis (Figure 5.10B). The saline group showed highest metastasis index in lung (61830) and liver (5438) compared to the groups with NP treatment. In contrast, CD/TOS/FA group presented the lowest metastasis index (1135 in lung and 31 in liver) in this experiment. CD/FA and scr/TOS/FA groups showed moderate index values in lung and liver. The results suggest both CD siRNA and α-TOS treatment can inhibit 4T1 metastasis to lung and liver, and the combination of gene and drug provide the best treatment efficacy. Specifically in liver, scr/TOS/FA treatment exerted a metastasis index that was 35.5 fold higher than that of CD/FA treatment (2669 vs.

75). This result suggested α-TOS treatment was not efficient at inhibiting 4T1 metastasis, especially in liver.

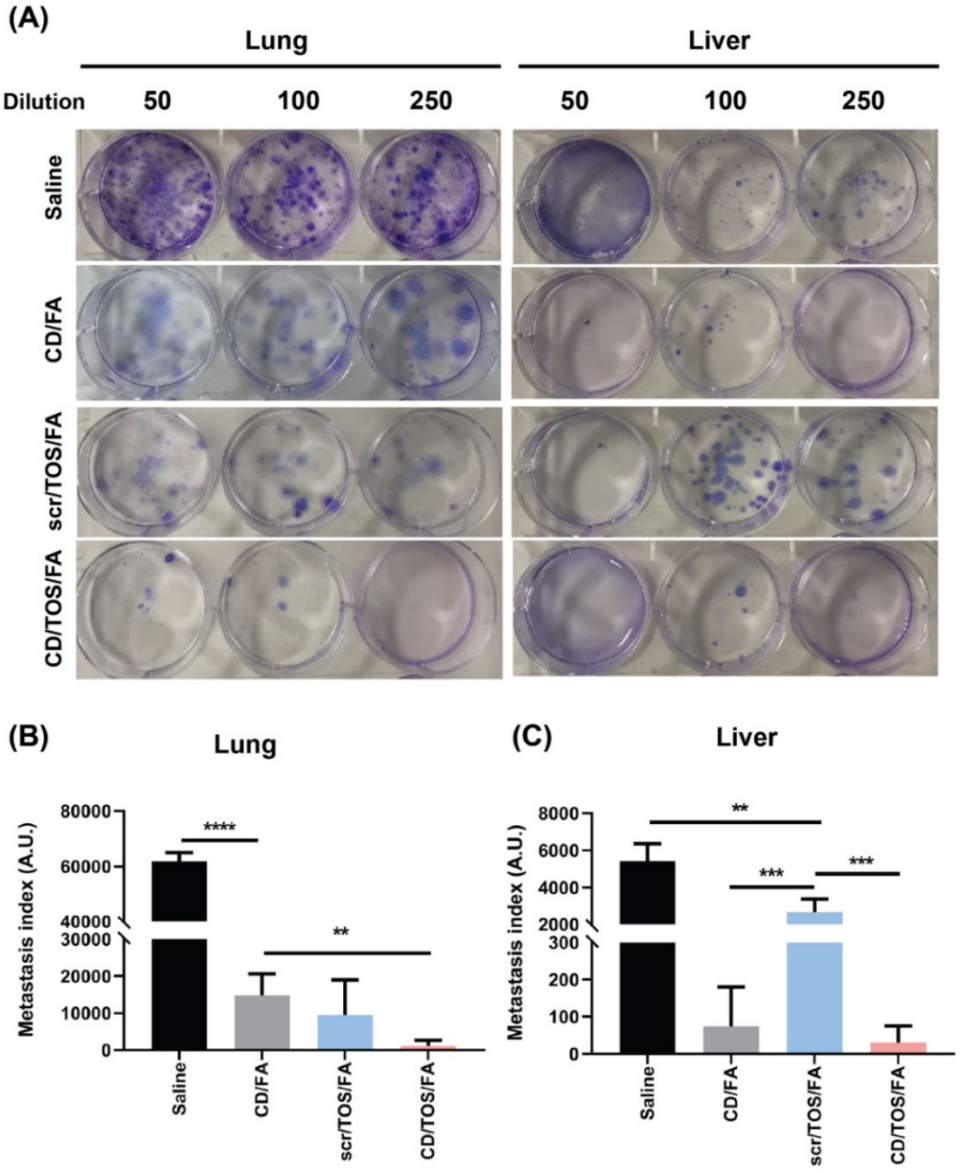

Figure 5.10 The metastasis detection in lung and liver. **(A)** Digital images of metastatic clone stained with crystal violet, and **(B)** the statistical data of metastasis index.

To further verify the metastasis in lung and liver, and check the treatment influence on organs, the H&E staining of major organs were taken for histopathological examination. Figure 5.11 showed the lung histopathological changes after treatment. The lungs in the saline group showed significant abnormal structure, and alveolar decrease. No typical metastatic tumour

nodules were clearly observed, suggesting the tumour cells may not evenly metastasize to the whole organ. In CD/FA and scr/TOS/FA groups, the typical alveolar structure was still observed. Typical tumour nodules with abnormal structure and slightly faint colour were captured (black arrow indicated). The morphology changes suggested moderate metastasis to lung after treatment. For the lung images obtained from CD/TOS/FA group, a structure with abundant alveolar was observed, and almost no tumour nodules and colour changes were found in the stained sections. The results indicated CD/TOS/FA treatment decreased the lung metastasis to the largest extent. The histological examination results were in accordance with that obtained from metastatic clone culture (Figure 5.10). The histological images of lung with 4T1 metastasis were similar to those reported previously [3, 4]. In addition, we did not find any morphology changes in lung cells and blood cells, suggesting our NPs were not toxic to this tissue.

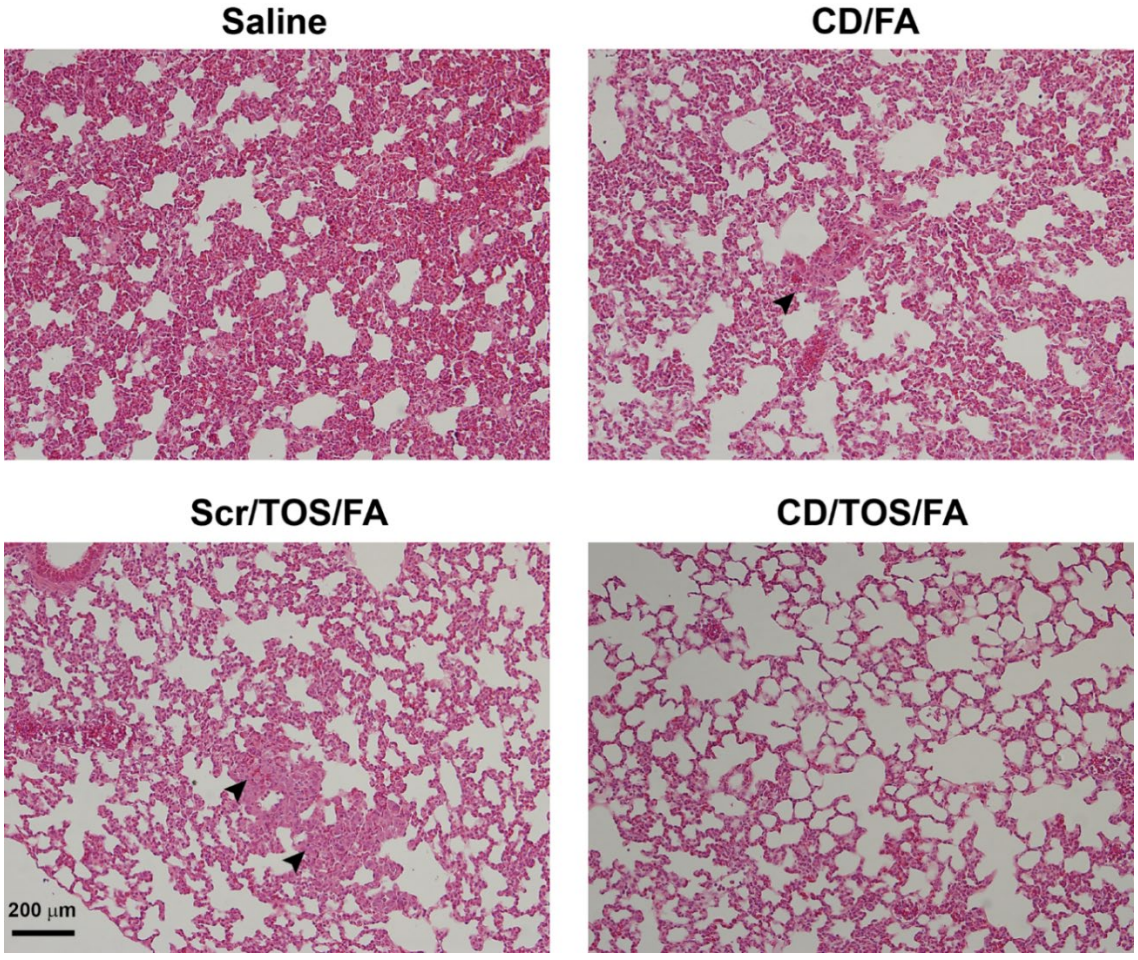

Figure 5.11 Histological examination of lung tissue sections with hematoxylin and eosin staining after treatment. Samples were taken with a 10× objective lens. **Black arrows:** typical metastatic tumour nodules.

The histological images of liver were shown in Figure 5.12. As shown in Figure 5.12A, some area with abnormal dark colour was observed around the central vein (CV) in these images. One of a typical CV was enlarged in each section for examination in Figure 5.12B. In saline group, a large cluster of metastatic cells was found, suggesting the 4T1 cancer cells were able to metastasize to liver through CV. Much less and smaller metastatic cell clusters were found in CD/FA, scr/TOS/FA, and CD/TOS/FA groups around CV in the zoom images in Figure 5.12B, suggesting these treatments led to metastasis inhibition. The histological examination confirmed the metastasis results obtained from clone culturing (Figure 5.10). In addition, some dark and small singlet cells were found in the sinusoid. These cells should be lymphocytes, suggesting these livers were under inflammatory condition due to cancer progression. The histological images of lung with 4T1 metastasis were similar to those reported previously [5, 6]. As shown, hepatocytes in all these section images displayed similar morphology, suggesting all treatments did not cause extra changes to normal liver cells.

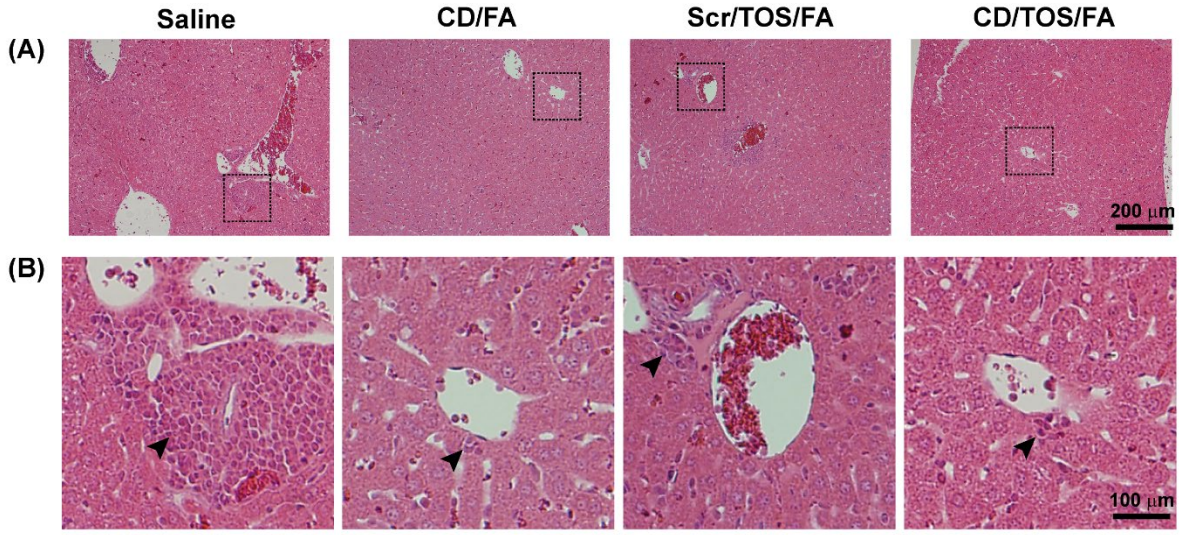

Figure 5.12 Histological examination of liver tissue sections with hematoxylin and eosin staining after treatment. **(A)** Section images captured with a 10× objective lens. **(B)** Enlargement of a typical CV in the dash line area in (A). **Black arrows:** typical metastatic tumour clusters.

The H&E images of heart, spleen, and kidney were shown in Figure 5.13. In general, no obvious changes were observed in all these organ sections. The enlarged images (data not shown) did not present any abnormal cells or regions, suggesting no significant cancer metastasis or treatment-related organ damage happened in these organs. These images indicated our NP related treatments are safe to these organs.

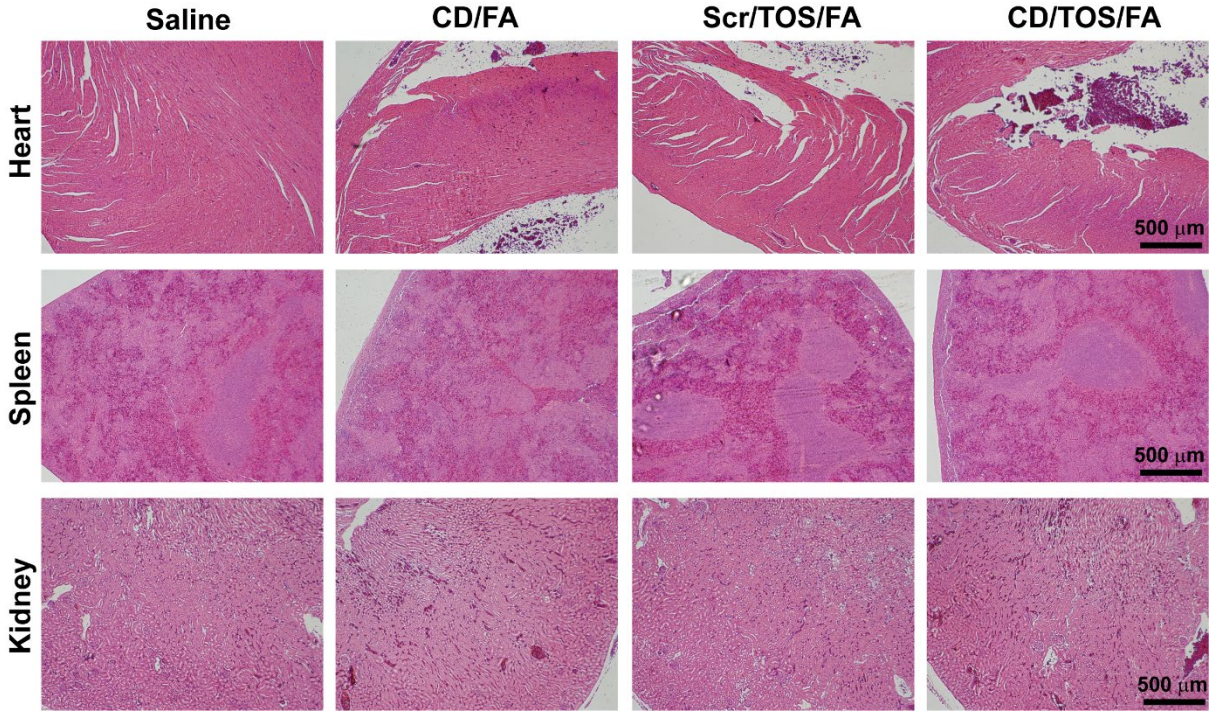

Figure 5.13 Images of heart, spleen and kidney sections stained with hematoxylin and eosin under 4× objective lens.

5.2.3 Conclusion

In this study, the well-designed CD/TOS/FA NPs were used to treat 4T1 tumour. The CD/TOS/FA NPs led to more significant inhibition of in situ cancer growth compared to NPs loading with only one therapeutics. Moreover, the NPs can minimize 4T1 metastasis to both lung and liver during progression. In particular, the combination of CD siRNA and α-TOS drug exhibited a remarkable decrease in both metastatic cancer clones and lesions in the lung and liver. Therefore, our designed CD/TOS/FA NPs provide a promising approach for targeted gene/drug combination cancer therapy.

5.2.4 Reference

[1] D. Redelman, K.W. Hunter Jr, Microenvironment of the murine mammary carcinoma 4T1: Endogenous IFN-γ affects tumor phenotype, growth, and metastasis, Exp Mol Pathol. 85(3) (2008) 174-188.
[2] Y. Wu, W. Gu, Z.P. Xu, Enhanced combination cancer therapy using lipid-calcium carbonate/phosphate nanoparticles as a targeted delivery platform, Nanomedicine 14(1) (2018) 77-92.
[3] C. Chen, Z. Nong, Q. Xie, J. He, W. Cai, X. Tang, X. Chen, R. Huang, Y. Gao, 2-Dodecyl-6-methoxycyclohexa-2, 5-diene-1, 4-dione inhibits the growth and metastasis of breast carcinoma in mice, Scientific reports 7(1) (2017) 6704.
[4] M. Smeda, A. Kieronska, M.G. Adamski, B. Proniewski, M. Sternak, T. Mohaissen, K. Przyborowski, K. Derszniak, D. Kaczor, M. Stojak, Nitric oxide deficiency and endothelial–mesenchymal transition of pulmonary endothelium in the progression of 4T1 metastatic breast cancer in mice, Breast Cancer Res. 20(1) (2018) 86.
[5] D.-W. Zheng, B. Li, C.-X. Li, J.-X. Fan, Q. Lei, C. Li, Z. Xu, X.-Z. Zhang, Carbon-dot-decorated carbon nitride nanoparticles for enhanced photodynamic therapy against hypoxic tumor via water splitting, ACS Nano 10(9) (2016) 8715-8722.
[6] K. Kus, A. Kij, A. Zakrzewska, A. Jasztal, M. Stojak, M. Walczak, S. Chlopicki, Alterations in arginine and energy metabolism, structural and signalling lipids in metastatic breast cancer in mice detected in plasma by targeted metabolomics and lipidomics, Breast Cancer Research 20(1) (2018) 148.

Chapter 6

Enhanced Prevention of Breast Tumour Metastasis by Nanoparticle-delivered Vitamin E in Combination with Interferon-gamma Treatment

Preventing cancer metastasis is one of the remaining challenges in cancer therapy. As an efficient nature product, alpha-tocopheryl succinate (α-TOS), the most effective form of Vitamin E, holds a great anticancer potentiality. To improve its efficacy and bioavailability, the lipid-coated calcium carbonate/phosphate (LCCP) nanoparticles (NPs) with folic acid and PEG modification were synthesised for efficient delivery of α-TOS to 4T1 cancer cells. The optimised LCCP-FA NPs (NP-TOS15) showed an α-TOS loading efficiency of ~60%, and enhanced the uptake by 4T1 metastatic cancer cells. Consequently, the NP-TOS15 NPs significantly enhanced the anticancer effect in combination with interferon-gamma (IFN-γ) treatment in terms of apoptosis facilitation and migration inhibition. Importantly, NP-TOS15 upregulated the anticancer immunity via downregulating program death ligand 1 (PD-L1) expression induced by IFN-γ, and remarkably prevented the lung metastasis, particularly in combination with IFN-γ. Further investigation revealed that this combination therapy also modulates the cytotoxic lymphocyte infiltration into the tumour tissue for tumour elimination. Taken together, the NP delivery of α-TOS in combination with IFN-γ provides an applicable strategy for cancer therapy.

6.1 Introduction

Cancer has been recognised as the leading cause of death worldwide. Apart from the morbidity associated with unrestrainable tumour growth, cancer metastasis remains the most significant cause of cancer-related death, due to the limited success of controlling metastatic progression [1, 2]. As is well known, the tumour invasion is companied with the modulation of the microenvironment and the suppression of anticancer immunity at the early stage [3, 4]. During this modulation, the immune cells are reshaped by tumour milieu to fulfil tumour invasion requirements. Therefore, enhancing the anticancer immunity will benefit the treatment of highly metastatic cancers.

Cytokines, small peptides secreted by immune cells, affect cell signalling and immunomodulation and are often employed in preventing cancer progression. One example is interferon-gamma (IFN-γ), a typical anticancer cytokine produced by activated T cells and natural killer cells. IFN-γ facilitates anticancer immunity via recruiting highly immunogenic cells such as $CD4^+$ and $CD8^+$ T cells, and infiltrates M1 phase tumour associated macrophages (TAMs) [5]. However, most of the clinical trials have failed in inhibiting cancer progression by IFN-γ [6]. The major reason is that long-term exposure to IFN-γ causes adaptive cancer immune resistance [3]. The most important mechanism of this resistance is induction of program death-ligand 1 (PD-L1) expression on the tumour surface. PD-L1 binds to its receptor program death 1 (PD-1) expressed on T cells, causing the inactivation of T cells and cancer immune escape [7]. In clinical, high PD-L1 expression correlates with metastasis and poor prognosis [8, 9]. Unlike the endogenous controlled expression of constitutive PD-L1s [10], IFN-γ-induced PD-L1 expression is associated with a quick response of the p65 subunit to IFN-γ stimulation for the nuclear factor kappa B (NF-κB) signalling in cancer cells [11].

To maintain the positive but minimise the negative effect on the anticancer immunity, IFN-γ treatment has been often combined with other therapy, such as chemotherapy [12, 13]. Some natural products, such as vitamins and their derivates, are able to reverse IFN-γ-mediated immune resistance. One example is alpha-tocopheryl succinate (α-TOS), the most effective derivate form of vitamin E that is often used in cancer treatment. As a broad spectrum anticancer agent, α-TOS has been reported to induce significant apoptotic cell death in about 50 cancer cell lines [14]. Related studies reveal that α-TOS exerts selective toxicity to cancer cells, with low toxicity to the non-cancer cells [15-17]. Moreover, α-TOS regulates the anti-

tumour immunity. Previous investigations indicate that α-TOS activates T cells and has been combined with other cancer treatment to facilitate the therapy [18, 19]. Particularly, α-TOS is able to regulate NF-κB signalling by limiting its typical protein p65's translocation [20]. In this context, we hypothesise that combining α-TOS with IFN-γ inhibits the tumour growth and moreover promotes suitable anti-tumour immunity for effective prevention of tumour metastasis.

Here is an issue that the application of α-TOS requires a high dose mainly due to its poor water solubility and bioavailability. Thus, a proper delivery system is required. The lipid-coated calcium carbonate/phosphate (LCCP) nanoparticles (NPs) have been proven to be efficient in gene/drug delivery in vitro and in vivo [21-23]. As demonstrated in our previous study, the outer lipid layer of LCCP NPs is able to load α-TOS, with further modifications for long circulation (PEGylation) and tumour targeting delivery (with folic acid, FA) [23]. In this research, we aimed to develop such a nano-platform and confirm whether NP-loaded α-TOS is able to inhibit tumour growth and prevent tumour metastasis in combination with IFN-γ treatment. Our data have revealed that NP-formulated α-TOS efficiently inhibited tumour growth and downregulated PD-L1 expression induced by IFN-γ, so as to promote anti-tumour immunity and prevent tumour metastasis. This research has thus provided a new cancer therapeutic regimen by just combining two commonly-used biomolecule drugs (α-TOS and IFN-γ) not only for the treatment of the primary metastatic tumour, but also for prevention of tumour metastasis.

6.2 Experimental

6.2.1 Materials

All chemicals were purchased from Sigma-Aldrich (St Louis, MO) if not specially mentioned. Antibodies were from BioLegend Inc. (San Diego, CA), with catalogue numbers shown in Table S6.1. All lipids were obtained from Avanti Polar Lipid. Mouse recombinant IFN- γ was from BioLegend Inc., and human recombinant IFN-γ was from Abcam. All chemicals and biomaterials were stored and used according to the manufactory's guide, without further modification.

6.2.2 Synthesis and characterisation of LCCP NPs loaded with α-TOS (NP-TOS)

The preparation of α-TOS loaded (NP-TOS) NPs was based on our previous method, with slight modification [23]. In particular, the molar percentage of each lipid composition in the second layer (Table S6.2) was tested in this research. The NPs were coded as NP-TOS0, NP-TOS15, NP-TOS20, and NP-TOS 30 according to the initial α-TOS percentage used for the second lipid layer. To prepare FITC labelled NP-TOS15 NPs (NP-TOS15-FI), BSA-FITC was added in the phosphate/carbonate micro-emulsion before mixing with calcium micro-emulsion. To prepare Rh-PE labelled NP-TOS15 NPs (NP-TOS15-Rh-PE), an extra 0.5 mol% of 18:1 Liss Rhod PE lipid was included in the second lipid layer.

The loading efficiency of α-TOS was examined by measuring its absorbance at 278 nm after dissolving NP-TOS NPs in pH 5 buffer solution. For quantifying FITC and Rhod-PE, NP-TOS15 NPs were dissolved in lysis buffer (2 mM EDTA, and 0.05% Triton X-100 at pH 7.8). The fluorescent intensity of the lysate was measured for FITC (Ex = 488 nm, Em = 525 nm) and Rhod-PE (Ex = 488 nm, Em = 585 nm) using a plate reader (BioTek, Winooski, VT, USA).

The hydrodynamic diameter and zeta potential of NP-TOS15 were measured using a Malvern NanoSizer (Malvern, UK). All samples were dispersed in water at about 40 μg/mL. The morphology of NP-TOS NPs was observed using a transmission electron microscope (TEM, JEM-3010, ZEOL, Tokyo, Japan) by drying a drop of NPs on a 300 mesh carbon-coated copper grid.

6.2.3 Cellular uptake of NP-TOS15

The 4T1 cells from the American Type Culture Collection (ATCC) were grown in RPMI-1640 medium supplemented with 10% fetal bovine serum (FBS) and 1% penicillin/streptomycin in an incubator at 37 °C with 5% CO_2. The cells were seeded in a 24-well plate with acid-treated coverslip at a density of 2×10^5 cells per well and cultured overnight. Then cells were cultured in fresh medium containing NP-TOS15-PE NPs with 300 nM Rhod-PE for 4 h. The coverslips were rinsed with PBS and fixed in 4% PFA, then mounted on a slice with a drop of DAPI-fluoshield. The specimens were visualised using a confocal laser scanning microscope.

Similarly, cells were seeded in a 12-well plate at 10^5 per well for detecting the intracellular fluorescence using flow cytometry. After the overnight culture, the cells were fed with NP-TOS15 NPs at 200 nM Rhod-PE and/or 1 μg/mL BSA-FITC. After culturing for 1-4 h, cells

were collected and re-suspended in PBS. The samples were analysed using a CytoFLEX flow cytometry (FACS, Beckman, IN).

6.2.4 Anticancer activity of NP-TOS15 in vitro

Cells were seeded in a flat-bottom 96-well plate at 8,000/well overnight. Then cells were treated with free α-TOS, NP-TOS15, and/or IFN-γ for 48 h. Fresh medium with MTT ((3-(4,5-Dimethylthiazol-2-yl)-2,5-diphenyltetrazolium bromide) was replenished and after 4 h incubation, the medium was replaced by 100 μL/well DMSO to dissolve formazan crystal. Values presenting cell viability were determined by the absorbance at 570 nm on a Tecan plate reader. Cell viability was calculated accordingly [24].

The apoptosis/necrosis of treated cells was analysed using a FITC Annexin V Apoptosis Detection Kit (BioLegend). Briefly, 4T1 cells in a 12-well plate at 2×10^5/well were treated with IFN-γ (5 ng/mL), free α-TOS (20 μM), NP-TOS15 (10 μM) and IFN-γ/NP-TOS15 (5 ng/mL and 10 μM) for 24 h. The cells were then collected and suspended to 10^6 cell/mL in Annexin V binding buffer, followed by adding 5 μL FITC Annexin V and 10 μL propidium iodide (PI) to each 0.1 mL suspension and incubating in the dark for 15 min. Then 400 μL of Binding buffer was added in each sample to cease the staining. Cells were analysed using a Beckman flow cytometer. Untreated cells without staining or with single staining were used for control to adjust the compensation.

The cell cycle analysis was performed using 12-well plates seeded with 2×10^5 4T1 cells in each well. After overnight culturing, cells were treated with IFN-γ (5 ng/mL), free α-TOS (20 μM), and/or NP-TOS15 (10 μM) for 24 h. Then the cells were harvested and fixed at 4 °C for 30 min using pre-chilled 70% ethanol, followed by staining with PI (50 μg/mL). The samples were analysed using a Beckman FACS flow cytometer. Singlet cells were gated for cell cycle phase analysis according to their PI intensity as Sub G1 (0-120 k), G1 (120 k-200 k), S (200 k-240 k), and G2/M (240 k-400 k).

6.2.5 NP-TOS15 effect on cell migration

The migration ability of 4T1 cells was assessed by the wound healing in vitro model. Briefly, 2×10^5 cells /well were seeded in a 12-well plate and cultured for 24 h to fully spread in the well. Then the wound was artificially made using a 200 μL yellow tip drawing a straight line

in each well. After washing with PBS to remove suspended cells, 1 mL of medium without FBS and PS was added in each well, containing 10 μM α-TOS or 5 μM NP-TOS15 in the presence/absence of 5 ng/mL IFN-γ. After 24 h treatment, the medium was replenished by fresh medium (FBS and PS free) for another 24 h culturing. Cells in complete medium with FBS/PS for 48 h, or with/out IFN-γ for 24 h were imaged to assess the influence on migration. The digital images were taken at 0 h, 24 h, and 48 h after wounding. The width of the wound was randomly measured in 6 places using ImageJ software and the average cell migration degree and average migration distance were calculated:

$$\text{Migration degree} = 100\% \times (WW0-WWt)/WW0$$

$$\text{Migration distance} = (WW0-WWt)/2$$

where WW0 is the wound width at 0 h and WWt the wound width at t h post treatment.

6.2.6 Evaluation of surface and intracellular PD-L1 expression

For surface PD-L1 expression detection, 10^5/well of 4T1 cells were seeded in a 12 well plate overnight, followed by 48 h treatment with IFN-γ, free α-TOS, NP-TOS and IFN-γ/NP-TOS15. The treated cells were then collected and stained with 1:1000 diluted PE-conjugated anti-mouse PD-L1 antibody (BioLegend) in FACS buffer (PBS containing 2% FBS). After 20 min staining, cells were rinsed with FACS buffer before analysis in a Beckman FACS flow cytometer. Similarly, this experiment was done in B16F0 and MCF-7 cell lines, with PE-conjugated mouse/human anti-PD-L1 staining.

For determining intracellular PD-L1 expression, the treated cells were stained with PD-L1 antibody firstly, then permeabilised with 1% saponin, and restained with PD-L1 antibody. Cells without first or second PD-L1 antibody staining were similarly prepared for comparison.

To prepare samples for reverse transcription PCR (RT-PCR), 4T1 cells were seeded in 6-well plates (4×10^5 cells/well) overnight. After treatment with IFN-γ, free α-TOS, NP-TOS15 and IFN-γ/NP-TOS15 for 24 h, the cells were rinsed and harvested in Trizol reagent (1 mL/well). The total RNA was extracted and the reverse transcription was performed using a High capacity RT kit (Invitrogen). Rea-time RT-PCR was carried out to quantify the expression of PD-L1 mRNA gene. Mouse β-actin was recorded in the same assay as the internal control for calculating the relative expression of PD-L1 mRNA gene.

To prepare cell fractionation lysate, 6-well plates were seeded with 10^6 /well of 4T1 cells. After 1 h treatment with IFN-γ, free α-TOS, NP-TOS15 and IFN-γ/NP-TOS15, the cells were collected and fractionated in a lysis buffer (20 mM HEPES, 10 mM KCl, 2 mM $MgCl_2$, 1 mM EDTA, 1 mM EGTA, 1 mM DTT, and 1×PI cocktail, pH adjusted to 7.4). The samples were kept on ice for about 40 min to allow adequate lysis, with the help of passing through a 25G needle occasionally. The suspension was centrifuged at 3,000 rpm for 10 min to harvest the pellet containing nuclei and supernatant containing cytoplasm. Nuclei were resuspended in RIPA buffer and homogenised to briefly shear the genomic DNA. Western blotting for nuclei and cytoplasm was conducted according to the previous protocol [23].

The confocal microscope observation of p65 protein was performed using the same method as for cellular uptake. The anti-p65 antibody (BioLegend) was incubated at 4°C overnight and the Alex 488-anti Rabbit IgG antibody (Abcam) was incubated at the ambient temperature for 1 h. Both antibodies were used at the recommended dilutions.

6.2.7 Evaluation of in vivo antitumor activity

All experiments were approved by the University of Queensland, and carried out in accordance with the institutional guidelines for animal experimentation. Female Balb/c mice at 6-8 weeks old were used for this set of experiment. For tumour model establishment, 2 million of 4T1 cells suspended in PBS were subcutaneously inoculated to the left flank of mice. When the tumour grew to about 100 mm^3 in volume, saline containing NP-TOS15 (5 mg/kg α-TOS equivalent) and/or IFN-γ (0.25 mg/kg, equivalent 5×10^5 IU/kg, BioLegend) was injected to each mouse intraperitoneally on day 0, 2, 4, and 6. Tumour size and body weight were measured with a digital calliper every other day. The tumour size was calculated using a simple algorithm ($0.5\times length\times wide^2$). Mice were sacrificed at day 10 as the tumour volume in the saline group reached the permitted size.

The freshly harvested organs were fixed in 4% PFA, followed by paraffin embedding to prepare 5 μm thick sections. Haematoxylin and eosin (H&E) staining was conducted for histological analysis. The slices were examined using an Olympus BX41 light microscope with 4×, 10×, and 20× lens.

6.2.8 Lung metastasis detection

Freshly harvested lung/liver tissues were digested using the method reported elsewhere [25]. After digestion, the tissue suspensions were spun down at 400 g for 5 min to collect dissociated cells. The pellets were resuspended in 10 mL medium with FBS and antibiotics at a 1:10 dilution, and passed through a 70 μm strainer. The obtained cells were then diluted to 1:100, 1:500 and 1:1000 in 6-well plates for further culturing. To select 4T1 cancer cells against normal tissue cells, 60 μM of 6-thioguanine was supplemented to each well. The medium was refreshed 3-4 times during the culture. After culture for 40 days, the 4T1 clones were fixed with 4% PFA for 30 min, followed by staining with 0.1% crystal violet for 30 min. The images were taken and analysed using ImageJ software to quantify the area% of clones in each well. An average metastasis index (MI) for each specimen was calculated as

$$MI = \sum_{i=1}^{3} (\mathrm{Ai\%} \times \mathrm{Ni})$$

Where Ai% is the clone area, and Ni the dilution time

6.2.9 Quantification of tumour cell population and surface marker expression

Tumours were harvested at day 10 and digested with Collagenase IV (1.5 mg/mL in PBS with calcium/magnesium, Sigma) for 1 h at 37 °C, followed by dispase (2 mg/mL in PBS with calcium/magnesium, Sigma) and DNase (0.1 mg/mL, Sigma) cocktail for 10 min at 37 °C. The digestion was ceased by adding exceeded medium, and the singlet cell suspension was collected by passing through a 70 μm strainer. The cell number was counted using trypan blue, and adjusted to 10^8 cells/mL. The suspension was stained with APC-anti CD45, APC-anti I-A/I-E, PE-anti PD-L1, FITC-anti CD4, PerCP-Cy5.5-anti CD8, and/or PE-anti PD-1 antibodies at recommended dilutions. After staining for 30 min, the cells were rinsed with FACS buffer and analysed using a Beckman flow cytometer.

6.2.10 Statistical analysis

In all cases, data are presented as the mean of at least two repeated data. When applicable, statistical analysis was performed by student's t-test using GraphPad if no further instructions. Data with a p-value <0.05 were deemed significant at a minimum. *, $p < 0.05$; **, $p < 0.01$; ***, $p < 0.001$; and ****, $p < 0.0001$.

6.3 Results

6.3.1 Physicochemical features of LCCP NPs loaded with α-TOS (NP-TOS)

The LCCP NPs with DSPE-PEG and DSPE-PEG-FA modification was synthesised based on the method reported previously [23]. Accordingly, partial outer layer lipids of LCCP NPs were supposedly replaced by a portion of α-TOS, as shown in Table S6.2 in detail. The size and morphology of these NPs are illustrated in Figure 6.1A and S6.1. The α-TOS-loaded NPs showed a slight increase in the hydrodynamic diameter from 39.5±6.4 to 67.9±4.3 nm with the nominal molar percentage of α-TOS changing from 0% to 30% in the outer layer composition. Simultaneously, the PDI increased from 0.24 to 0.55, suggesting α-TOS loading resulted in a broader size distribution [23]. The TEM image in Figure 6.1B elucidated the morphology changes after drug loading. Generally, the LCCP NPs showed ~20 nm dark core coated with a faint lipid layer, in accordance with the shape of LCP and LCC NPs [26, 27]. The overall size of LCCP-α-TOS (NP-TOS) NPs in TEM images was about 30 nm in all cases. These observations indicate that α-TOS loading does not affect the basic shape of NP-TOS NPs, especially the core size. In Figure 6.1B, NP-TOS0 and NP-TOS15 showed singlet dispersed cores in their corresponding TEM images, consistent with their narrow PDI value obtained from DLS. In comparison, NP-TOS20 and NP-TOS30 exhibited some agglomeration in the TEM images (Figure S6.1). The agglomeration may be caused by the inclusion of α-TOS, which destabilize the outer layer in the aqueous phase considering the acetate group grafted on α-TOS reduces the amphiphilicity. Some irregular lipid packing was observed in the TEM image of NP-TOS30 (arrow indicated in Figure S6.1). Similarly, previous studies on phospholipid liposomes indicate that non-liposomal structures could be observed if the liposomal formulation containing ≥20 mol% of α-TOS [28]. As shown in Figure 6.1C, α-TOS loading led to the surface charge of NP-TOS NPs dropping from -15 mV to around -18 mV. The negative charge was attributed to the negatively charged carboxyl group in α-TOS in deionised water.

As shown in Figure 6.1D, the loading efficiency of α-TOS was 60.0±2.0%, 47.4±1.9%, and 35.0±0.7% in NP-TOS15, NP-TOS20, and NP-TOS30, respectively, corresponding to approximately 6.7, 7.0, and 7.6 wt% of the NP-TOS NPs. The α-TOS loading efficiency is comparable to that in previous reports [23, 29]. The loading efficiency was decreased with the increasing nominal loading, probably due to the short hydrocarbon chain of α-TOS and subsequent irregular lipid structure in the outer layer. Reduction of the phospholipid percentage

led to weak interactions between these biomolecules, thus losing some α-TOS payload. As NP-TOS15 exhibited the highest α-TOS loading and a good size distribution with a narrow PDI, we chose this composition in the following experiments. NP-TOS15 NPs were also lyophilised for storage and further applications, which displayed the similar size and distribution after redispersed in deionised water under gentle sonication (Figure 6.1B).

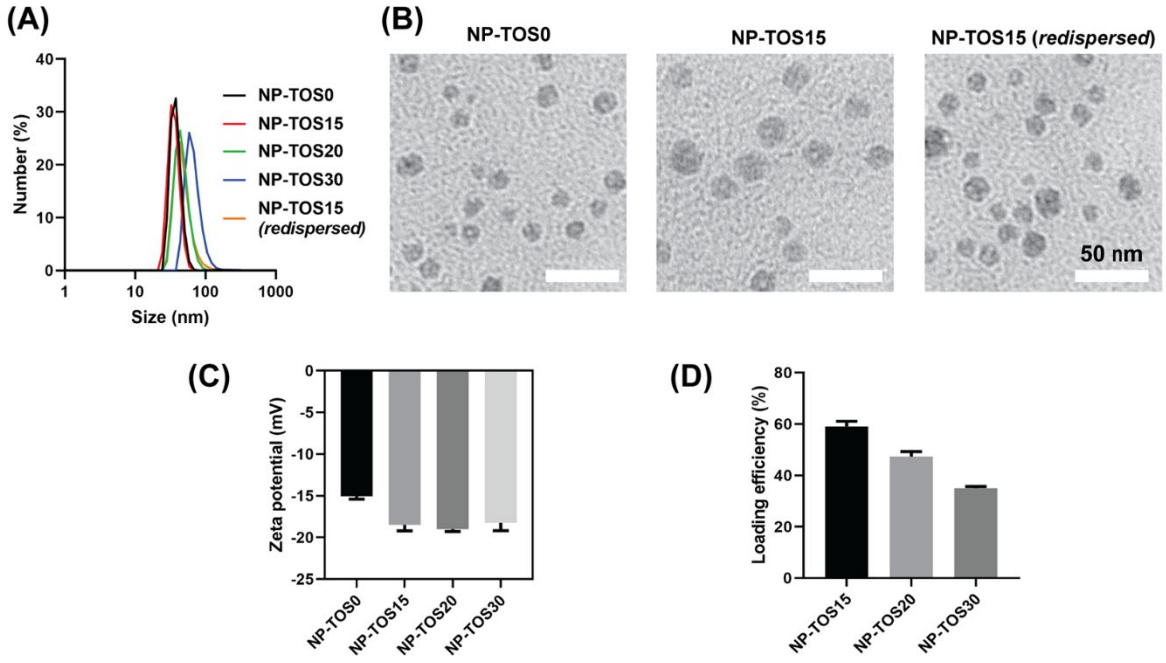

Figure 6.1 Characterisation of LCCP NPs with α-TOS loading (NP-TOS NPs). (A) Hydrodynamic size, and **(B)** morphology from TEM images of NP-TOS0, NP-TOS15 and redispersed NP-TOS15; **(C)** zeta potential of NP-TOS NPs in deionised water; **(D)** the loading efficiency of α-TOS for NP-TOS with different composition.

6.3.2 Enhanced cellular uptake and inhibition of cancer cell growth and migration

To monitor the particle structure integrity, 0.5 mol% of Liss-Rhod-PE phospholipid (Liss-PE) and BSA-FITC were loaded into the lipid layer and the core (NP-TOS15-FI/PE), respectively, for dual labelling (Figure 6.2A). As shown in Figure 6.2B, NP-TOS15-FI/PE increased the PE positive cell percentage and mean fluorescence intensity (MFI) when compared to free Liss-PE lipids. Interestingly, the uptake profiles by 4T1 cells were very similar in terms of both PE and FITC positive cell percentage (Figure 6.2C). Furthermore, the confocal microscope images

(Figure 6.2D) display the overlapping distributions of two fluorescent molecules within cells, revealing that the NPs maintain the lipid-coated structural integrity after cellular internalisation.

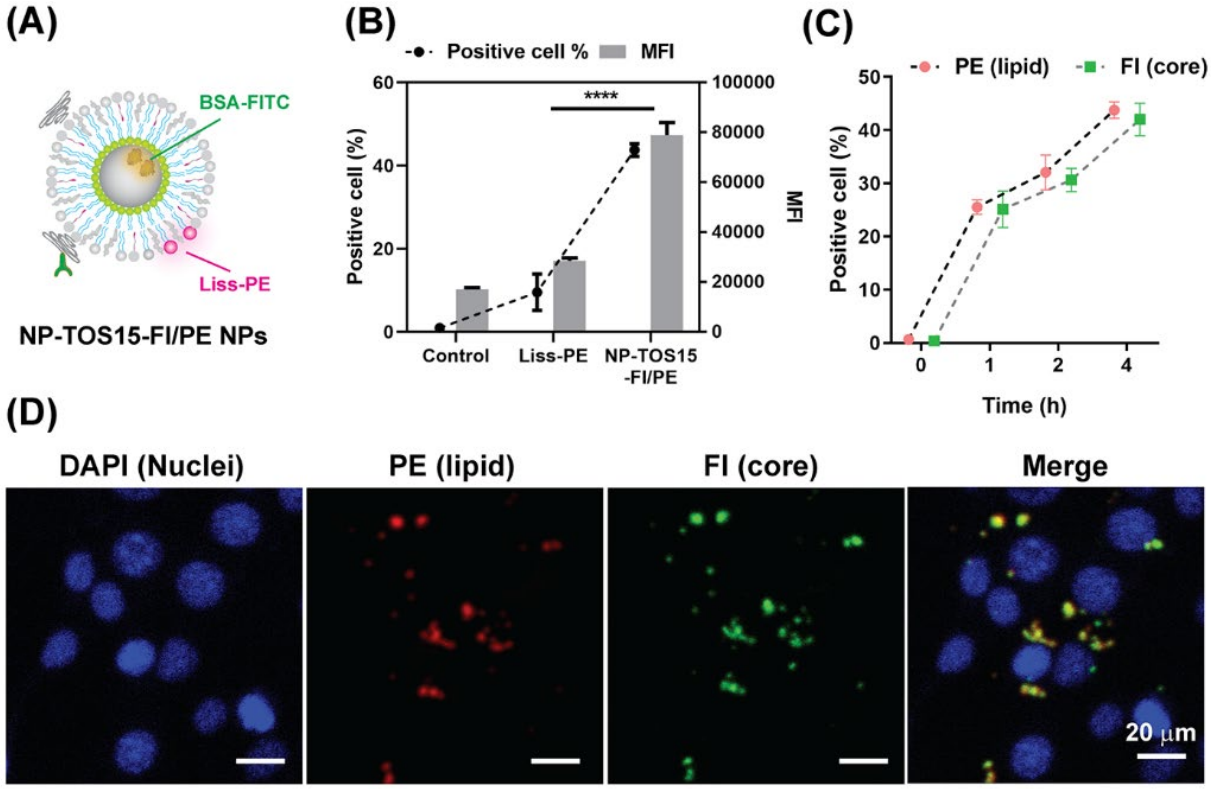

Figure 6.2 Cellular uptake and intracellular distribution of NP-TOS15-FI/PE. (A) The model of dual labelled NP-TOS15-FI/PE NP; Cellular uptake of 4T1 cells incubated with **(B)** free PE lipids or NP-TOS15-FI/PE, and **(C)** the influence of incubation time on positive cell percentage; **(D)** Intracellular distribution of NP-TOS15-FI/PE after incubating with 4T1 cells for 4 h.

As shown in Figure 6.3A, both NP-TOS15 and free α-TOS displayed inhibition effect to 4T1 cancer cells after 48 h treatment in a dose-dependent manner. The IC_{50} values for NP-TOS15 and α-TOS were 5.0 vs. 22.3 μM, indicating the efficacy of NP-TOS15 was 4 times higher than that of free α-TOS. Moreover, the combination of α-TOS and IFN-γ treatment enhanced the cell apoptosis, as shown in Figure 6.3B. IFN-γ did not exert significant inhibition to 4T1 cell growth at 5 ng/mL. The limited anticancer effect of IFN-γ in vitro is understood as IFN-γ-mediated anticancer activity is majorly through activation of immune cells in vivo. However,

5 ng/mL of IFN-γ with 20 μM of free α-TOS and 10 μM of α-TOS in NP-TOS15 significantly decreased the 4T1viability from 68.0% to 45.1%, and 23.4% to 12.4%. The combination index calculated [30] (Figure S6.2) indicates that the combination treatment of IFN-γ and α-TOS in both formulations generated an additive to a moderate synergistic effect.

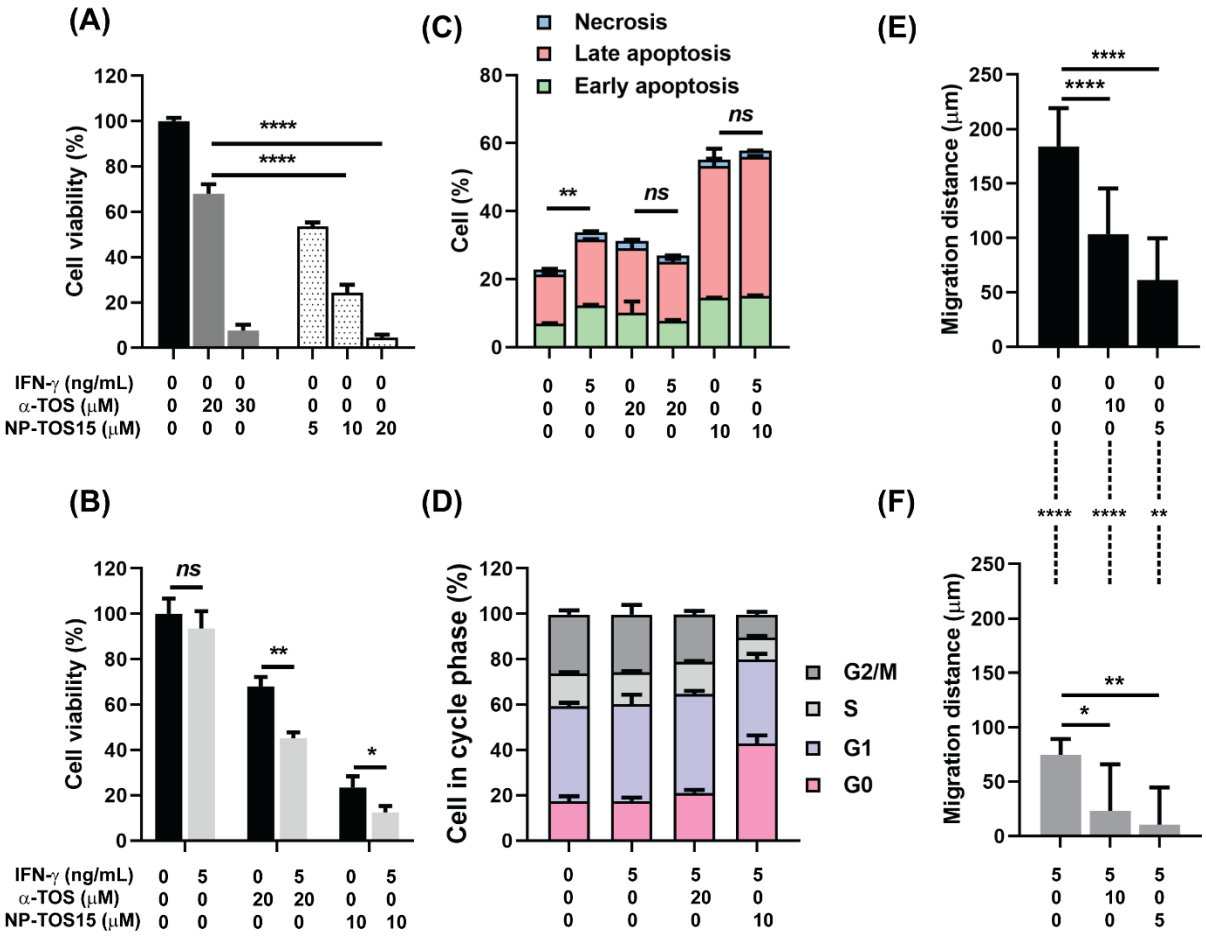

Figure 6.3 The effect of NP-TOS15 and α-TOS combined with IFN-γ on cell growth and migration. (A) The inhibition of NP-TOS15 and free α-TOS to cells after 48 h treatment. **(B)** The effect of IFN-γ dose on the cells in 48 h combination. The influence on **(C)** apoptosis induction and **(D)** cell cycle arrest to 4T1 cells with 5 ng/mL IFN-γ, 20 μM α-TOS, and/or 10 μM NP-TOS15 for 24 h. Migration distance of 4T1 cells in vitro with **(E)** 0 ng/mL and **(F)** 5ng/mL IFN-γ.

Furthermore, NP-TOS15 treatment resulted in increased early and late apoptosis (Figure 6.3C and S6.3A), as reported in the literature [20]. Specifically, this treatment increased the late apoptotic cells from 14.4% to 38.7% and the early apoptosis from 6.9 to 15.1%. The large

increase of late apoptosis upon NP-TOS15 treatment is mainly attributed to the enhanced cellular uptake (Figure 6.2) and subsequent cell death (Figure 6.3A). As expected, IFN-γ exhibited limited facilitation to early/late apoptosis when combined with α-TOS and NP-TOS15 (Figure 6.3C and S6.3). Actually, IFN-γ induced limited cell apoptosis (Figure 6.3C).

Interestingly, NP-TOS15 caused the significant cell cycle changes of 4T1 cells (Figure 6.3D and S6.3B). Compared to the control group, IFN-γ treatment led to no change in the cell cycle composition, while α-TOS-treated at 20 μM showed 10% increase in G1 phase (52% vs. 42%) and a small sub-G1 phase increase (21% vs. 17%) (Figure S6.3B), as reported in previous literature [31]. In sharp contrast, NP-TOS15 treatment led to a significant sub G1 phase increase (43% vs. 17%), indicating a strong induction of apoptosis to cells, in consistence with our previous observation (Figure 6.3C). The IFN-γ combination treatment increased the sub G1 phase to 47%, further suggesting the limited apoptosis induced by IFN-γ.

The 4T1 cell migration ability was examined in a 700-1000 μm wound model. The data are shown in Figure 6.3E and F and S6.4. Generally, free α-TOS or NP-TOS15-treated cells migrated at a much shorter distance (50-100 μm) in 24 h, suggesting that α-TOS inhibited cancer cell migration [32]. Meanwhile, exposure to IFN-γ (5 ng/mL) led the migration distance to be decreased from 184 to 75 μm (Figure 6.3E and F), similarly in previous studies [25]. The combination of α-TOS or NP-TOS15 with IFN-γ led to an even shorter migration distance. The similar trend was observed in cell migration degree (Figure S6.4). To minimise the wound healing mediated by cell proliferation, the above experiment was performed in serum-free medium. The serum-free control led to 20-25% decrease of cell migration degree (160-200 μm in distance) after 24-48 h.

6.3.3 Suppression of PD-L1 expression upon NP-TOS15 treatment

The single treatment of free α-TOS did not exert significant influence on pristine PD-L1 expression in 4T1 (8% pristine PD-L1) and B16 (97% pristine PD-L1) cells, with exceptions at extremely high dose (80 μM, Figure S6.5). In comparison, 5 ng/mL IFN-γ treatment led to a tremendous increase (8% to 72%) in PD-L1 expression on the 4T1 cell surface (Figure 6.4A). The PD-L1 induction by IFN-γ has been previously reported, and this regulation impairs the immunity for cancer therapy [3, 11].

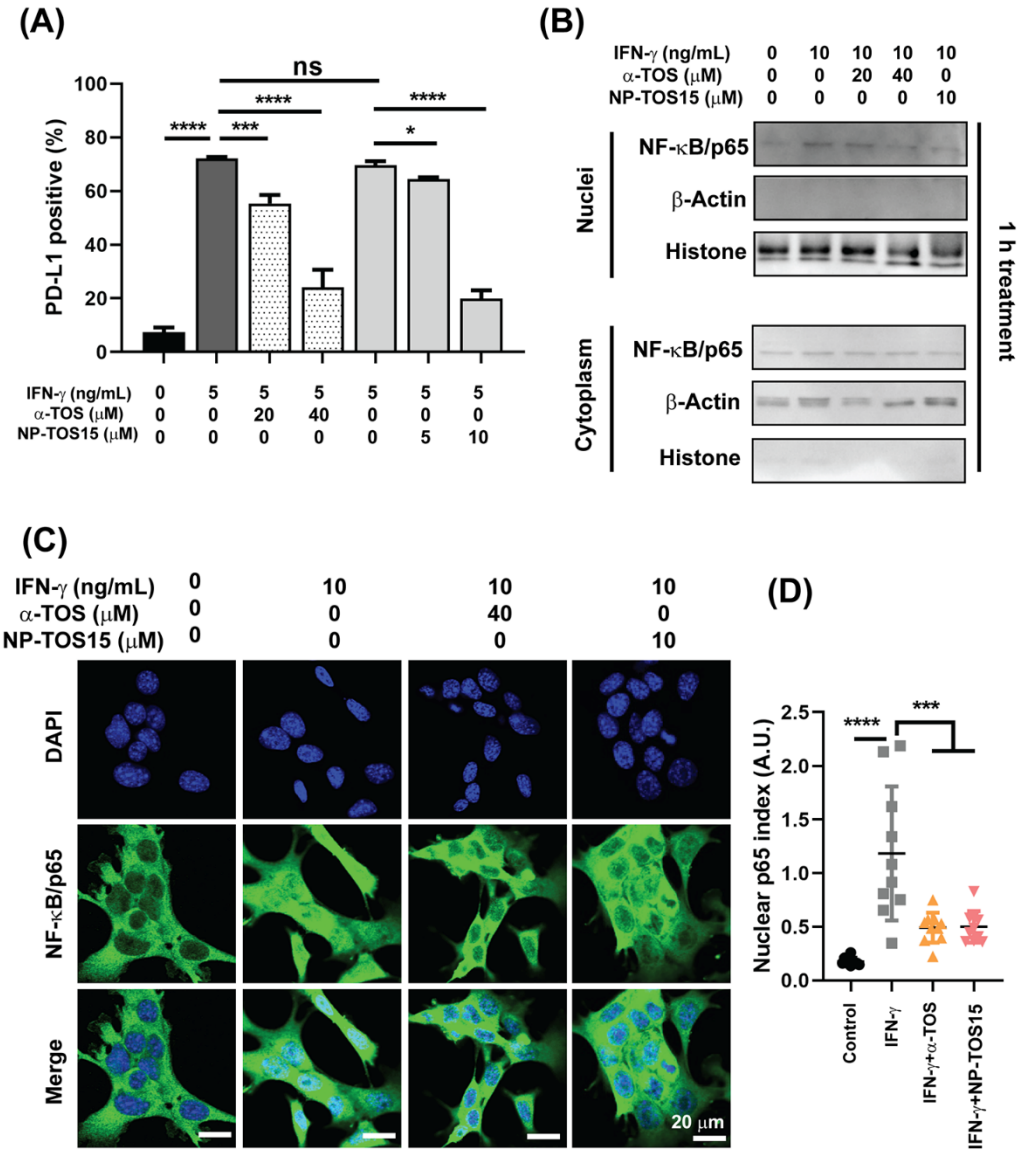

Figure 6.4 The influence of α-TOS on IFN-γ induced PD-L1 expression and translocation of NF-κB. (A) The PD-L1 regulation effect of α-TOS and IFN-γ after 48 h. **(B)** The western blotting bands for NF-κB p65 protein located in nuclei and cytoplasm after 1 h treatment. **(C)** Immunofluorescent images for visualising the intracellular distribution of p65 subunit in NF-κB complex. **(D)** The p65 index obtained from fluorescence located in nuclei area.

Very remarkably, free α-TOS and NP-TOS15 in combination with IFN-γ downregulated IFN-γ-induced PD-L1 expression in a dose-dependent manner (Figure 6.4A). To modulate PD-L1 expression in 4T1 to a significantly low level (~20%), the α-TOS concentration was 4 times less for NP-TOS15 than for free α-TOS (10 μM v.s. 40 μM). As the blank NPs (e.g. NP-TOS0)

could not reverse PD-L1 induction (data not shown), the enhanced reversion efficacy of NP-TOS15 is due to the enhanced α-TOS delivered by NPs (Figure 6.2). The PD-L1 induction by IFN-γ and reversion by α-TOS has been further verified by RT-PCR. As shown in Figure S6.6, the β-actin normalised PD-L1 expression suggested a limited influence of free α-TOS (20 μM) on pristine PD-L1 expression, but a significant upregulation upon IFN-γ (5 ng/mL) stimulation. Combined with 40 μM of α-TOS, the PD-L1 expression dropped to the level similar to that in the control group.

Interestingly, intracellular PD-L1 induction was also reversed by α-TOS (Figure S6.7). According to calculated data in Table S6.3, free α-TOS only exerted weak inhibition to cytoplasm PD-L1, while this inhibition effect was enhanced in the combination therapy. Moreover, the effect that α-TOS reverses PD-L1 induction by IFN-γ was also observed in other cell lines such as MCF-7 and B16 (Figure S6.8), suggesting this down-regulation of PD-L1 induction is not related to a certain specific cell line, but the instinct of α-TOS.

Previous studies suggest that IFN-γ upregulates PD-L1 expression through regulating the translocation of NF-κB complex [11]. Therefore the migration of NF-κB, represented by its p65 subunit, was checked by western blot upon treatments (Figure 6.4B and S6.9). Within the initial 1 h, the IFN-γ treatment led to a quick accumulation of nuclear p65 protein by 2.4 times compared to the control. With α-TOS or NP-TOS15 involved in, the nuclear p65 decreased to a certain degree. Increasing the dose of α-TOS from 20 to 40 μM resulted in nuclear p65 decreasing from 2.1 to 0.7 times of that in the control. Note that 10 μM of α-TOS in NP-TOS15 treatment resulted in p65 nuclear accumulation (0.8 fold) comparable to that upon 40 μM α-TOS treatment.

Furthermore, the translocation of NF-κB p65 subunit was monitored via the immunofluorescence images (Figure 6.4C). The green signal from p65 antibody in the control group (first column) presented preferable accumulation in the cytoplasm. With 10 ng/mL IFN-γ treatment, the p65-related fluorescence was evenly distributed in nuclei and cytoplasm. The combination of α-TOS or NP-TOS15 with IFN-γ resulted in the p65 amount in nuclei comparable to that of the control group, with little merged p65/green and DAPI/blue area around the nuclei. The nuclear p65 index from ImageJ software analysis indicates that the treatment influence on the p65 distribution was significant (Figure 6.4D).

6.3.4 Inhibition of tumour progression

To validate the anticancer effect of NP-TOS15 in vivo, different formulations were injected intraperitoneally (i.p.) to Balb/c mice bearing 4T1 tumour every other day for 4 times. As shown in Figure 6.5A and anatomy images in Figure S6.10, IFN-γ, NP-TOS15, and NP-TOS15/ IFN-γ formulations showed a significant antitumor ability with the tumour growth rate of 63.4±23.0%, 27.0±3.8%, and 20.7±6.8%, respectively. The in vivo inhibition rate thus confirmed the anticancer ability of NP-TOS15. The similar trend was also observed for the tumour weigh collected at day 10 (Figure 6.5B). The IFN-γ treatment showed a large variation in both the tumour size and the tumour weight, reflecting the mouse individual difference. Mice treated with NP-TOS15 and NP-TOS15/IFN-γ formulations had a similar tumour inhibition rate, indicating IFN-γ did not enhance NP-TOS15 therapy until day 10 post injection. No significant changes in the mouse body weight were observed within the treatment (Figure S6.11), showing the used NP formulations are in the safe level, together with the H&E images presented below (Figure S6.12).

The 4T1 cells are able to metastasize to lung, causing the tumour recurrence after treatment [25]. However, early metastasis could not be observed from the morphology changes of the lung due to the limited cell number in this research (Figure S6.10). Therefore, the cancer cells from dissociated lungs were cultured to examine the early metastasis. As indicated in Figure 6.6A, mice treated with placebo exerted the highest metastasis index. In comparison, much less metastatic clones and much smaller metastasis index values were found in the lungs from mice treated with other three formulations. The metastasis index is in accordance with the migration inhibition trend obtained from in vitro assay (Figure 6.3E-F), confirming IFN-γ and/or NP-TOS15 did not compromise the inhibition of metastasis in vivo. A notable decrease of metastasis in the combination group (Figure 6.6B) was found, probably due to the combined anti-metastasis ability of both IFN-γ and α-TOS.

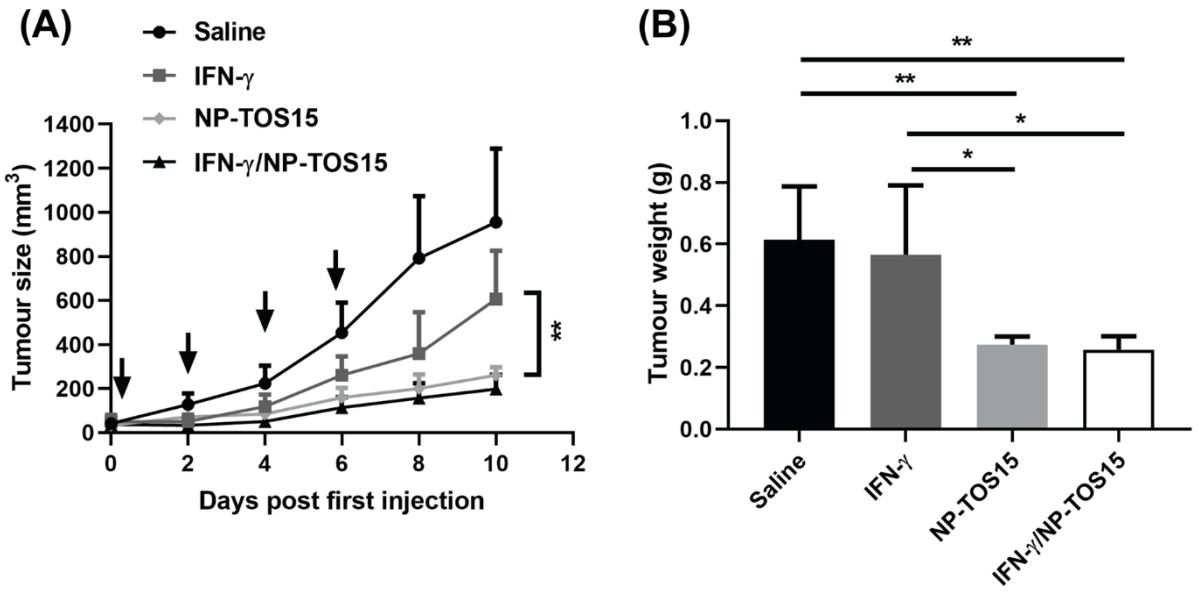

Figure 6.5 The anticancer effect of NP-TOS15 combined with IFN-γ in vivo. (A) Tumour growth curve, and **(B)** tumour weight in corresponding groups at day 10 post first injection were shown. (n = 5). Dosage for each injection: [IFN-γ] = 0.25 mg/kg, and/or [α-TOS] = 5 mg/kg in NP-TOS15.

To confirm the metastasis analysis, the H&E staining images of representative sections of lungs are illustrated in Figure 6.6C. Typical tumour nodules were observed in the saline group, visualising the metastasised cancer cells and their localisation as reported previously [33, 34]. Smaller and fewer nodules were found in lungs with IFN-γ and NP-TOS15 treatment, indicating the lung metastasis was inhibited by IFN-γ and NP-TOS15. After IFN-γ/NP-TOS15 combination therapy, the mouse lungs presented almost no nodules, suggesting that the combination therapy has significantly enhanced the inhibition of metastasis. In addition, no obvious pathological lesions in the heart, liver, spleen, and kidney were found in the H&E stained tissue images (Figure S6.12), indicating the good biocompatibility of these formulations, which can serve as a safe delivery system in vivo.

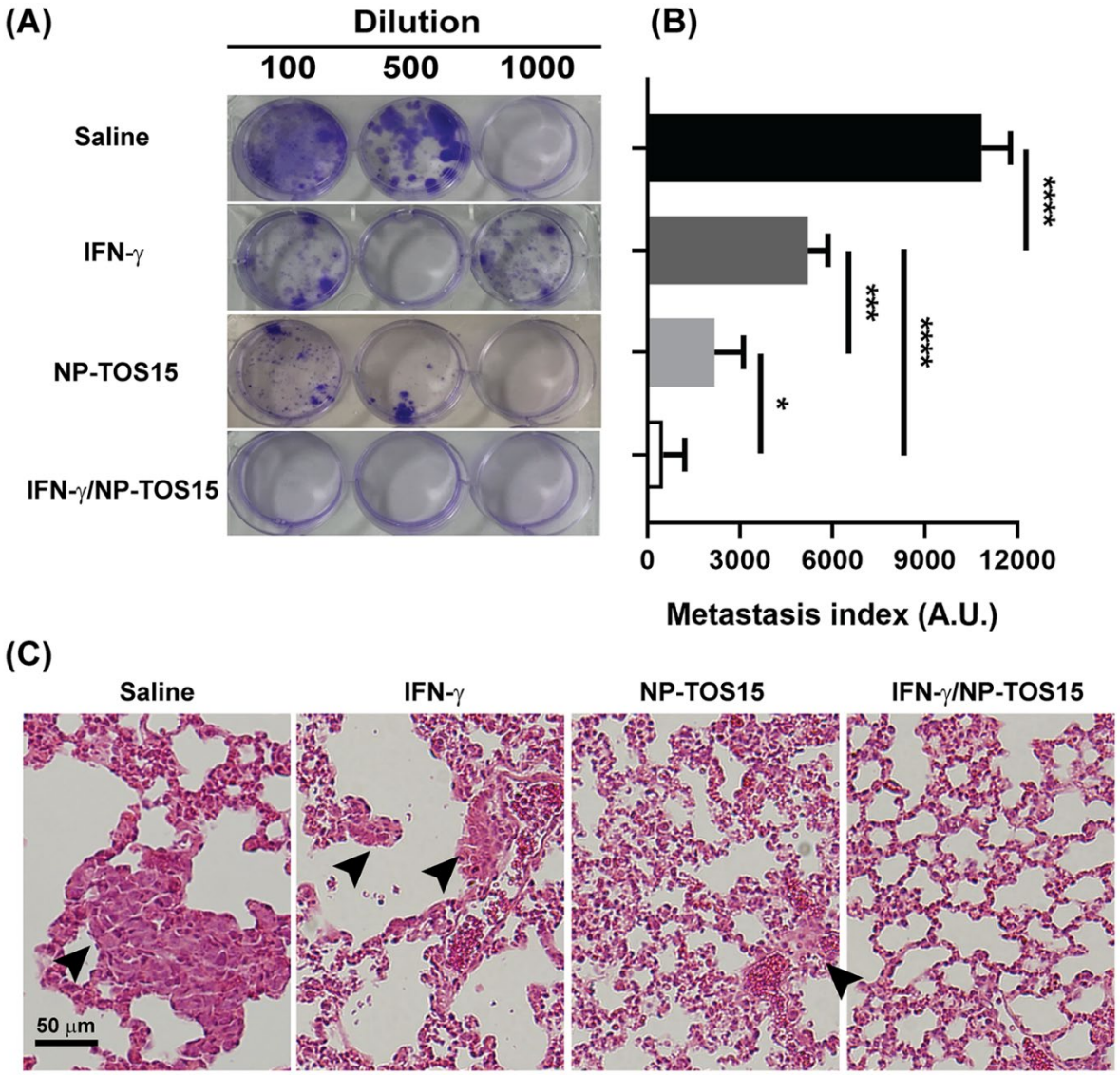

Figure 6.6 Inhibition of lung metastasis. (A) Images of 4T1 clones in plates, and **(B)** the histogram of metastasis index after selective incubation for 40 days with 60 μM of 6-thioguanine.; **(C)** Typical images of lung tissue sections with H&E staining taken with 10× lens were shown. Black arrows indicate typical tumour nodules.

6.3.5 Modulation of tumour immune microenvironment

To assess the modulation of tumour microenvironment, we harvested the tumour and dissociated cells for FACS analysis (Figure 6.7). The tumour cell population was sorted as CD45 and MHC-II double negative, and gated in the lower panel (black box) in each cell distribution (Figure 6.7A). The grey gating (in the 1st and 2nd quadrant) suggests a population

of either CD45 or MHC-II positive, predominated by infiltrated leukocytes and antigen presenting cells, and the red gating (in the 1st and 4th quadrant) the PD-L1 positive cell population. As shown, the tumour cells and infiltrated lymphocytes were separated clearly by the gating.

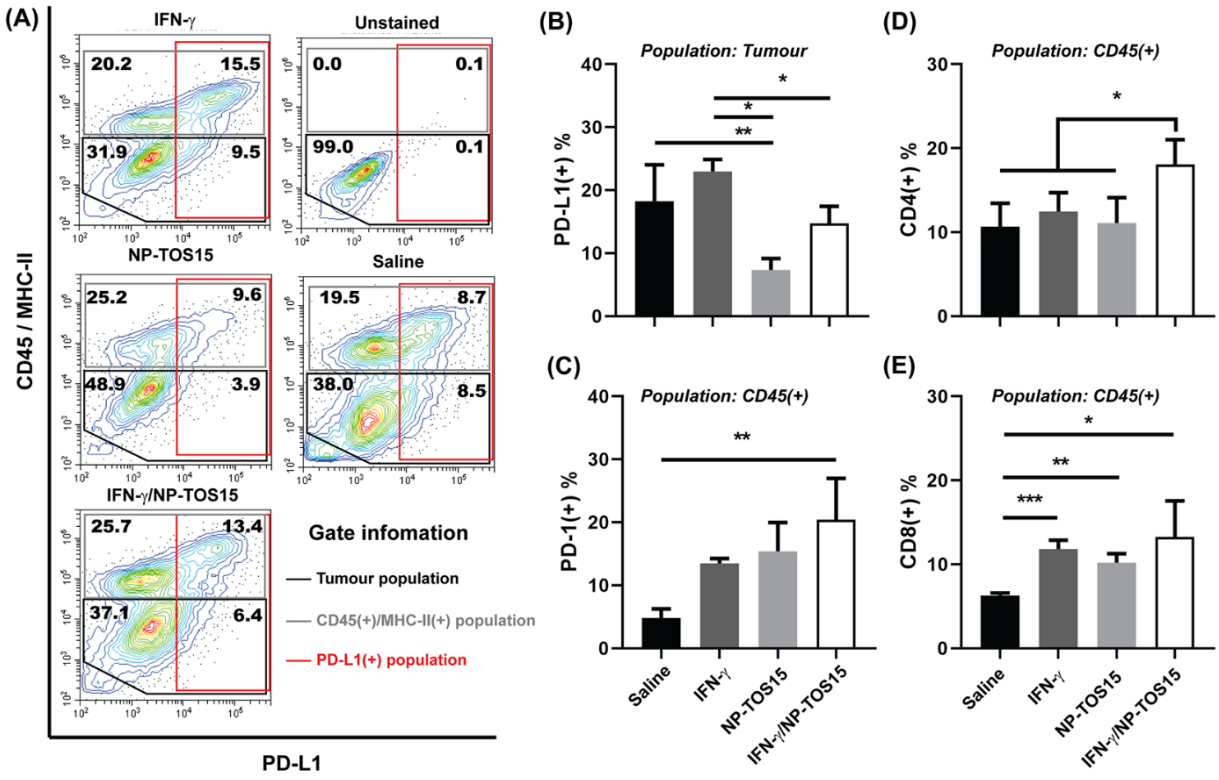

Figure 6.7 Modulation of the immune microenvironment. (A) Cell sorting information to obtain cancer cells for PD-L1 analysis. **(B)** PD-L1 expression in tumour population. Analysis of **(C)** $CD4^+$, **(D)** $CD8^+$, and **(E)** $PD\text{-}1^+$ TILs in tumour.

The PD-L1 expression in tumour cell population is shown in Figure 6.7B. Generally, IFN-γ induced PD-L1 expression, which could be reversed by NP-TOS in the same treatment, similar to the in vitro studies (Figure 6.4). IFN-γ treatment increased PD-L1 expression from 18% to 23%, whereas NP-TOS15 treatment significantly decreased the tumour cell PD-L1 expression singly or in combination (Figure 6.7B). Note the endogenous IFN-γ would have some influence in all 4 groups, so the expression of PD-L1 could be further stimulated in mice treated with exogenous IFN-γ or IFN-γ/NP-TOS15. Therefore, NP-TOS15 treatment led to the lowest PD-L1 expression in tumour cells and IFN-γ/NP-TOS15 the second lowest, as endogenous IFN-γ

was much less than the injected dose [35, 36]. The PD-L1 expression in CD45 and/or MHC-II positive population (Figure S6.13) is quite similar to that in the cancer cells but not significantly.

Next, cells from tumour tissues were assorted by the CD45 expression for analysis of $CD4^+$, $CD8^+$, and PD-1^+ tumour infiltrated lymphocytes (TILs, Figure S6.14 and S6.15). As shown in Figure S6.16, the recruitment of $CD45^+$ cells was enhanced after IFN-γ and/or NP-TOS15 treatment (32-35% v.s. 20% in the control group), suggesting the infiltration of leukocytes has surged. Moreover, the $CD4^+$ and $CD8^+$ TILs increased after IFN-γ/NP-TOS15 combination therapy (Figure 6.7D and E), indicating a pro-antitumor modulation in tumour microenvironment. In addition, an increase of $CD8^+$ TILs in either IFN-γ or NP-TOS15 treatment group were also observed compared to the control group (Figure 6.7E), as the treatment facilitated anti-tumour immunity. In $CD45^+$ cell cohort, the PD-1 expression exhibited a slight increase in mice with IFN-γ and/or NP-TOS15 treatment (Figure 6.7C) [37].

6.4 Discussion

In this study, we provide a practical regimen to inhibit 4T1 breast cancer growth/metastasis. The NP-TOS15 NPs were developed for effective α-TOS drug delivery (Figure 6.1). Based on this efficient drug delivery platform, the IFN-γ/NP-TOS15 combination therapy effectively prevented cancer growth and metastasis (Figure 6.5 and 6.6). In general, the cancer cells have to invade the surrounding environment as the first step, which is then accompanied with the local immunosuppression [4, 38]. With the IFN-γ/NP-TOS15 combination therapy, the tumour immune microenvironment was modulated to facilitate anti-tumour immunity (Figure 6.7). The tumour PD-L1 expression was controlled to a moderate level, and the tumour microenvironment was tentatively ameliorated with more leukocyte infiltration, increase of $CD4^+$ and $CD8^+$ TILs, and activation of T lymphocytes. Meanwhile, NP-TOS and/or IFN-γ exhibited abilities to inhibit cancer cell migration in vitro (Figure 6.3E and F), benefiting the metastasis inhibition. As a consequence, our combination regimen has shown much less lung metastasis compared to the single IFN-γ or NP-TOS15 treatment.

Herein, we first reported how α-TOS facilitates immunity by reversing the PD-L1 induction. Due to its influence on NF-κB signalling, α-TOS downregulates the PD-L1 expression induced by IFN-γ (Figure 6.4), through decreasing the synthesis and transportation of p65 protein from the cytoplasm to the cell membrane. These phenomena were further validated in the mouse

model (Figure 6.7). Although the existence of endogenous IFN-γ (~1 ng/mL [39]) may show some influence, more exogenous IFN-γ (0.25 mg/kg) was administrated to mice to strengthen its induction of PD-L1 expression. The IFN-γ-induced tumour PD-L1 expression decreased tremendously when in combination with NP-TOS15 compared to that with IFN-γ treatment only. As a consequence, the immune surveillance in the tumour microenvironment tends to be modulated to be anti-tumour active.

Simultaneously, tumour growth was also efficiently reduced with different treatments. In particular, NP-TOS15 formulation was 4 times effective in inducing cell death in vitro (Figure 6.3), and presented much better tumour growth control in vivo [40] when compared to free α-TOS. This enhancement in α-TOS anticancer ability is attributed to (1) the enhanced accumulation at the tumour site [24], and (2) FA-mediated quick cellular uptake (Figure 6.2). In contrast, IFN-γ exhibited limited anticancer effect in vitro (Figure 6.3), and its influence on tumour growth was also limited (Figure 6.5). Thus apparently, the anticancer efficacy in mice treated with IFN-γ/NP-TOS15 is similar to that with NP-TOS15 (Figure 6.5). Interestingly, IFN-γ-defined beneficial outcomes are seldom reported when used alone [6], as IFN-γ upregulates PD-L1 expression, causing the adaptive cancer immune resistance although it can also activate anticancer immunity. In this study, PD-L1 expression was well controlled by IFN-γ/NP-TOS15 combination treatment, tumour growth was effectively inhibited, and tumour metastasis was magnificently prevented in the short observation period. As further revealed, IFN-γ/NP-TOS15 combination treatment significantly promoted the infiltration of T helper cells and cytotoxic lymphocytes into the tumour tissue, which are expected to contribute to the effective prevention of tumour growth and metastasis. Of course, further studies are necessary to confirm the long-term effect of IFN-γ /NP-TOS15 combination therapy.

As shown in Figure 6.8, the IFN-γ/NP-TOS15 combination therapy provided benefit in both tumour site and remote organs (such as the lung). Considering its quick clearance after administration (30-270 min, [41, 42]), the IFN-γ affects the cancer therapy majorly by the quickly activating lymphocytes and boosting the immunity, improve lymphocyte recruitment, [43, 44], and further preventing cancer metastasis (Figure 6.8A). In this study, IFN-γ exerted metastasis inhibition (Figure 6.6) even with the lack of sufficient tumour inhibition (Figure 6.5). Within a short period post-administration, a small portion of IFN-γ may diffuse through circulation, and enhance immunity systematically. In contrast, NP-TOS15 NPs exert longer circulation time (detectable even after 24 h, [22]), and higher accumulation in tumour site

(Figure 6.8B). The NP-TOS15 NPs effectively inhibit tumour growth (Figure 6.5), which eliminate the potency of cancer cell migration. Importantly, they reverse the PD-L1induction of IFN-γ in tumour cells thus modulate the TME to facilitate lymphocyte infiltration (Figure 6.7). As a consequence, IFN-γ/NP-TOS15 combination therapy further prevents 4T1 metastasis (Figure 6.6).

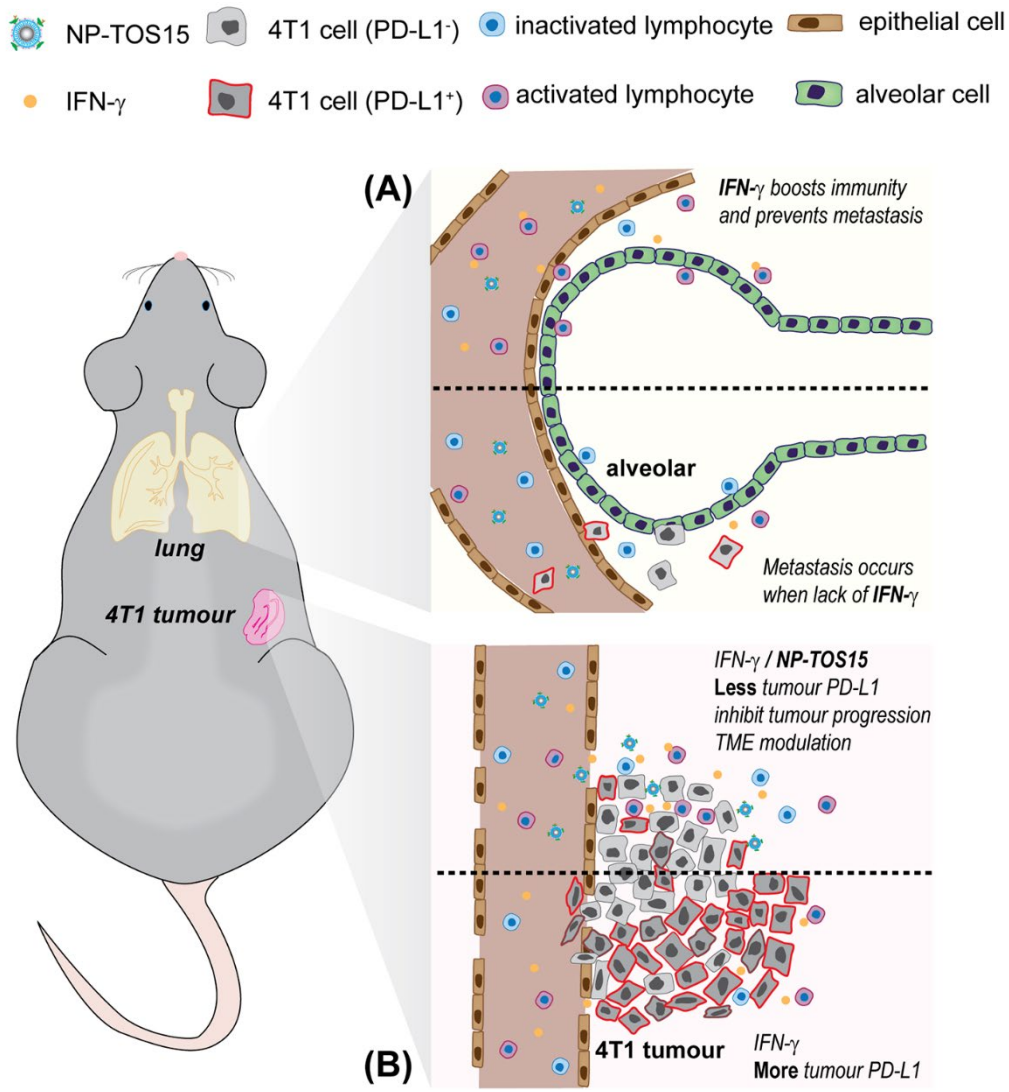

Figure 6.8 Schematically illustration of the effect of IFN-γ/NP-TOS15 treatment in different organs. (A) In the lung, IFN-γ boosts the immunity and prevents metastasis, while NP-TOS15 NPs may lack accumulation due to the integrity of vessels. **(B)** In the tumour site, IFN-γ treatment results in high PD-L1 expression and failure of tumour inhibition, while IFN-γ/NP-TOS15 combination treatment effectively controlled tumour progression, with a reverse of PD-L1 overexpression on tumour cells.

6.5 Conclusions

To conclude, we successfully fabricated FA-targeted NPs to deliver α-TOS for enhanced cancer therapy in combination with IFN-γ. The optimised NP-TOS15 NPs exhibited high α-TOS payload and efficacious cellular uptake. Compared to free α-TOS, NP-TOS15 NPs were more efficient in inhibition of breast cancer cell growth and migration with/without IFN-γ presence. Significantly, IFN-γ induced PD-L1 expression was effectively downregulated by NP-TOS15 via weakening NF-κB signalling. Therefore, the IFN-γ/NP-TOS combination therapy significantly inhibited tumour growth and prevented tumour metastasis to lung, with the immune system well activated via the good control of PD-L1 expression on the cancer cell surface. This research may inspire further work on the delivery of α-TOS for cancer immunotherapy for potential clinical application.

6.6 Reference

[1] J. Massagué, A.C. Obenauf, Metastatic colonization by circulating tumour cells, Nature 529(7586) (2016) 298.
[2] P. Parcesepe, G. Giordano, C. Laudanna, A. Febbraro, M. Pancione, Cancer-associated immune resistance and evasion of immune surveillance in colorectal cancer, Gastroenterol Res Pract. 2016 (2016).
[3] D.M. Pardoll, The blockade of immune checkpoints in cancer immunotherapy, Nat. Rev. Cancer 12(4) (2012) 252.
[4] J.A. Joyce, J.W. Pollard, Microenvironmental regulation of metastasis, Nat Rev Cancer 9(4) (2009) 239.
[5] E. Alspach, D.M. Lussier, R.D. Schreiber, Interferon γ and its important roles in promoting and inhibiting spontaneous and therapeutic cancer immunity, Cold Spring Harb Perspect Biol 11(3) (2019) a028480.
[6] Y. Nagai, H. Tsuchiya, E.A. Runkle, P.D. Young, M.Q. Ji, L. Norton, J.A. Drebin, H. Zhang, M.I. Greene, Disabling of the erbB pathway followed by IFN-γ modifies phenotype and enhances genotoxic eradication of breast tumors, Cell Rep. 12(12) (2015) 2049-2059.
[7] G.J. Freeman, A.J. Long, Y. Iwai, K. Bourque, T. Chernova, H. Nishimura, L.J. Fitz, N. Malenkovich, T. Okazaki, M.C. Byrne, Engagement of the PD-1 immunoinhibitory receptor by a novel B7 family member leads to negative regulation of lymphocyte activation, J. Exp. Med. 192(7) (2000) 1027-1034.
[8] Y.-M. Lin, W.-W. Sung, M.-J. Hsieh, S.-C. Tsai, H.-W. Lai, S.-M. Yang, K.-H. Shen, M.-K. Chen, H. Lee, K.-T. Yeh, High PD-L1 expression correlates with metastasis and poor prognosis in oral squamous cell carcinoma, PloS One 10(11) (2015) e0142656.
[9] L. Chen, D.L. Gibbons, S. Goswami, M.A. Cortez, Y.-H. Ahn, L.A. Byers, X. Zhang, X. Yi, D. Dwyer, W. Lin, Metastasis is regulated via microRNA-200/ZEB1 axis control of tumour cell PD-L1 expression and intratumoral immunosuppression, Nature Comm. 5 (2014) 5241.

[10] X. Jiang, J. Zhou, A. Giobbie-Hurder, J. Wargo, F.S. Hodi, The activation of MAPK in melanoma cells resistant to BRAF inhibition promotes PD-L1 expression that is reversible by MEK and PI3K inhibition, Clin. Cancer Res. 19(3) (2013) 598-609.
[11] K. Gowrishankar, D. Gunatilake, S.J. Gallagher, J. Tiffen, H. Rizos, P. Hersey, Inducible but not constitutive expression of PD-L1 in human melanoma cells is dependent on activation of NF-κB, PloS One 10(4) (2015) e0123410.
[12] Q. Lv, C. He, F. Quan, S. Yu, X. Chen, DOX/IL-2/IFN-γ co-loaded thermo-sensitive polypeptide hydrogel for efficient melanoma treatment, Bioactive materials 3(1) (2018) 118-128.
[13] Y. Yin, Q. Hu, C. Xu, Q. Qiao, X. Qin, Q. Song, Y. Peng, Y. Zhao, Z. Zhang, Co-delivery of Doxorubicin and Interferon-γ by Thermosensitive Nanoparticles for Cancer Immunochemotherapy, Mol. Pharmaceutics 15(9) (2018) 4161-4172.
[14] J. Neuzil, M. Tomasetti, A.S. Mellick, R. Alleva, B.A. Salvatore, M. Birringer, M.W. Fariss, Vitamin E analogues: a new class of inducers of apoptosis with selective anti-cancer effects, Curr. Cancer Drug Targets 4(4) (2004) 355-372.
[15] M.W. Fariss, M.B. Fortuna, C.K. Everett, J.D. Smith, D.F. Trent, Z. Djuric, The selective antiproliferative effects of α-tocopheryl hemisuccinate and cholesteryl hemisuccinate on murine leukemia cells result from the action of the intact compounds, Cancer Res. 54(13) (1994) 3346-3351.
[16] J. Neuzil, T. Weber, N. Gellert, C. Weber, Selective cancer cell killing by α-tocopheryl succinate, Br J Cancer 84(1) (2001) 87.
[17] T. Weber, M. Lu, L. Andera, H. Lahm, N. Gellert, M.W. Fariss, V. Korinek, W. Sattler, D.S. Ucker, A. Terman, Vitamin E succinate is a potent novel antineoplastic agent with high selectivity and cooperativity with tumor necrosis factor-related apoptosis-inducing ligand (Apo2 ligand) in vivo, Clin. Cancer Res. 8(3) (2002) 863-869.
[18] T.H. Kang, J. Knoff, W.-H. Yeh, B. Yang, C. Wang, Y.S. Kim, T.W. Kim, T.-C. Wu, C.-F. Hung, Treatment of tumors with vitamin E suppresses myeloid derived suppressor cells and enhances CD8+ T cell-mediated antitumor effects, PloS One 9(7) (2014) e103562.
[19] L.V. Ramanathapuram, J.J. Kobie, D. Bearss, C.M. Payne, K.T. Trevor, E.T. Akporiaye, α-Tocopheryl succinate sensitizes established tumors to vaccination with nonmatured dendritic cells, Cancer Immunol. Immunother. 53(7) (2004) 580-588.
[20] Y. Sun, Y. Zhao, L. Hou, X. Zhang, Z. Zhang, K. Wu, RRR-α-tocopheryl succinate induces apoptosis in human gastric cancer cells via the NF-κB signaling pathway, Oncol. Rep. 32(3) (2014) 1243-1248.
[21] Y. Wu, W. Gu, J. Tang, Z.P. Xu, Devising new lipid-coated calcium phosphate/carbonate hybrid nanoparticles for controlled release in endosomes for efficient gene delivery, J. Mater. Chem. B 5(34) (2017) 7194-7203.
[22] J. Tang, C.B. Howard, S.M. Mahler, K.J. Thurecht, L. Huang, Z.P. Xu, Enhanced delivery of siRNA to triple negative breast cancer cells in vitro and in vivo through functionalizing lipid-coated calcium phosphate nanoparticles with dual target ligands, Nanoscale 10(9) (2018) 4258-4266.
[23] Y. Wu, W. Gu, Z.P. Xu, Enhanced combination cancer therapy using lipid-calcium carbonate/phosphate nanoparticles as a targeted delivery platform, Nanomedicine 14(1) (2018) 77-92.
[24] F.-F. Fu, B.-Q. Zhou, Z.-J. Ouyang, Y.-L. Wu, J.-Y. Zhu, M.-W. Shen, J.-D. Xia, X.-Y. Shi, Multifunctional cholesterol-modified dendrimers for targeted drug delivery to cancer cells expressing folate receptors, Chinese J. Polym. Sci. 37(2) (2019) 129-135.

[25] D. Redelman, K.W. Hunter Jr, Microenvironment of the murine mammary carcinoma 4T1: Endogenous IFN-γ affects tumor phenotype, growth, and metastasis, Exp Mol Pathol. 85(3) (2008) 174-188.
[26] S.K. Kim, M.B. Foote, L. Huang, Targeted delivery of EV peptide to tumor cell cytoplasm using lipid coated calcium carbonate nanoparticles, Cancer Lett. 334(2) (2013) 311-318.
[27] J. Tang, L. Li, C.B. Howard, S.M. Mahler, L. Huang, Z.P. Xu, Preparation of optimized lipid-coated calcium phosphate nanoparticles for enhanced in vitro gene delivery to breast cancer cells, J. Mater. Chem. B 3(33) (2015) 6805-6812.
[28] Š. Koudelka, J. Mašek, J. Neuzil, J. Turánek, Lyophilised liposome - based formulations of α - tocopheryl succinate: Preparation and physico - chemical characterisation, J. Pharm. Sci. 99(5) (2010) 2434-2443.
[29] W. Stillwell, T. Dallman, A.C. Dumaual, F.T. Crump, L.J. Jenski, Cholesterol versus α-tocopherol: Effects on properties of bilayers made from heteroacid phosphatidylcholines, Biochemistry 35(41) (1996) 13353-13362.
[30] N. Yin, W. Ma, J. Pei, Q. Ouyang, C. Tang, L. Lai, Synergistic and antagonistic drug combinations depend on network topology, PloS One 9(4) (2014) e93960.
[31] J. Neuzil, M. Tomasetti, Y. Zhao, L.F. Dong, M. Birringer, X.F. Wang, P. Low, K. Wu, B.A. Salvatore, S.J. Ralph, Vitamin E analogs, a novel group of "mitocans," as anticancer agents: The importance of being redox-silent, Mol. Pharm. 71(5) (2007) 1185-1199.
[32] B. Kim, H.-H. Kim, Z.H. Lee, α-Tocopheryl succinate inhibits osteolytic bone metastasis of breast cancer by suppressing migration of cancer cells and receptor activator of nuclear factor-κB ligand expression of osteoblasts, J Bone Metab. 25(1) (2018) 23-33.
[33] C. Chen, Z. Nong, Q. Xie, J. He, W. Cai, X. Tang, X. Chen, R. Huang, Y. Gao, 2-Dodecyl-6-methoxycyclohexa-2, 5-diene-1, 4-dione inhibits the growth and metastasis of breast carcinoma in mice, Sci. Rep. 7(1) (2017) 6704.
[34] M. Smeda, A. Kieronska, M.G. Adamski, B. Proniewski, M. Sternak, T. Mohaissen, K. Przyborowski, K. Derszniak, D. Kaczor, M. Stojak, Nitric oxide deficiency and endothelial–mesenchymal transition of pulmonary endothelium in the progression of 4T1 metastatic breast cancer in mice, Breast Cancer Res. 20(1) (2018) 86.
[35] F.N. Lauw, A.J. Simpson, J.M. Prins, M.D. Smith, M. Kurimoto, S.J. Van Deventer, P. Speelman, W. Chaowagul, N.J. White, T. Van Der Poll, Elevated plasma concentrations of interferon (ifn)-γ and the Ifn-γ—inducing cytokines interleukin (il)-18, Il-12, and Il-15 in severe melioidosis, J. Infect. Dis. 180(6) (1999) 1878-1885.
[36] G.C. Koo, Y.-H. Gan, The innate interferon gamma response of BALB/c and C57BL/6 mice to in vitro Burkholderia pseudomallei infection, BMC Immunol. 7(1) (2006) 19.
[37] S. Simon, N. Labarriere, PD-1 expression on tumor-specific T cells: Friend or foe for immunotherapy?, Oncoimmunology 7(1) (2018) e1364828.
[38] Q. Gao, X.-Y. Wang, S.-J. Qiu, I. Yamato, M. Sho, Y. Nakajima, J. Zhou, B.-Z. Li, Y.-H. Shi, Y.-S. Xiao, Overexpression of PD-L1 significantly associates with tumor aggressiveness and postoperative recurrence in human hepatocellular carcinoma, Clin Cancer Res 15(3) (2009) 971-979.
[39] M. Jupelli, M.N. Guentzel, P.A. Meier, G. Zhong, A.K. Murthy, B.P. Arulanandam, Endogenous IFN-γ production is induced and required for protective immunity against pulmonary chlamydial infection in neonatal mice, J Immunol. 180(6) (2008) 4148-4155.

[40] K. Kogure, S. Manabe, S. Hama, A. Tokumura, K. Fukuzawa, Potentiation of anti-cancer effect by intravenous administration of vesiculated α-tocopheryl hemisuccinate on mouse melanoma in vivo, Cancer Lett. 192(1) (2003) 19-24.
[41] I. RUTENFRANZ, H. KIRCHNER, Pharmacokinetics of recombinant murine interferon-γ in mice, J Interferon Res 8(5) (1988) 573-580.
[42] R.J. Wills, Clinical Pharmacokinetics of Interferons, Clin. Pharmacokinet. 19(5) (1990) 390-399.
[43] J.W. Greiner, F. Guadagni, D. Goldstein, R.V. Smalley, E.C. Borden, J.F. Simpson, A. Molinolo, J. Schlom, Intraperitoneal administration of interferon-gamma to carcinoma patients enhances expression of tumor-associated glycoprotein-72 and carcinoembryonic antigen on malignant ascites cells, J Clin Oncol 10(5) (1992) 735-746.
[44] H.M. Karpoff, C. Tung, B. Ng, Y. Fong, Interferon gamma protects against hepatic tumor growth in rats by increasing Kupffer cell tumoricidal activity, Hepatology 24(2) (1996) 374-379.

6.7 Supporting information

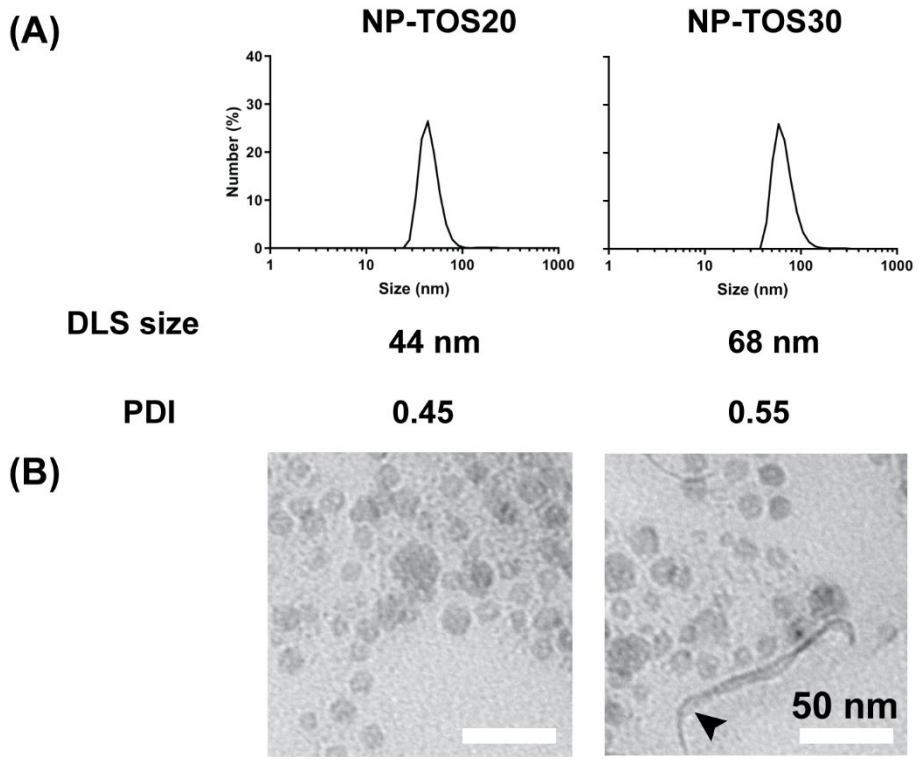

Figure S6.1 Characterization of LCCP NPs with α-TOS loading. **(A)** Hydrodynamic size and **(B)** corresponding morphology from TEM images. Black arrow in **(B)** indicating the abnormal structures (non-LCCP shaped structures). **Scale bar:** 50 nm.

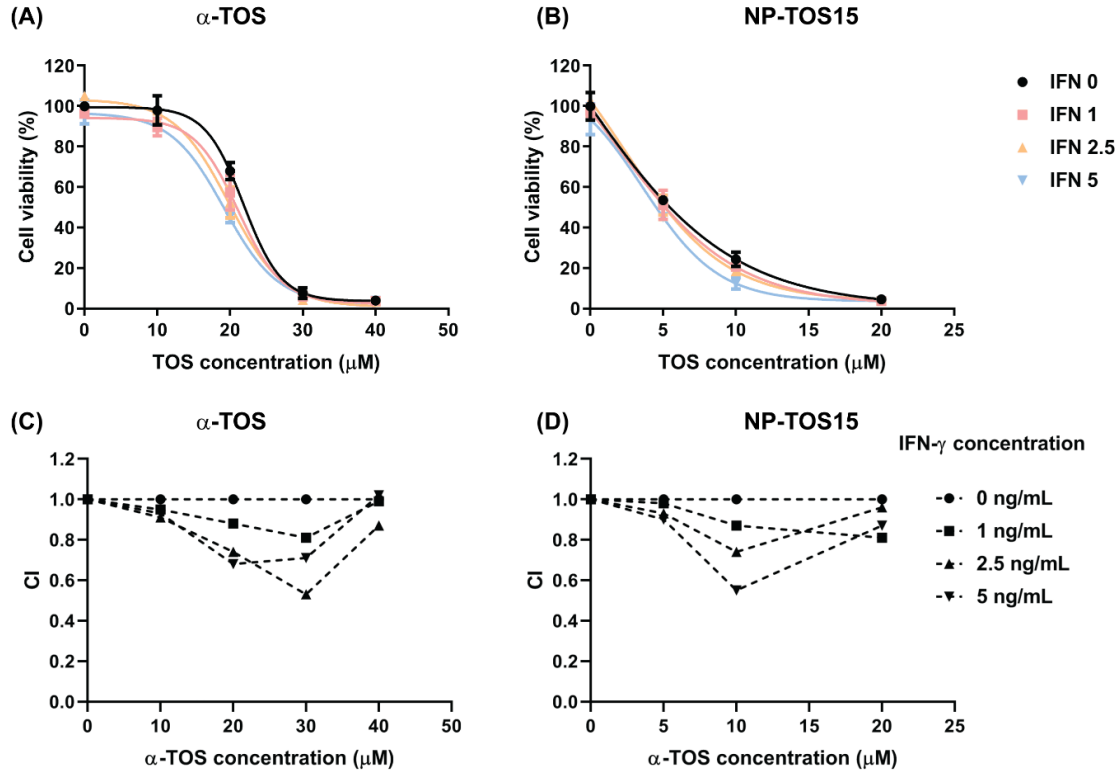

Figure S6.2 The combined inhibition of IFN-γ with **(A)** α-TOS or **(B)** NP-TOS15 for 48 h. The combination index (CI*) values for **(C)** α-TOS and **(D)** NP-TOS15.

* CI = [TOS+IFN]/([TOS]*[IFN])

Where [TOS] is the viability of cells with α-TOS or NP-TOS15, [IFN] the viability with IFN-γ, and [TOS+IFN] the viability with combination therapy.

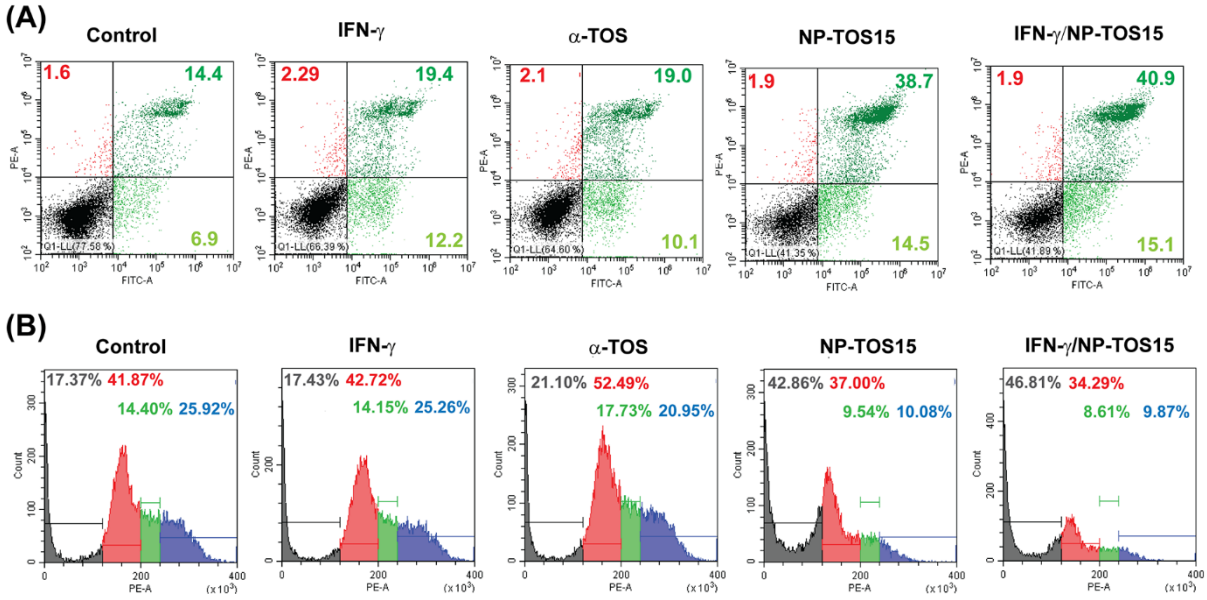

Figure S6.3 The influence on **(A)** apoptosis induction and **(B)** cell cycle arrest to 4T1 cells with 5 ng/mL IFN-γ, 20 μM α-TOS, and/or 10 μM NP-TOS15 for 24 h. Colors indicating different phases in cell cycle. Grey, sub-G1; red, G1; green, S; and blue, G2/M.

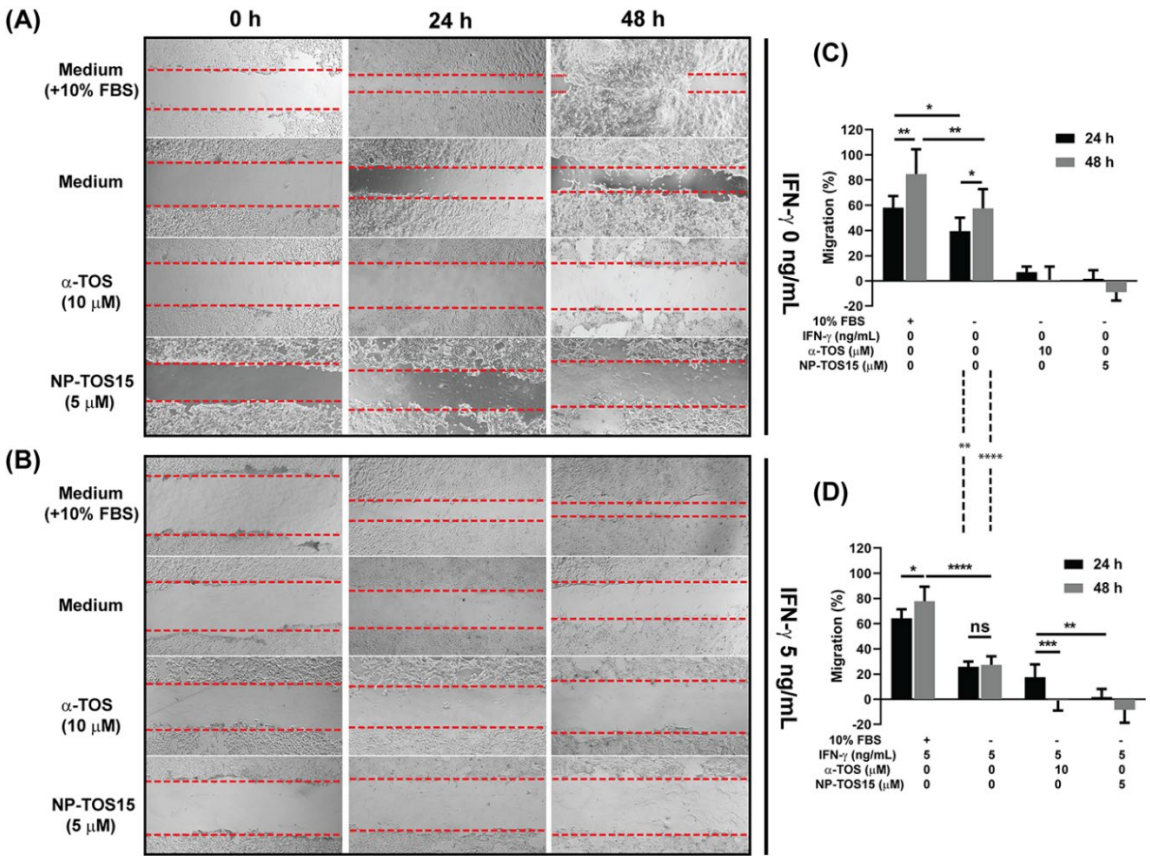

Figure S6.4 (A) and (B) Images of cells with different treatment, with dashed red line schematically shown the wound distance. **(C) and (D)** Statistical data.

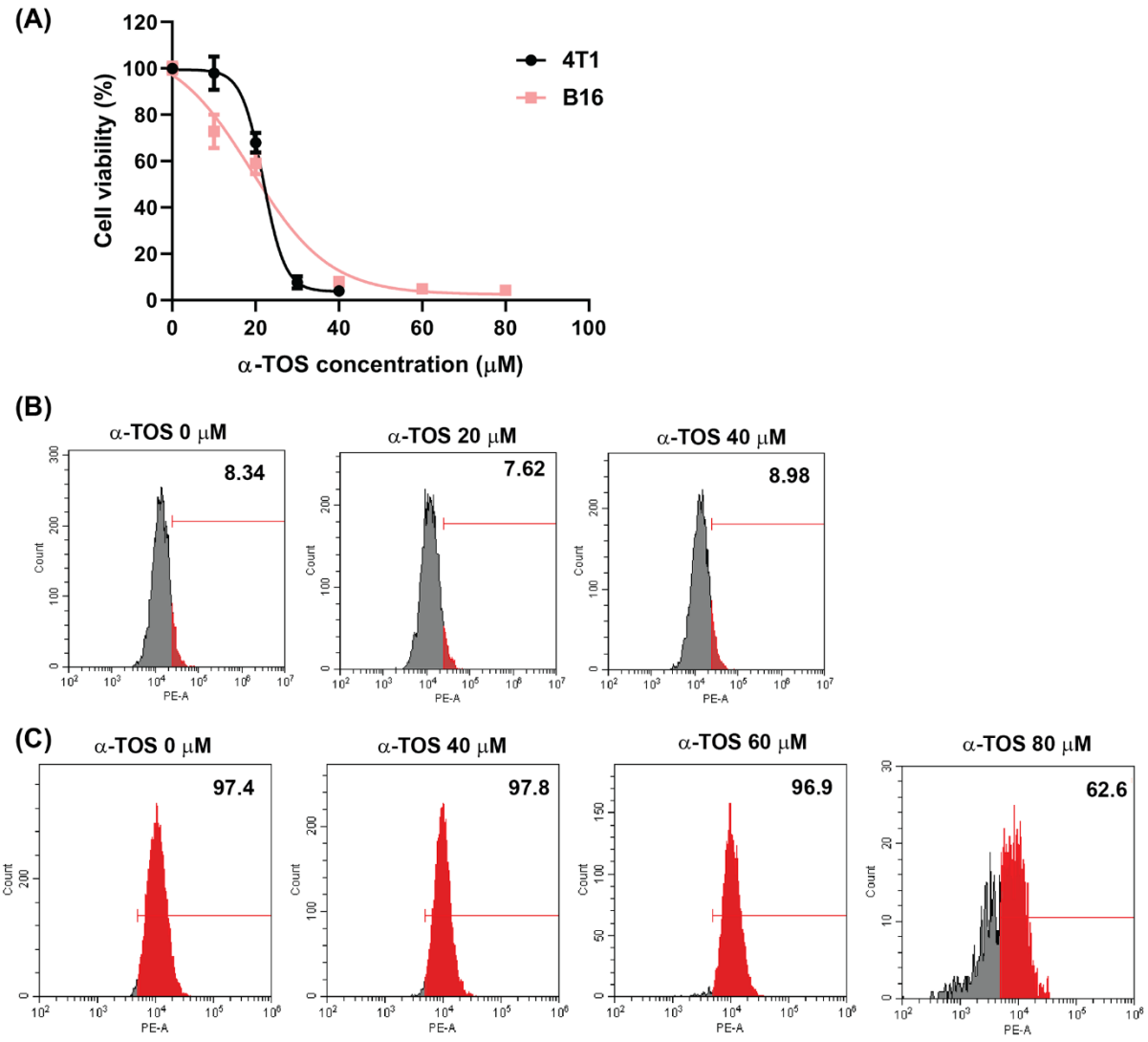

Figure S6.5 (A) The cell viability of 4T1 and B16 to α-TOS at different concentrations for 48 h. **(B)** Surface expression of PD-L1 in 4T1 cells with 48 h treatment of α-TOS. **(C)** Surface expression of PD-L1 in B16 cells with 48 h treatment of α-TOS. The number (upper right corner) in (B) and (C) indicated the PD-L1 positive percentage.

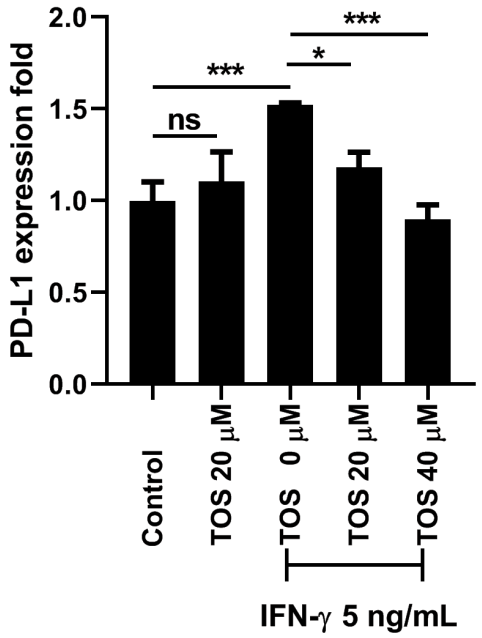

Figure S6.6 Quantification of the PD-L1 mRNA expression after 24 h treatment

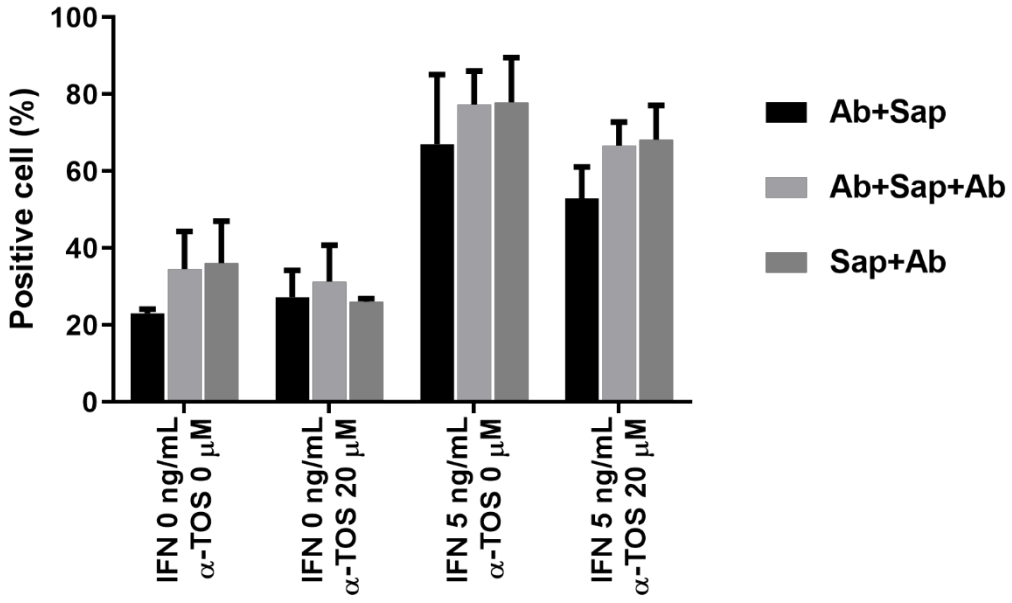

.

Figure S6.7 Intracellular PD-L1 expression with IFN-γ and/or α-TOS for 48 h. After co-culturing upon IFN-γ/α-TOS, the cells with different treatments were represented as following: **Ab+Sap**, PD-L1 antibody staining, followed by saponin treatment; **Ab+Sap+Ab,** PD-L1 antibody staining, saponin treatment, followed by a second time PD-L1 antibody staining;

Sap+Ab, isotype antibody staining, saponin treatment, followed by PD-L1 antibody staining. Ddetailed data and calculation refer to **Table S6.3**.

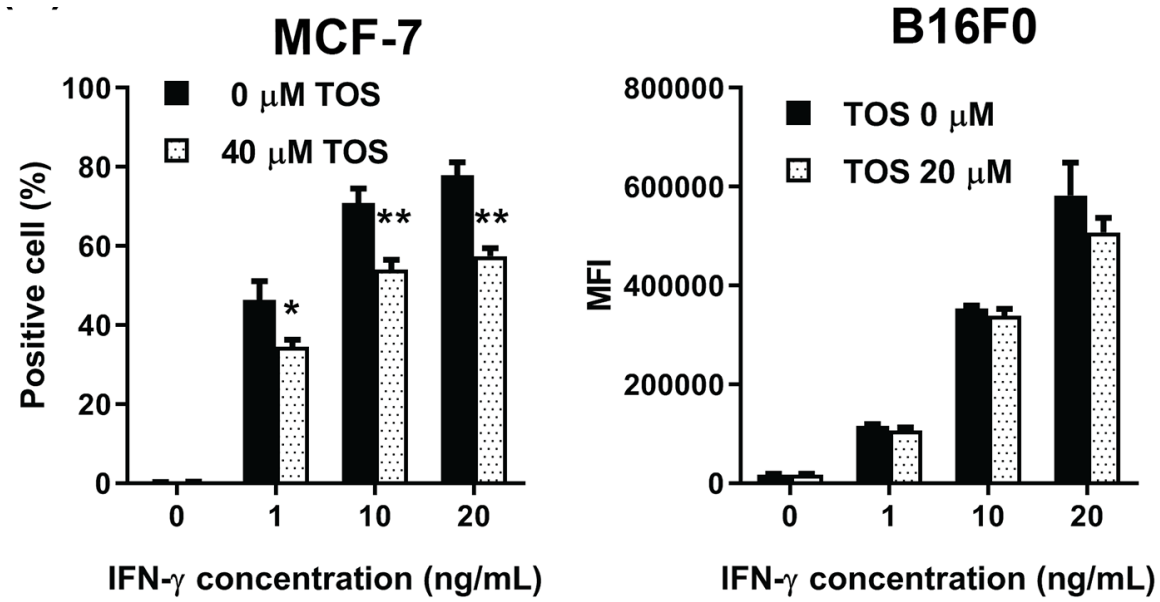

Figure S6.8 The inhibition of IFN-γ induced PD-L1 expression by free α-TOS after 48 h treatment.

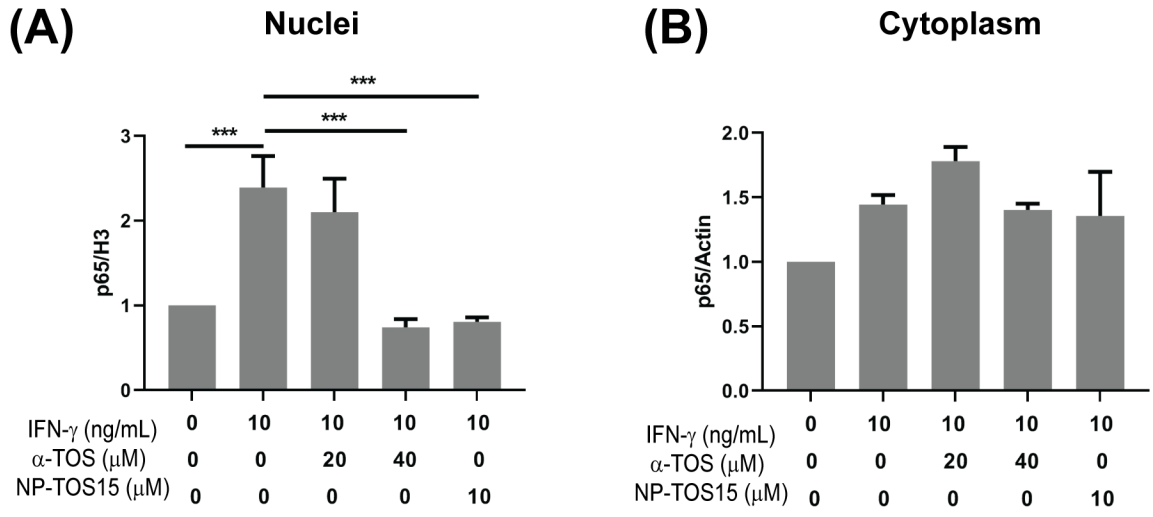

Figure S6.9 Densitometry of western blot bands for **(A)** Nuclei and **(B)** cytoplasm.

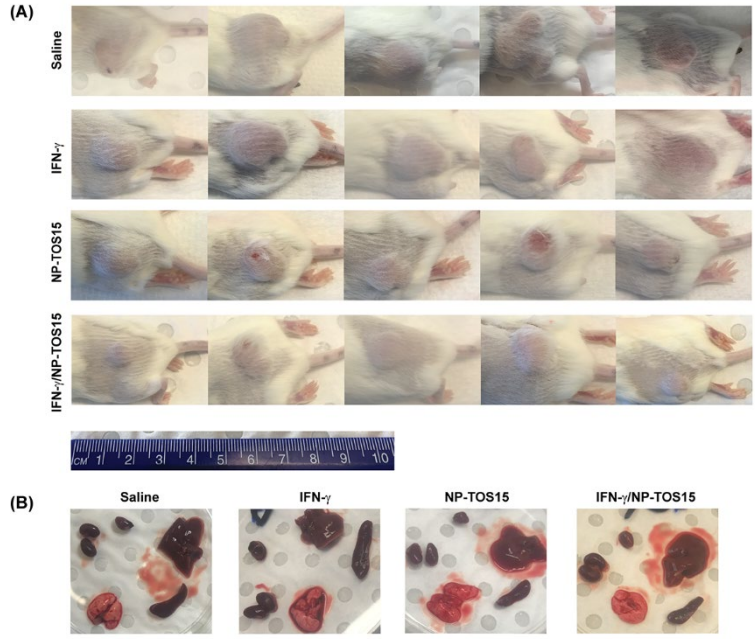

Figure S6.10 (A) Tumor images and **(B)** a representative organ image in each group.

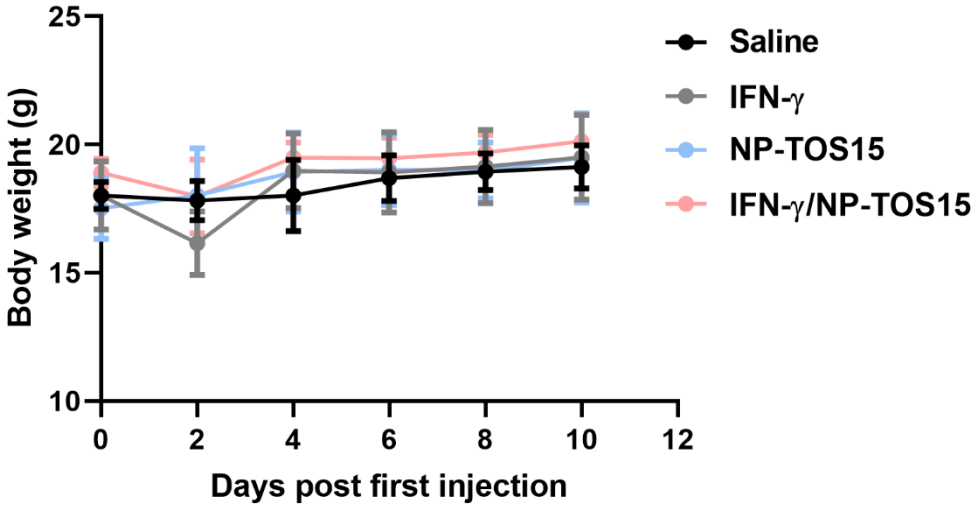

Figure S6.11 Body weight of mice with different treatment.

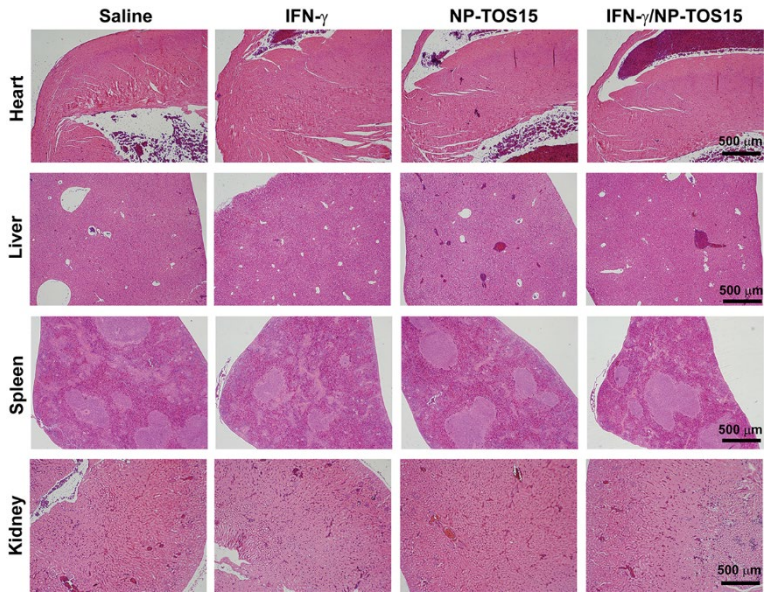

Figure S6.12 Histological images of major organs with hematoxylin & eosin staining.

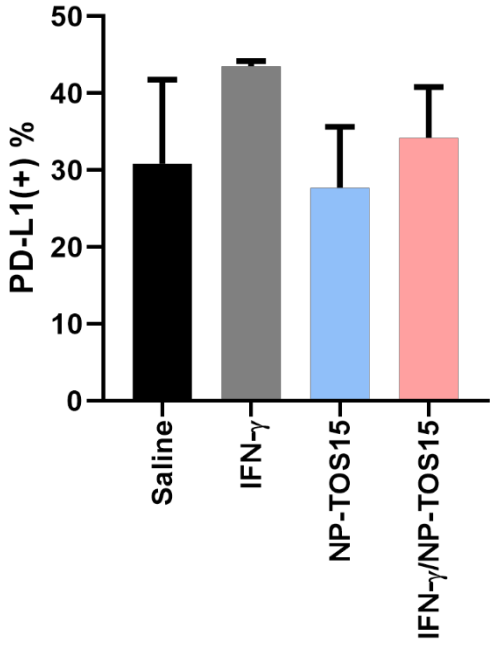

Figure S6.13 PD-L1 positive percentage in the CD45/MHC-II (+) population.

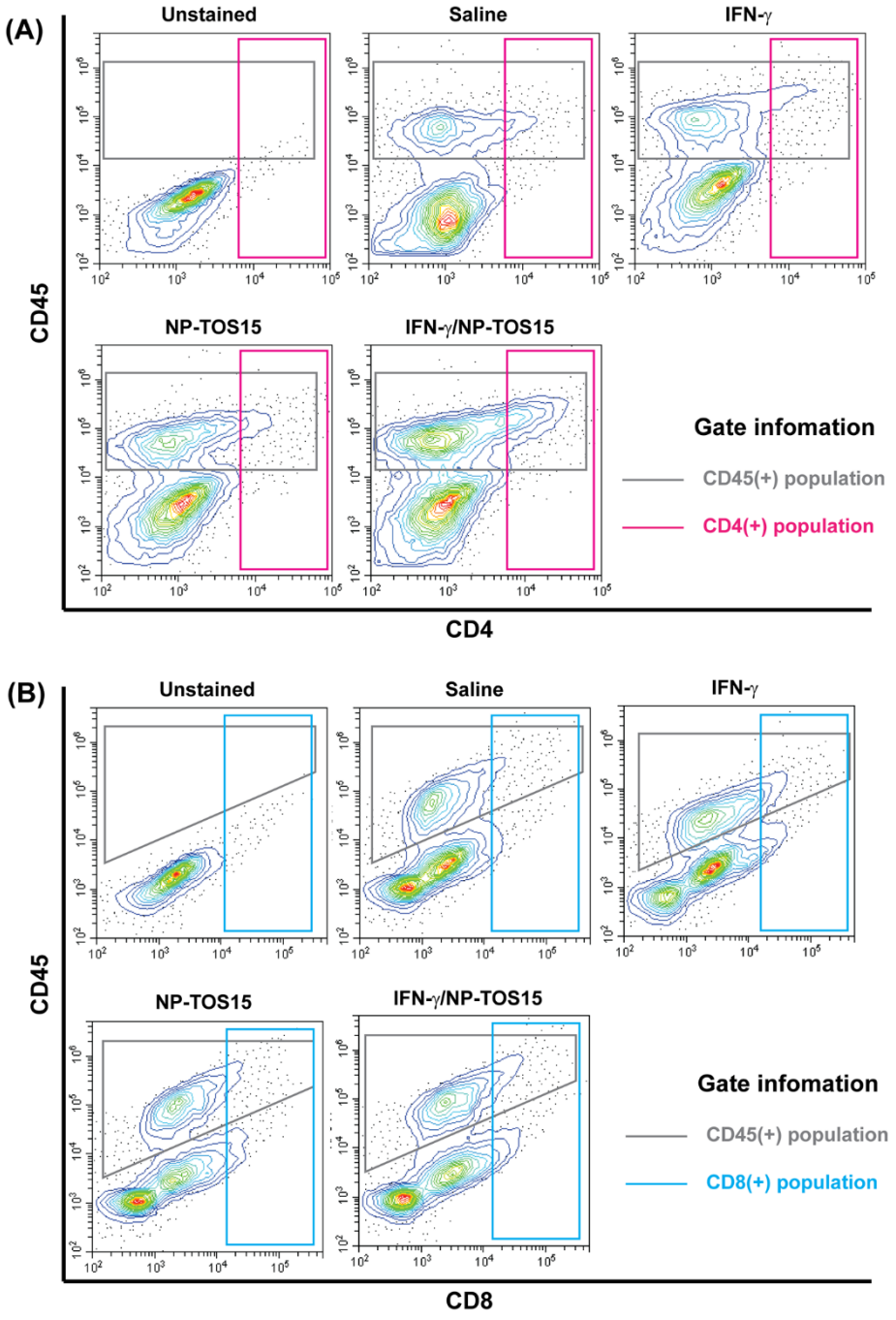

Figure S6.14 FACS images indicating the gating of cells to analyze **(A)** CD4+ and **(B)** CD8+ lymphocytes.

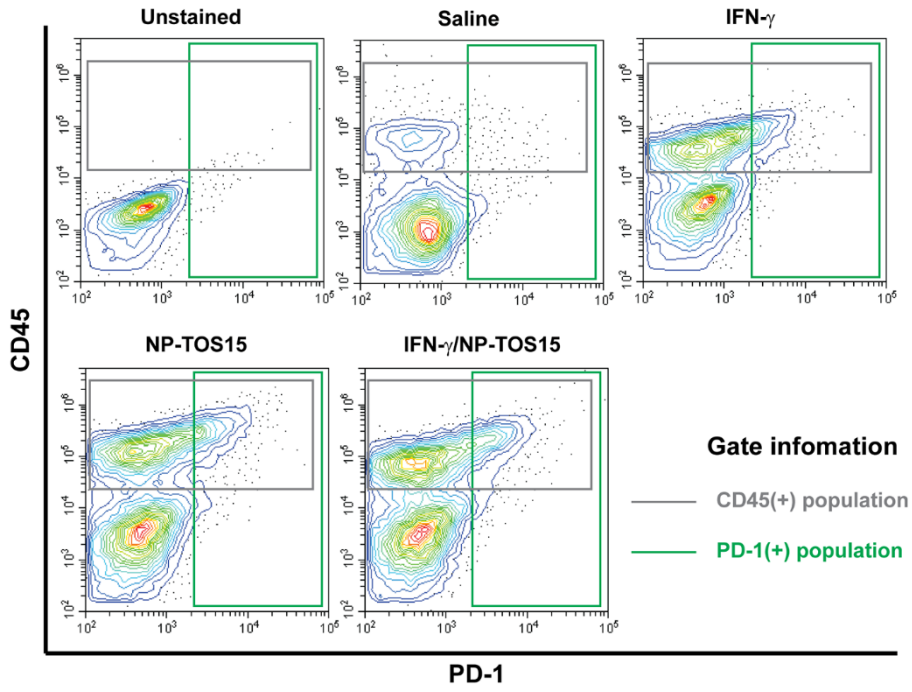

Figure S6.15 The gating information of PD-1 expression in tumor cite.

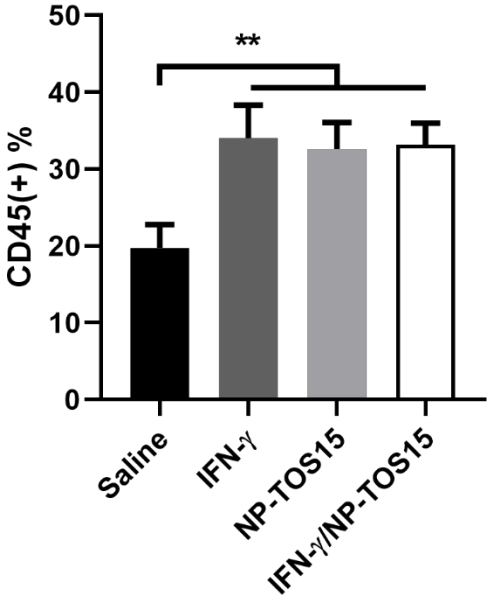

Figure S6.16 CD45 positive population percentage in different groups.

Table S6.1 Detailed information of antibodies

Name	Supplier	Catalogue Number
Purified anti-mouse CD274 (B7-H1, PD-L1) Antibody	BioLegend	124301
Cy3 Goat anti-rat IgG (minimal x-reactivity) Antibody	BioLegend	405408
Purified anti-mouse CD8a Antibody	BioLegend	100801
Purified anti-mouse CD279 (PD-1) Antibody	BioLegend	114101
FITC anti-mouse CD4 Antibody	BioLegend	100405
Purified anti-mouse/human Ki-67 Antibody	BioLegend	151202
APC anti-mouse CD45 Antibody	BioLegend	147707
APC anti-mouse I-A/I-E Antibody	BioLegend	107613

Table S6.2 Molar percentage of each composition in second layer lipid of NP-TOS.

NP code	DOPC %	Cholesterol %	DSPE-PEG	DSPE-PEG-FA	α-TOS
NP-TOS0	40	50	5	5	0
NP-TOS15	32.5	42.5	5	5	15
NP-TOS20	30	40	5	5	20
NP-TOS30	25	35	5	5	30

Table S6.3 The positive cell percentage data obtained/calculated from Figure S6.5.

IFN-γ 5 ng/mL	**α-TOS 20 μM**	**PD-L1 (s) surface Ab+Sap**	**PD-L1 (s+c) surface+cytoplasm Ab+Sap+Ab**	**PD-L1 (c) cytoplasm***
-	-	23.0	34.5	11.5
-	+	27.1	31.3	4.2
+	-	67.1	77.3	10.2
+	+	53.0	66.7	13.7

* The values of PD-L1 (s) and PD-L1 (s+c) were obtained from the average positive cell % of Ab+Sap, and Ab+Sap+Ab from Figure S6.5, respectively. The values of PD-L1 (c) were calculated by [PD-L1 (s+c)] – [PD-L1 (s)].

The staining method Ab+Sap resulted in the staining of surface PD-L1, with a portion of disruption due to Sap treatment. The staining method Ab+Sap+Ab resulted in further intracellular staining compensation. The staining method Sap+Ab resulted in the surface and cytoplasm PD-L1 staining together to the Sap disrupted cells. Theoretically, the results from Sap+Ab should be equal to that from corresponding Ab+Sap+Ab.

The PD-L1 (c) percentage exerted a 7% decrease in cytoplasm PD-L1 with 20 μM of α-TOS, and no significant changes in those cells with 5 ng/mL IFN-γ. However, the results of the combination showed a 2% increase in cytoplasm PD-L1. All the intracellular changes were not statistically significant, as the Sap treatment enlarged the variation of data.

Chapter 7

Discussion, Conclusion and Future Directions

7.1 General discussion

Calcium based nanoparticles (NPs) have great potentials in biomedical applications. In this thesis, we developed lipid-coated calcium carbonate/phosphate (LCCP) NPs to deliver various therapeutics to enhance cancer treatment efficacy. Here, the breakthrough in NP platforms and the demonstration in cancer therapy are discussed.

7.1.1 Breakthrough in NP development and payload strategy

Firstly, a novel NP was developed. As reviewed in Chapter 2, the calcium phosphate (CaP) and calcium carbonate (CaC) hybrid NPs maintain the characters from both materials, and exhibit some new merits. However, the stability and dispersity of these NPs limit their applications. To solve these issues, we considered employing lipid-like biomolecules to coat the NPs. Inspired by the synthesis techniques to prepare lipid-coated CaP (LCP) and CaC (LCC) NPs [1, 2], the LCCP NPs were designed and synthesised. As shown in Chapter 4, the obtained LCCP NPs were around 40 nm in size, much smaller than bare CaP/CaC hybrid NPs [3] and that with polymer coating [4]. Moreover, the LCCP NPs performed much better in colloidal stability, uniform dispersity, and gene transfection compared to that without lipid coating. In specific, the release pH of LCCP NPs is adjustable by changing the phosphate/carbonate ratio. The responsive pH of LCCP NPs locates between those of LCP and LCC NPs, and can be precisely controlled to the early/late endosomal pH. This property has accelerated the cargo release in cytosol after NP endocytosis.

Moreover, a new drug payload strategy was proposed to make lipid-coated calcium-based NPs in this study. Current payload method relies on co-precipitation of the therapeutics with calcium-based cores. This strategy endows the high payload of LCP/LCC to selected therapeutics (such as siRNA and phosphorylated peptides) [1, 2], as the phosphate groups from these molecules exhibit high affinity to calcium and easily form precipitates when they are mixed in the aqueous phase. However, for hydrophobic drug molecules without phosphate groups, this method seems not applicable. Inspired by the payload strategy of bilayer liposomes [5], we proposed to load a vitamin E (VE) derivative model drug, α-tocopheryl succinate (α-TOS), to the LCCP NPs by replacing the outer layer lipid. As demonstrated in Chapter 5 and 6, the LCCP NPs can entrap α-TOS in the outer layer without affecting the physical stability by replacing up to 15% of the outer layer lipids. The α-TOS loading in this specific structure is limited to the irregular lipid packing in the outer layer when some phospholipids are replaced by α-TOS. However, this payload is high enough and comparable to that in liposomes [6]. A previous study suggests the chromanol head of VE analogue can anchor to liposome by interacting with nearby phospholipids [5]. To extend, this strategy can be used in other lipid-coated NPs, including LCP and LCC, as well as many other hydrophobic drugs.

7.1.2 Demonstration in cancer therapy

Generally, the siRNAs can downregulate their target gene expression. In some cases, a specific siRNA treatment can be lethal to cancer cells, while the lethal gene and siRNA dosage to different cells may be different. To ensure efficient cancer cell killing, a commercialized cell death siRNA (CD siRNA) was used to demonstrate the gene delivery performance of developed LCCP NPs in Chapter 5. The definite target for CD siRNA is confidential, while previous studies indicate CD siRNA can induce cell apoptosis [7]. In this study, we confirmed the apoptosis induction effect, and illustrated that this effect was enhanced when combined with α-TOS in the same NPs. These observations demonstrate that our developed LCCP NPs are able to co-deliver two therapeutics into cancer cells efficiently to induce cell death.

Moreover, a cytokine interferon-gamma (IFN-γ) was strategically selected in this study (Chapter 6). As reviewed in Chapter 2, the main approach for IFN-γ to participate cancer inhibition is through the recruitment and maturation of immunogenic cells, although a direct pro-apoptotic behaviour to cancer cells via JAK-STAT pathway is observed [8, 9]. Therefore, we administered free IFN-γ molecules instead of using NP delivery method to induce the relevant immune responses in Chapter 6, as the NP delivery may facilitate IFN-γ internalisation

that is not required. Of note, related studies on IFN-γ delivered by NPs can also achieve a good anticancer effect in vivo, with moderate immune responses [10].

Particularly, some natural products, or derivatives, such as α-TOS, provide selective toxicity to malignant cells, which is related to the mitochondrial signalling regulation [11]. Meanwhile, the relative high lethal dosage of α-TOS limits its anticancer application. We have shown that the NP delivery enhanced α-TOS inhibition effect to cancer cells in Chapter 5, and firstly reported how α-TOS facilitated the immunity in cancer therapy in Chapter 6. The IFN-γ induced programme death ligand 1 (PD-L1) expression was downregulated by α-TOS loaded NPs via weakening NF-κB signalling. Further studies demonstrated that this regulation is applicable in other cell lines. Therefore, our studies inspire the practical idea that α-TOS can benefit anti-PD-L1 treatment universally.

7.1.3 Clinical translation and bottlenecks

The novel LCCP-based NPs have potential clinical translation outcomes. Herein, the possible applications and their prospective bottlenecks are discussed.

Firstly, an LCCP-based formula can be developed as a commercialised vector for gene therapy in clinic. This novel vector could overcome the drawbacks of viral vectors (such as immunogenicity and cytotoxicity) [12], and the bottlenecks of traditional CaP materials (such as size and surface charge) [13]. Moreover, the LCCP NPs are even more efficacious in siRNA-based gene therapy than the commercialised product (Oligofectamine®), as demonstrated in Chapter 4. This result would be strongly associated with the precisely controlled gene release within the endosomal pH range. However, there are still some bottlenecks for this clinical translation. A series of standard operation procedures (SOPs) and quality controls (QCs) should be determined to commercially manufacture LCCP NP products. Meanwhile, although lipids and CaP are biosafety materials, LCCP NPs should undergo long term observation after administration for investigating the chronic adverse effect and systematic influence. Moreover, the application in gene therapy also relies on the development of proper gene products (such as safe and efficient siRNAs that are approved for clinical use), and some of the ethical debate may lie in this aspect [14].

Secondly, we well documented the CD/TOS/FA NPs and their anticancer ability in multiple cancers in Chapter 5, and these results may inspire cancer combination therapy using siRNA and α-TOS. This therapy regimen illustrated synergetic/additive anticancer effect with the

possible mechanism demonstrated, and was tested in both melanoma and breast cancer cells. The major bottleneck lies in the application of CD siRNA. This commercialised product, with the confidential sequence, induces cancer cell apoptosis with unclarified mechanism, but need the official approval to be used in clinic.

Thirdly, the study of IFN-γ/NP-TOS15 combination therapy in Chapter 6 may inspire the current IFN-γ treatment in cancer. Current recombinant IFN-γ products failed in Phase II/III trials in melanoma patients due to low response rate and significant adverse effects [15, 16]. Recent studies implied PD-L1 induction may be the most important barrier in the cancer treatment application of IFN-γ [16]. On this foci, we demonstrated α-TOS could effectively reverse this PD-L1 induction and provided an efficient formula (NP-TOS15 NPs) for cancer therapy. The combination therapy is designed for obtaining a higher response rate. However, the NP-TOS15 NPs would not relieve the adverse effects introduced by the recombinant IFN-γ products (such as fever, injection site reactions, and flu-like symptoms), as the adverse effects are related to the hyperactivation of immune system. Moreover, the NP-TOS15 NPs may only benefit in selected cancer types. These NPs may be limited in improving the therapeutic effect in those patients with high constitutive PD-L1 expression, such as patients with melanoma and colon cancers.

7.2 Conclusions

In summary, we designed and synthesised LCCP nanoparticles (NPs) as potential drug/gene delivery platforms for combination cancer therapy. The controlled release of payloads from LCCP NPs was firstly adjusted for targeted endosomal pH release. With further folic acid (FA) modification, the targeted LCCP NPs were then employed for enhanced co-delivery of α-TOS and CD siRNA to kill cancer cells. At last, the optimised LCCP NPs were used for α-TOS delivery to enhance cancer immunotherapy in combination with IFN-γ.

To achieve precise release at the endosomal pH, the LCCP NPs were prepared by partially substituting phosphate with carbonate, and further employed for efficient gene transfection to B16F10 cells (Chapter 4). The obtained LCCP NPs were comparable with LCP NPs in colloidal stability, gene loading capacity, and cellular uptake efficacy. Moreover, LCCP NPs have higher sensitivity and quicker release under mild acidic pH conditions (6.0-5.5) than LCP NPs. This tendency endows faster siRNA release during/after the endocytosis and subsequently quicker gene down-regulation. However, the release profile divergence between LCCP and LCP NPs

did not affect their long term gene silencing efficacy. Therefore, this research suggests that the novel LCCP NPs were successfully developed, and the obtained NPs hold the potential as a promising quicker gene delivery vehicle with the precise release property at the endosomal pH.

After the establishment of the pristine LCCP NP platform, the LCCP NPs were further modified with FA for targeted co-delivery of α-TOS and CD siRNA to treat cancer in vitro and in vivo (Chapter 5). More specifically, the hydrophobic drug α-TOS was firstly loaded into the lipid bilayer by replacing some lipid molecules and the hydrohphilic drug siRNA in the core. The obtained NPs, with the similar physical structure and physicochemical properties to pristine LCCP NPs, were taken up more effectively by B16F0 cells via the FA-mediated pathway in a dose-dependent manner. In particular, the combination of CD siRNA and α-TOS in LCCP NPs more effectively inhibited cell growth in an additive/synergic manner. The mechanism may be involved in an enhanced apoptotic induction through interactions between ROS generation and Bcl-2 downregulation, and the cell cycle arrest in G1 phase. The in vivo study demonstrated that the obtained NPs loaded with two therapeutics led to more significant 4T1 tumour shrink than that with only single therapeutic agent. Moreover, the combination of CD siRNA and α-TOS induced remarkable decrease in both metastatic cancer clones and the lesion area in lung and liver. Thus, this research (Chapter 5) suggests that the FAR-targeted NPs are able to co-deliver hydrophilic (CD siRNA) and hydrophobic drugs (α-TOS), which provides a promising approach for targeted combination cancer therapy.

To be applied for a practical cancer therapy, the developed LCCP NPs (Chapter 4) and the new α-TOS loading strategy (Chapter 5) were combined with IFN-γ to develop cancer immunotherapy (Chapter 6). Compared to free α-TOS, the NP-TOS NPs were more efficient in inhibition of breast cancer cell growth and migration, no matter whether IFN-γ was present or not, presumably due to the efficacious cellular uptake. Importantly, the IFN-γ-induced PD-L1 expression was downregulated by α-TOS loaded NPs via weakening NF-κB signalling. The combination of NPs-loaded α-TOS and free IFN-γ relieved the tumour growth and metastasis, with the immune system efficiently activated due to downregulation of PD-L1 on cancer cells and increasing T helper cells. Therefore, this research may inspire further research on delivery of α-TOS for practical cancer immunotherapy.

Taken all together, the novel LCCP NPs with adjustable release property are promising nano-platforms for efficient delivery of various therapeutics to treat cancers. The development of LCCP NPs is highly significant for improving the current cancer treatment strategy by

providing (1) a novel nano-platform for efficient payload and controllable release at the precise endosomal pH; (2) the methodology for co-loading hydrophobic/hydrophilic drugs by LCCP NPs; and (3) practical regimens for efficacious drug/gene or drug/cytokine based combination cancer therapy.

7.3 Future directions

The novel LCCP NPs exhibit good biocompatibility and biodegradability, with almost no obvious toxicity found in the in vivo studies. Therefore, these NPs hold a great potential to act as a platform for other biomedical applications, and some potential examples are proposed below.

7.3.1 Mechanism study

Previous studies on LCP NPs reveal how cells overcome calcium toxicity introduced by the internalisation and dissolution of these NPs [17]. Therefore, we postulate that the LCCP NPs undergo a similar process to efflux exceed calcium ions, and the calcium, phosphate, and lipids released from this NP would not cause any toxicity to cells, however, the detailed mechanism is not clear.

Considering that LCCP NPs can also generate gas (CO_2), we face a new issue that how the calcium carbonate and the generated CO_2 affect the cells. In general, the carbonate could affect the intracellular/extracellular pH due to the following reactions:

$$CO_3^{2-} + H_2O \leftrightarrow HCO^{3-} + OH^-$$

$$HCO^{3-} + H_2O \leftrightarrow H_2CO_3 + OH^-$$

$$H_2CO_3 \leftrightarrow CO_2(g) + H_2O$$

Therefore, some mechanism studies are necessary to reveal whether and how the extracellular and intracellular pHs are maintained before, during and after LCCP endocytosis. The release study in Chapter 4 suggests a small portion of genes loaded in LCCP cores could be leaked at pH 7.4-6.5. This result may suggest some extracellular dissolution of LCCP NPs, especially the calcium carbonate precipitate in cores. So a proper method may be applied to investigate whether the calcium carbonate would dissolve, or partially dissolve before, during and after endocytosis. In addition, it remains unknown whether the generated CO_2 can induce some

stress to cancer cells. These studies can lead to a better understanding on the cellular effects of LCCP NPs, and may enlighten the application designs.

7.3.2 Modification of cholesterol in outer layer lipids

In this thesis, modification of LCCP NPs, including PEGylation and FA ligand conjugation, was achieved by replacing the phospholipid in the outer lipid layer (Chapter 5 and 6). Meanwhile, more than 30 mol% cholesterol is maintained in this layer. Further studies can focus on utilising these cholesterol molecules for NP modification. Some pioneering work on cholesterol conjugation chemistry may provide some practical methods for this modification [18-20]. Completing this study will result in modified LCCP NPs with more pristine phospholipid molecules in their outer layers, which may stabilise the NPs with more α-TOS loading.

7.3.3 Cancer immunotherapy

In this thesis, we used LCCP NPs to (1) deliver PD-L1 siRNA to knockdown constitutive PD-L1 expression (Chapter 4), and (2) deliver a drug to downregulate inducible PD-L1 expression (Chapter 6). These researches provide approaches for potential cancer immunotherapy. These LCCP-based PD-L1 suppression processes would be further applied for cancer vaccine development. As reviewed in Chapter 2, recent studies provide some examples of regimen designs of NP based cancer vaccine and their administration [21, 22]. Inspired by these pioneer outcomes, the LCCP NPs can be used to deliver some therapeutics to induce immunogenic cell death (ICD) for tumour-associated antigen release, followed by LCCP-based PD-L1 knockdown process. The outcome of this cancer vaccination development would lead to generate systemic immunological responses, eliminate the remaining tumour, and prevent tumour recurrence and metastasis.

7.3.4 Multi-functional LCCP NPs for diagnosis

In this thesis, we utilised LCCP NPs to deliver therapeutics for cancer therapy. Considering the NPs may generate gas (CO2), the LCCP NPs may be applied to enhance ultrasound imaging signals at the same time. As is well known, the calcium carbonate particles are able to generate CO2 gas molecules in neutral and slightly acidic conditions (such as tumour microenvironment pH). Current studies indicate the gas-generation NPs can be used as the contrast agent to improve the quality of ultrasound imaging. As introduced in Chapter 2, there is a successful

paradigm of calcium carbonate (CaC) NPs used as the ultrasound contrast agent [23] Similarly, the LCCP NPs may be used in ultrasound image-guided drug delivery in vivo. By adjusting the carbonate composition in LCCP NPs, the LCCP NPs may be optimised in aspects such as the gas generation rate and responsive pH. This design of diagnostic NP platforms thus takes advantage of by-products of the NP biodegradation for multifunctional applications in biomedicine.

7.4 References

[1] Y. Yang, J. Li, F. Liu, L. Huang, Systemic Delivery of siRNA via LCP Nanoparticle Efficiently Inhibits Lung Metastasis, Mol. Ther. 20(3) (2012) 609-615.
[2] S.K. Kim, M.B. Foote, L. Huang, Targeted delivery of EV peptide to tumor cell cytoplasm using lipid coated calcium carbonate nanoparticles, Cancer Lett. 334(2) (2013) 311-318.
[3] D. Zhao, C.-Q. Wang, R.-X. Zhuo, S.-X. Cheng, Modification of nanostructured calcium carbonate for efficient gene delivery, Colloids Surf., B 118 (2014) 111-116.
[4] C. Wu, M.-Q. Gong, B.-Y. Liu, R.-X. Zhuo, S.-X. Cheng, Co-delivery of multiple drug resistance inhibitors by polymer/inorganic hybrid nanoparticles to effectively reverse cancer drug resistance, Colloids Surf. B 149 (2017) 250-259.
[5] S. Koudelka, P.T. Knotigova, J. Masek, L. Prochazka, R. Lukac, A.D. Miller, J. Neuzil, J. Turanek, Liposomal delivery systems for anti-cancer analogues of vitamin E, J. Controlled Release 207 (2015) 59-69.
[6] Š. Koudelka, J. Mašek, J. Neuzil, J. Turánek, Lyophilised liposome - based formulations of α - tocopheryl succinate: Preparation and physico - chemical characterisation, J. Pharm. Sci. 99(5) (2010) 2434-2443.
[7] L. Li, W. Gu, J. Chen, W. Chen, Z.P. Xu, Co-delivery of siRNAs and anti-cancer drugs using layered double hydroxide nanoparticles, Biomaterials 35(10) (2014) 3331-3339.
[8] Y. Liu, X. Liang, X. Yin, J. Lv, K. Tang, J. Ma, T. Ji, H. Zhang, W. Dong, X. Jin, Blockade of IDO-kynurenine-AhR metabolic circuitry abrogates IFN-γ-induced immunologic dormancy of tumor-repopulating cells, Nat. Comm. 8 (2017) 15207.
[9] E. Alspach, D.M. Lussier, R.D. Schreiber, Interferon γ and its important roles in promoting and inhibiting spontaneous and therapeutic cancer immunity, Cold Spring Harb Perspect Biol 11(3) (2019) a028480.
[10] Y. Yin, Q. Hu, C. Xu, Q. Qiao, X. Qin, Q. Song, Y. Peng, Y. Zhao, Z. Zhang, Co-delivery of doxorubicin and interferon-γ by thermosensitive nanoparticles for cancer immunochemotherapy, Mol. Pharm. 15(9) (2018) 4161-4172.
[11] J. Neuzil, M. Tomasetti, Y. Zhao, L.F. Dong, M. Birringer, X.F. Wang, P. Low, K. Wu, B.A. Salvatore, S.J. Ralph, Vitamin E analogs, a novel group of "mitocans," as anticancer agents: The importance of being redox-silent, Mol. Pharm. 71(5) (2007) 1185-1199.
[12] V. Sokolova, M. Epple, Inorganic nanoparticles as carriers of nucleic acids into cells, Angew. Chem. Int. Ed. 47(8) (2008) 1382-1395.
[13] D. Olton, J. Li, M.E. Wilson, T. Rogers, J. Close, L. Huang, P.N. Kumta, C. Sfeir, Nanostructured calcium phosphates (NanoCaPs) for non-viral gene delivery: influence

of the synthesis parameters on transfection efficiency, Biomaterials 28(6) (2007) 1267-1279.
[14] L. Walters, J.G. Palmer, J.G. Palmer, The ethics of human gene therapy, Oxford University Press, USA1997.
[15] J.H. Schiller, M. Pugh, J.M. Kirkwood, D. Karp, M. Larson, E. Borden, Eastern cooperative group trial of interferon gamma in metastatic melanoma: an innovative study design, Clin. Cancer Res. 2(1) (1996) 29-36.
[16] M.R. Zaidi, G. Merlino, The two faces of interferon-γ in cancer, Clin. Cancer Res. 17(19) (2011) 6118-6124.
[17] Y.-C. Tseng, A. Yang, L. Huang, How does the cell overcome LCP nanoparticle-induced calcium toxicity?, Mol. Pharm. 10(11) (2013) 4391-4395.
[18] W. Miao, G. Shim, C.M. Kang, S. Lee, Y.S. Choe, H.-G. Choi, Y.-K. Oh, Cholesteryl hyaluronic acid-coated, reduced graphene oxide nanosheets for anti-cancer drug delivery, Biomaterials 34(37) (2013) 9638-9647.
[19] Y. Chi, X. Yin, K. Sun, S. Feng, J. Liu, D. Chen, C. Guo, Z. Wu, Redox-sensitive and hyaluronic acid functionalized liposomes for cytoplasmic drug delivery to osteosarcoma in animal models, J. Controlled Release 261 (2017) 113-125.
[20] F.-F. Fu, B.-Q. Zhou, Z.-J. Ouyang, Y.-L. Wu, J.-Y. Zhu, M.-W. Shen, J.-D. Xia, X.-Y. Shi, Multifunctional cholesterol-modified dendrimers for targeted drug delivery to cancer cells expressing folate receptors, Chinese J. Polym. Sci. 37(2) (2019) 129-135.
[21] Q. Chen, L. Xu, C. Liang, C. Wang, R. Peng, Z. Liu, Photothermal therapy with immune-adjuvant nanoparticles together with checkpoint blockade for effective cancer immunotherapy, Nat. Comm. 7 (2016) 13193.
[22] W. Song, L. Shen, Y. Wang, Q. Liu, T.J. Goodwin, J. Li, O. Dorosheva, T. Liu, R. Liu, L. Huang, Synergistic and low adverse effect cancer immunotherapy by immunogenic chemotherapy and locally expressed PD-L1 trap, Nat. Comm. 9(1) (2018) 2237.
[23] K.H. Min, H.S. Min, H.J. Lee, D.J. Park, J.Y. Yhee, K. Kim, I.C. Kwon, S.Y. Jeong, O.F. Silvestre, X. Chen, pH-controlled gas-generating mineralized nanoparticles: a theranostic agent for ultrasound imaging and therapy of cancers, ACS Nano 9(1) (2015) 134-145.

Appendix

Animal Ethics Approval Certificate

THE UNIVERSITY OF QUEENSLAND
AUSTRALIA

Office of Research Ethics
Director
Nicole Shively

Animal Ethics Approval Certificate

03-Dec-2018

Please check all details below and inform the Animal Ethics Unit within 10 working days if anything is incorrect.

Activity Details

Chief Investigator:	Professor Gordon Xu, Australian Institute for Bioengineering and Nanotechnology
Title:	Nanoparticles as adjuvants/delivery vehicles/imaging agents for disease treatment and diagnosis
AEC Approval Number:	AIBN/224/18
Previous AEC Number:	AIBN/082/18/
Approval Duration:	01-Aug-2018 to 01-Aug-2021
Funding Body:	ARC, NHMRC
Group:	Anatomical Biosciences
Other Staff/Students:	Wenyi Gu, Bing Zhang, Fatemeh Movahedi, Jianping Liu, Cora Lau, Nyoman Kurniawan, Li Li, Yilun Wu, Bei Li, Pei Cao, Jie Liu, Maya Patrick, Barbara Amts, Kym French
Location(s):	St Lucia Bldg 75 - AIBN

Summary

Subspecies	Strain	Class	Gender	Source	Approved	Remaining
Mice - non genetically modified	BALB/c	Adults	Female	Commercial breeding colony	277	277
Mice - non genetically modified	BALB/c Nude	Adults	Unknown	Commercial breeding colony	72	72
Mice - non genetically modified	C57Bl/6J	Adults	Female	Commercial breeding colony	56	56

Permits

Provisos

Approval Details

Description	Amount	Balance
Mice - non genetically modified (BALB/c, Female, Adults, Commercial breeding colony)		
1 Aug 2018 Initial approval	277	277
Mice - non genetically modified (BALB/c Nude, Unknown, Adults, Commercial breeding colony)		
1 Aug 2018 Initial approval	40	40
28 Nov 2018 Mod #1	32	72
Mice - non genetically modified (C57Bl/6J, Female, Adults, Commercial breeding colony)		
3 Dec 2018 Mod #2	56	56

Please note the animal numbers supplied on this certificate are the total allocated for the approval duration

Please use this Approval Number:

1. When ordering animals from Animal Breeding Houses
2. For labelling of all animal cages or holding areas. In addition please include on the label, Chief Investigator's name and contact phone number.
3. When you need to communicate with this office about the project.

It is a condition of this approval that all project animal details be made available to Animal House OIC.
(UAEC Ruling 14/12/2001)

The Chief Investigator takes responsibility for ensuring all legislative, regulatory and compliance objectives are satisfied for this project.

This certificate supersedes all preceding certificates for this project (i.e. those certificates dated before 03-Dec-2018)

Animal Ethics Unit
Office of Research Ethics
The University of Queensland

Cumbrae-Stewart Building
Research Road
St Lucia Qld 4072 Australia

+61 7 336 52925 (Enquiries)
+61 7 334 68710 (Enquiries)
+61 7 336 52713 (Coordinator)

animal.ethics@research.uq.edu.au
uq.edu.au/research